The Extension of a Non-Hydrostatic Dynamical Core into the Thermosphere

Submitted by Daniel Joe Griffin, to the University of Exeter as a thesis for the degree of Doctor of Philosophy in Mathematics, August 2018.

I certify that all material in this thesis which is not my own work has been identified and that no material has previously been submitted and approved for the award of a degree by this or any other University.

(Signature) ....

Daniel Joe Griffin

8th October 2018

Abstract

The non-hydrostatic dynamical core ENDGame (Even Newer Dynamics for the General Atmospheric Modelling of the Environment) is extended into the thermosphere to test its feasability as a whole-atmosphere dynamical core that can simulate the large scale fluid dynamics of the whole atmosphere from the surface to the top of the thermosphere at 600 km. This research may have applications in the development of a Sun-to-Earth modelling system involving the Met Office Unified Model, which will be useful for space weather forecasting and chemical climate modelling.

Initial attempts to raise the top boundary of ENDGame above ∼100 km give rise to instabilities. To explore the potential causes of these instabilities, a one-dimensional column version of ENDGame: ENDGame1D, is developed to study the effects of vertically propagating acoustic waves in the dynamical core. A 2D ray-tracing scheme is also developed, which accounts for the numerical effects on wave propagation. It is found that ENDGame's numerics have a tendency towards the excessive focussing of wave energy towards vertical propagation, and have poor handling of large amplitude waves, also being unable to handle shocks.

A key finding is that the physical processes of vertical molecular viscosity and diffusion prevent the excessive growth of wave amplitudes in the thermosphere in ENDGame, which may be crucial to improving ENDGame's stability as it is extended upwards. Therefore, a fully implicit-in-time implementation of vertical molecular viscosity and diffusion is developed in both ENDGame1D and the full three-dimensional version of ENDGame: ENDGame3D. A new scheme is developed to deal with the viscous and diffusive terms with the dynamics terms in a fully coupled way to avoid time-splitting errors that may arise.

The combination of a small amount of off-centring of ENDGame's semi-implicit formulation and the inclusion of vertical molecular viscosity and diffusion act to make ENDGame significantly more stable, as long as the simulation is able to remain stable up to the molecularly diffused region above an altitude of ∼130 km.

Contents

List of Illustrations **8**

1 Introduction **11**

1.1 Motivation for the use of a whole atmosphere model 11

1.2 Research aims 11

1.3 Potential applications and space weather 12

1.4 The structure of this thesis 14

2 Literature Review on Whole Atmosphere Modelling **15**

2.1 The physics of the thermosphere 15

2.2 Connections between terrestrial and space weather 17

2.3 Whole atmosphere modelling 20

2.4 Current whole atmosphere and thermosphere models 21

2.5 Whole atmosphere modelling in ENDGame 26

2.6 Summary 27

3 ENDGame1D Summary **29**

3.1 Grid settings 29

3.2 Temperature profiles 30

3.3 Acoustic waves in ENDGame 30

3.4 Stability tests 34

3.5 Summary 38

4 Numerical Effects on Vertical Wave Propagation **39**

4.1 Literature review 39

4.2 Ray-tracing equations 42

4.3 Wave equation with background density variation 43

4.4 Dispersion relations and group velocities 47

4.5 Ray-tracing simulations 54

4.6 Summary 73

5 **Vertical Molecular Viscosity and Diffusion in 1D** **75**

5.1 Motivation 76

5.2 Continuous equations 77

5.3 Semi-implicit semi-Lagrangian discretisation 78

5.4 Residual estimation 79

5.5 Constructing the boundary value problems 80

5.6 Solving the boundary value problem for w' 83

5.7 Solving the boundary value problem for Θ' 86

5.8 Comparison to the non-viscous formulation 88

5.9 Summary 92

6 **Vertical Molecular Viscosity and Diffusion in 3D** **93**

6.1 Motivation 93

6.2 Continuous equations 95

6.3 Semi-implicit semi-Lagrangian discretisation 97

6.4 Residual estimation 98

6.5 Constructing the elliptic problems 100

6.6 Solving the problem for Π' 106

6.7 Solving the elliptic problem for Θ' 111

6.8 Solving the elliptic problems for u' and v' 114

6.9 Comparison to the non-viscous formulation 116

6.10 Summary 122

7 **Conclusions** **123**

7.1 Summary 123

7.2 Future Research 123

A **ENDGame1D Formulation** **125**

A.1 Continuous equations 125

A.2 Semi-implicit semi-Lagrangian discretisation 130

A.3 Spatial discretisation 133

A.4 Finding departure points 134

A.5 Residual estimation 136

A.6 Constructing the boundary value problem 139

A.7 Solving the boundary value problem 140

B ENDGame code details **145**

B.1 Initialising the dynamical core 145

B.2 Inner and outer loops 146

B.3 Grid settings in ENDGame3D 148

C Acoustic Waves **149**

C.1 1D Acoustic wave theory 149

C.2 Growth rate of acoustic waves 151

D Ray-Tracing **153**

D.1 Smooth temperature profile 153

D.2 Terms for $\partial\widehat{\omega}/\partial z$ 154

D.3 Conservation of frequency along the ray 156

D.4 The WKB approximation 156

E Vertical molecular viscosity and diffusion **159**

E.1 Derivation of continuous equations for ENDGame1D 159

E.2 Explicit-in-time vertical molecular viscosity and diffusion 162

E.3 Testing the explicit scheme 164

E.4 Separate viscous timestep 167

E.5 Stability analysis of the diffusion equation 169

E.6 Scale analysis of the elliptic problem for the viscous scheme 170

E.7 1D and 3D approximation comparison 172

E.8 Comparison of the 1D and 3D problems 173

E.9 Full coefficient definitions 174

E.10 Smooth temperature profiles in ENDGame3D 176

F Spherical Polar Coordinates **177**

F.1 Vector calculus identities 177

F.2 The rate-of-strain tensor and stress tensor 178

Acronyms **183**

Mathematical Notation **184**

Bibliography **188**

List of Illustrations

Figures

2.1 Global mean temperature profiles for the whole atmosphere. 16
2.2 Density profiles for different gas constituents. 17
2.3 Variations of northern hemisphere temperature anomalies since the mid-17th century. 18
2.4 Sunspot number and Ap index for the last 2 1/4 solar cycles. 18
2.5 Nighttime ionospheric emissions showing the EIA. 19

3.1 ENDGame1D temperature profiles for the whole atmosphere. 31
3.2 Vertical acoustic wave propagation in an isothermal atmosphere. . . . 32
3.3 Analytical and numerical acoustic wave dispersion relations. 33
3.4 ENDGame1D stability tests for different grid and gravity settings. . . 36
3.5 ENDGame1D stability tests for different temperature profiles 36
3.6 ENDGame1D stability tests for a range of implicitness parameters. . 38

4.1 Kinetic energy spectra from the ARW model. 42
4.2 Wave propagation for a range of analytical wavevector angles. 55
4.3 Comparison of continuous and spatially-discrete acoustic wave propagation for a small wavenumber. 56
4.4 Critical angles for acoustic wave turning. 57
4.5 Acoustic wave propagation near the critical angle plot dip. 58
4.6 Comparison of continuous and spatially-discrete acoustic wave group velocity angles. 59
4.7 Illustration of analytical and numerical wavevector and group velocity directions. 60
4.8 Comparison of continuous and spatially-discrete acoustic wave propagation with different critical angles. 61

4.9 Comparison of continuous and spatially-discrete acoustic wave propagation for a large wavenumber. 62
4.10 Comparison of continuous and temporally-discrete acoustic wave propagation. 63
4.11 Comparison of wave energy of acoustic waves with and without molecular viscosity and diffusion. 64
4.12 Comparison of wave energy of acoustic waves for a range of total wavenumbers. 65
4.13 Comparison of wave energy of acoustic waves with a range of implicitness parameters. 66
4.14 Comparison of continuous and spatially-discrete gravity wave propagation for a small wavenumber. 67
4.15 Critical angles for gravity wave turning. 69
4.16 Gravity wave propagation near the critical angle plot peak. 69
4.17 Comparison of continuous and spatially-discrete gravity wave group velocity angles 70
4.18 Comparison of continuous and spatially-discrete gravity wave propagation with different critical angles. 71
4.19 Comparison of continuous and temporally-discrete gravity wave propagation. 72
4.20 Log wave energy of acoustic and gravity waves. 73
4.21 Comparison of wave energy with a range of implicitness parameters. . 73

5.1 ENDGame1D stability tests for the viscous formulation. 89
5.2 Maximum velocities observed in the viscous and inviscid formulations. 90
5.3 ENDGame1D stability tests with the viscous formulation and a range of implicitness parameters. 91
5.4 ENDGame1D stability tests with the viscous formulation and a range of time-steps 92

6.1 ENDGame3D grid cell illustration. 98
6.2 ENDGame3D stability tests for the viscous formulation. 117
6.3 Dispersion relations for acoustic and gravity waves in ENDGame. . . 118
6.4 Vertical velocity profile at the equator with the viscous formulation (160 km). 119

6.5 Vertical velocity profile at the equator with the viscous formulation (50 km). . . . 119
6.6 Vertical velocity profile at 45^o longitude with the viscous formulation. 120
6.7 High altitude vertical velocity profiles with the viscous formulation. . 121
6.8 Hydrostatic and non-hydrostatic vertical velocity profiles with the viscous formulation. . . . 121

A.1 Semi-Lagrangian time-step illustration. . . . 131
A.2 ENDGame1D vertical staggered grid. . . . 134
A.3 Estimation of $w_D^{(n,d)}$ using linear interpolation. . . . 136
A.4 ENDGame1D grid cell illustration. . . . 141

D.1 Brunt Väisälä frequency N^2 plot 155
D.2 Comparison of ENDGame and ray-tracing scheme wave amplitudes. . 158
D.3 Comparison of wavenumbers in ENDGame and the ray-tracing scheme.158

E.1 Maximum velocities observed in the inviscid and explicit-viscous formulations. . . . 165
E.2 Maximum velocities observed in the inviscid and explicit-viscous formulations with theoretical inviscid wave growth. . . . 166
E.3 ENDGame1D stability tests with the split viscous formulation and a range of large time-steps 168

Tables

2.1 Comparison of models considered in the literature review. . . . 22

4.1 Time taken for waves to reach the top boundary with different Δt. . . 66

5.1 Acoustic wave growth and diffusion damping time-scale comparison. . 77
5.2 ENDGame1D convergence tests 91

6.1 Wave growth and horizontal diffusion damping time-scale comparison. 94
6.2 ENDGame3D convergence tests 122

B.1 Flattening parameter and density scale height comparison. . . . 148

Chapter 1

Introduction

1.1 Motivation for the use of a whole atmosphere model

The Met Office used to have separate models for forecasting weather on short time-scales of hours or days, and for simulating climate on a time-scale of years [Brown *et al.* , 2012]. However, in 1990 the Met Office introduced the Unified Model (UM) that could be used for both weather and climate applications [Cullen & Davies, 1991]. The *dynamical core* is the component of a global circulation model (GCM) that solves the dynamical equations of motion on resolved scales: Newton's laws applied to a gas, in order to simulate the large-scale fluid dynamics of the atmosphere. The UM originally had an Eulerian dynamical core, but in 2002 the Met Office introduced a new semi-Lagrangian dynamical core called *New Dynamics.* Since the same tool could seamlessly model the atmosphere in vastly different time-scales, there could be greater confidence and understanding in its modelling of physical processes that govern both the weather and climate [Davies *et al.* , 2005; Brown *et al.* , 2012].

In a similar way, there is currently a lot of interest in developing a seamless *whole atmosphere model* dynamical core. This would involve including all of the levels of the atmosphere, from the troposphere to the thermosphere, in the same model, simulating all processes that occur in the lower atmosphere and the thermosphere, as well as the coupling between layers, detailed in section 2.2. This research will consider whether it is possible to produce a satisfactory whole atmosphere dynamical core by vertically extending an existing dynamical core up into the thermosphere.

1.2 Research aims

The aim of this research is to find out whether it is possible to vertically extend a non-hydrostatic formulation of a dynamical core into the thermosphere, to produce a whole atmosphere model dynamical core.

The dynamical core being extended is called *Even Newer Dynamics for the General atmospheric modelling of the environment* (ENDGame). ENDGame was developed by the Dynamics Research team at the Met Office and Professor John Thuburn at the University of Exeter, and it is the dynamical core currently being used operationally in the UM at the Met Office [Bush *et al.* , 2014]. The version of ENDGame that will be considered for this project is a stripped-down, independent implementation of the dynamical core which solves the governing equations of geophysical fluid dynamics for the atmosphere.

ENDGame has a number of unique features that should make it suitable for extending into the thermosphere. These are detailed in the literature review in section 2. It is hoped that ENDGame can be developed to become a fully coupled whole atmosphere dynamical core which better represents the weather and climate from the surface up to the exobase at 600 km: the region for which the Navier-Stokes equations are applicable [Akmaev, 2011]. This is further motivated by observational evidence of interactions between terrestrial weather and space weather, detailed in section 2.2, as these observations would be difficult to reproduce in separate models for the lower and upper atmosphere.

In practice, it may turn out that a non-hydrostatic whole atmosphere dynamical core cannot be obtained. It may be that there are issues with applying the Navier-Stokes equations of fluid motion to the tenuous upper thermosphere. Some other questions that might arise is whether the fluctuation in height of the exobase is too great, or whether the interactions between the thermosphere and the lower levels of the atmosphere are significant enough to justify the extra difficulties of developing a whole atmosphere model.

1.3 Potential applications and space weather

Space weather encompasses the physical state and phenomena of the sun, the solar wind, the magnetosphere, the ionosphere and the neutral atmosphere [World Meteorological Organization, 2008]. This includes the magnetic fields, radiation, particles and matter that are ejected from the sun, travel through space and then interact with the Earth's *ionosphere*: the ionised part of the upper atmosphere. Cannon *et al.* [2013] lists some possible impacts that an extreme space weather event (a solar superstorm that should occur only once every 200 years) would have on the UK:

- Damage to the electricity grid, with power outages likely. Modelling estimates that around six super grid transformers in England and Wales, and a further seven in Scotland, could be damaged through geomagnetic disturbances and taken out of service. [Cannon *et al.* , 2013]

- Approximately 10% of satellites will suffer temporary outages and some may be lost. The entire satellite fleet will be aged through radiation damage.
- High energy particles may cause individual avionic components to malfunction, and passengers and crew airborne at the time of an extreme event would be exposed to a high one-off radiation dose.
- GPS will become partially or completely inoperable for 1-3 days, which will have important operational consequences for those that rely upon it, such as defence or emergency services.

The disruptions that can be caused by damage to these systems could potentially endanger life and property. Less severe space weather can still affect the atmospheric drag on satellites.

For this reason, the Met Office is interested in simulating and forecasting space weather, and it has recently opened its own Space Weather Operations Centre (MOSWOC) to inform people of dangerous space weather events. MOSWOC has a number of tools for observing the Sun. One of these is the Wang-Sheeley-Arge (WSA) Enlil model for predicting the arrival times of coronal mass ejections and solar winds [Taktakishvili *et al.* , 2009]. Another is the Relative Electron Forecast Model (REFM) which simulates the 72 meV electron fluence in the radiation belt of the Earth's magnetosphere [Space Weather Prediction Center (SWPC), 2008; Baker *et al.* , 1990]. The D-Region Absorption (D-RAP) model simulates the impact of solar flares and solar energetic particle events on high frequency radio absorption in the D-region of the ionosphere (between around $50 - 80\,\mathrm{km}$) [Sauer & Wilkinson, 2008]. However, future MOSWOC operational forecasts would benefit from using a coupled Sun-to-Earth modelling system, instead of these separate uncoupled models. This system would also benefit from the use of a whole-atmosphere dynamical core.

If the extension of ENDGame into a whole atmosphere dynamical core is successful, then the Met Office already has the infrastructure in place to be able to develop it further so that it can be used in forecasting or modelling space weather in the future.

1.4 The structure of this thesis

Chapter 2 gives a review of the current literature on whole atmosphere modelling, including the motivation for developing whole atmosphere models, and the justification for extending the existing ENDGame dynamical core into the thermosphere.

A simplified one-dimensional vertical column version of ENDGame has been developed in order to cheaply and easily implement and test new numerical methods and physical processes before implementing them into the full three-dimensional version of ENDGame. From this point on, this column version of ENDGame will be referred to as *ENDGame1D*, while the full three-dimensional version of ENDGame will be referred to as *ENDGame3D*. In chapter 3, a summary of ENDGame1D is given and stability tests are performed to characterise the problem of stability in the thermosphere. Appendix A goes into more detail on deriving the equations that ENDGame1D solves.

In chapter 4, a ray-tracing scheme is developed to analyse the numerical effects on wave propagation in ENDGame. Some of these effects include the tendency of ENDGame to channel wave energy vertically caused by its coarse horizontal resolution, and the slow propagation of waves caused by the time discretisation. The damping effect of molecular viscosity and diffusion on wave amplitudes are also demonstrated.

Chapter 5 details the formulation of the ENDGame1D equations including vertical molecular viscosity and diffusion, and stability tests are performed. It is found that with a small amount of off-centring, the ENDGame1D with vertical molecular viscosity and diffusion is able to remain stable with a top boundary at 600 km.

Chapter 6 details the formulation of ENDGame3D with vertical molecular viscosity and diffusion, and again, includes a demonstration of the stability of the new scheme as it is extended into the thermosphere. It turns out that ENDGame3D with vertical molecular viscosity and diffusion is able to remain stable with a top boundary up to 270 km with much less off-centring than is required by the scheme without vertical molecular viscosity and diffusion.

Lastly in chapter 7, conclusions are drawn and a summary of the future research and development of ENDGame that will lead to a complete Sun-to-Earth modelling system is given.

Chapter 2

Literature Review on Whole Atmosphere Modelling

This literature review has three main purposes. The first is to introduce the thermosphere, and its structure and dynamical properties. The second is to introduce the concept of whole atmosphere modelling and justify the need for modelling the atmosphere from the surface to the top of the thermosphere. The third is to analyse the current status of research in the area of whole atmosphere modelling. The key purpose of this endeavour is to justify the research project by explaining how the extension of the ENDGame dynamical core into the thermosphere is a worthwhile contribution to this field of research, and what ENDGame does differently compared with other models that are already being used for whole atmosphere modelling.

2.1 The physics of the thermosphere

The thermosphere is the layer of the atmosphere between the mesopause at 90 km and the exobase at around 600 km: the height of the exobase varies with solar and geomagnetic activities. The gas temperatures in the thermosphere vary from 200 K at the mesopause to values ranging from 800 K to 2000 K in the upper thermosphere, depending on solar activity [Salby, 1996]. This rise in temperature is chiefly due to heating from exothermal chemical reactions, but also due to solar UV (ultraviolet) and EUV (extreme ultraviolet) heating and Joule heating. A graphical representation of the neutral temperature profile in the thermosphere can be seen on the plot on the left-hand side of Figure 2.1.

EUV heating is the dominant source of energy in the thermosphere above 150 km. Above these heights, ion drag associated with magnetospheric convection is the dominant factor controlling thermospheric winds [Roble, 1983]. Below heights of

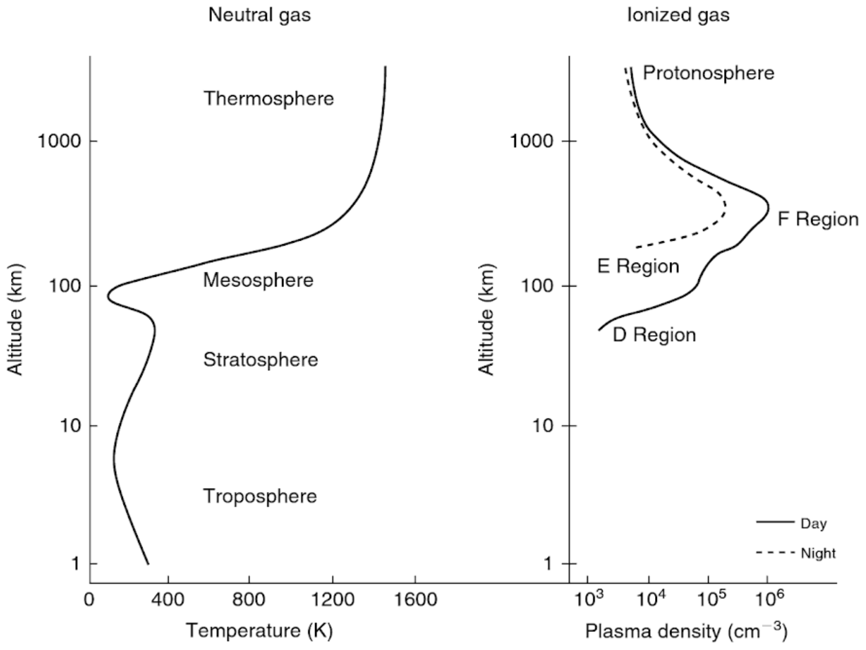

Figure 2.1: From Kelley [2009]: Typical profiles of neutral atmospheric temperature (left) and ionospheric plasma density (right) with the various layers labelled.

150 km, changes in the optical depth cause a decrease in the absorption of solar UV and EUV radiation, which means that the lower thermosphere is more strongly affected by semidiurnal tides and gravity waves propagating upwards from the lower atmosphere. It also has a lower ion drag than the upper thermosphere [Roble, 1983].

There are also variations in the dynamical properties of the thermosphere during geomagnetic storms, where intense Joule heating and momentum forcing at high latitudes produce energy inputs that exceed solar EUV and UV heating. Auroral processes even have effects on the circulation, temperature and compositional structure of the thermosphere at low latitudes [Roble, 1983].

Figure 2.2 shows the calculated mean number density profiles from the global mean model and MSIS-83, for the most prominent gas species: O, O_2 and N_2, in the thermosphere at the solar minimum and maximum. ENDGame currently assumes a single gas species, and so has a constant scale height. It will be outside the scope of this thesis to consider multiple gas species, but this project will be a stepping stone towards a model that can accurately capture thermospheric physics and chemistry.

The Earth's ionosphere is the ionised part of the upper atmosphere above an altitude of about 60 km [Akmaev, 2011]. A graphical representation of the plasma density profile of the ionised gas is shown on the plot on the right-hand side of Figure 2.1. The ionosphere is very sensitive to changes in solar or magnetospheric inputs: the D, E and F regions have their own diurnal variation, but changes can

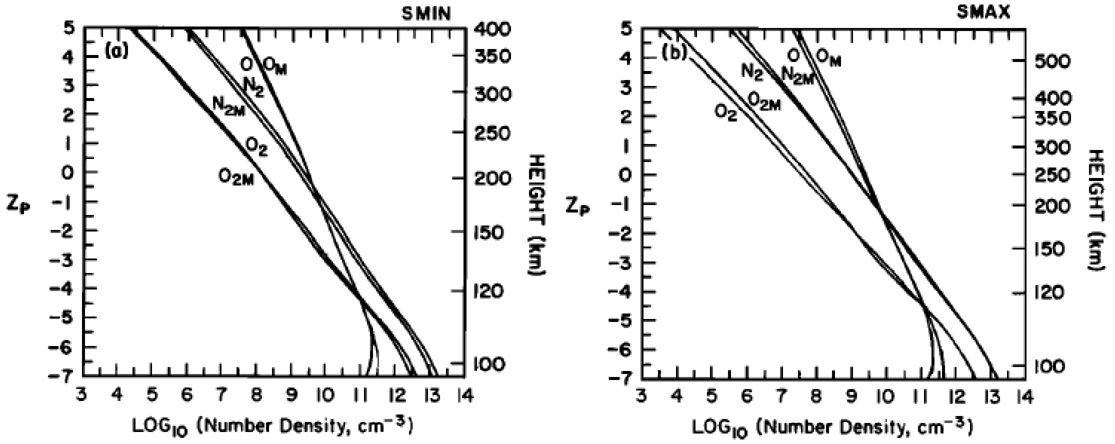

Figure 2.2: From Roble *et al.* [1987]: Calculated $\log_{10}$ O, O_2 and N_2 number density profiles (cm^{-3}) from the global mean model and from MSIS-83 (indicated by the M subscript) for (a) solar minimum and (b) solar maximum conditions.

occur on time-scales of minutes to an entire solar cycle. The ionosphere occupies a similar altitude range to the thermosphere, but it constitutes only 0.1 % of the atmosphere's total mass and is mostly ionised by solar radiation that passes into the Earth's atmosphere [Liu *et al.* , 2010].

2.2 Connections between terrestrial and space weather

Changes in solar forcing due to the 11-year solar cycle is one mechanism by which space weather can have an effect on the thermosphere and surface climate. By comparing temperature observations in the United Kingdom (UK) and the solar flux using Figure 2.3, it can be seen that uncharacteristically cold winters in the UK seem to occur more commonly during periods of low solar activity, such as during the minimum phase of the 11-year sunspot cycle [Lockwood *et al.* , 2010]. Changes in radiative heating during different levels of solar output affect the mean state of the stratosphere, which in turn causes changes in patterns in surface pressure and temperature that are associated with changes in the North Atlantic Oscillation [Ineson *et al.* , 2011], and can affect the North Atlantic and European climate.

Space weather can also have an effect on stratosphere and surface climate via energetic particle precipitation on nitric oxides and reactive hydrogen oxides. This effect disturbs the chemical composition from the upper stratosphere to the lower thermosphere, and changes to the nitric oxide budget contribute to ozone loss in the stratosphere and mesosphere where nitric oxide is one of the main participants in catalytic ozone destruction [Sinnhuber *et al.* , 2012]. A correlation between solar activity and energetic auroral particle precipitation can be seen in Figure 2.4. En-

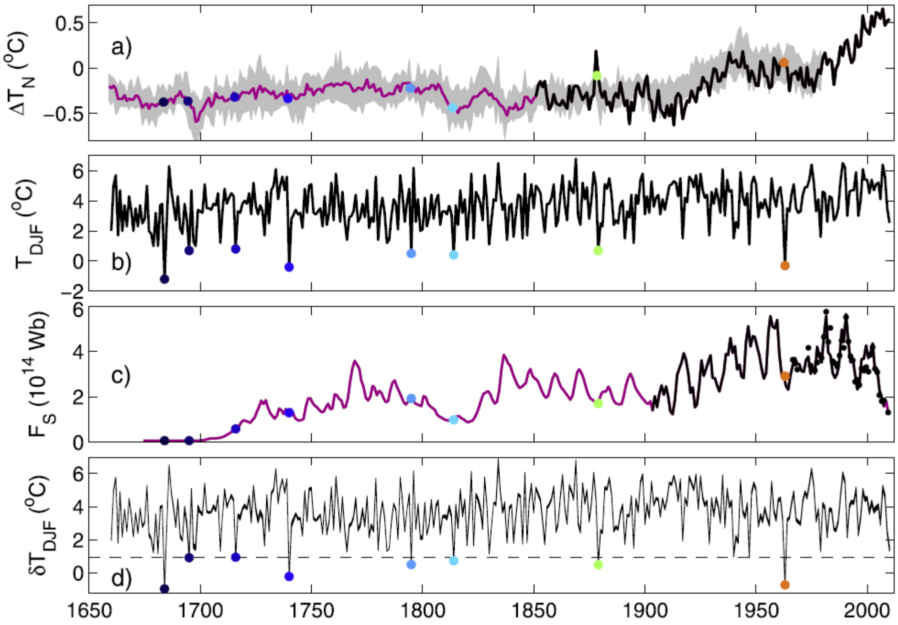

Figure 2.3: From Lockwood *et al.* [2010]: Variations since the mid-17th century of the following. (a) The mean northern hemisphere temperature anomaly with the decile range. (b) Average winter Central England Temperatures (CETs) for December, January and February, T_{DJF}. (c) The one-year means of the open solar flux, from a model based on sunspot numbers up to 1905, and using ground-based geomagnetic data after 1905. The black dots are annual means of interplanetary satellite data. (d) Detrended winter CETs, δT_{DJF}. The dots in all plots are for years with $\delta T_{\mathrm{DJF}} < 1\,°\mathrm{C}$ (the dashed horizontal line in (d)).

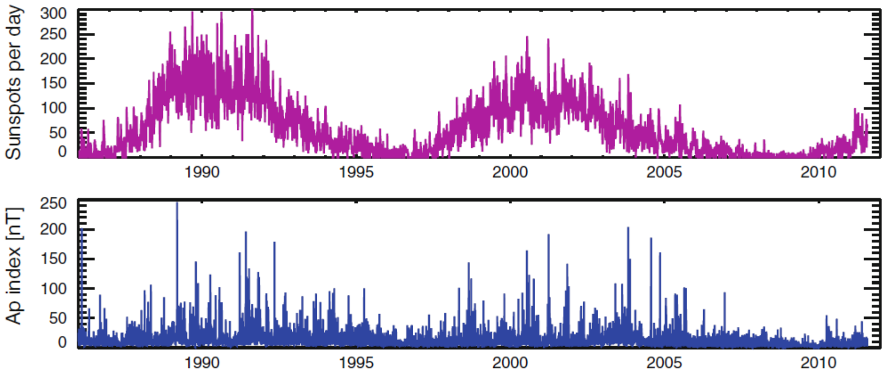

Figure 2.4: From Sinnhuber *et al.* [2012]: (above) the sunspot number per day, a proxy for solar activity, for the last 2 1/4 solar cycles, and (below) the *Ap* index, a proxy for geomagnetic activity linked to the precipitation of auroral particles, for the last 2 1/4 solar cycles.

ergetic particle precipitation also affects temperatures and dynamics from the thermosphere down to the surface, due to changes of chemical composition affecting atmospheric heating and cooling rates, mean circulation and wave propagation.

The current understanding of these mechanisms, and to what extent they affect the surface climate, is still being developed [Akmaev, 2011], but a whole atmosphere model that is capable of representing them well will be a useful tool for weather and climate research.

During geomagnetic storms in October 2003, density measurements showed en-

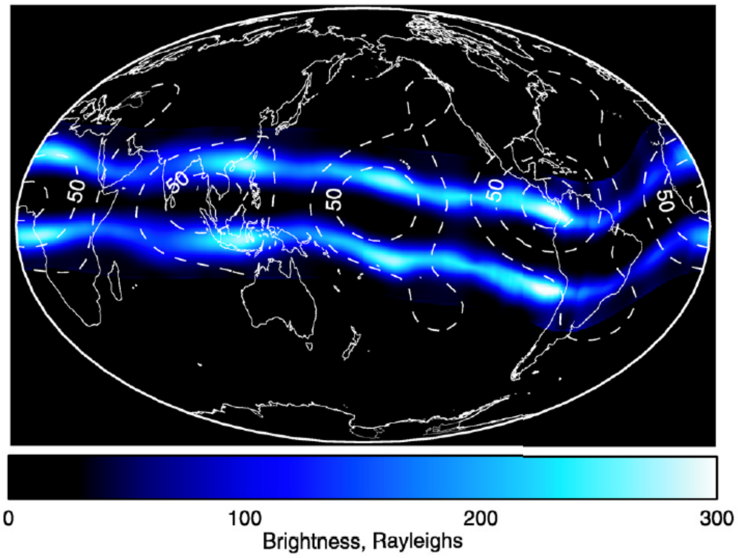

Figure 2.5: From Immel *et al.* [2006]: A reconstruction of nighttime ionospheric emissions from 30 days of observations with the IMAGE-FUV (far-ultraviolet) imager. This presentation highlights the average location and brightness of the equatorial ionospheric anomaly.

hancements of 200 – 300 % near 400 km [Sutton *et al.* , 2005], while the largest relative density enhancements observed by the GRACE (Gravity Recovery And Climate Experiment) satellites between 2003 and 2010 was 750 % [Krauss *et al.* , 2015]. Density changes of up to 15 % can also occur during small geomagnetic storms and solar flares [Pawlowski & Ridley, 2008]. Understanding these density enhancements is important for calculating the drag on low-Earth-orbit satellites. However, the Earth's upper atmosphere is not only affected by solar inputs from above: there is also observational evidence from different data sources which all suggest that various physical processes in the lower atmosphere have effects on the upper atmosphere [Fuller-Rowell *et al.* , 2008].

A particular phenomenon has been observed, whereby the spatial morphology of the equatorial ionosphere is controlled by lower atmosphere dynamics [Akmaev *et al.* , 2008]. A 1000 km scale longitudinal variation in ionospheric densities has been observed by the IMAGE (Imager for Magnetopause-to-Aurora Global Exploration) satellite [Immel *et al.* , 2006]. It observed the characteristic four peak structure of the equatorial ionospheric anomaly which can be seen in Figure 2.5, and it has been deduced that ionospheric densities vary with the strength of atmospheric tides that are driven mainly by weather near the tropopause. Models that represent the thermosphere and ionosphere well should be able to reproduce this four peak structure.

A similar feature was observed in the total electron count (TEC) in the ionosphere by the Formosat-3/ COSMIC (Constellation Observing System for Meteorology, Ionosphere and Climate) satellite [Lin *et al.* , 2007]. Further studies show that the planetary wave periodicities from tropospheric weather appear above 100 km altitude as a modulation of tidal amplitudes, rather than the planetary waves propagating directly into the thermosphere. This means that planetary wave periodicities are carried into the thermosphere by different vertically propagating waves like tides. This conclusion is further supported by other studies that have indicated links between Stratospheric Sudden Warmings (SSWs) (which implies large changes in planetary wave forcing) and ionosphere electron counts [Goncharenko *et al.* , 2010]. Variability in tides in the lower thermosphere results in changes in electric fields in the upper atmosphere, as was observed [Fuller-Rowell *et al.* , 2008].

There is ample evidence of interactions between terrestrial weather and space weather. However, many of these mechanisms are poorly understood, and they would benefit from using whole-atmosphere modelling to learn more about these interactions.

2.3 Whole atmosphere modelling

Whole atmosphere modelling is the simulation of the entire planet's atmosphere, from the surface to the exobase at around 600 km. To better understand the behaviour of the upper atmosphere, it is necessary to determine the extent to which the coupling between different levels of the atmosphere, and solar impacts on all levels of the atmosphere, affect the whole atmosphere system [Liu *et al.* , 2010]. Using separate models for surface weather and climate and for space weather will be unlikely to be able to capture the coupling between the two regions satisfactorily. Therefore, there is a need for numerical models that simulate the whole atmosphere [Liu *et al.* , 2010], as simulations show that these have the capability to model the connections and interactions between different levels of the atmosphere [Akmaev, 2011].

One technique for creating a whole atmosphere model is to couple or merge existing lower and upper atmosphere models [Liu *et al.* , 2010]. Coupling models can bring about many complications, such as the requirement to combine data stored at different resolutions. Another potentially more viable technique is to use existing lower atmosphere climate models as a starting point and to extend them vertically upwards [Akmaev, 2011]. The vertical extension of existing climate models has been motivated by the potentially detrimental feedbacks from sponge layers that are often employed at the top layers of models: these are layers with increased numerical dissipation, used to keep the model codes stable [Akmaev, 2011]. The linear drag from these sponge layers does not conserve momentum, which can have deleterious implications on the dynamical core, making it particularly sensitive to changes in the model lid height, for example [Shaw & Shepherd, 2007].

Processes to consider include tides generated in the tropopause that can cause changes to electric fields in the upper atmosphere [Fuller-Rowell *et al.* , 2008], dissipating gravity waves and acoustic waves that can have effects of cooling or heating the upper atmosphere respectively [Hickey *et al.* , 2001], and the transportation of gas constituents through the atmosphere. Therefore, the ability to model coupling processes such as these, by considering factors that are important in the thermosphere such as electrodynamics, chemistry and molecular diffusive transport, is important for any whole atmosphere model [Akmaev, 2011].

Akmaev's review of whole atmosphere modelling [Akmaev, 2011] gives an objective, consistent definition for a whole atmosphere model. This includes having an upper boundary of zero pressure, having the molecular mean free path increase inversely proportionally to the density, and defining the pressure at the exobase, above which, the air may no longer be treated as a continuous fluid. This definition sets out pragmatic criteria that are established by considering the limits of applicability of the equations that are used in atmospheric models. The following models satisfy the criteria that are given by this definition:

- Whole Atmosphere Model (WAM) [Akmaev *et al.* , 2008]
- Ground to topside model of Atmosphere and Ionosphere for Aeronomy (GAIA) [Jin *et al.* , 2011]
- Whole Atmosphere Community Climate Model eXtension (WACCM-X) [Liu *et al.* , 2010]

The *Global Ionosphere-Thermosphere Model* (GITM) [Ridley *et al.* , 2006] will also be considered due to its non-hydrostatic formulation.

These models will be compared to the ENDGame dynamical core [Wood *et al.* , 2014b], to demonstrate what sets ENDGame apart from these models, and why its vertical extension into a whole-atmosphere dynamical core would be worthwhile.

2.4 Current whole atmosphere and thermosphere models

Table 2.1 lists the properties of the various models that are considered in this literature review. The whole atmosphere models that currently exist have all taken

	WAM	GAIA	WACCM-X	GITM	ENDGame
Whole atmosphere model	Yes	Yes	Yes	No	No
Range of altitudes	0 - 600 km	0 - 500 km	0 - 500 km	95 km - 600 km	0 - 80 km
Number of layers	150	75	125	40	70
Resolution (lat × long)	1.8° × 1.8°	1.0° × 5.0°	1.9° × 2.5°	1.25° × 5.0°	1.8° × 1.8°
Non-hydrostatic	No	No	No	Yes	Yes
Includes molecular viscosity	Yes	Yes	Yes	Yes	No
Includes ion drag	Yes	Yes	Yes	Yes	No

Table 2.1: A selection of parameters of the models considered in this literature review. Note that settings for numbers of layers and resolution are often able to be changed when running the model.

measures to include some of the effects that are important in the thermosphere.

2.4.1 WAM

WAM is an extended version of the US National Weather Service's Global Forecast System (GFS) model, made to simulate the dynamical interactions through the whole atmosphere. WAM includes a spectral dynamical core, with a number of physical atmospheric processes including radiative processes, the hydrological cycle, planetary boundary layer and surface exchange processes, parametrised ozone photochemistry and orographic gravity waves [Akmaev *et al.* , 2008].

The *semi-implicit* (SI) scheme used in WAM treats large-scale motions explicitly, while heavily damping and slowing the small-scale acoustic and gravity waves that are considered unimportant in the lower atmosphere [Akmaev, 2011]. However, the sharp temperature increase in the thermosphere can cause numerical instabilities in SI time integration schemes. The need to solve an elliptic problem at each time-step can also be computationally expensive [Akmaev *et al.* , 2008], although the spectral core helps reduce the computational expense considerably.

WAM uses the *hydrostatic assumption*, which involves making the approximation that all terms in the vertical momentum equation may be neglected except the gravity and pressure gradient terms [Akmaev, 2011]. This is a very good approximation when the horizontal length scale is significantly larger than the vertical length scale of the region being considered (where length scales here refer to the derivatives of velocities being observed), which is the case when simulating the lower atmosphere. However, large vertical winds have been observed in the thermosphere, and can frequently persist for periods of over an hour [Larsen & Meriwether, 2012]. In the presence of large vertical accelerations like these, the hydrostatic approximation is no longer valid [Curry & Webster, 1998]. Comparisons of hydrostatic and non-hydrostatic simulations also show that the hydrostatic approximation eliminates vertically propagating acoustic waves and distorts high frequency gravity waves

[Akmaev, 2011].

The *shallow atmosphere assumption* uses the fact that the depth of the atmosphere is much shallower than the Earth's radius r_E, so the geocentric distance r may be replaced by r_E in the governing equations. This approximation is well justified in the lower atmosphere. However, WAM still makes this assumption on being extended into the thermosphere, where using r_E instead of r may introduce errors of about 10 - 20 % [Akmaev, 2011]. A corollary of the shallow atmosphere assumption includes the neglect of some Coriolis force terms in the zonal and vertical momentum equations. WAM also makes the assumption of constant gravity. The gravitational acceleration is nearly 20 % smaller near the top of the domain of WAM than near the surface, so this assumption may result in substantial errors [Akmaev, 2011].

Models of the lower atmosphere often need to include damping *sponges* in the form of Rayleigh friction, or a similar scheme, to alleviate the effects of spurious wave reflection and numerical instabilities, although this can have its own deleterious impact on simulation results [Akmaev, 2011; Shaw & Shepherd, 2007]. Horizontal molecular transport of momentum, heat and gas constituents have been incorporated into WAM, as these molecular dissipative processes become very fast in the thermosphere and cannot be treated only in the vertical direction. As the thermosphere is a naturally dissipative medium, there is less need for sponge layers when these processes are included [Akmaev *et al.* , 2008].

WAM also includes parametrisations of UV and EUV radiative heating, infrared radiative cooling, ion drag, and Joule and particle heating [Akmaev *et al.* , 2008], and incorporates separate models for plasma density and electric fields [Akmaev, 2011]. WAM treats the major species (O, O_2, N_2) self-consistently, including large-scale transport, simple oxygen chemistry and mutual diffusion [Akmaev, 2011].

WAM has been validated by comparing its simulations with observations from the TIMED (Thermosphere, Ionosphere, Mesosphere, Energetics and Dynamics) satellite, which confirms that WAM reproduces seasonal tidal variability very well. WAM simulations can represent the effects of both migrating and non-migrating tides on the spatial morphology of the equatorial ionosphere [Akmaev *et al.* , 2008].

2.4.2 GAIA

GAIA is a global spectral model created by coupling together three different, independently developed models: a whole atmosphere GCM [Miyoshi *et al.* , 2014], with an ionospheric model [Shinagawa *et al.* , 2007] and an electrodynamics model [Jin *et al.* , 2008]. It seamlessly simulates the atmosphere from the ground to the exobase, and focuses on dynamical interactions throughout the atmosphere, including electrodynamic interactions between the thermosphere and ionosphere [Jin *et al.* , 2011].

GAIA includes a full set of physical processes appropriate for each level of the thermosphere with the hydrostatic assumption, with schemes for hydrology, boundary layers, radiative processes, eddy diffusion and moist convection. The ionospheric part solves mass, momentum and energy equations for several major ion species and electrons, including photochemical reactions, ion diffusion and convection processes. The electrodynamics model treats the closure of ionospheric currents induced by the neutral wind dynamo and the polarisation electric field. The coupler then handles the procedures for running the integrated model: setting common parameters, initial/ boundary conditions, controlling the time increment, and exchanging physical variables between the three models. As the three models have different grid distributions, coordinate conversion is used when exchanging variables [Jin *et al.* , 2011].

GAIA includes the thermospheric major gas species (O, O_2, N_2) as WAM does, and also includes radiatively active gases (O_3, CO_2, NO) [Akmaev, 2011] and ion densities (O^+, O_2^+, N_2^+, NO^+) [Jin *et al.* , 2011]. The ionospheric model is able to solve the governing equations for several major ion species and electrons, including photochemical reactions, ion diffusion and convective processes. GAIA includes a full set of physical processes that are appropriate for each level of the atmosphere, including moist convection under the hydrostatic approximation [Jin *et al.* , 2011].

GAIA is able to reproduce the four-peak structure of the equatorial ionospheric anomaly that has been observed, and simulate the processes that lead to its formation: in particular, non-migrating tides in tropospheric moist convection and their upward propagation [Jin *et al.* , 2011].

2.4.3 WACCM-X

The whole atmosphere model: WACCM-X, is vertically extended from the National Center for Atmospheric Research (NCAR) WACCM, which is a superset of the NCAR Community Atmospheric Model (CAM). CAM has historically accommodated several dynamical cores, but WACCM-X uses only the finite-volume dynamical core, modified to consider species dependent gas constants and phase velocities. WACCM-X also includes the physics and chemistry models that are used in WACCM and CAM. The physics module takes into account the molecular diffusion of the major gas species. [Liu *et al.* , 2010]. The finite-volume semi-Lagrangian scheme suffers from the same drawbacks as the semi-implicit scheme used in WAM: including the damping of small-scale waves and computational cost [Akmaev, 2011].

WACCM-X deals with the short time-scales of thermospheric processes using a time-splitting scheme: a long 5 minute time-step is used for the integration of the tracer transport equations, and a shorter time-step of 50 seconds is used for the dynamics, which helps to stabilise the fast waves. The chemistry module interacts with the dynamics through transport and exothermic heating. WACCM-X also includes parametrisations of radiative heating, ion drag and gravity waves. The gravity wave parametrisation ensures that gravity waves will be increasingly damped by molecular viscosity and diffusion in the thermosphere [Liu *et al.* , 2010].

WACCM-X simulates the Earth's atmosphere from the surface and extends the top boundary of WACCM from ∼145 km to ∼500 km [Liu *et al.* , 2010]. It includes an interactive chemistry module to resolve the production and loss of electrons and five ions (O^+, O_2^+, N_2^+, NO^+, N_2^+), as well as neutral species of interest in the thermosphere and ionosphere. The chemistry module interacts with the dynamics, and many other upper atmosphere processes are also included in the model. WACCM-X also employs a time splitting scheme: a time-step of 5 minutes is used for the integration of tracer transport equations and a much smaller time-step of 50 seconds is used for the dynamics, in order to help stabilise the fast waves, which is necessary because of the short timescales of thermospheric processes [Liu *et al.* , 2010].

WACCM-X has been validated by comparing effects and seasonal variation of migrating and non-migrating tides with observations from the TIMED, SABER (SAtellite Broadband for European Regions) and TIDI (TIMED Doppler Interferometer) satellites. There are some variations from the expected temperature values due to excessive heating from the gravity wave parametrisation [Liu *et al.* , 2010].

2.4.4 GITM

GITM is a three-dimensional global thermosphere-ionosphere model. It is not a whole atmosphere model, as are the others that have been considered so far, but it is described here because of its non-hydrostatic formulation. Its other most important features are its adjustable non-uniform grid in the altitude and latitude coordinates and its explicit solving of advection and chemistry (including the neutral densities and ion species of a large number of gases). It can also be combined with different models of electric fields, particle precipitation patterns and magnetic fields [Ridley *et al.* , 2006].

GITM demonstrates that more accurate simulations of the thermosphere can be made using non-hydrostatic modelling. GITM is able to reproduce observations of the thermosphere that are not typically reproduced by hydrostatic models, in particular: the large vertical winds of 150 (250) $\mathrm{m\,s^{-1}}$ at 300 (400) km altitude during a large perturbation from hydrostatic equilibrium [Deng *et al.* , 2008]. GITM is also able to explicitly model the effects of ion drag on the neutral circulation [Ridley *et al.* , 2006], which cannot be quantified and evaluated in existing hydrostatic models [Akmaev, 2011].

2.5 Whole atmosphere modelling in ENDGame

To improve space weather forecasting capabilities, there is a need to develop a fully coupled modelling system for the Sun-to-Earth domain, with data assimilation to provide up-to-date and accurate initial conditions. Data assimilation uses the most recent available observations in conjunction with previously made forecasts to obtain a best estimate of current atmospheric conditions. Models are then updated to reflect these changes in order to improve the next forecast that is produced.

One benefit to extending ENDGame into a whole atmosphere dynamical core is that the Met Office in the UK has the infrastructure in place to be able to develop it to become viable for the provision of operational space weather forecasts in the future. The Met Office data assimilation system has already been successfully coupled with the ENDGame dynamical core [Wood *et al.* , 2014b], which makes ENDGame a natural choice of dynamical core to develop.

The main features of ENDGame are its semi-implicit, semi-Lagrangian (SISL) timestepping scheme, that it has the option for being inherently mass-conserving and it has switches for controlling the hydrostatic approximation, deep or shallow atmosphere approximations such as varying gravity with altitude, and the various geometries that can be used [Wood *et al.* , 2014b]. These features are detailed in the ENDGame1D formulation in appendix A. The ENDGame dynamical core only considers the unforced, dry governing equations, but it may be coupled with a suite of physics parametrisations, a data assimilation scheme and an ocean model .

ENDGame is currently only able to simulate the atmosphere and remain stable between 0 and around 85 km altitude, as demonstrated for ENDGame1D in section 3.4. *Stability* here refers to numerical stability: that in this range, the approximated solutions to the governing equations are not excessively sensitive to small perturbations, do not diverge rapidly from the true solution or give unphysical results. A linear stability analysis of ENDGame's timestepping scheme is given by Payne [2008]. If its top boundary is set higher than 100 km, the simulations will most likely crash, due to some other cause which needs to be investigated. Therefore, ENDGame cannot currently be referred to as a whole atmosphere dynamical core. ENDGame needs to be developed to introduce effects that are important in the thermosphere and to remain stable at high altitudes.

ENDGame has a number of factors that set it apart from whole atmosphere models that currently exist and demonstrate that extending it into the thermosphere will be a useful endeavour. The main one is its non-hydrostatic formulation, which means that it should be able to reproduce observations of the thermosphere that models using the hydrostatic approximation are not able to. These include the large vertical winds that have been observed in the thermosphere that are generated by vertically propagating acoustic waves from the troposphere [Hickey *et al.* , 2001].

ENDGame's SISL timestepping scheme also allows it to represent acoustic waves without needing extremely short time-steps: it remains stable when using larger time-steps than for a fully explicit scheme, and has less of a compromise on accuracy than a fully implicit scheme [Wood *et al.* , 2014b].

ENDGame avoids the usual shallow atmosphere and hydrostatic approximations so that when it is extended upwards, it will be possible to explicitly incorporate important thermospheric processes, such as molecular diffusion, ion drag and other chemical processes involving separate gas species, which must be parametrised in other whole atmosphere models. ENDGame still requires a significant amount of development to make it ready to use as a whole atmosphere dynamical core, but due to the way it has been constructed so far, it should be highly suitable for being extended into the thermosphere and can provide this field of research with a unique new whole atmosphere modelling tool.

2.6 Summary

The thermosphere is the layer of the atmosphere between 90 km and 600 km, with incoming solar UV and EUV radiation being the most significant energy source in the system above 150 km. The lower thermosphere below 150 km is more strongly affected by semidiurnal tides and gravity waves propagating upwards from the lower atmosphere. However, there is a lot of observational evidence of vertical interactions between all levels of the atmosphere, and it is apparent that these couplings can best be captured using whole atmosphere modelling.

A number of whole atmosphere models currently exist (WAM, WACCM-X and GAIA), but these all currently use hydrostatic dynamics which are not able to capture the large vertical winds that have been observed in the thermosphere. The non-hydrostatic thermosphere model (GITM) does not extend down to the surface, so it will be unable to capture the couplings between the lower atmosphere and the thermosphere. As ENDGame has a non-hydrostatic, deep-atmosphere formulation, it should be particularly suitable for being extended into a whole atmosphere dynamical core that provides features that are not present in currently available models.

Chapter 3

ENDGame1D Summary

In this chapter, a summary is given of how ENDGame1D is set up, how acoustic waves are initialised in the dynamical core, and how its stability will be assessed. Stability tests of ENDGame1D are performed, which serve to characterise the problem that is to be addressed in this thesis. Full details of the equations that ENDGame1D is based on and the numerical methods it uses can be found in appendix A.

The simplified 1D vertical column version of ENDGame narrows one's focus onto the vertical processes that occur near the top boundary, that are likely to be causing instabilities in the dynamical core. By considering only the vertical component of the governing equations in a column of atmosphere, ENDGame1D can capture the vertical processes that are of interest. It will also make it easier to implement and test new numerical methods and processes, and greatly reduce the integration times. By assessing whether development of ENDGame1D makes an improvement to its stability with higher top boundaries, it can later be determined whether ENDGame3D should be developed in the same way.

3.1 Grid settings

ENDGame1D is set up with the option to use either uniform or quadratically stretched grid spacing[1]. The uniform grid is such that grid spacing is the same throughout the model, with each grid section being 1 km high. The quadratically stretched grid is such that the distance between separate grid levels grows with altitude, so that they are very small in the troposphere (starting at 10 m) but become more spread out in the upper atmosphere (up to 2 km). The quadratically stretched grid is able to capture additional detail close to the Earth's surface.

It is worth noting that non-uniform grids can cause problems in some schemes

---

[1] In ENDGame3D, a slightly different stretched grid is used that gives more control over the resolution near the surface. This is detailed in appendix B.3.

for solving wave equations. For example, a wave of a particular frequency cannot propagate into a region where the grid is too coarse for a wave of that frequency to be resolved: they will instead be refracted or reflected in a non-physical way [Long & Thuburn, 2011]. Therefore, some mechanisms must be included to dissipate such waves so that these refractions and reflections do not affect the solution.

The grid in ENDGame1D is also set up with two hard boundaries at the Earth's surface and at the top of the atmosphere in the simulation, as shown in Figure A.2. Waves that grow significantly will reflect from this boundary in a non-physical way. These spurious reflections can be damped with some form of dissipative mechanism, or by making the boundary layers absorbing or viscous.

3.2 Temperature profiles

ENDGame1D is set up to use either isothermal atmosphere, or more detailed temperature profile initial conditions. An *isothermal atmosphere* is such that the initial temperature is set to a constant value throughout the whole atmosphere. The *US Standard Atmosphere (USSA) temperature profile* is a more detailed initial condition for temperature [United States Committee on Extension to the Standard Atmosphere (COESA), 1976]. The USSA gives specific average data values for the temperature between the surface and a height of 86 km. Above this altitude, the temperature profile is approximated by a smooth function (the construction of which is detailed in the USSA documentation by the COESA). The shape of this function is determined by the exospheric temperature, which can vary hugely, between 800 K and 2000 K [Salby, 1996], and which greatly influences the temperature profiles in the thermosphere. Plots of the isothermal temperature profile and of USSA temperature profiles for a variety of exospheric temperatures are shown in Figure 3.1.

3.3 Acoustic waves in ENDGame

It has already been established that fast acoustic waves propagating upwards into the thermosphere from the troposphere are likely to be a potential cause of large vertical winds that are observed in the thermosphere [Hickey *et al.* , 2001], and that ENDGame needs to be developed to give realistic dissipation of acoustic waves in the thermosphere. In this section, the growth of acoustic waves in ENDGame1D is observed, and ENDGame1D's stability is tested under different settings when an acoustic wave is propagating vertically through the atmosphere.

Acoustic waves are a type of longitudinal wave that propagate by means of

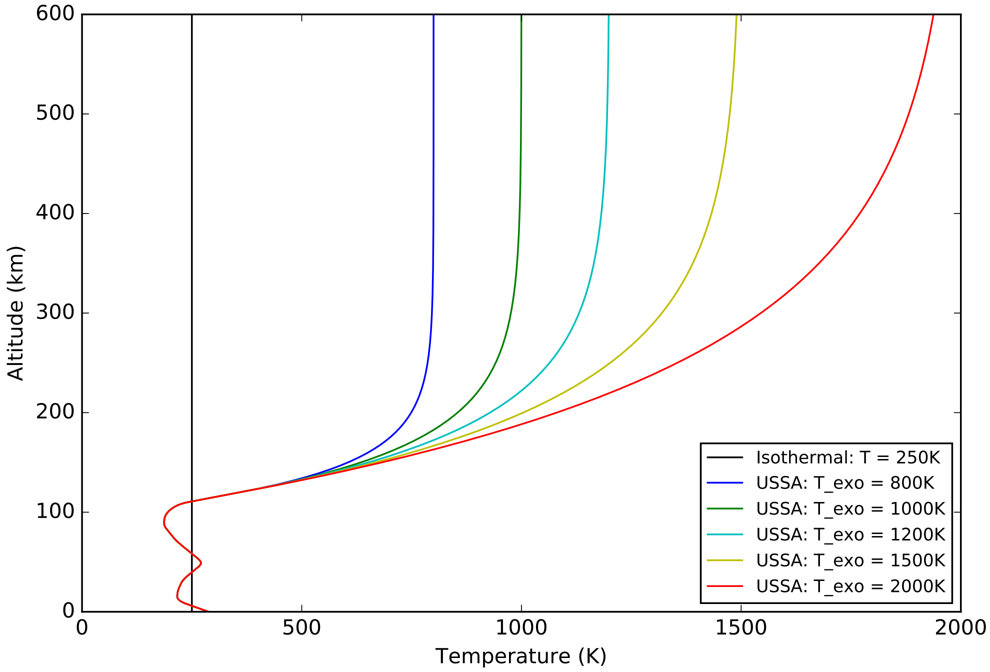

Figure 3.1: Plot of a range of different temperature profiles implemented in ENDGame1D: an isothermal atmosphere with $T = 250\,\mathrm{K}$, and the US Standard Atmosphere (USSA) temperature profile with a range of exospheric temperatures that can be adjusted.

adiabatic compression and decompression, travelling at the speed of sound depending on the medium they are travelling through [Salby, 1996]. They can be caused by thunderstorms, ocean waves, earthquakes, nuclear explosions [Yeh & Liu, 1974; Walterscheid *et al.* , 2003], or rocket launches [Afraimovich *et al.* , 2001] for example.

Figure 3.2 shows the first five minutes of a simulation of a vertically propagating acoustic wave in ENDGame. These plots show normalised density perturbations, i.e. how the density is perturbed compared to the background density at a particular altitude, which is given by ρ'/ρ_0, where ρ_0 is the steady, hydrostatically balanced state of ρ before the acoustic wave is initiated, and ρ' is the difference between the current value for ρ and the initial state of ρ: ρ_0.

The first plot shows the initial density perturbation: a Gaussian-shaped disturbance at an altitude of 5 km, that is intended to be a a simple representation of a disturbance in the troposphere, caused by a thunderstorm, for example. The amplitude of the acoustic wave is determined by the size of the initial density perturbation. The same effect can also be achieved by perturbing the vertical velocity w.

The density perturbations can be seen to grow with time in proportion to $\rho_0^{1/2}$, as shown in appendix C.2. A lack of acoustic wave observations in the thermosphere makes it difficult to ascertain how acoustic waves should grow by the time they reach

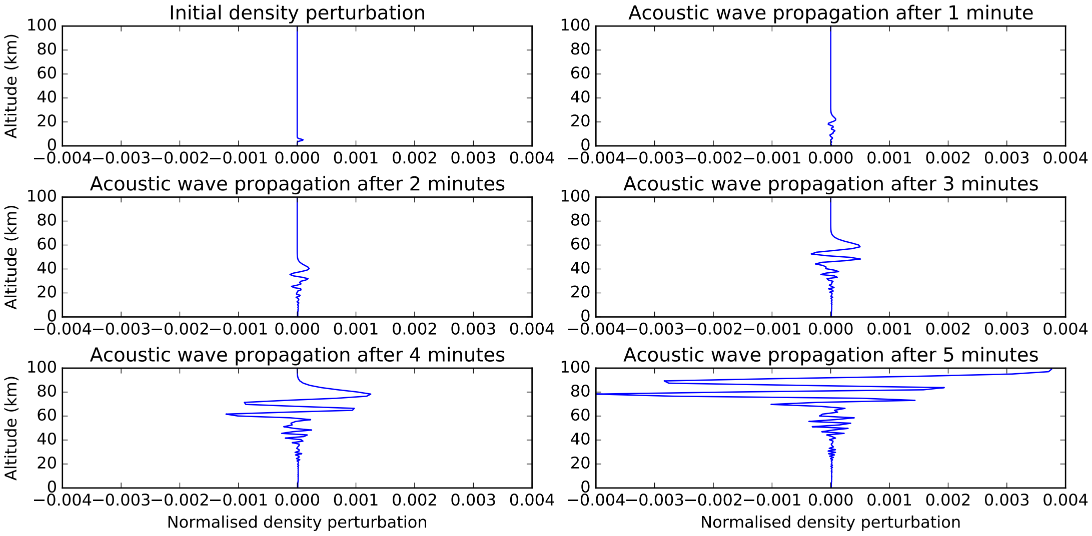

Figure 3.2: Plots of normalised density perturbations ρ'/ρ_0 with height to show the propagation of an acoustic wave upwards through an isothermal atmosphere using a three second time-step with an initial relative density perturbation of 10^{-4}. The acoustic wave propagates vertically at the speed of sound in an isothermal atmosphere, and its amplitude grows at the expected rate of $\rho_0^{1/2}$.

the thermosphere, but there are observations in the thermosphere of the natural density being perturbed by up to 11 % [Zettergren & Snively, 2013], so this can be used as a rough guide for realistic values of ρ'.

Aside from the off-centring of ENDGame's SI timestepping scheme, there are no physical or numerical mechanisms in place to limit or damp the growth of vertically propagating acoustic waves in ENDGame. As the top model boundary is lifted higher, the wave amplitudes grow so much that the density perturbations become too large for ENDGame's iterative solver to be able to converge onto a solution. The density perturbations can be so great that unphysical negative density values are obtained, which immediately causes the scheme to produce erroneous values and the simulation breaks instantly. Addressing these excessively large wave amplitudes is key to solving the problem of ENDGame's stability in the thermosphere.

In appendix C.1, the *theoretical dispersion relation* for 1D linear acoustic waves is shown to be $\omega^2 = c_s^2 m^2$, where ω is the *frequency*, c_s is the *speed of sound wave propagation*, and m is the *vertical wave number*[2]. From this, the *group velocity*, $c_g = \partial\omega/\partial m$, and *phase velocity*, $c_p = \omega/m$, of acoustic waves are found to be $c_p = c_g = c_s$. This should mean that acoustic waves are approximately non-dispersive according to the theoretical equations.

The frequency of waves in ENDGame simulations is found later in chapter 4,

---

[2] This is a well-known result, and can also be obtained from the 2D wave equation (4.31) with $k = 0$ and the assumption that $m \gg \Gamma$, where Γ is the inverse scale height.

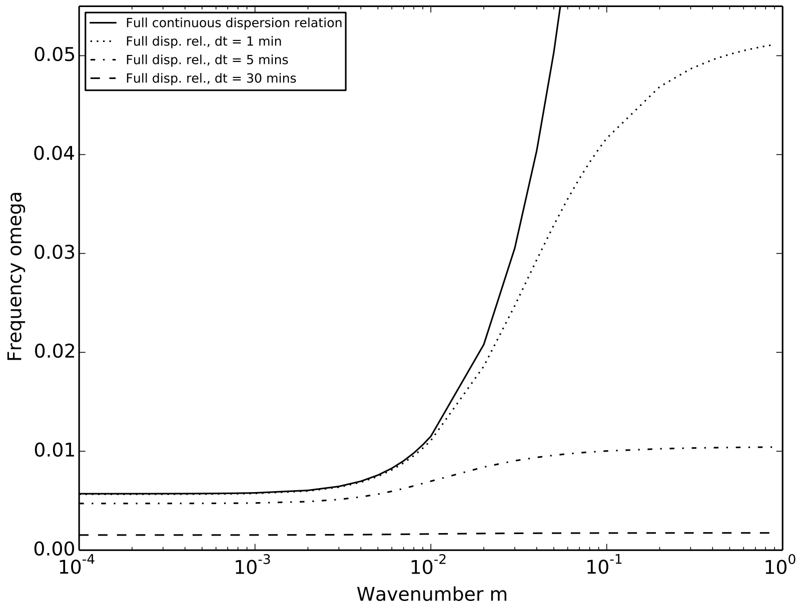

Figure 3.3: Plot of the vertical wavenumber m against acoustic wave frequencies ω. The acoustic wave frequencies are calculated using the full dispersion relation found later in chapter 4, given by equation (4.33). The solid line represents the 'true' dispersion relation, while the dotted/ dashed lines show the temporally-discrete dispersion relations for different sized time-steps Δt.

given by equation (4.33), which takes different values based on the spatial and temporal resolutions. Due to the SISL nature of ENDGame's formulation, there are upper limits to both the frequency ω and the vertical wavenumber m that are able to be resolved by ENDGame, and these cannot be avoided completely. The highest resolvable frequency in ENDGame's SI scheme is $\omega_{\text{num}} = 2\pi/2\Delta t$ (i.e. waves with a period of $2\Delta t$). The highest resolvable wavenumber on a grid with constant spacing of Δz is $m_{\text{num}} = 2\pi/2\Delta z$ (i.e. waves with a wavelength of $2\Delta z$) [Durran, 1999].

A plot of the continuous and temporally-discrete acoustic wave dispersion relations is given by Figure 3.3. The 'true' continuous dispersion relation is given by the solid black line, while the temporally-discrete dispersion relations are shown by the various dotted/ dashed lines. When a small 1 min time-step is used, the highest resolvable frequency is quite high and the temporally-discrete dispersion relation is quite close to the true dispersion relation until the curve approaches the highest resolvable frequency.

This figure also shows how the upper limits on the frequency and the wavenumber change the numerical group velocity and phase velocity. The value of the numerical group velocity, $c_g = \partial\omega/\partial m$, i.e. the slope of the curve, begins to level off for particularly high wavenumbers m. The value of the numerical phase velocity, $c_p = \omega/m$, is also no longer equal to c_s for larger m. This effect can be seen in the acoustic wave simulations shown in Figure 3.2, where the short, high frequency waves get left behind the main front of the wave as their group velocities are slower. Instead of travelling upwards as a single pulse, the numerics artificially slow down the propagation of the high frequency acoustic waves.

This effect is not necessarily a significant problem if small Δt and Δz are used. However, if a larger Δt is used, such as $\Delta t = 30\,\text{min}$ as in Figure 3.3, then the highest resolvable frequency is much lower and the temporally-discrete dispersion relation does a much poorer job of representing the true dispersion relation. The group velocity becomes close to zero for almost all waves. This means that the wave packet will hardly propagate upwards at all, but will just invert with each time-step as the numerical phase velocity is still non-zero. In these cases, the longwaves are still propagating upwards and perturbing the density at high levels, so the effects of acoustic waves on ENDGame's stability may still be considered.

Another property of ENDGame's SISL scheme is that it does not enforce mass conservation. The absence of this property means that ENDGame is not suitable for simulating shocks.

3.4 Stability tests

In this section, stability tests of ENDGame1D are performed. A notion of stability is defined to be used as an appropriate measure of how well the dynamical core is performing after an acoustic wave is introduced. Currently, if the acoustic wave reaches the top boundary and the solver is still able to converge onto a solution, then the simulation seems to be able to run indefinitely from that point on. Therefore, a run is considered to be stable if the simulation is still running for some model-time after the acoustic wave hits the top boundary.

In appendix C.1, the speed of sound is found to be $\sim 300\,\text{m}\,\text{s}^{-1}$ in an isothermal atmosphere at $250\,\text{K}$, and at this speed, it takes an acoustic wave ~ 30 minutes to reach a top boundary set at $600\,\text{km}$. A reasonably long 5 minute time-step is chosen to be comparable to operational ENDGame simulations, and a run is deemed to be stable if it successfully performs a 4 week simulation without crashing.

Stability tests in ENDGame1D are performed by initialising the simulation with a range of sizes of density perturbations that cause acoustic waves to propagate upwards. If it remains stable for 4 weeks, then the top boundary is extended upwards until it can no longer remain stable for the full 4 week runtime. The higher that the top boundary can be lifted, the greater the stability of ENDGame1D can be presumed to be under its current settings.

Some standard baroclinic wave tests [Jablonowski & Williamson, 2006] have been performed in ENDGame3D and the magnitude of unbalanced perturbations was estimated. It is found that ENDGame3D can be expected to generate relative density perturbations of order 10^{-4} to 10^{-3} in the mid-troposphere. It should be noted that these are likely to be larger than would be observed in the real atmosphere, but as they are generated by the numerics, the dynamical core must be able to withstand the effects of wave growth due to density perturbations of this size in the troposphere. Similar density perturbations will be used here to produce acoustic waves that ENDGame3D would be likely to deal with.

3.4.1 Comparison of gravity formulations and grid spacing

In this section, stability tests are performed using different grids and gravity formulations. Figure 3.4 shows the results of the stability tests for these different settings. The lines on this plot represent the maximum possible height of the top boundary for which simulations with 5 minute time-steps remains stable for 4 weeks. These simulations have either constant gravity or gravity decreasing with height according to the inverse square law, and either a uniform or quadratically stretched grid.

In general, larger density perturbations corresponding to larger wave amplitudes are more likely to cause instabilities at lower altitudes in ENDGame1D. With the most basic settings and an isothermal atmosphere set to 250 K, ENDGame1D does not remain stable above 250 km for even the smallest density perturbations. From this plot, a small but consistent improvement in stability can be seen for the simulations with a quadratically stretched grid compared with a uniform grid. The variable gravity doesn't have a systematic effect, although it may have more of an effect on a model with a more realistic gas composition.

3.4.2 Comparison of temperature profiles

In this section, stability tests are performed in atmospheres with either an isothermal atmosphere temperature profile set to 250 K, or the USSA temperature profile with an exospheric temperature $T_{\text{exo}} = 1000\,\text{K}$. The results of these stability tests can be seen in Figure 3.5. For now, solar minimums or maximums obtained by setting different exospheric temperatures are not considered. Simulations using uniform and quadratically stretched grids are included.

For relative density perturbations less than 10^{-4}, it can be seen that the simula-

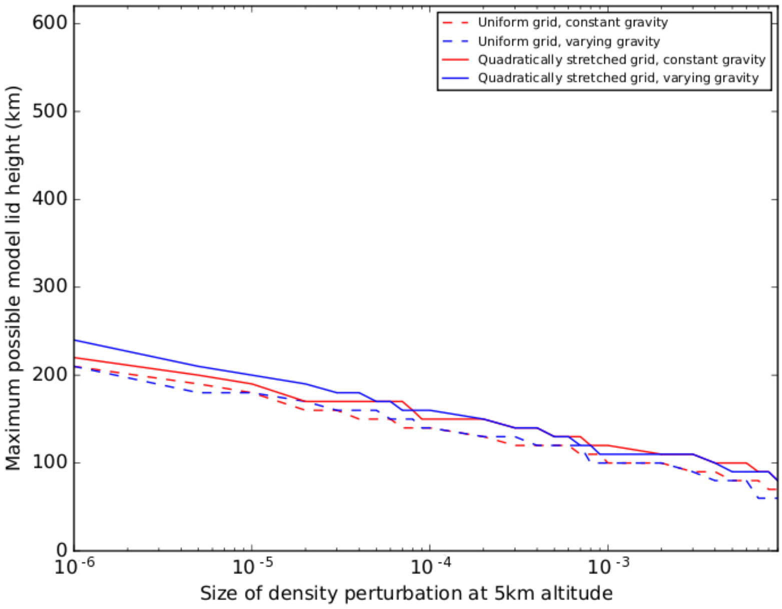

Figure 3.4: Stability tests of ENDGame1D comparing the use of uniform and quadratically stretched grids, and of constant gravity and varying gravity with height, for an isothermal atmosphere of 250 K. The lines on this stability test plot represent the maximum possible top boundary height for which a simulation with 5 minute time-steps remains stable for 4 weeks for different sized density perturbations.

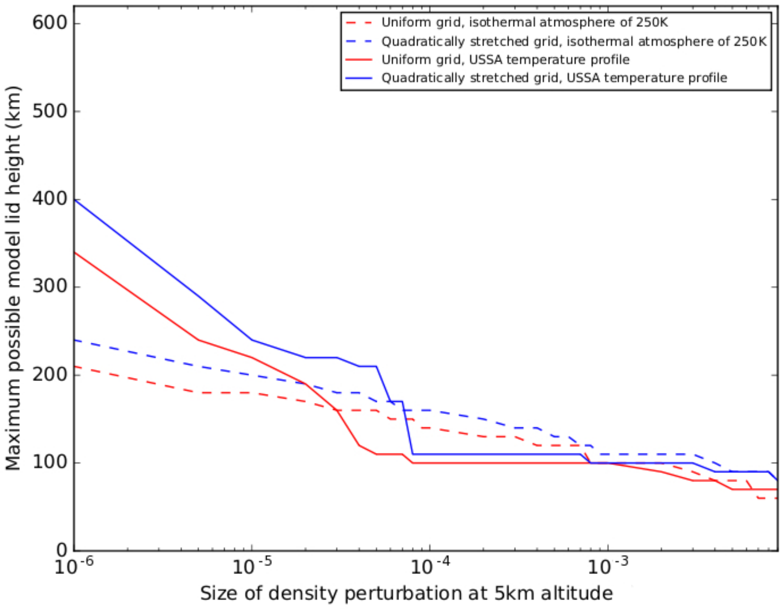

Figure 3.5: Stability tests of ENDGame1D comparing the use of isothermal and USSA temperature profiles, and of uniform and quadratically stretched grids. The lines on this stability test plot represent the maximum possible top boundary height for which a simulation with 5 minute time-steps remains stable for 4 weeks for different sized density perturbations.

tions with a quadratically stretched grid and the USSA temperature profile are able to have the top boundary extended significantly higher up to ∼400 km. But EN-

DGame is expected to be able to deal with density perturbations greater than 10^{-4}. For large density perturbations and acoustic waves, the most stable simulations have a quadratically stretched grid and an isothermal atmosphere.

The temperature in the USSA is warmer, particularly above ~150 km, and so the background density ρ decreases more slowly with height. This means that relative density perturbations are smaller at higher altitudes when using the USSA temperature profile compared with an isothermal atmosphere, so the wave growth with height is reduced, letting simulations remain stable at higher altitudes. For larger perturbations however, this makes less of a difference because acoustic waves cause instabilities before they reach levels where the temperature increases in the USSA act to decrease the wave growth rate. Overall, it is worth using a more realistic temperature profile for its own sake, and because it is consistent with the understanding of the problem that relative density perturbations will vary based on the temperature profile.

3.4.3 Comparison of implicitness parameters

In this section, stability tests are performed with varying implicitness parameters α, using the USSA temperature profile and a quadratically stretched grid. As described in appendix A.2, α varies between 0.5 and 1.0. For $\alpha = 0.5$, the SI scheme has no damping, and for $\alpha > 0.5$, the scheme becomes more stable but has an increased amount of numerical damping [Payne, 2008].

Only small increases to the α from the centred value of $\alpha = 0.5$ are considered here. This is because off-centred schemes are heavily damping to small-scale acoustic waves and gravity waves, and hence while potentially increasing stability, they also have a detrimental effect on the accuracy of ENDGame1D simulations [Akmaev, 2011]. By increasing the implicitness a small amount, it may be possible to make the dynamical core more stable without losing too much of the representation of acoustic waves. The results of the stability tests for the different α are shown in Figure 3.6.

For $\alpha = 0.53$, it can be seen that the top boundary can be lifted to 600 km for almost all density perturbations that ENDGame is expected to be able to deal with. However, it will be ideal to be able to use as small an α as possible to reduce the amount of damping of high frequency waves, so it will be prudent to include more physical processes in ENDGame1D so that less off-centring is needed.

Experiments with different levels of precision were also performed with EN-

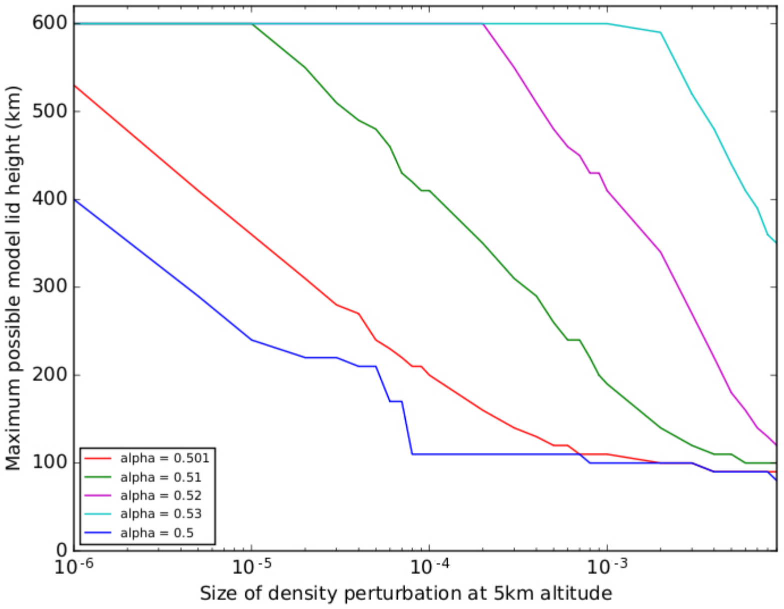

Figure 3.6: Stability tests of ENDGame1D comparing the use of different implicitness parameters, for simulations with the USSA temperature profile and a quadratically stretched grid. The lines on this stability test plot represent the maximum possible top boundary height for which a simulation with 5 minute time-steps remains stable for 4 weeks for different sized density perturbations.

DGame1D. However, changing the number of significant figures to which values are stored in ENDGame1D does not yield a significant change in stability as a result.

3.5 Summary

ENDGame1D is a single column version of the ENDGame dynamical core that can be used to simulate vertically propagating acoustic waves. It is set up to use either uniform or quadratically stretched vertical grids, variable or constant gravity and a temperature profile based on the USSA standard atmosphere. Stability tests are performed with a variety of settings: it is found that no combination of settings allows for the simulation to remain stable with the top boundary set at 600 km for the density perturbations ENDGame is expected to have to deal with, unless large amounts of off-centring are used. However, a quadratically stretched grid gives a small systematic increase in stability, and the variable gravity will be used for accuracy in a deep domain.

Chapter 4

Numerical Effects on Vertical Wave Propagation

This chapter is based heavily on the publication written by Griffin & Thuburn [2018], so this citation applies to the whole chapter.

The aim of this chapter is to better understand the instability in the thermosphere in ENDGame. It has been established in section 3.3 that instabilities in ENDGame seem to be related to the propagation of fast acoustic waves from the lower atmosphere into the thermosphere. The density perturbations of such waves grow roughly exponentially with height because of the exponential decrease of the background density with height. The numerical methods can affect the generation of these waves, their upward propagation, and their eventual fate when they reach large amplitudes. Here, ray-tracing techniques are used to compare the propagation of acoustic and gravity waves in ENDGame with that for the corresponding continuous governing equations. In this way, the numerical effects on the propagation of acoustic and gravity waves may be investigated.

4.1 Literature review

In this section, a brief overview of existing research on numerical wave propagation and the study of group velocity and ray-tracing techniques is given.

On large scales, the lower atmosphere is approximately in hydrostatic and geostrophic balance. Unbalanced motions such as gravity waves, and especially acoustic waves, are generally weak. Nevertheless, a variety of mechanisms, including nonlinear spontaneous emission by the balanced flow, can generate unbalanced motions. This wave generation can be greatly exaggerated in numerical models, as demonstrated by, for example, Mohebalhojeh & Dritschel [2000]. It has been shown in section 3.4 that unbalanced density and divergence perturbations that produce acoustic waves are generated near the surface with relative amplitude of order 10^{-4} to 10^{-3}. Although very weak, these are significantly stronger than is realistic. Moreover, because model grids are typically much finer in the vertical than in the horizontal, any marginally resolved waves will tend to be generated with nearly vertical wavenumbers. It is shown in section 3.4 that if ENDGame is initialised with a relative density perturbation of 10^{-3}, once it reaches an altitude of 110 km, the amplitude becomes so large that it causes the code to fail: the SISL scheme is not suitable for handling very large amplitude acoustic waves that result from upward propagation.

Ray-tracing has been used previously to study the propagation and dissipation of gravity waves in the real atmosphere (e.g. Vadas [2007] and references therein). Here, the emphasis is on how the propagation and dissipation of waves is modified in ENDGame by the numerical methods used, for both gravity and acoustic waves.

Trefethen [1982] studied the relevance of group velocity for the behaviour of finite difference models of time dependent partial differential equations, and presented a variety of applications of group velocity in the study of finite difference schemes to show that group velocity is essential to understanding their behaviour. Trefethen studied group velocity in 1D and 2D, with dispersion and anisotropy being introduced in the 2D finite difference model, and they found that poorly resolved wave packets can travel at the wrong speed and in the wrong direction. As wave energy propagation is governed by the group velocity, this would cause the incorrect propagation of wave energy.

Because of the background structure of the atmosphere, waves propagating upwards at certain angles may be refracted back towards the surface. However, it is well documented that the propagation of waves can be captured imperfectly by numerical models. One example, illustrated by Trefethen [1982], is that the dispersion relation for the numerical solution of the governing equations, and hence its phase and group velocities, depend on the local grid resolution. In addition, they note that the appearance of computational modes and the group velocities of associated *parasitic waves*: waves that manifest themselves at computational boundaries or interior points of non-uniform grids [Vichnevetsky, 1987a], are connected to the stability of finite difference models.

Vichnevetsky [1987b] looked in more detail at wave propagation in non-uniform grids for hyperbolic equations. They found that for non-dissipative schemes, the spurious solutions can end up becoming trapped in the computing domain, and that these spurious solutions can only be eliminated by some form of artificial dissipation. Vichnevetsky [1981] also found that it is possible for wave energy to become trapped between a coarse region of the grid and a reflecting boundary. If the hard reflection of a wave against boundary surfaces causes problems, then the spurious parasitic solutions could be eliminated by modifying the numerical boundary scheme so that it is absorbing [Vichnevetsky, 1987b].

Long & Thuburn [2011] also looked at wave propagation behaviour of centred difference schemes in non-uniform grids for the shallow water equations. They found that a wave of a given frequency is unable to propagate into a region where the grid is too coarse for that wave to be resolved, and also suggest that a mechanism must be included to dissipate such waves to avoid spurious reflections. Of particular interest here is whether the numerical methods used in ENDGame, in combination with grid anisotropy, could underestimate the downward refraction of wave packets and hence cause an excessive focussing of wave energy into the thermosphere.

A physical process that becomes very important in the thermosphere, but is currently not included in ENDGame, is *molecular viscosity and diffusion*. It might be expected that molecular viscosity and diffusion, if included, would help to control the amplitude of upward propagating waves and hence help to stabilise the dynamical core. The ray-tracing calculations introduced in this chapter will be extended to include a time-scale for the effects of molecular viscosity and diffusion on wave amplitude.

ENDGame's numerical methods contribute a certain amount of numerical damping. In particular, the SI time integration scheme (described in appendix A.2) includes an off-centring parameter $\alpha \in [0.5, 1.0]$ that can be varied to change the implicitness of the scheme. Setting $\alpha = 0.5$ gives a centered time-step that has no damping, while higher values for α give more implicit time-steps, which can have a detrimental effect on the accuracy of the solution due to their artificial damping of high-frequency waves, but can provide more stability. A time-scale for the effects of varying the off-centring parameter is also introduced in this chapter and included in the ray-tracing calculations, enabling an investigation into whether a modest off-centring can stabilise upward propagating waves until they reach the altitude of strong molecular damping.

Waves are produced by numerical models in a number of ways, depending on the model. They are often numerical artefacts: a product of the governing equations being badly resolved at the chosen grid scale, or caused by orography, convection, or

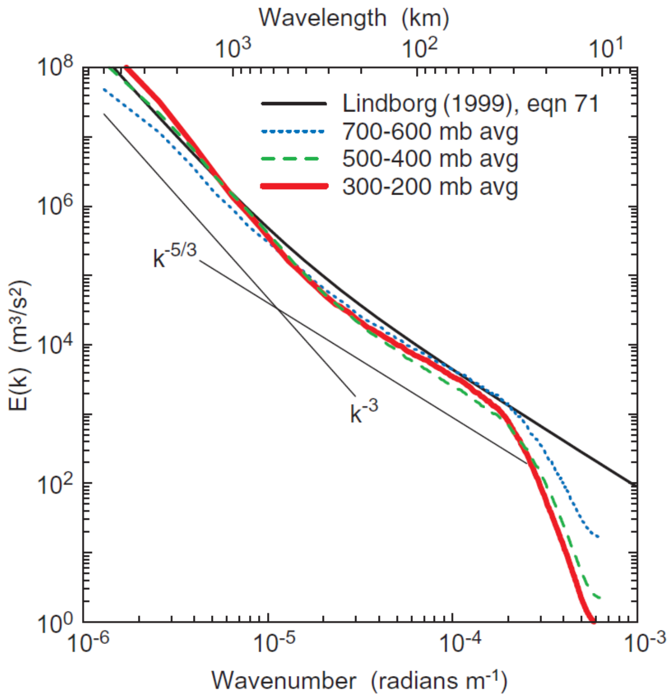

Figure 4.1: From Skamarock & Klemp [2008]: Kinetic energy spectra from the ARW model averaged over 7 - 25 January 2005 Developmental testbed center Winter Forecasting Experiment (DWFE) forecasts for the continental US. The ARW forecasts were produced using $\Delta x = 5\,\text{km}$.

other physical processes that are included in the model. The waves that are produced can have wavenumbers and wave energies of a wide range of orders of magnitude, as demonstrated in Figure 4.1 which shows the energy spectra of the ARW (Advanced Research WRF (Weather, Research and Forecasting)) model [Skamarock & Klemp, 2008]. Observations also indicate a broad energy spectrum in the atmosphere [Nastrom & Gage, 1985]. Therefore, it is worth considering a wide range of wavenumbers in this study of numerical wave propagation in ENDGame.

4.2 Ray-tracing equations

The theory of ray-tracing [Lighthill, 1978] assumes that waves are locally sinusoidal in space and time, and that the scales on which the wavevector varies are large compared to the wavelength. Here, the propagation in a 2D vertical cross-section of the atmosphere is considered. A nearly monochromatic wave packet with *wavevector* $\boldsymbol{k} = (k, m)$ and *frequency* ω approximately satisfies the local dispersion relation $\omega = \Omega(k, m; x, z, t)$, where the dependence on space $\boldsymbol{x} = (x, z)$ and time t can arise through, for example, variations in the background wind, temperature or stratification. The wave then propagates along a space-time trajectory (i.e. a *ray*) at the group velocity $\boldsymbol{c}_g$ and the wavevector evolves according to the following coupled system of ray-tracing equations:

$$\frac{D_{\boldsymbol{c}_g}}{Dt}(\boldsymbol{x}) \;=\boldsymbol{c}_g(\boldsymbol{k},\boldsymbol{x}) \;=\; \boldsymbol{\nabla}_{\boldsymbol{k}}\,\Omega, \tag{4.1}$$

$$\frac{D_{\boldsymbol{c}_g}}{Dt}(\boldsymbol{k}) \;=\; -\,\boldsymbol{\nabla}_{\boldsymbol{x}}\,\Omega, \tag{4.2}$$

where the derivative operator:

$$\frac{D_{\boldsymbol{c_g}}}{Dt} = \frac{\partial}{\partial t} + \boldsymbol{c}_g \cdot \boldsymbol{\nabla}_{\boldsymbol{x}} \tag{4.3}$$

represents the rate of change of a variable with time at a position moving with the group velocity $\boldsymbol{c_g}$ [Lighthill, 1978]. It is shown in appendix D.3 that from the ray-tracing equations (4.1) and (4.2), it can be shown that frequency is conserved along the ray, i.e. $D_{\boldsymbol{c}_g}\omega/Dt = 0$ provided that $\partial\Omega/\partial t = 0$, i.e. provided that the background is steady. In this study, $\boldsymbol{c}_g$ depends on $\boldsymbol{x}$ only through the temperature T, which is treated as a function of z only.

Lighthill [1978] also introduces the wave energy conservation law that describes the evolution of the wave's amplitude:

$$\frac{D_{\boldsymbol{c}_g}}{Dt}(\log W) + \boldsymbol{\nabla}_{\boldsymbol{x}} \cdot \boldsymbol{c}_g + \frac{2}{\tau} = 0. \tag{4.4}$$

Here, W represents the wave energy per unit volume and τ represents the time-scale for any processes that act to damp the waves (such as molecular viscosity and diffusion or the damping effect of the off-centring parameter α). Note that, for a stratified atmosphere in which the background density ρ_0 decreases exponentially with height, a constant W corresponds to a constant exponential growth rate of wave fields such as relative density perturbations ρ'/ρ_0.

In section 4.3, expressions for Ω, $\boldsymbol{\nabla}_{\boldsymbol{k}}\Omega$ and $\boldsymbol{\nabla}_{\boldsymbol{x}}\Omega$ are obtained for the continuous and discrete cases in order to solve the ray-tracing equations (4.1) and (4.2) and the wave energy conservation law (4.4). The wave propagation and the rate of wave amplitude growth may then be compared when using the analytical governing equations or the spatially- and temporally-discrete governing equations.

4.3 Wave equation with background density variation

In order to obtain the dispersion relation and the corresponding group velocities for the analytical governing equations and the spatially- and temporally-discrete governing equations, a 2D wave equation that includes a variation in background density is obtained in this section.

4.3.1 Continuous equation set

From the Navier-Stokes momentum (A.13), thermodynamic (A.16), continuity (A.18) and state (A.11) equations, and by neglecting the Coriolis[1] and source terms, the following governing equations on the (x, z)-plane are obtained:

$$
\begin{aligned}
\frac{\partial \rho}{\partial t} + \frac{\partial(\rho u)}{\partial x} + \frac{\partial(\rho w)}{\partial z} &= 0, && (4.5)\\
\frac{D\Theta}{Dt} &= 0, && (4.6)\\
\frac{Du}{Dt} + C_p \Theta \frac{\partial \Pi}{\partial x} &= 0, && (4.7)\\
\frac{Dw}{Dt} + C_p \Theta \frac{\partial \Pi}{\partial z} + g &= 0, && (4.8)\\
\Pi^{\frac{1-\kappa}{\kappa}} &= \frac{R}{p_e} \rho\, \Theta. && (4.9)
\end{aligned}
$$

This equation set is fully non-hydrostatic, but it can be made hydrostatic by neglecting the Dw/Dt term in the vertical momentum equation (4.8). Note that by taking R and C_p to be constant, a uniform gas composition is assumed rather than accounting for the various gas species shown in Figure 2.2.

4.3.2 Linearised equation set

A wave equation for a single purely oscillatory variable, and hence a dispersion relation, can be obtained by linearising the governing equations (4.5) - (4.8) about a basic state. This is done by separating the *current state* of the system of the system $(u, w, \rho, \Pi, \Theta)$ into the *basic state* $(u_0, w_0, \rho_0, \Pi_0, \Theta_0)$ which satisfies the governing equations at rest and in hydrostatic balance, and a *small perturbation term* $(u', w', \rho', \Pi', \Theta')$, so that any variable φ can be expressed as $\varphi = \varphi_0 + \varphi'$. Note that $\rho_0 = \rho_0(z)$, $\Pi_0 = \Pi_0(z)$ and $\Theta_0 = \Theta_0(z)$, and that products of the small perturbation terms may be neglected. The resulting linear system will have solutions proportional to $\exp(-\mathrm{i}\omega t)$ for some ω, so the time derivatives can be replaced by a factor $-\mathrm{i}\omega$, giving the linearised governing equation set:

$$
\begin{aligned}
-i\omega\rho' + \rho_0 \frac{\partial u'}{\partial x} + \frac{\partial(\rho_0 w')}{\partial z} &= 0, && (4.10)\\
-i\omega\Theta' + \frac{N^2}{g}\Theta_0 w' &= 0, && (4.11)\\
-i\omega u' + C_p \Theta_0 \frac{\partial \Pi'}{\partial x} &= 0, && (4.12)
\end{aligned}
$$

---

[1] Neglecting the Coriolis term is reasonable for almost all acoustic waves, and for gravity waves except in cases where the wavevector is almost vertical, i.e. $\widehat{m} \gg \widehat{k}$, where $\widehat{k}$ is the horizontal wavenumber and $\widehat{m}$ is the vertical wavenumber.

$$-i\delta_V\omega w' + C_p\left(\Theta_0\frac{\partial\Pi'}{\partial z} + \frac{\partial\Pi_0}{\partial z}\Theta'\right) = 0, \tag{4.13}$$

$$\frac{1-\kappa}{\kappa}\frac{\Pi'}{\Pi_0} - \frac{\rho'}{\rho_0} - \frac{\Theta'}{\Theta_0} = 0. \tag{4.14}$$

Here N^2 is the *Brunt Väisälä frequency*, or the *buoyancy frequency*, given by

$$\frac{N^2}{g} = \frac{1}{\Theta_0}\frac{\partial\Theta_0}{\partial z}, \tag{4.15}$$

[Salby, 1996]. The linearised state equation (4.14) is found in appendix A by taking the logarithm of the equation of state, and using a Taylor series expansion of log, and is given by (A.58).

4.3.3 Obtaining an equation for a single variable

Equations (4.10) - (4.14) form a system of equations for the variables $(u', w', \rho', \Pi', \Theta')$, which can be eliminated in turn to obtain a single equation for one unknown variable.

Begin by eliminating ρ' between the linearised equation of state (4.14) and the linearised continuity equation (4.10) to obtain:

$$0 = -i\omega\frac{1-\kappa}{\kappa}\frac{\Pi'}{\Pi_0} + \frac{i\omega}{\Theta_0}\Theta' + \frac{\partial u'}{\partial x} + \frac{1}{\rho_0}\frac{\partial(\rho_0 w')}{\partial z}. \tag{4.16}$$

Next, eliminate Θ' between (4.16) and the linearised thermodynamic equation (4.11) to obtain:

$$0 = -i\omega\frac{1-\kappa}{\kappa}\frac{\Pi'}{\Pi_0} + \frac{\partial u'}{\partial x} + \left(\frac{N^2}{g} - \frac{1}{H_\rho} + \frac{\partial}{\partial z}\right)w', \tag{4.17}$$

where H_ρ is the *density scale height*, given by

$$\frac{1}{H_\rho} = -\frac{1}{\rho_0}\frac{\partial\rho_0}{\partial z}. \tag{4.18}$$

By noting that the basic state satisfies hydrostatic balance, so:

$$C_p\Theta_0\frac{\partial\Pi_0}{\partial z} + g = 0, \tag{4.19}$$

then Θ' can also be eliminated between the linearised thermodynamic equation (4.11) and the linearised vertical momentum equation (4.13) to obtain

$$0 = \left(\delta_V\omega^2 - N^2\right)w' + i\omega C_p\Theta_0\frac{\partial\Pi'}{\partial z}. \tag{4.20}$$

Lastly, eliminate w' between equations (4.17) and (4.20) and substitute this into $\partial(4.12)/\partial x$ to obtain an equation for Π' only:

$$0 = \omega^2 \frac{1-\kappa}{\kappa}\frac{\Pi'}{\Pi_0} + \omega^2 C_p \left(\frac{N^2}{g} - \frac{1}{H_\rho} + \frac{\partial}{\partial z}\right)\left(\frac{\Theta_0}{\delta_V \omega^2 - N^2}\frac{\partial \Pi'}{\partial z}\right) + C_p \Theta_0 \frac{\partial^2 \Pi'}{\partial x^2}, \quad (4.21)$$

Finally, divide through by $C_p\Theta_0$ and use equation (C.10) for the speed of sound and the identities $\kappa \equiv R/C_p$ and $T_0 \equiv \Theta_0 \Pi_0$ to obtain

$$0 = \frac{\omega^2}{c_s^2}\Pi' + \omega^2 \left(\frac{2N^2}{g} - \frac{1}{H_\rho} + \frac{\partial}{\partial z}\right)\left(\frac{1}{\delta_V \omega^2 - N^2}\frac{\partial \Pi'}{\partial z}\right) + \frac{\partial^2 \Pi'}{\partial x^2}. \quad (4.22)$$

4.3.4 Obtaining a wave equation

The solutions to equation (4.22) for Π' have a strong, nearly exponential, dependence of the amplitude on height. In order to avoid this near-exponential dependence, a change to a more wavelike, purely oscillatory variable is required. First, define:

$$q(z) = F(z)\Pi', \quad (4.23)$$

and seek $F(z)$ such that substituting Π' for q in equation (4.22) leads to a wave equation. First, from Thuburn *et al.* [2002] and Daley [1998], the following identity for the density scale height is given:

$$\frac{1}{H_\rho} = \frac{N^2}{g} + \frac{g}{c_s^2}. \quad (4.24)$$

Also, from appendix C.2, it is known that the relative density grows as $\rho'/\rho_0 \sim \rho_0^{-1/2}$, and from the identity $T_0 \equiv \Theta_0\Pi_0 \sim 1$ and the definition for N^2/g given by (4.15), it can be deduced that $\Pi_0 \sim \exp[-(N^2/g)z]$. Then the growth rate for Π' is related to the background Exner pressure Π_0 and the relative density as follows:

$$\begin{aligned}\Pi' \sim \frac{\Pi_0 \rho'}{\rho_0} \sim \Pi_0 \rho_0^{-1/2} &\sim \exp\left[\left(\frac{1}{2H_\rho} - \frac{N^2}{g}\right)z\right] \\ &= \exp\left[\frac{1}{2}\left(\frac{g}{c_s^2} - \frac{N^2}{g}\right)z\right]. \quad (4.25)\end{aligned}$$

Define the inverse height scale Γ as follows:

$$\Gamma(z) = \frac{1}{2}\left(\frac{g}{c_s^2} - \frac{N^2}{g}\right), \quad (4.26)$$

so $\Pi' \sim \exp(\Gamma z)$. Using the definition for q (4.23) and the growth rate of Π' (4.25), setting $F(z) = \rho_0^{-1/2}\Theta_0$ gives the rescaled wavelike variable $q(z)$: as follows:

$$q = \rho_0^{1/2}\Theta_0\Pi', \tag{4.27}$$

Note that

$$\begin{aligned} \Pi' &= q\exp\left(\Gamma z\right), && (4.28)\\ \frac{\partial \Pi'}{\partial z} &= \left(\frac{\partial}{\partial z} + \Gamma + z\frac{\partial \Gamma}{\partial z}\right) q\exp\left(\Gamma z\right). && (4.29)\end{aligned}$$

Using the new rescaled variable q in place of Π' in equation (4.22), and the identity for the density scale height (4.24), an equation for q can be obtained:

$$0 = \frac{\omega^2}{c_s^2}q + \omega^2\left(\frac{\partial}{\partial z} - 2\Gamma\right)\left[\frac{1}{\delta_V\omega^2 - N^2}\left(\frac{\partial}{\partial z} + \Gamma + z\frac{\partial \Gamma}{\partial z}\right)q\right] + \frac{\partial^2 q}{\partial x^2} \tag{4.30}$$

Up to this point, no assumptions have been made about the buoyancy frequency N^2 or the inverse scale height Γ^2: they have been treated as functions of hieght z. This is almost a wave equation for q, but the $1/(\delta_V\omega^2 - N^2)$ term is still dependent on z. At this point, the *WKB approximation* is invoked: this involves assuming that the solution is a rapid oscillation/ has a large wavenumber and a small frequency, and that the wave amplitude and phase velocity $\boldsymbol{c}_p = \omega/\boldsymbol{k}$ vary slowly with height z [Howison, 2005]. This implies that the $1/(\delta_V\omega^2 - N^2)$ term is only weakly dependent on z and can be brought outside the derivative and the solution will remain locally similar. The same assumption applies to Γ. Now equation (4.30) can be rearranged to obtain a 2D wave equation with a variation in background density as follows:

$$\boxed{\frac{\partial^2 q}{\partial x^2} + \frac{\omega^2}{\delta_V\omega^2 - N^2}\frac{\partial^2 q}{\partial z^2} + \left(\frac{\omega^2}{c_s^2} - \frac{\omega^2\Gamma^2}{\delta_V\omega^2 - N^2}\right)q = 0.} \tag{4.31}$$

This equation gives wavelike solutions, and agrees with the wave equation derived by Thuburn *et al.* [2002] when T_0 is constant.

4.4 Dispersion relations and group velocities

In this section, the wave equation (4.31) is used to obtain expressions for the dispersion relation and group velocity for the continuous wave equation. The changes that are made to these expressions when the wave equation is discretised in space and time are then discussed.

For both the continuous and discrete cases, it is assumed that q has wavelike solutions that are locally proportional to $\exp[i(kx+mz-\omega t)]$. In other words, k, m and ω are the values of wavenumber and frequency that would be obtained by applying a Fourier transform to the solution for q. The objective here is to determine the dispersion relation $\omega = \Omega(k, m; x, z)$. If $\omega = \widehat{\Omega}(k, m; x, z)$ is defined to be the dispersion relation for the continuous system (4.31), it turns out that the continuous and the discrete cases can all be written in the form $\widehat{\omega} = \widehat{\Omega}(\widehat{k}, \widehat{m}; x, z)$ for particular choices of $\widehat{k}(k)$, $\widehat{m}(m)$, and $\widehat{\omega}(\omega)$. Here, $\widehat{k}$, $\widehat{m}$ and $\widehat{\omega}$ may be thought of as the effective wavenumbers and frequency as seen by the continuous dispersion relation.

4.4.1 Continuous dispersion relation

In the continuous case, $\widehat{\boldsymbol{k}}$ and $\widehat{\omega}$ are simply given by $\widehat{\boldsymbol{k}} = \boldsymbol{k}$ and $\widehat{\omega} = \omega$. Substituting a solution for q proportional to $\exp[\mathrm{i}(\widehat{k}x + \widehat{m}z)]$ into the wave equation (4.31) gives a quadratic for $\widehat{\omega}^2$:

$$0 = \frac{\delta_V}{c_s^2}\widehat{\omega}^4 - \left(\delta_V \widehat{k}^2 + \widehat{m}^2 + \frac{N^2}{c_s^2} + \Gamma^2\right)\widehat{\omega}^2 + N^2\widehat{k}^2. \tag{4.32}$$

The four solutions for $\widehat{\omega}$ from (4.32) are

$$\widehat{\omega} = \pm\frac{\sqrt{2}c_s}{2}\left\{A^2 \pm \left[(A^2)^2 - \frac{4N^2\widehat{k}^2}{c_s^2}\right]^{1/2}\right\}^{1/2}, \tag{4.33}$$

where:

$$A^2 = \left(\delta_V \widehat{k}^2 + \widehat{m}^2 + \frac{N^2}{c_s^2} + \Gamma^2\right). \tag{4.34}$$

If the second '±' in the solution for $\widehat{\omega}$ (4.33) is set to be a '+', then the contents of the outer square root are quite large, giving a large frequency $\widehat{\omega}$, which corresponds to the two high-frequency acoustic wave solutions. Conversely, if the second '±' is set to be a '−', then the two A^2 terms almost cancel. In this case, the contents of the outer square root are quite small, giving a smaller frequency $\widehat{\omega}$, which corresponds to the lower-frequency gravity wave solutions.

As an aside, the pure acoustic wave dispersion relation can be considered by neglecting the buoyancy frequency N^2 and the inverse height scale Γ^2 in the full dispersion relation (4.33) to obtain:

$$\widehat{\omega}^2_{\text{acoustic}} = c_s^2\widehat{K}^2, \tag{4.35}$$

where $\widehat{K}^2 = \widehat{k}^2 + \widehat{m}^2$. Similarly, letting $c_s \to \infty$, neglecting the inverse height scale Γ

gives the pure gravity wave dispersion relation:

$$\widehat{\omega}^2_{\text{gravity}} = \frac{N^2\widehat{k}^2}{\widehat{K}^2}. \tag{4.36}$$

Next, the group velocity $\boldsymbol{c}_g = \boldsymbol{\nabla}_{\boldsymbol{k}}\Omega$ can be obtained as follows:

$$\boldsymbol{c_g} = \boldsymbol{\nabla}_{\boldsymbol{k}}\Omega \ = \frac{\partial\omega}{\partial\widehat{\omega}}\left(\frac{\partial\widehat{\Omega}}{\partial\widehat{k}}\frac{\partial\widehat{k}}{\partial k}, \frac{\partial\widehat{\Omega}}{\partial\widehat{m}}\frac{\partial\widehat{m}}{\partial m}\right). \tag{4.37}$$

In the continuous case, $\partial\omega/\partial\widehat{\omega} = 1$, and $\partial\widehat{k}/\partial k = 1$ and $\partial\widehat{m}/\partial m = 1$, so only $\boldsymbol{\nabla}_{\widehat{\boldsymbol{k}}}\widehat{\Omega}$ is needed. Define $D(\widehat{\omega})$ to be the right-hand side of the quadratic for $\widehat{\omega}^2$ (4.32). Then D' is the derivative of D with respect to $\widehat{\omega}$ and is:

$$D'(\widehat{\omega}) \ \equiv \ \frac{\partial D}{\partial\widehat{\omega}} \ = \ -2\widehat{\omega}\left[\delta_V\widehat{k}^2 + \widehat{m}^2 + \frac{N^2 - 2\delta_V\widehat{\omega}^2}{c_s^2} + \Gamma^2\right]. \tag{4.38}$$

By differentiating the quadratic for $\widehat{\omega}^2$ (4.32) with respect to $\widehat{k}$ and $\widehat{m}$ and rearranging, expressions for $\partial\widehat{\Omega}/\partial\widehat{k}$ (4.39) and $\partial\widehat{\Omega}/\partial\widehat{m}$ (4.40) can be found.

$$\frac{\partial\widehat{\Omega}}{\partial\widehat{k}} = \frac{2\widehat{k}(\widehat{\omega}^2 - N^2)}{D'}, \tag{4.39}$$

$$\frac{\partial\widehat{\Omega}}{\partial\widehat{m}} = \frac{2\widehat{m}\widehat{\omega}^2}{D'}. \tag{4.40}$$

Next, $\boldsymbol{\nabla}_{\boldsymbol{x}}\Omega$ is obtained, which is used in the ray-tracing equation for describing the evolution of the wavenumber along the trajectory (4.2). Since the background state is independent of x, $\partial\Omega/\partial x = 0$. Then $\boldsymbol{\nabla}_{\boldsymbol{x}}\Omega$ is as follows:

$$\boldsymbol{\nabla}_{\boldsymbol{x}}\Omega = \frac{\partial\omega}{\partial\widehat{\omega}}\boldsymbol{\nabla}_{\boldsymbol{x}}\widehat{\Omega} = \frac{\partial\omega}{\partial\widehat{\omega}}\left(0, \frac{\partial\widehat{\Omega}}{\partial z}\right), \tag{4.41}$$

so k is constant along the ray. In the continuous case, $\partial\omega/\partial\widehat{\omega} = 1$, so only $\partial\widehat{\Omega}/\partial z$ is needed. This can be found by differentiating the quadratic for $\widehat{\omega}^2$ (4.32):

$$\begin{aligned} 0 \ &= \frac{\partial}{\partial z}[D(\widehat{\omega})]\bigg|_{\widehat{k},\widehat{m}} \\ &= \frac{\partial}{\partial z}[D(\widehat{\omega})]\bigg|_{\widehat{k},\widehat{m},\widehat{\omega}} + D'(\widehat{\omega})\frac{\partial\widehat{\Omega}}{\partial z}, \end{aligned} \tag{4.42}$$

where the subscripts $|_{\widehat{k},\widehat{m}}$ and $|_{\widehat{k},\widehat{m},\widehat{\omega}}$ indicate that these values are held constant as the derivatives are taken. Evaluating (4.42) and rearranging gives

$$\boxed{\frac{\partial\widehat{\Omega}}{\partial z}=\frac{1}{D'}\left[\frac{\widehat{\omega}^2(\widehat{\omega}^2-N^2)}{c_s^4}\frac{\partial(c_s^2)}{\partial z}+\left(\frac{\widehat{\omega}^2}{c_s^2}-\widehat{k}^2\right)\frac{\partial(N^2)}{\partial z}+2\Gamma\frac{\partial\Gamma}{\partial z}\widehat{\omega}^2\right],} \tag{4.43}$$

where analytical expressions for $\partial(N^2)/\partial z$, $\partial(c_s^2)/\partial z$ and $\partial\Gamma/\partial z$ are found in appendix (D.2).

4.4.2 Spatially-discrete expressions

In this section, expressions for $\widehat{\boldsymbol{k}}$, $\partial\widehat{k}/\partial k$ and $\partial\widehat{m}/\partial m$ are found in the spatially-discrete case, which appear in the equations for the dispersion relation (4.33), the group velocity (4.37) and $\partial\widehat{\Omega}/\partial z$ (4.43). These equations will then describe wave propagation behaviour in ENDGame, with the dynamical core discretised in space using an Arakawa C-grid horizontal staggering of variables [Arakawa & Lamb, 1977] and a Charney-Phillips vertical staggering of variables [Charney & Phillips, 1953].

In the spatially-discrete case, derivatives are replaced with finite differences. First, consider horizontal derivatives. Provided the grid resolution x is uniform (or slowly varying), it is still possible to obtain locally wavelike solutions [Long & Thuburn, 2011]. However, the finite-difference approximation to the horizontal derivative of a wavelike variable is

$$\frac{\mathrm{e}^{\mathrm{i}k(x+\Delta x/2)}-\mathrm{e}^{\mathrm{i}k(x-\Delta x/2)}}{\Delta x}=\frac{\mathrm{i}\sin(k\Delta x/2)}{\Delta x/2}\mathrm{e}^{\mathrm{i}kx}, \tag{4.44}$$

rather than $\mathrm{i}k\mathrm{e}^{\mathrm{i}kx}$. Thus, the effective horizontal wavenumber seen by the dispersion relation in the spatially-discrete case is

$$\boxed{\widehat{k}=\frac{\sin(k\Delta x/2)}{\Delta x/2}.} \tag{4.45}$$

The effect of spatial discretisation on vertical derivatives is more subtle as the sinusoidal structure of the perturbation fields will be scaled by a roughly exponential dependence on height. Consequently, the dispersion relation then sees not only a modified effective vertical wavenumber:

$$\boxed{\widehat{m}=\frac{\sin(m\Delta z/2)}{\Delta z/2},} \tag{4.46}$$

but also a modified effective N^2 and Γ [Thuburn, 2006]. However, provided the vertical resolution Δz is finer than the density scale height H_ρ (4.18), as is usually the case in numerical models, the effective N^2 and Γ should be close to their true values. Therefore, to simplify the calculations in this section, N^2 and Γ are taken to have their true values.

These expressions for $\widehat{k}$ and $\widehat{m}$ are then used in equation (4.33) for $\widehat{\omega}$ and equations (4.39), (4.40) and (4.43) for $\partial\widehat{\Omega}/\partial\widehat{k}$, $\partial\widehat{\Omega}/\partial\widehat{m}$ and $\partial\widehat{\Omega}/\partial z$ respectively. The group velocity is given by equation (4.37), but $\partial\widehat{k}/\partial k$ and $\partial\widehat{m}/\partial m$ are now found by differentiating (4.45) and (4.46):

$$\boxed{\frac{\partial\widehat{k}}{\partial k} = \cos\left(\frac{k\Delta x}{2}\right), \ \frac{\partial\widehat{m}}{\partial m} = \cos\left(\frac{m\Delta z}{2}\right).} \tag{4.47}$$

Note that in this chapter, Δx and Δz are assumed to be uniform in space. Non-uniformity of Δx or Δz would introduce an explicit spatial dependence into the expressions for $\widehat{k}$ (4.45) and $\widehat{m}$ (4.46), which would then require additional terms in (4.41) and (4.42).

4.4.3 Temporally-discrete expressions

In this section, expressions for ω and $\partial\omega/\widehat{\omega}$ are found in the temporally-discrete case, which appears in the equations for the dispersion relation (4.33), the group velocity (4.37) and $\partial\widehat{\Omega}/\partial z$ (4.43). These equations will then describe wave propagation behaviour in ENDGame, with the dynamical core discretised in time using a SI timestepping scheme [Wood *et al.* , 2014b].

Recall that the equations in the linearised equation set (4.10) - (4.13) are of the form $\delta_t\varphi + \mathcal{L}(\varphi) = 0$, where $\delta_t = \partial/\partial t$ and $\mathrm{i}\widehat{\omega}$ is an eigenvalue for the $\mathcal{L}$ operator. Discretising $\delta_t\varphi$ between times n and $n+1$ for one eigenmode using a centred-in-time SI scheme gives:

$$\frac{\varphi^{(n+1)} - \varphi^{(n)}}{\Delta t} = -i\widehat{\omega}\frac{\varphi^{(n+1)} + \varphi^{(n)}}{2}. \tag{4.48}$$

For wavelike solutions, it is expected that $\varphi^{(n)} \propto \exp(-\mathrm{i}\omega t)$, so at the next time step, $\varphi^{(n+1)} \propto \exp[-\mathrm{i}\omega(t + \Delta t)]$, where Δt is the SI time-step. The use of this expression and the identity:

$$\mathrm{i}\tan(\alpha\Delta t/2) = \frac{\exp(\mathrm{i}\alpha\Delta t) - 1}{\exp(\mathrm{i}\alpha\Delta t) + 1} \tag{4.49}$$

gives ω in terms of $\widehat{\omega}$:

$$\boxed{\omega = \frac{\arctan(\widehat{\omega}\Delta t/2)}{\Delta t/2}.} \tag{4.50}$$

In the temporally-discrete case, the group velocity is given by equation (4.37) and $\boldsymbol{\nabla}_{\boldsymbol{x}}\omega$ is given by equation (4.41), but $\partial\omega/\partial\widehat{\omega}$ is now found by differentiating (4.50)

$$\boxed{\frac{\partial\omega}{\partial\widehat{\omega}} = \frac{1}{(\widehat{\omega}\Delta t/2)^2 + 1}.} \tag{4.51}$$

4.4.4 Time-scales for decaying processes

In this section, expressions for the time-scales of decaying processes are found, so that they may be used with the wave energy conservation law (4.4) to describe how they affect the growth of wave amplitudes.

The effect of off-centring parameters in the SI scheme can be considered by finding the resulting decaying time-scale. Discretising $\delta_t\varphi$, for some variable φ, between times n and $n+1$ using a SI scheme with off-centring parameter $\alpha \in [0.5, 1.0]$ gives:

$$\frac{\varphi^{(n+1)} - \varphi^{(n)}}{\Delta t} = -i\widehat{\omega}\left[\alpha\varphi^{(n+1)} + \beta\varphi^{(n)}\right], \tag{4.52}$$

where $\beta = 1 - \alpha$. Rearranging and expressing $\varphi^{(n+1)}$ in terms of $\varphi^{(n)}$ gives:

$$\varphi^{(n+1)} = \frac{1 - \mathrm{i}\beta\widehat{\omega}\Delta t}{1 + \mathrm{i}\alpha\widehat{\omega}\Delta t}.\varphi^{(n)} \tag{4.53}$$

This can be compared to the expression $\varphi^{(n+1)} \propto \exp(-\mathrm{i}\omega\Delta t)\varphi^{(n)}$ for wavelike solutions. Equate these and rearrange the result to obtain an expression for ω:

$$\omega = \frac{\mathrm{i}}{\Delta t}\log\left[\frac{1 - \mathrm{i}\beta\widehat{\omega}\Delta t}{1 + \mathrm{i}\alpha\widehat{\omega}\Delta t}\right]. \tag{4.54}$$

Note also that $\widehat{\omega}$ is comprised of a real part $\widetilde{\omega}$ that describes oscillations, and an imaginary part $-1/\tau_\alpha$ that describes the decaying time-scale, as follows:

$$\omega = \widetilde{\omega} - \frac{\mathrm{i}}{\tau_\alpha}. \tag{4.55}$$

The imaginary part of (4.55) gives the required time-scale for off-centring which can be used with the wave energy conservation law (4.4) to describe the effect of off-centring on the growth of wave amplitudes:

$$\frac{1}{\tau_\alpha} = -\frac{1}{\Delta t}\mathrm{Im}\left\{ \log\left[\frac{1 - \mathrm{i}\beta\widehat{\omega}\Delta t}{1 + \mathrm{i}\alpha\widehat{\omega}\Delta t}\right]\right\}. \tag{4.56}$$

Above the turbopause, located in the lower thermosphere between around 100 and 120 km, gas constituents are no longer well mixed by turbulence: they instead adopt their individual distributions with height as a result of molecular viscosity and diffusion, which itself is dependent on the viscosity of the fluid. Molecular viscosity and diffusion are introduced more rigorously in appendix E. The effect of molecular viscosity and diffusion can also be considered by finding its decaying time-scale. Consider the temperature diffusion equation:

$$\rho\, C_p \frac{\partial T}{\partial t} = \boldsymbol{\nabla} \cdot (\lambda \boldsymbol{\nabla} T), \tag{4.57}$$

where $\lambda = C_p\mu/P_r$ is the *thermal conductivity*, $P_r \approx 0.7$ is the *Prandtl number* and μ is the *scalar coefficient* of molecular viscosity, which may be approximated as:

$$\mu = 3.34 \times 10^{-7} T^{0.71}\,\mathrm{kg\,m^{-1}\,s^{-1}}, \tag{4.58}$$

which typically has values of order 10^{-5} [Vadas, 2007]. Considering the approximate magnitude of the individual terms in the temperature diffusion equation (4.57) gives the following:

$$\left.\frac{\partial T}{\partial t}\right|_{\text{diff}} \sim -\frac{\Delta T}{\tau_{\text{diff}}} \sim -\frac{\mu}{P_r\rho}\widehat{K}^2\Delta T, \tag{4.59}$$

where $\widehat{K}^2 = \widehat{k}^2 + \widehat{m}^2$ Here, τ_{diff} is the decaying time-scale for molecular viscosity and diffusion and ΔT is a temperature perturbation. The time-scale for molecular viscosity and diffusion is then:

$$\frac{1}{\tau_{\text{diff}}} \sim \frac{\mu K^2}{P_r\rho}. \tag{4.60}$$

For simplicity, this is used by the wave energy conservation law (4.4) to describe the effect of molecular viscosity and diffusion on the growth of wave amplitudes. This decreases with altitude: a smaller time-scale means that molecular viscosity and diffusion acts more quickly.

Of interest here is whether these damping mechanisms are strong enough to offset the non-dissipative wave growth due to the background density variation. In the absence of dissipation, the velocity perturbations $\boldsymbol{u}'$ and relative density perturbations ρ'/ρ_0 grow in proportion to $\rho \propto \exp(z/2H_\rho)$. Hence, the growth time-scale following an acoustic wave packet (and hence propagating at the speed of sound c_s) is given by:

$$\frac{1}{\tau_{\text{growth}}} \sim \frac{c_s}{2H_\rho}. \tag{4.61}$$

Whichever of the decaying time-scales is most significant will effectively damp wave growth in the dynamical core if the following is satisfied:

$$\max\left(\frac{1}{\tau_\alpha}, \frac{1}{\tau_{\text{diff}}}\right) > \frac{1}{\tau_{\text{growth}}}. \tag{4.62}$$

4.5 Ray-tracing simulations

In this section, acoustic and gravity waves are simulated using the 2D wave equation with a variation in background density (4.31) by solving the ray-tracing equations (4.1) - (4.4). A sufficiently small time-step is used such that numerical errors are negligible in the solutions of (4.1) - (4.4). Note that this time-step is unrelated to the time-step Δt of the SI scheme introduced in section 4.4.3, and discussed further in sections 4.5.2 and 4.5.5. The purpose of these calculations is to explore how wave propagation in the '*real*' atmosphere, simulated using the continuous wave equation, differs from wave propagation with ENDGame's discrete grid and SI timestepping scheme, by using the spatially- and temporally-discrete wave equations.

4.5.1 Acoustic waves in ENDGame's spatially-discrete grid

In this section, acoustic waves are simulated by using the solution for the dispersion relation (4.33) that corresponds to the frequency for acoustic waves. Figure 4.2 shows a *ray plot*: a plot of trajectories of wave packets, initiated with a range of wavevector angles, using the continuous wave equation. The total wavenumber $K = 1 \times 10^{-4}$ rad m^{-1} is chosen to illustrate how waves in the '*real*' atmosphere can be refracted by the temperature profile and can turn over.

The features of the rays worth noting in Figure 4.2 are that in the '*real*' atmosphere, the rays are able to propagate quite far horizontally, and that their group velocity is influenced by the background temperature profile. The background USSA temperature profile has the effect of refracting waves, and for small wavenumbers up to 4×10^{-5} rad m^{-1}, waves are refracted back to the surface before even passing the tropopause. An examination of rays with varying wavenumbers shows that rays initiated with total wavenumbers up to 7×10^{-5} rad m^{-1} propagate to an altitude of no higher than 110 km before turning over (see Figure 4.4).

In this section, ray-tracing techniques are used to examine the effects that ENDGame's Arakawa C-grid horizontal staggering of variables and Charney-Phillips

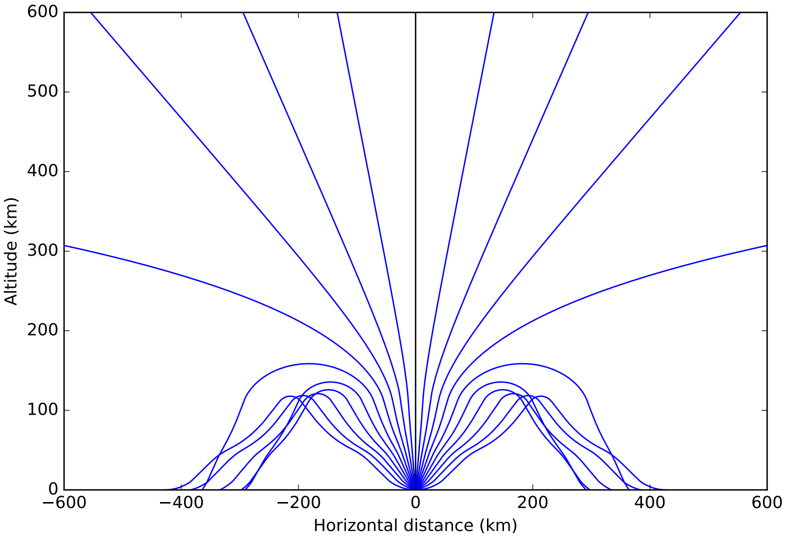

Figure 4.2: A ray plot of acoustic waves with a total wavenumber of 1×10^{-4} rad m^{-1} initiated with a range of wavevector angles measured from the horizontal, from 0 to π, using the analytical wave equation with the US Standard Atmosphere background temperature profile [United States Committee on Extension to the Standard Atmosphere (COESA), 1976].

vertical staggering of variables will have on wave propagation within ENDGame, and to determine the extent to which this is responsible for excessive focussing of wave energy into the thermosphere. Figure 4.3 shows a comparison of ray plots between the continuous wave equation and the spatially-discrete wave equation for rays initiated with a small total wavenumber of $K = 4 \times 10^{-5}\,\text{rad}\,\text{m}^{-1}$ and a range of wavevector angles from 0 to $\pi/2$.

It can be seen that the coarse horizontal resolution in ENDGame's Arakawa C-grid ($\Delta x \sim 100\,\text{km}$ in operational simulations) causes waves using the spatially-discrete wave equation to be less well-resolved in the horizontal direction than in the vertical direction which has a much finer grid spacing ($\Delta z \sim 1\,\text{km}$). This prevents waves from being able to propagate far in the horizontal direction compared to the continuous wave equation. For the continuous wave equation, the group velocity is approximately parallel to the wavevector; but this is no longer necessarily true in the spatially-discrete case, as demonstrated later by Figure 4.6. This means that even waves initiated with low wavevector angles in the spatially-discrete case have high group velocity angles and can reach up to 110 km before turning over.

However, *wave turning* does not always occur; whether or not waves turn over depends on the total wavenumber K and the initial angle of the wavevector $\boldsymbol{k} = (k, m)$. This relationship can be seen in Figure 4.4. This plot contains a lot of information and will be referred to a number of times in this section.

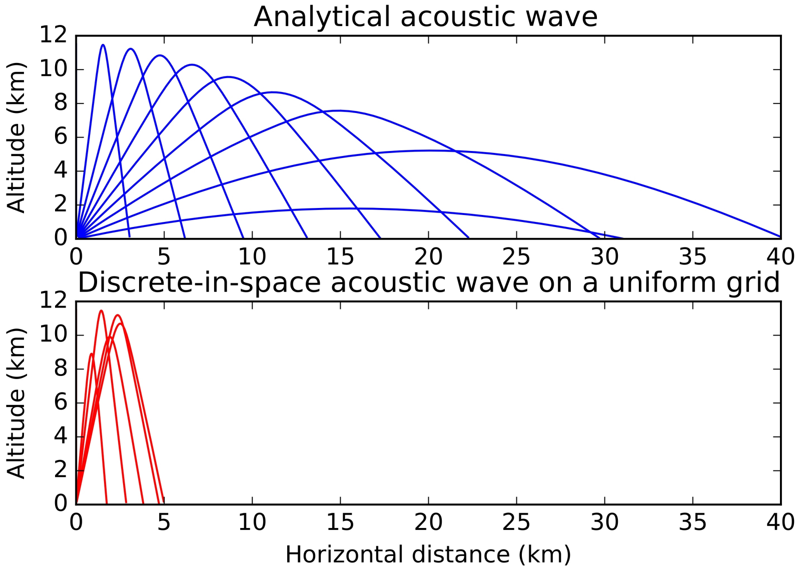

Figure 4.3: A comparison of ray plots of acoustic waves between (above) the continuous wave equation, and (below) the spatially-discrete wave equation with a uniform grid with $\Delta x = 100\,\mathrm{km}$ and $\Delta z = 1\,\mathrm{km}$. These acoustic waves have a total wavenumber of $K = 4 \times 10^{-5}\,\mathrm{rad\,m^{-1}}$ and are initiated with a range of wavevector angles measured from the horizontal, from 0 to $\pi/2$, with the USSA background temperature profile.

In the most general case, waves turn over at the height where the vertical component of the group velocity $\boldsymbol{c}_g$ is no longer positive, i.e. $\partial\widehat{\Omega}/\partial\widehat{m} = 0$. From the general expression for $\partial\widehat{\Omega}/\partial\widehat{m}$ (4.40), it follows that acoustic waves turn over at the height where $\widehat{m} = 0$. For pure acoustic waves described by the pure acoustic wave dispersion relation (4.35), the height at which waves turn over, where $\widehat{m} = 0$, corresponds to the height at which $c_s^2(z) = \widehat{\omega}^2/\widehat{k}^2$.

The dotted line in Figure 4.4 represents the critical wavevector angle of acoustic waves for a range of total wavenumbers K, using the pure acoustic wave dispersion relation (4.35). The *critical wavevector angle* is the angle measured from the horizontal up to which waves with a particular wavenumber will be refracted and turn over, and above which these rays will propagate upwards and into the thermosphere. In reality, these waves would be very strongly dissipated above ~150 km by molecular viscosity and diffusion (as discussed further in section 4.5.3), and this would need to be reflected in ENDGame either with damping by off-centring the SI scheme, or in a more physically sound way with molecular viscosity and diffusion. With no gravity wave terms, the critical angle for the pure acoustic wave dispersion relation is a constant $\sim 0.32\pi$ for all wavenumbers, because it can be seen from (4.35) that its group velocity is independent of K. Note that the wavevector angles and the group velocity angles do not necessarily match for the spatially-discrete case: their

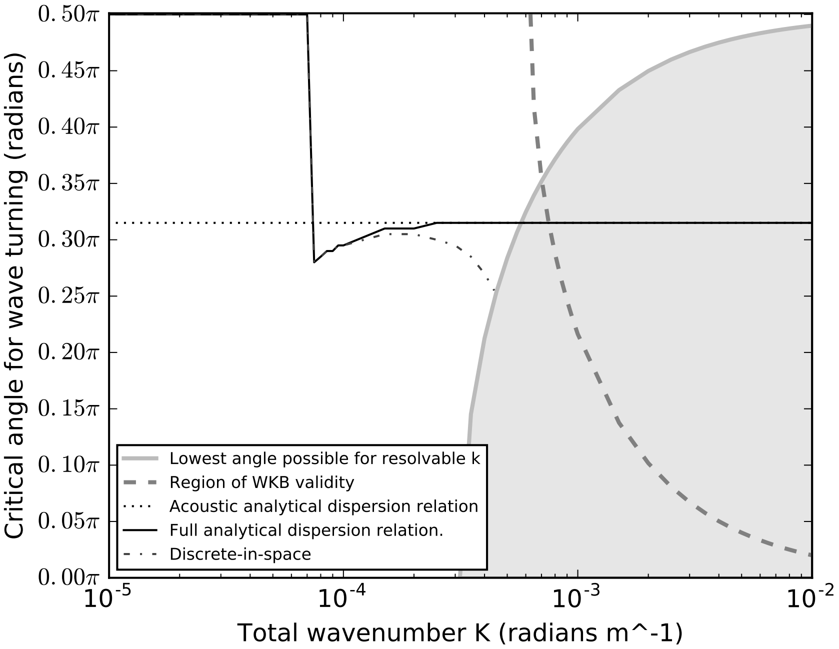

Figure 4.4: The critical wavevector angle (from parallel to the surface, 0, to perpendicular to the surface, $\pi/2$) up to which acoustic wave turning occurs, for a range of total wavenumbers K. The dotted line represents the critical angles for the continuous acoustic wave dispersion relation (4.35), and the solid black line represents the critical angle for the acoustic wave solution of the full continuous dispersion relation (4.33). The grey dashed-dotted line represents the critical angles for the spatially-discrete wave equation with $\Delta x = 10\,\text{km}$ and $\Delta z = 1\,\text{km}$.
In order for the horizontal wavenumber k to be resolved horizontally, it is required that $k < \pi/\Delta x$. This restriction in the numerical case is illustrated with the grey area showing where k is not resolved for this choice of Δx.
The area to the right of the thick grey dashed line indicates wavenumbers that satisfy WKB theory, although it is shown in Appendix D.4 that WKB theory can still be used to describe the behaviour of wave propagation outside this limit.

relationship for acoustic waves is shown later in Figure 4.6.

For acoustic waves described by the full dispersion relation (4.33), the height at which waves turn over, where $\widehat{m} = 0$, is the height at which the following expression is satisfied:

$$0 = \frac{\widehat{\omega}^2}{c_s^2} - \widehat{k}^2 - \frac{\widehat{\omega}^2\Gamma^2}{\widehat{\omega}^2 - N^2}, \tag{4.63}$$

where c_s, N and Γ are all functions of height z. The solid black line in Figure 4.4 represents the critical angle of acoustic waves for a range of total wavenumbers K, using the acoustic wave solution to the full dispersion relation (4.33). Waves with small wavenumbers up to 7×10^{-5} rad m^{-1} always turn over, even if they are initiated with vertical wavevectors. This is due to the relatively large buoyancy frequency N^2 and inverse height scale Γ that act to bring the expression in (4.63) to 0 at a lower height z, causing the wave to turn over sooner. This is illustrated by the ray plots of Figure 4.3, where the waves always turn over and no wave energy reaches the

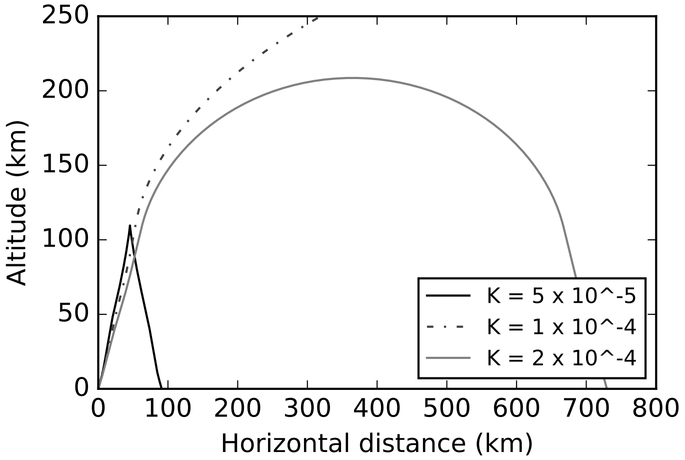

Figure 4.5: Ray plot of acoustic waves using the analytical wave equation with an initial wavevector angle of 0.3π from the horizontal, for a range of total wavenumbers near the dip on the critical angle plot in Figure 4.4.

thermosphere. For large wavenumbers and higher frequency waves, the buoyancy frequency N^2 and inverse height scale Γ become negligible, so the critical angle is the same as for the pure acoustic wave dispersion relation.

The unusual feature of the critical angle line for acoustic waves described by the full dispersion relation (4.33) is the dip that occurs for total wavenumbers just above $7 \times 10^{-5}\,\mathrm{rad\,m^{-1}}$. This warrants a closer analysis: a sample of rays of varying wavenumbers near this dip at an angle of 0.3π are shown in Figure 4.5. For total wavenumbers just to the left of the dip between 6×10^{-5} and $7 \times 10^{-5}\,\mathrm{rad\,m^{-1}}$, the waves turn over very sharply at about 110 km. It turns out that there is a feature of the USSA temperature profile at 110 km that makes N^2 particularly large at this altitude (as shown and described in appendix D.2). This acts to bring the expression in (4.63) to 0, and hence $\widehat{m}$ to 0 at about 110 km, causing the wave to turn over.

For wavenumbers slightly larger than 7×10^{-5} rad m^{-1} with an initial wavevector angle of 0.3π, the peak of N^2 is no longer sufficient to bring the expression in (4.63) to 0 at 100 km. Hence, these waves do not turn over and instead propagate to the top of the thermosphere, as can be seen by the dashed-dotted line in Figure 4.5, and is indicated in Figure 4.4 by the dip in the solid black line. As the wavenumber increases further, the waves become more like pure acoustic waves as the large wavenumbers k and m dominate the gravity wave terms in the full dispersion relation (4.33). Therefore, the waves are more easily refracted by the higher temperatures in the thermosphere and turn over more quickly for increasingly high wavenumbers, as illustrated by the grey line in Figure 4.5.

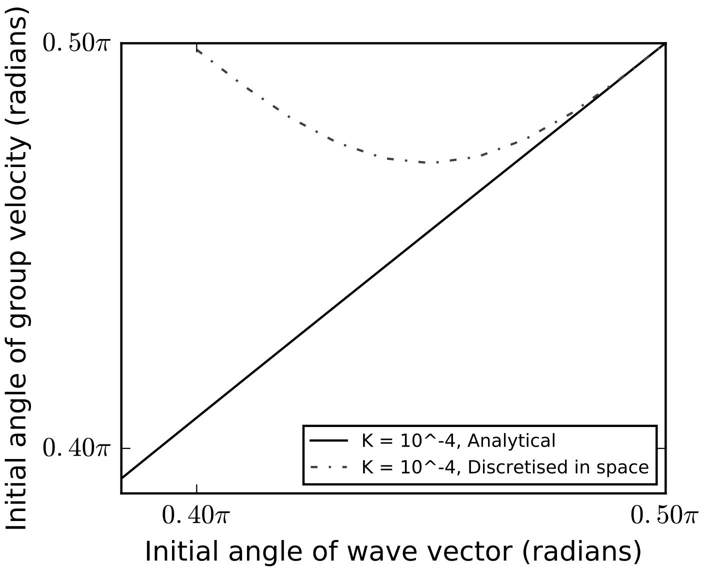

Figure 4.6: Initial group velocity angles for a range of initial wavevector angles for acoustic waves with a total wavenumber of $1 \times 10^{-4}\,\mathrm{rad\,m^{-1}}$, either using the pure acoustic wave dispersion relation (4.35), the acoustic wave solution to the full dispersion relation (4.33) or the spatially-discrete wave equation with $\Delta x = 100\,\mathrm{km}$ and $\Delta z = 1\,\mathrm{km}$, using the USSA background temperature profile.

The grey dashed-dotted on Figure 4.4 shows the critical angle for the spatially-discrete wave equation. However, the region marked by the greyed out area denotes wavevectors for acoustic waves that are unable to be resolved in a discrete grid with $\Delta x = 10\,\mathrm{km}$. For the horizontal component of waves to be resolved, the horizontal wavenumber k must satisfy the condition that $0 < k < \pi/\Delta x$.

Where the grey area of Figure 4.4 puts a lower limit on the initial wavevector angles that can be used with the spatially discrete wave equation, an interesting phenomenon occurs. Figure 4.6 compares the initial angles of the wavevector and group velocity for continuous and spatially-discrete acoustic waves. In the continuous case, the initial group velocity is almost parallel to the initial wavevector. However, as the discretised case is only resolved for $0 < k < \pi/\Delta x$, only a small range of wavevector angles, between $\sim 0.4\pi$ and 0.5π, are able to be considered in this particular case, so that the horizontal wavenumber k is not too big. For the higher allowable values of k, and hence lower initial wavevector angles, the initial group velocity angle diverges and becomes much higher than the initial wavevector angle.

This phenomenon can be explained by the group velocity equation (4.37). In the spatially-discrete case, the $\partial\widehat{k}/\partial k$ factor of the horizontal component of the group velocity is given by equation (4.47). This term, $\cos(k\Delta x/2)$, approaches 0 as k approaches its upper limit $\pi/\Delta x$. This means that, for waves initiated with the lowest resolvable wavevector angle, the horizontal component of the group velocity

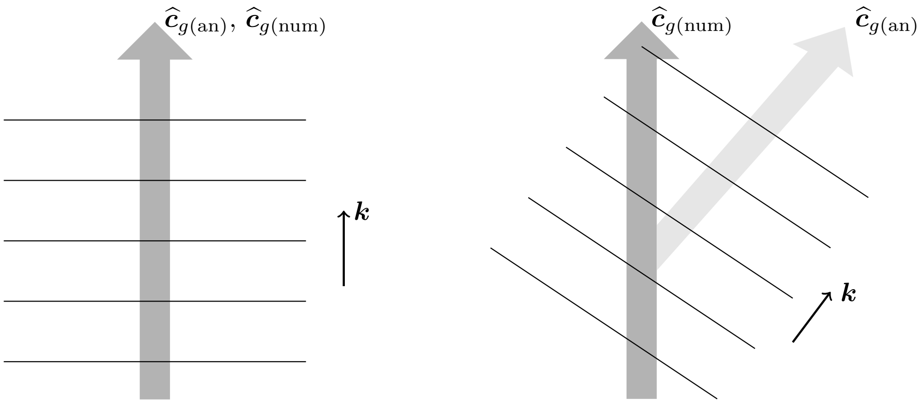

Figure 4.7: Illustrations of the directions of analytical group velocities $\widehat{\boldsymbol{c}}_{g(\mathrm{an})}$ and spatially-discrete group velocities $\widehat{\boldsymbol{c}}_{g(\mathrm{num})}$ of acoustic waves for varying wavevector $\boldsymbol{k}$.
Where $\boldsymbol{k} = 0$ (left), the wavevector, analytical group velocity $\widehat{\boldsymbol{c}}_{g(\mathrm{an})}$ and numerical group velocity $\widehat{\boldsymbol{c}}_{g(\mathrm{num})}$ go in the same direction.
Where $\boldsymbol{k} = \pi/\Delta x$ (right), the angle of the wavevector is as low as possible in order for the wave to still be resolved. The analytical group velocity $\widehat{\boldsymbol{c}}_{g(\mathrm{an})}$ goes in the same direction as the wavevector $\boldsymbol{k}$, but the numerical group velocity $\widehat{\boldsymbol{c}}_{g(\mathrm{num})}$ is still vertical.

is 0: so only the vertical component of the group velocity has a positive value, and hence the wave propagates vertically. This may cause excessive amounts of wave energy to be channelled upwards into the thermosphere in ENDGame, when in the real atmosphere, more energy would be channelled horizontally. This effect is illustrated in Figure 4.7. This particular result comes about due to the centred in space discretisation on an Arakawa C-grid [Purser & Leslie, 1988].

Referring back to the critical angle plot (Figure 4.4), the thick grey dashed line indicates that WKB theory is valid to the right of the line. For WKB theory to be valid, it is ideal for the wavelength to be significantly shorter than the length scale L at which the background varies ($L \sim 10\,\mathrm{km}$ for height z) [Howison, 2005], or equivalently:

$$\theta > \arcsin\left(\frac{2\pi}{KL}\right), \tag{4.64}$$

where θ is the angle of the wavevector. While this provides a rough indication of the conditions of the validity of WKB theory, it should still be indicative of the behaviour of wave propagation outside the WKB limit. Justification for this statement is given in appendix (D.4), and is supported by Dingle [1973] and Vadas [2007].

In the critical angle plot (Figure 4.4), it can be seen that the critical angles of the continuous acoustic wave equation and for the spatially-discrete wave equation end up diverging for larger total wavenumbers K up to about $5 \times 10^{-4}\,\mathrm{rad\,m^{-1}}$. There is a small range of wavevectors where analytical waves will turn over, but

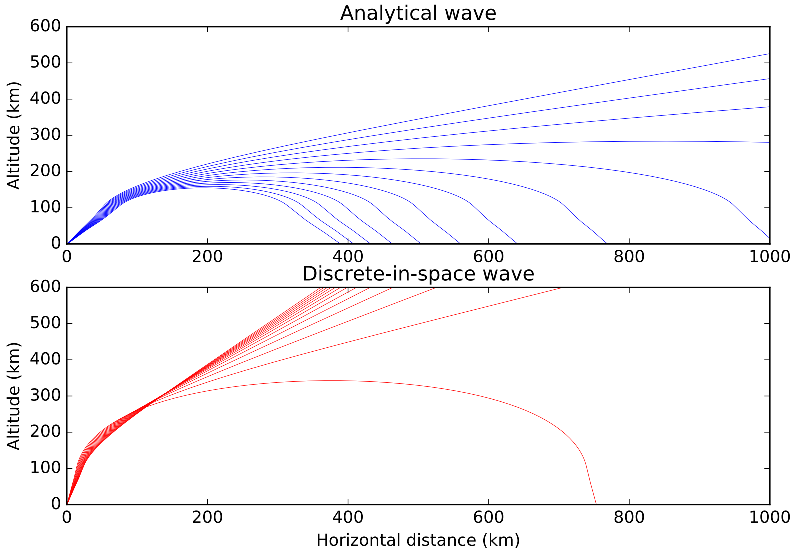

Figure 4.8: A comparison of ray plots of acoustic waves between (above) the continuous wave equation and (below) the spatially-discrete wave equation with a uniform grid with $\Delta x = 10\,\text{km}$ and $\Delta z = 1\,\text{km}$. These acoustic waves have a total wavenumber of $4 \times 10^{-4}\,\text{rad}\,\text{m}^{-1}$, and are initiated with a range of wavevector angles measured from the horizontal from 0.27π to 0.33π, with the USSA background temperature profile. These plots illustrate the difference in ray propagation where the lines for the critical angle of the analytical and spatially-discrete wave equations diverge in Figure 4.4.

spatially-discrete waves will propagate to the top of the thermosphere. Some of the rays in this region are shown in Figure 4.8. The rays in the spatially-discrete case are not able to propagate as far in the horizontal direction because the waves are not well resolved horizontally. Another feature is that the initial group velocity is at a lower angle for higher wavenumbers, but this changes at $\sim$280 km where the rays appear to cross over, and the group velocity for higher wavenumbers becomes more vertical. This again is due to the $\cos(k\Delta x/2)$ factor which is applied to the horizontal component of the group velocity, influencing the angle of wave propagation.

Next, the analytical and spatially-discrete propagation of waves for higher total wavenumbers are compared. Figure 4.9 shows another comparison of analytical and spatially-discrete wave propagation, as in Figure 4.3, but for a larger total wavenumber of $1 \times 10^{-4}\,\text{rad}\,\text{m}^{-1}$ for a small range of wavevector angles from $\sim 0.4\pi$ to $\sim 0.5\pi$, for which the spatially-discrete waves are resolved in the horizontal direction. For this wavenumber, there are no circumstances in which a wave in the spatially-discrete case can be refracted and turn over, but they are also unable to propagate as far in the horizontal direction as in the analytical case. This is due to the effect of the $\cos(k\Delta x/2)$ term in the horizontal component of the group velocity preventing many waves from being resolved in the horizontal direction. Figure 4.6 shows that

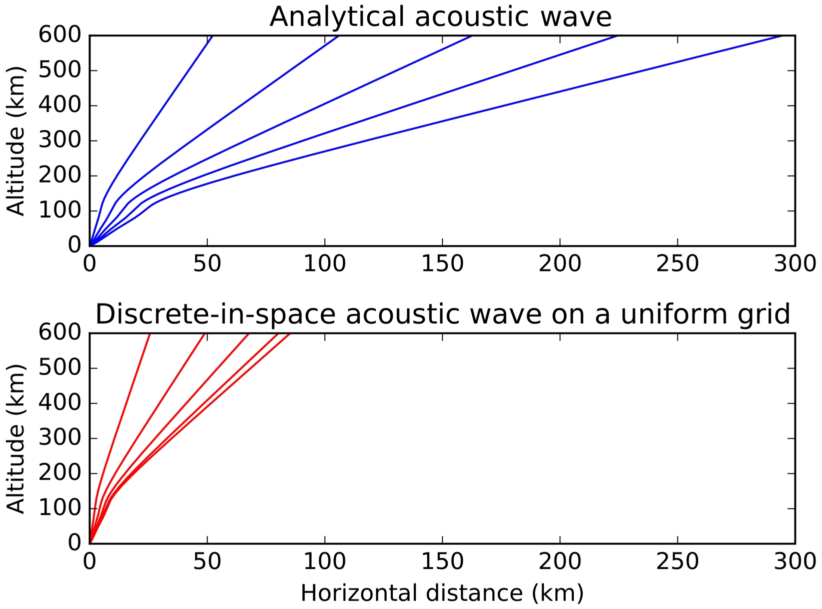

Figure 4.9: A comparison of ray plots of acoustic waves between (above) the continuous wave equation, and (below) the spatially-discrete wave equation with a uniform grid with $\Delta x = 100\,\mathrm{km}$ and $\Delta z = 1\,\mathrm{km}$. These acoustic waves have a total wavenumber of $1 \times 10^{-4}\,\mathrm{rad\,m^{-1}}$, and are initiated with a range of wavevector angles measured from the horizontal, from $\sim 0.4\pi$ to $\sim 0.5\pi$, with the USSA background temperature profile.

each initial group velocity angle corresponds to two potential initial wavevectors, so each curve in the second plot of Figure 4.9 refers to two wavevector angles.

4.5.2 Acoustic waves with ENDGame's semi-implicit scheme

In this section, acoustic wave propagation is simulated with the SI time discretisation. Figure 4.10 demonstrates the slowing effect that the temporally-discrete wave equation has on acoustic wave propagation. Here, a ray calculation has been run for 30 mins, and the time-step for the temporally-discrete case is just 3 s: an unrealistically short time-step chosen for illustrative purposes. The rays both have the same trajectory, but it can be seen that the wave in the temporally-discrete case travels at a slower rate. This phenomenon can be explained by the equation for group velocity (4.37). In the temporally-discrete case, the $\partial\omega/\partial\widehat{\omega}$ factor of the group velocity is given by (4.51), which is constant along the ray as $D_{\boldsymbol{c}_g}\widehat{\omega}/Dt = 0$. This acts to slow the horizontal and vertical components of the group velocity $\boldsymbol{c}_g$ by the same constant factor while maintaining the angle of propagation.

The larger the value of $\omega\Delta t$, the greater the slowing effect the time discretisation has on the wave. For a larger, more widely practiced time-step, an acoustic wave propagates upwards extremely slowly, but for waves with smaller frequencies ω, the time discretisation has less of a slowing effect. For this reason, gravity waves are

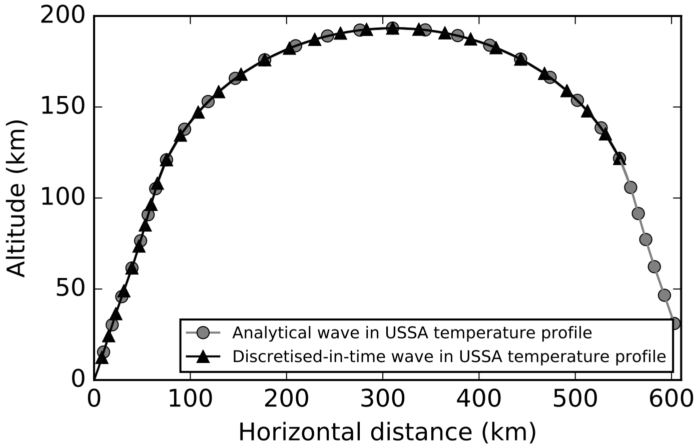

Figure 4.10: Ray plot of acoustic waves with a total wavenumber of $1 \times 10^{-3}\,\mathrm{rad\,m^{-1}}$ initiated with a wavevector angle of 0.3π and using either the continuous wave equation or the temporally-discrete wave equation with a centred-in-time ($\alpha = 0.5$) time-step of 3 s, and using the USSA background temperature profile. The dots represent 1 min intervals, and the simulation was run for 30 mins.

less slowed by the time discretisation, as shown later in section 4.5.5.

The experiments performed in this section are not spatially-discrete. However, when including the effects of both space and time discretisations, they interact as expected.

4.5.3 Wave amplitude growth of acoustic waves

In this section, the evolution of the wave energy W of vertically propagating waves is considered. W is analogous to a wave amplitude growth factor if $W = 1$ is taken at the launch of the acoustic wave [Lighthill, 1978]. In a stratified atmosphere, a constant value for W corresponds to an exponential growth of the relative density ρ'/ρ_0, while a strong drop in W is required for ρ'/ρ_0 to remain small. Note from the wave energy conservation law (4.4) that if dissipation is negligible and the background is independent of position x, then $c_g^z W$ is constant along the ray (where c_g^z denotes the vertical component of $\boldsymbol{c}_g$), and so the vertical profile of W reflects the vertical profile of $\boldsymbol{c}_g(\boldsymbol{k}, T)$, which in turn reflects that of the background temperature profile.[2]

Figure 4.11 shows how W changes with height for vertically propagating acoustic waves with a total wavenumber of $K = 1 \times 10^{-4}\,\mathrm{rad\,m^{-1}}$ with the continuous wave equation and the temporally discrete wave equation with centred-in-time ($\alpha = 0.5$) time-steps, with and without the decaying time-scale for molecular viscosity from (4.60). The values for W from the analytical and temporally-discrete wave equations are both given by the grey line in Figure 4.11. This is because ω and $\widehat{\omega}$ are both constant along the ray, so the wave energy in each of these cases follows the same

---

[2] This is why the plots of W resemble the mirror image of the USSA temperature profile.

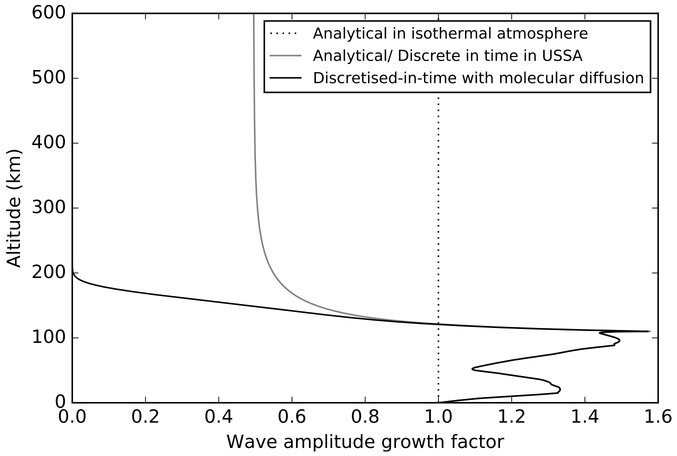

Figure 4.11: The wave energy/ wave amplitude growth factor at each height for a vertically propagating acoustic wave with a total wavenumber of $1 \times 10^{-4}\,\mathrm{rad\,m^{-1}}$ under different conditions:
1. using the continuous wave equation with an isothermal atmosphere of 250 K,
2. using the continuous wave equation with the USSA background temperature profile,
3. using the temporally-discrete wave equation with centred-in-time ($\alpha = 0.5$) 5 min time-steps and the USSA background temperature profile, and
4. using the temporally-discrete wave equation with centred-in-time ($\alpha = 0.5$) 5 min time-steps and molecular viscosity and diffusion with the USSA background temperature profile.

line, but the waves propagate upwards at different speeds.

The wave energy for the temporally-discrete wave equation with the decaying timescale for molecular viscosity and diffusion τ_{diff} (4.60) is given by the black line in Figure 4.11. Below 130 km, W is indistinguishable between the cases with and without the decaying timescale for molecular viscosity and diffusion. Between 130 km and 150 km, the decaying effect of molecular viscosity and diffusion makes W decrease very rapidly, which can be seen more clearly in the log plot for W later in Figure 4.20, and effectively prevents the growth of waves above this altitude. Including molecular viscosity and diffusion in ENDGame would not only improve its accuracy by incorporating a new physical process that has a significant effect in the thermosphere, but it will likely also improve its stability by preventing excessive wave growth in the upper atmosphere of the dynamical core.

The features that can be observed in Figure 4.11 (such as the sharp increase in W due to the peak in N^2 at 110 km described in appendix D.2, and the altitude at which molecular viscosity and diffusion begin to have a significant damping effect) are dependent on the total wavenumber K. Figure 4.12 shows how sensitive W is to different values of K. The reasons for this dependence are twofold: first, diffusive damping varies like the inverse of the diffusion time-scale τ_{diff} (4.60) which is proportional to K^2. Second, the time discretisation also has the effect of slowing

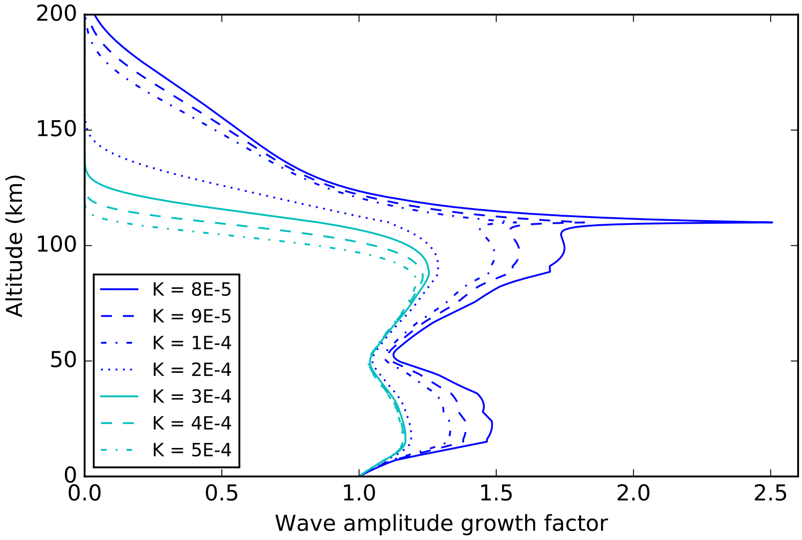

Figure 4.12: The wave energy at each height for a vertically propagating acoustic wave with a range of total wavenumbers for which the wave does not turn over, using the temporally-discrete wave equation with centred-in-time ($\alpha = 0.5$) 5 min time-steps and the decaying timescale for molecular viscosity and diffusion with the USSA background temperature profile.

the group velocity of the acoustic wave by the factor $\partial\omega/\partial\widehat{\omega}$ (4.51). Using the approximate acoustic wave dispersion relation (4.35) and the acoustic wave growth time-scale (4.61), the *propagation time-scale* τ_{prop} can be given by

$$\frac{1}{\tau_{\text{prop}}} \propto \frac{\partial\widehat{\omega}}{\partial\omega}\frac{1}{\tau_{\text{growth}}} \approx \frac{1}{(c_s\widehat{k}\Delta t/2)^2}\frac{c_s}{2H_\rho} \tag{4.65}$$

For smaller wavenumbers/ bigger wavelengths, W gets very large and molecular viscosity and diffusion does not have a significant damping effect until the wave reaches an altitude above 150 km. Fortunately, as demonstrated by Figure 4.4 for $K < 8 \times 10^{-5}\,\text{rad}\,\text{m}^{-1}$, the waves turn over before the wave amplitudes get too large. For larger wavenumbers/ smaller wavelengths, W does not grow much, and molecular viscosity and diffusion has a more significant damping effect at lower altitudes.

The decaying time-scale for the off-centring parameter from the SI timestepping scheme (4.56) can be altered to account for different amounts of off-centring, as shown in Figure 4.13. It can be seen that increasing levels of off-centring artificially damps the wave energy throughout the whole atmosphere, regardless of whether the decaying time-scale for molecular viscosity and diffusion is also included. These results also vary depending on the total wavenumber K that is used. It must be considered that the artificial damping also has to compensate for the exponential growth of the wave, which means that the rapid decrease in W with the increase in

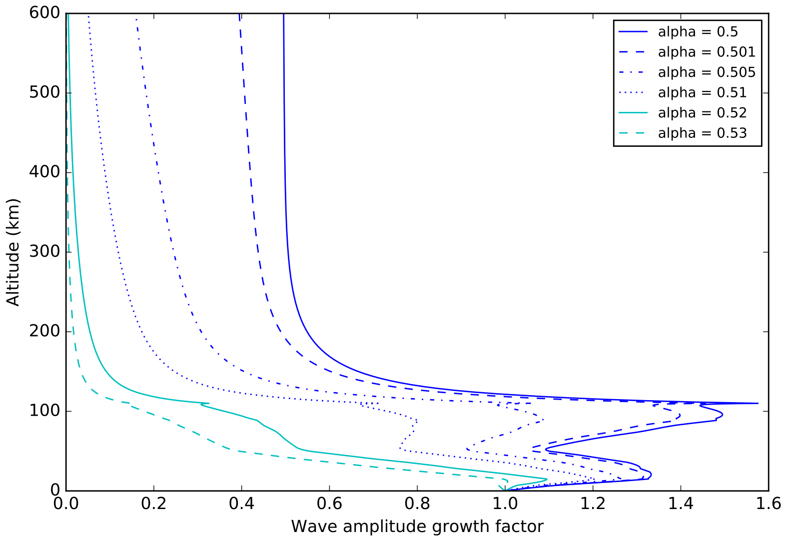

Figure 4.13: The wave energy at each height for a vertically propagating acoustic wave with a total wavenumber of $1 \times 10^{-4}\,\mathrm{rad\,m^{-1}}$ using the temporally-discrete wave equation with 1 min time-steps, with varying amounts of off-centring, and the USSA background temperature profile.

Time-step Δt	Off-centring parameter α	Total time
Analytical		20 mins
1 min	0.5	51 mins
1 min	0.53	51 mins
5 mins	0.5	12.25 h
30 mins	0.5	428 h

Table 4.1: Comparison of the time taken for acoustic waves initiated with a vertical wavevector and total wavenumber of $1 \times 10^{-4}\,\mathrm{rad\,m^{-1}}$ to reach the top boundary at 600 km with the continuous wave equation and with the temporally-discrete wave equation with different sized time-steps.

off-centring shown in Figure 4.13 is not as severe as it might appear.

In Figure 4.13, a small time-step of $\Delta t = 1\,\mathrm{min}$ is used for illustrative purposes. For larger Δt, the damping effect of the higher off-centring parameters is even greater. This is due to the contribution of the effects of the decaying timescale for off-centring (4.56) which depends on $\widehat{\omega}\Delta t$ and α, and of the propagation timescale τ_{prop} which depends on Δt. The effect of changing Δt on the time taken for the wave to propagate up to 600 km is shown in Table 4.1.

4.5.4 Gravity waves in ENDGame's spatially-discrete grid

In this section, gravity waves are simulated by using the solution for the dispersion relation (4.33) that corresponds to the frequency for gravity waves. Gravity waves are characterised by their smaller frequencies ω and slower group velocities $\boldsymbol{c}_g$ that propagate approximately perpendicularly to the wavevector. Note that gravity waves initiated with a wavevector angle of $\pi/2$ will not propagate: from the pure

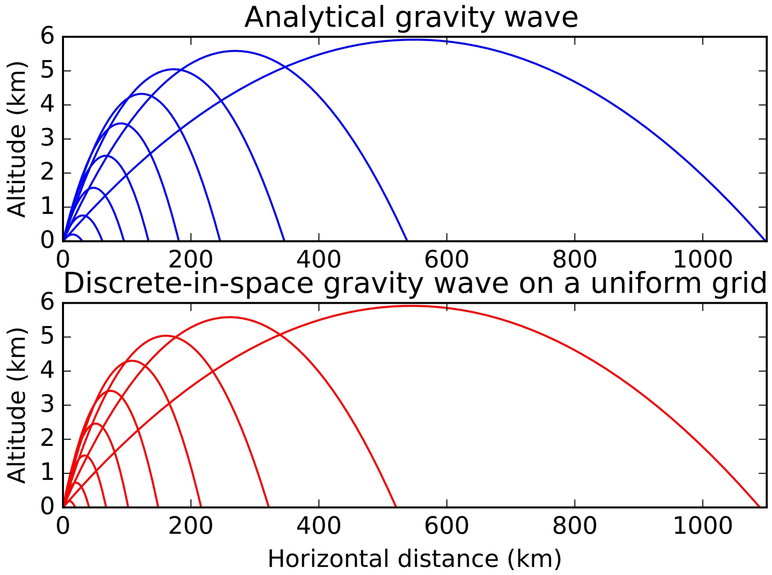

Figure 4.14: A comparison of ray plots of gravity waves between (above) the continuous wave equation and (below) the spatially-discrete wave equation with a uniform grid with $\Delta x = 100\,\mathrm{km}$ and $\Delta z = 1\,\mathrm{km}$. These gravity waves have a total wavenumber of $2 \times 10^{-5}\,\mathrm{rad\,m^{-1}}$ and are initiated with a range of wavevector angles measured from the horizontal from $\pi/2$ to π, with the USSA background temperature profile.

gravity wave dispersion relation (4.36), it can be seen that at this angle, there is no mechanism to produce gravity waves.

Gravity waves initiated with small total wavenumbers $K = 2 \times 10^{-5}\,\mathrm{rad\,m^{-1}}$ (chosen to look at cases where the rays always turn over) and a range of wavevector angles from $\pi/2$ to π using the continuous and spatially-discrete wave equations are shown in Figure 4.14. For acoustic waves, the effects of the space discretisation prevents the waves from being well resolved in the horizontal direction, which is immediately apparent in Figure 4.3. It can be seen in Figure 4.14 however that the propagation of gravity waves with a small total wavenumber is not affected much by the space discretisation, because gravity waves are still well resolved in the grid for this wavenumber. This can be seen by using a smaller value of $\widehat{\omega}$ in the horizontal and vertical components of the group velocity of gravity waves (4.37): the $\partial\widehat{\Omega}/\partial\widehat{k}$ and $\partial\widehat{\Omega}/\partial\widehat{m}$ factors are then smaller and hence do not influence the group velocity by as large an amount as in the acoustic wave case.[3]

As with acoustic waves, whether or not gravity waves turn over due to the background USSA temperature profile depends on the total wavenumber K and the initial angle of the wavevector. This relationship can be seen in Figure 4.15. For pure gravity waves described by the pure gravity wave dispersion relation (4.36),

---

[3] The space discretisation does affect the propagation of gravity waves with a larger total wavenumber, as discussed later and shown in Figure 4.18.

the height at which waves turn over, where $\widehat{m} = 0$, corresponds to the height at which $N \to \omega^+$ (i.e. the height at which N approaches ω from above). The group velocity obtained from the pure gravity wave dispersion relation is given by

$$\boldsymbol{c}_g = +\frac{2N^2\widehat{k}}{\widehat{K}^4}(\widehat{m}^2, -\widehat{k}\widehat{m}). \tag{4.66}$$

The dotted black line in Figure 4.15 represents the critical angle of gravity waves for a range of K using the pure gravity wave dispersion relation (4.36). The critical wavevector angle here is measured from $\pi/2$ to π, *up to which* the wave reaches an altitude of 600 km, and *above which* the wave is refracted and turns over. The critical angle for the pure gravity wave dispersion relation (4.36) is a constant $\sim 0.78\pi$ for all wavenumbers, because the direction of its group velocity is independent of K. In the continuous gravity wave case, the group velocity is almost perpendicular to the wavevector, but this is not true in the spatially-discrete case, as shown later in Figure 4.17.

For gravity waves described by the full dispersion relation (4.33), the height at which the waves turn over, where $\widehat{m} = 0$, is the height at which the expression in (4.63) is satisfied. The solid black line in Figure 4.15 represents the critical angle of gravity waves for a range of total wavenumbers K, using the gravity wave solution to the full dispersion relation (4.36). For large wavenumbers and higher frequency waves, the buoyancy frequency N^2 and inverse height scale Γ become negligible, so the critical angle is the same as for the pure gravity wave dispersion relation.

The unusual feature of this critical angle line is the peak that occurs between the total wavenumbers 2×10^{-5} and $1 \times 10^{-4}\,\mathrm{rad\,m^{-1}}$. This also warrants a closer analysis: a sample of rays of varying wavenumbers near the peak at a wavevector angle of 0.9π are shown in Figure 4.16. For total wavenumbers to the left of the peak in Figure 4.15, gravity waves turn over very quickly, never propagating above the tropopause at 10 km before turning over, as in Figure 4.14. On the right side of the peak, if the wave does turn over, it still reaches a high altitude close to 600 km. These waves slow down greatly before turning over, giving the appearance on the ray plot that they turn over very sharply.

The slowing of gravity waves as they reach the upper atmosphere is due to the buoyancy frequency N^2 becoming small at high altitudes due to the USSA temperature profile, as illustrated in Figure D.1. The small N^2 feeds into the group velocity for gravity waves (4.66). From this, it can be seen that as $m \to 0$, both $c_g^x \to 0$

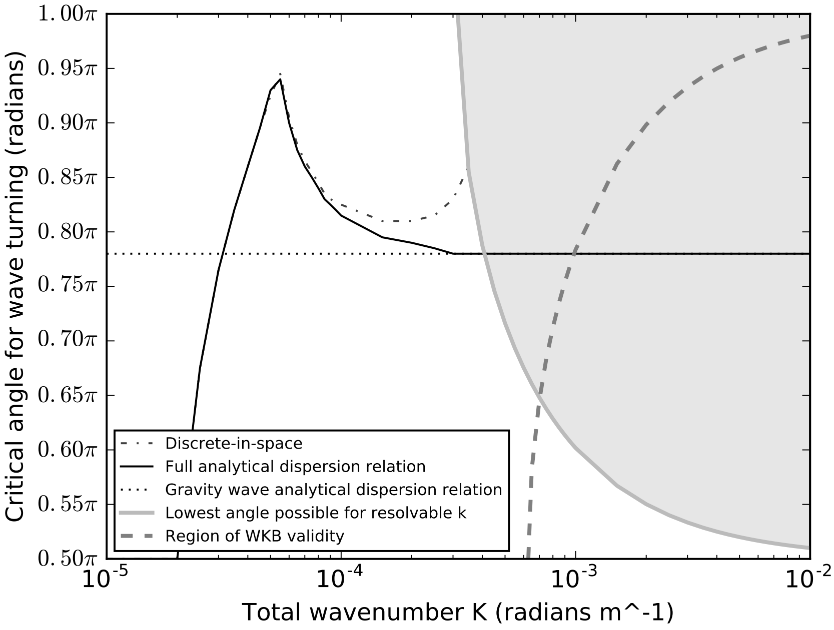

Figure 4.15: The critical wavevector angle (from perpendicular to the surface, $\pi/2$, to parallel to the surface, π) above which gravity wave turning occurs, for a range of total wavenumbers K. The dotted line represents the critical angles for the continuous gravity wave dispersion relation (4.36), and the solid black line represents the critical angles for the gravity wave solution of the full analytical dispersion relation (4.33). The grey dashed-dotted line represents the critical angle for the spatially-discrete wave equation with $\Delta x = 10\,\text{km}$ and $\Delta z = 1\,\text{km}$.
In order for the horizontal wavenumber k to be resolved in the grid, it is required that $k < \pi/\Delta x$. This restriction in the numerical case is illustrated by the greyed out area showing where k is not resolved for this choice of Δx.
The area to the right of the thick grey dashed line indicates wavenumbers that satisfy WKB theory, although it is shown in Appendix D.4 that WKB theory can still be used to describe the behaviour of wave propagation outside this limit.

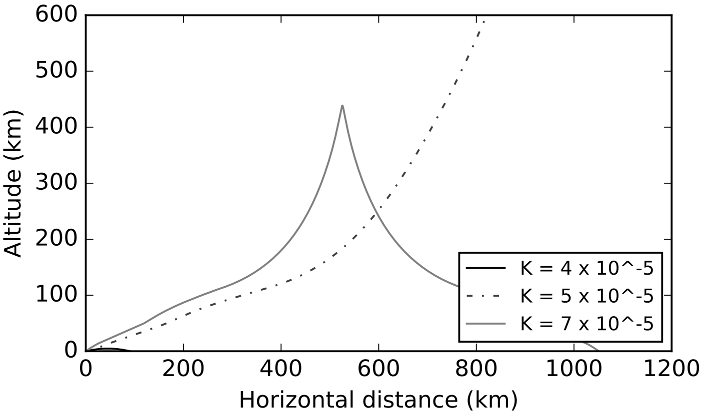

Figure 4.16: Ray plot of gravity waves using the continuous wave equation with an initial wavevector angle of 0.9π from the horizontal, for a range of total wavenumbers near the peak on the critical angle plot in Figure 4.15.

and $c_g^z \to 0$, but $c_g^x \to 0$ at a faster rate, so the horizontal group velocity becomes smaller more quickly, resulting in the cusp of the rays that turn over, as seen in

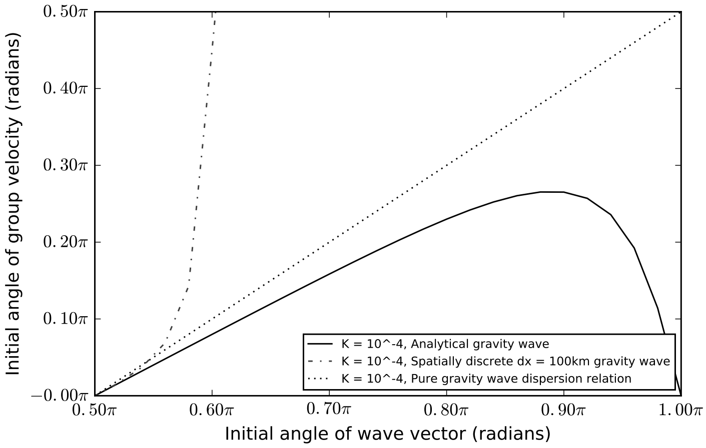

Figure 4.17: Initial group velocity angles for a range of initial wavevector angles for gravity waves with a total wavenumber of $1 \times 10^{-4}\,\mathrm{rad\,m^{-1}}$, either using the pure gravity wave dispersion relation (4.36), the gravity wave solution to the full dispersion relation (4.33) or the spatially-discrete wave equation with $\Delta x = 100$km and $\Delta z = 1\,$km, using the USSA background temperature profile.

Figures 4.16, 4.18 and 4.19.

As the total wavenumber increases further, the large k and m terms dominate the gravity terms in the full dispersion relation (4.33). Therefore, the gravity waves are more easily refracted by the higher temperatures in the thermosphere, and turn over more quickly for increasingly high total wavenumbers.

The dashed-dotted line on Figure 4.15 shows the critical angle for the spatially-discrete gravity wave equation. The greyed out area denotes wavevectors for gravity waves that are unable to be resolved in a discrete grid with $\Delta x = 10\,$km. Where this puts an upper limit on the wavevector angles that can be used with the spatially-discrete wave equation, due to the condition that $0 < k < \pi/\Delta x$, the same phenomenon occurs as for spatially-discrete acoustic waves in Figure 4.6.

Figure 4.17 compares the initial angles of the wavevector and group velocity for continuous and spatially-discrete gravity waves. The pure gravity wave dispersion relation (4.36) suggests that the initial group velocity is perpendicular to the initial wavevector angle. When using the continuous gravity wave solution to the full dispersion relation (4.33), the initial group velocity is similar to the pure gravity wave case for bigger total wavenumbers K. As the spatially-discrete case is only resolved for $0 < k < \pi/\Delta x$, only a small range of wavevector angles between 0.5π and 0.6π can be considered in this particular case for $\Delta x = 100\,$km. For the higher allowable values of k, and hence higher initial wavevector angles, the initial group velocity angle diverges from the angle perpendicular to the wavevector angle.

This phenomenon is equivalent to what happens to spatially-discrete acoustic

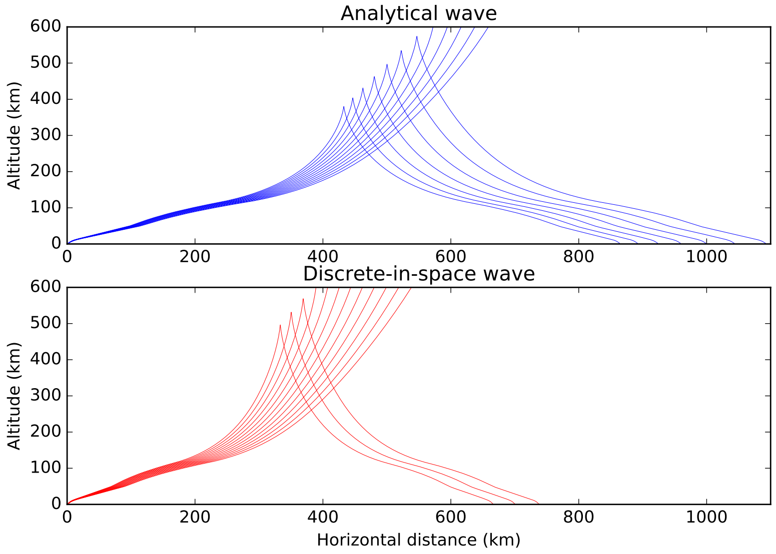

Figure 4.18: A comparison of ray plots of gravity waves between (above) the continuous wave equation and (below) the spatially-discrete wave equation with a uniform grid with $\Delta x = 10\,\mathrm{km}$ and $\Delta z = 1\,\mathrm{km}$. These gravity waves have a total wavenumber of $2 \times 10^{-4}\,\mathrm{rad\,m^{-1}}$ and are initiated with a range of wavevector angles measured from the horizontal from -0.77π to 0.83π, with the USSA background temperature profile. These plots illustrate the difference in ray propagation where the lines for the critical angle of the analytical and spatially-discrete wave equations diverge in Figure 4.15.

waves, and is illustrated by Figure 4.7: the $\cos(\widehat{k}\Delta x/2)$ term in the horizontal component of the group velocity (4.37) approaches 0 as k reaches its upper limit $\pi/\Delta x$, meaning that only the vertical component of the group velocity has a positive value, which forces the wave straight upwards.

In the critical angle plot: Figure 4.15, it can be seen that there is a small range of wavevectors where analytical waves will turn over, but spatially-discrete waves will propagate to the top of the thermosphere: some of the rays in this region are shown in Figure 4.18. For higher wavenumbers (as in Figure 4.18) which are less well resolved in the grid, the space discretisation significantly affects the extent of horizontal and vertical gravity wave propagation compared to well resolved small wavenumbers (as in Figure 4.14).

4.5.5 Gravity waves with ENDGame's semi-implicit scheme

In this section, gravity wave propagation is simulated with the SI time discretisation. Figure 4.19 demonstrates the slowing effect that the temporally-discrete wave equation has on gravity wave propagation. Here, a ray calculation has been run for 8 h, and the time-step for the temporally-discrete case is 5 min. The rays both have the same trajectory, but it can be seen that the wave in the temporally-discrete case travels at a much slower speed. This is explained in the same way as for temporally-

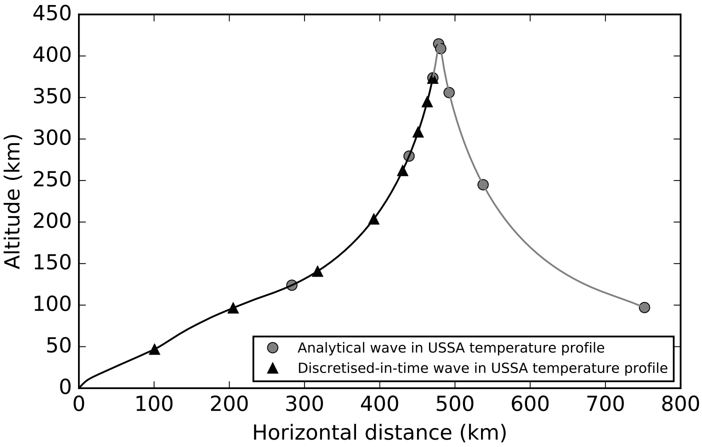

Figure 4.19: Ray plot of gravity waves with a total wavenumber of $1 \times 10^{-3}\,\mathrm{rad\,m^{-1}}$ initiated with a wavevector angle of 0.85π and using either the continuous wave equation or the temporally-discrete wave equation with a centred-in-time ($\alpha = 0.5$) time-step of 5 min, and using the USSA background temperature profile. The dots represent 1 h intervals, and the simulation ran for 8 h.

discrete acoustic waves: the $\partial\omega/\partial\widehat{\omega}$ factor of the group velocity (4.37) takes a value less than 1 in the temporally-discrete case, which acts to slow the horizontal and vertical components of the group velocity by the same constant factor while maintaining the angle of propagation. The wave can be seen to slow down as it reaches the cusp before speeding up again after it turns over.

The time discretisation has a lesser slowing effect on gravity waves than on acoustic waves: a 3 s time-step, as used in Figure 4.10 severely slows the temporally-discrete acoustic wave, but it would have a negligible effect on gravity waves. A 5 min time-step would have an even greater slowing effect on acoustic waves. The amount of slowing caused by the time discretisation is again governed by the size of $\widehat{\omega}\Delta t$. As $\widehat{\omega}$ is much smaller for gravity waves, $\widehat{\omega}\Delta t$ is also much smaller, so gravity waves are less slowed by the time discretisation.

4.5.6 Wave amplitude growth of gravity waves

In this section, the evolution of wave energy W for gravity waves is considered. In general, it behaves in a similar way to what is observed for acoustic waves in Figure 4.11, but there are a few differences: in Figure 4.20, it can be seen that the molecular viscosity begins to have a significant effect on gravity waves at a lower altitude than it does for acoustic waves. This is because gravity waves propagate more slowly, so there is more time for molecular viscosity and diffusion to act on them, and so they act to damp gravity waves more effectively at slightly lower altitudes. The altitude at which molecular viscosity and diffusion begin to have a significant damping effect on gravity waves is also dependent on the total wavenumber K,

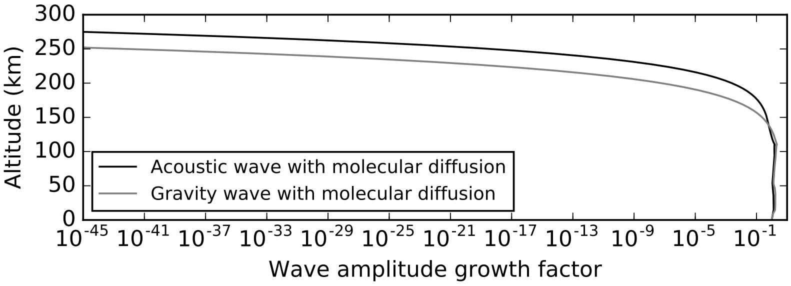

Figure 4.20: Log plot of the wave energy of acoustic waves and gravity waves propagating with an initial wavevector angle of 0.7π and a total wavenumber of $1^{-4}\,\mathrm{rad\,m^{-1}}$ using the temporally-discrete wave equation with centred-in-time ($\alpha = 0.5$) 5 min time-steps with molecular viscosity and diffusion and the USSA background temperature profile.

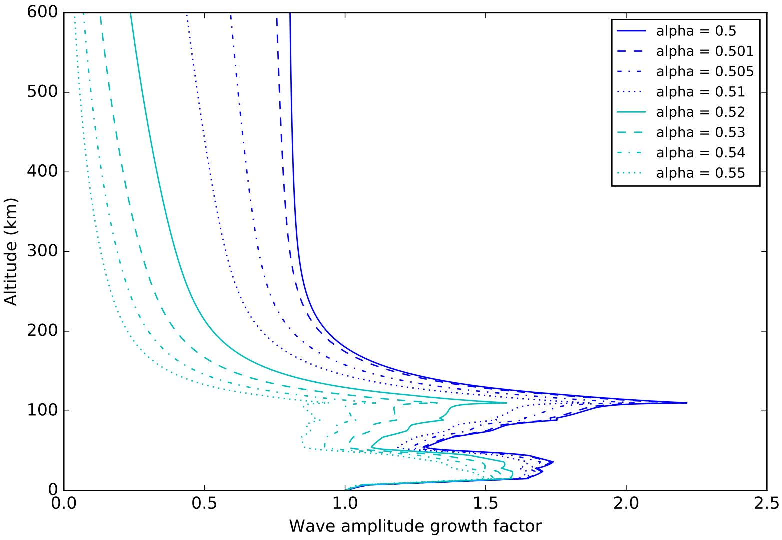

Figure 4.21: The wave energy at each height for a gravity wave propagating at an angle of 0.7π with a total wavenumber of $1 \times 10^{-4}\,\mathrm{rad\,m^{-1}}$ using the temporally-discrete wave equation with 1 min time-steps, with varying amounts of off-centring, and the USSA background temperature profile.

similarly to acoustic waves in Figure 4.12.

The effect of the decaying time-scale for the off-centring parameter (4.56) from the SI timestepping scheme on the wave energy is shown in Figure 4.21 for different amounts of off-centring. As for acoustic waves, increasing the amount of off-centring artificially damps the wave energy throughout the whole atmosphere. It can be seen by comparing with Figure 4.13 that low-frequency gravity waves are less damped by off-centring than high-frequency acoustic waves.

4.6 Summary

In this chapter, ray-tracing experiments were performed to study the effects of numerical methods on wave propagation in ENDGame.

A coarse horizontal resolution in numerical models prevents waves from being well-resolved in the horizontal direction. The limit on resolvable horizontal wavenumbers has a significant effect on wave propagation, redirecting waves vertically that would usually propagate at much lower angles, causing excessive, unphysical amounts of wave energy to be transferred into the upper atmosphere.

An important effect that has not been considered in this ray-tracing analysis is that of varying vertical and horizontal grid model spacing. A coarser vertical resolution at higher altitudes could trap short wavelengths at low altitudes, preventing them from propagating upwards and transferring excessive amounts of wave energy into the upper atmosphere. It would therefore likely have a positive effect on dynamical core stability, but its effect on wave propagation has not been studied here. Appendix B.3 considers how non-uniform grids are selected in ENDGame so that vertical processes can be well-resolved.

The SI timestepping scheme is severely slowing to high-frequency acoustic waves, but less so to gravity waves. On its own, it has no effect on the direction of wave propagation.

The inclusion of the timescale for molecular viscosity and diffusion confirms that molecular viscosity has a significant damping effect on wave amplitudes in the thermosphere. This suggests that the inclusion of molecular viscosity and diffusion in ENDGame should be beneficial for its stability when simulating the thermosphere by preventing excessive wave growth at high altitudes. Simulating acoustic waves in ENDGame seems potentially more problematic than simulating gravity waves because they are less damped by molecular viscosity. On the other hand, they are more strongly damped by the off-centring of the semi-implicit time-step.

Chapter 5

Vertical Molecular Viscosity and Diffusion in 1D

When simulating the whole atmosphere, it would be ideal to incorporate physical processes that have a more significant effect in the thermosphere, and could also have the added benefit of damping fast waves at high altitudes in a realistic way.

Above the turbopause, located in the lower thermosphere at $100 - 120\,\mathrm{km}$, gas constituents are no longer well mixed by turbulence as they are in the lower atmosphere. Therefore, the inclusion of Eddy diffusivity [Salby, 1996], which describes the turbulent mixing of a fluid, would not be appropriate. Instead, gas constituents adopt their individual distributions with height as a result of *molecular viscosity and diffusion*, which itself is dependent on the viscosity of the fluid. Molecular viscosity and diffusion are realistic physical damping mechanisms that have a significant effect in the thermosphere (which will be demonstrated in section 5.1), so they need to be included in order to extend ENDGame into the thermosphere [Akmaev, 2011].

There exist methods that involve adding a layer of artificial numerical viscosity near the top boundary in a model to artificially damp fast waves that grow too much at high altitudes and prevent spurious reflections of waves off the top boundary, improving stability. Another benefit of including molecular viscosity and diffusion is that they may eliminate the need for artificial viscosity near the top model boundary.

In this chapter, the discretisation of the continuous governing equations including vertical molecular viscosity and diffusion and their implementation into the ENDGame1D code is discussed. New solver technology must be developed to cope with the strong vertical molecular viscosity and diffusion in the thermosphere. The key novelty of this work is the fully-implicit treatment of vertical molecular viscosity and diffusion fully coupled to the semi-implicit (SI) treatment of the dynamics. It is also possible to consider the viscous properties of separate gas species, although this is outside the scope of this chapter. It is found that this new scheme, combined with a small amount of artificial damping by off-centring the SI timestep, is able to remain stable with a top boundary at 600 km for the kinds of waves that ENDGame1D is expected to be able to deal with.

5.1 Motivation

In order to further motivate the inclusion of molecular viscosity and diffusion in ENDGame along with the results of section 4.5.3, the time-scale on which molecular diffusion acts: τ_{diff} (4.60) and the decaying time-scale of the effect of the SI off-centring parameter: τ_α (4.56) are both compared to the growth time-scale of acoustic waves: τ_{growth} (4.61), in order to show whether the effects of molecular viscosity and diffusion are likely to have a significant enough damping effect on acoustic wave growth in the thermosphere. This will be the case if the time-scale on which diffusion takes place is shorter than the time-scale at which an acoustic wave grows (and similarly for the off-centring decaying time-scale); i.e. the condition that must be satisfied is:

$$\max\left(\frac{1}{\tau_{\text{diff}}}, \frac{1}{\tau_\alpha}\right) > \frac{1}{\tau_{\text{growth}}}. \tag{5.1}$$

There is enough information to substitute numbers for all of the values in (5.1). The vertical length scale used is the size of the uniform grid spacing: 1 km. The other constants are the gas constant $R = 278.04\,\mathrm{m}^2\,\mathrm{s}^{-2}\,\mathrm{K}^{-1}$, and $\kappa = R/C_p \approx 0.28$. Note here that in ENDGame, the gas constant for dry air is used, but in reality it varies depending on the altitude and the constituent gas species of the atmosphere at that altitude. The acceleration due to gravity also decreases with altitude.

The speed of sound is found in appendix C.1, and is given by

$$c_s^2 = \frac{RT}{1-\kappa}. \tag{5.2}$$

Lastly, approximations for the USSA temperature profile can be obtained from Figure 3.1, and approximations for the density values ρ at various levels when using USSA temperature profile can be obtained from the hydrostatically balanced background state. Using these, approximations for the diffusion time-scale τ_{diff} and the acoustic wave growth rate time-scale τ_{growth} at different levels of the atmosphere can be obtained, which are shown in Table 5.1.

$r - r_{\text{Earth}}$ (km)	ρ (kg m^{-3})	T (K)	g (m s^{-2})	τ_{diff} (s)		τ_{growth} (s)
0	1.2×10^{0}	285	9.80	6.4×10^{10}	$>$	49
100	4×10^{-7}	196	9.50	23000	$>$	42
110	6×10^{-8}	246	9.47	3140	$>$	46
120	1×10^{-8}	366	9.44	516	$>$	56
130	4×10^{-9}	474	9.41	148	$>$	65
135	3×10^{-9}	531	9.40	104	$>$	68
140	2×10^{-9}	564	9.39	57	$<$	71
150	9×10^{-10}	638	9.35	26	$<$	76
200	7×10^{-11}	856	9.22	1.77	$<$	90
300	2×10^{-12}	976	8.94	0.04	$<$	99

Table 5.1: Comparison of diffusion and acoustic wave growth time-scales at various altitudes, with the USSA temperature profile and a uniform grid with a vertical length scale of $L = 1$ km.

Table 5.1 shows that for 135 km and below, the diffusion time-scale τ_{diff} is much larger than the acoustic wave growth rate time-scale τ_{growth}. This indicates that diffusion acts too slowly here to have a significant damping effect on acoustic waves. However, between the altitudes of 135 km and 140 km, τ_{diff} becomes smaller than τ_{growth}, and gets even smaller at higher altitudes. This shows that at these altitudes, diffusion acts quickly enough to be able to damp acoustic waves. This matches the results of the experiment performed in section 4.5 in which the damping effect of molecular viscosity and diffusion on the wave energy in the thermosphere was demonstrated. This evidence indicates the benefit of the inclusion of molecular viscosity and diffusion in the vertical extension of ENDGame into the thermosphere.

5.2 Continuous equations

In appendix E.1, the continuous equations with vertical molecular viscosity and diffusion is derived and are are given by (A.19), (E.12), (E.20) and (A.11), and are given here by (5.3)-(5.6).

$$\frac{D\rho}{Dt} + \frac{\rho}{r^2}\frac{\partial (r^2 w)}{\partial r} = 0, \tag{5.3}$$

$$\frac{Dw}{Dt} - \Psi = \frac{1}{\rho}\frac{\partial}{\partial r}\left[\frac{\mu}{r^2}\frac{\partial (r^2 w)}{\partial r}\right], \tag{5.4}$$

$$C_p \rho \Pi \frac{D\Theta}{Dt} = \widetilde{\kappa}\left[\frac{1}{r^2}\frac{\partial (r^2 w)}{\partial r}\right]^2 + \frac{1}{r^2}\frac{\partial}{\partial r}\left(r^2 \lambda \frac{\partial T}{\partial r}\right), \tag{5.5}$$

$$\Pi^{\frac{1-\kappa}{\kappa}} = \frac{R}{p_e}\rho\Theta \tag{5.6}$$

where Ψ, also given by equation (A.26), is:

$$\Psi \equiv -\left(C_p \Theta \frac{\partial \Pi}{\partial r} + \frac{\partial \Phi}{\partial r}\right), \tag{5.7}$$

and μ is the coefficient of molecular viscosity (E.2), $\widetilde{\kappa}$ is the bulk viscosity (E.3), λ is the *coefficient of molecular thermal conductivity* (E.5). Note that there is a contribution from expansion damping as shown in appendix E.1), which is critical in 1D for damping acoustic waves as there is no shear.

5.3 Semi-implicit semi-Lagrangian discretisation

In this section, the continuous 1D governing equations including vertical molecular viscosity and diffusion are discretised. The viscous and diffusive terms are added to the momentum equation (5.4) and energy equation (5.5) fully implicitly in time. The potential improvement that vertical molecular viscosity and diffusion should have on ENDGame1D's stability and accuracy by limiting wave amplitude growth has been demonstrated in section 4.5.3, and verified with a scale analysis in section 5.1.

An explicit implementation of vertical molecular viscosity and diffusion has been tested in appendix E.2, and for very small timesteps, its damping effect in the thermosphere can be verified. It then remains to perform an implicit implementation that remains stable for larger time-steps.

The continuity, momentum and energy equations including vertical molecular viscosity and diffusion, (5.3), (5.4) and (5.5) respectively are discretised in a similar way as in appendix A.2, but this problem includes new viscous and diffusive terms which must be handled fully-implicitly-in-time in a fully coupled way in the semi-implicit semi-Lagrangian (SISL) discretisation of the dynamics.

Since vertical molecular viscosity and diffusion are fast acting processes in the thermosphere, as shown in section 5.1, the viscosity must be combined with the rest of the dynamics in a fully coupled way, rather than being solved in a separate time-step, to avoid big time-splitting errors that would otherwise occur. The viscous terms are handled fully implicitly rather than semi-implicitly because viscosity is expected to only have a damping effect on the system, so a fully implicit treatment of these terms will unconditionally damp the numerical solution without introducing any wavelike oscillations. Experiments testing the viability of solving the dynamics and viscosity in separate time-steps are performed in appendix E.4. It is found that the time-splitting errors prevent this scheme from working well with large time-steps.

The discretised governing equations including vertical molecular viscosity and diffusion are given by equations (5.8)- (5.10), where $\overline{(\ldots)}$ denotes the linear vertical interpolation of variables and δ_V is the hydrostatic switch. For brevity, continuous notation is used for the spherical spatial derivatives.

$$\left\{\rho\left[1+\frac{\alpha_\rho\Delta t}{r^2}\frac{\partial(r^2w)}{\partial r}\right]\right\}^{(n+1)} = \left\{\rho\left[1-\frac{\beta_\rho\Delta t}{r^2}\frac{\partial(r^2w)}{\partial r}\right]\right\}^{(n)}_D, \tag{5.8}$$

$$\left\{(\delta_V+\nu\Delta t)w-\alpha_w\Delta t\Psi-\frac{\Delta t}{\overline{\rho}}\frac{\partial}{\partial r}\left[\frac{\mu}{r^2}\frac{\partial(r^2w)}{\partial r}\right]\right\}^{(n+1)} = \left(\delta_V w+\beta_w\Delta t\Psi\right)^{(n)}_D, \tag{5.9}$$

$$\left\{\Theta-\frac{\Delta t}{C_p\overline{\rho\overline{\Pi}}}\left[\widetilde{\kappa}\left\{\overline{\frac{1}{r^2}\frac{\partial(r^2w)}{\partial r}}\right\}^2+\frac{1}{r^2}\frac{\partial}{\partial r}\left(r^2\lambda\frac{\partial T}{\partial r}\right)\right]\right\}^{(n+1)} = \Theta^{(n)}_D, \tag{5.10}$$

The dynamics terms of these equations are discretised in the same way as in appendix A.2, using a SISL discretisation. In a SI scheme, some terms are evaluated explicitely at the current time-step level n, and some terms are evaluated implicitly at the next time-step level $n+1$. The level of implicitness of the scheme can be varied by an off-centring parameter $\alpha \in [0.5, 1.0]$: higher values for α make the scheme more implicit, which can improve the stability of the scheme by artificially damping high frequency waves. The grid in a SL scheme is a grid of arrival points of Lagrangian parcels of air: the departure points are then calculated, as shown in appendix A.4. Then the explicit part of the scheme is evaluated at the departure point D at time-step level n while the implicit part of the scheme is evaluated at the arrival point of the Lagrangian parcel of air at time-step level $n+1$. A more thorough overview of the SISL timestepping scheme is given in appendix A.2.

These equations will require a completely new solution method from the one used for the set of discretised governing equations from the original formulation of ENDGame1D given in appendix A.2, due to the new viscous and diffusive terms that must now be accounted for.

5.4 Residual estimation

The discretised governing equations (5.8), (5.9) and (5.10) form a coupled non-linear system. The approximate Newton's method can be used to find successively better approximations for the solution to this system of equations. This system will not be completely satisfied after any number of iterations, so the equations will have some residuals R_w, R_Θ and R_ρ respectively, which should be as small as possible.

Newton's method for finding successively better roots to a function in multiple dimensions, i.e. to estimate $\boldsymbol{x}$ such that $\boldsymbol{f}(\boldsymbol{x}) = \boldsymbol{0}$, may be written:

$$\boldsymbol{0} \approx \boldsymbol{f}\left[\boldsymbol{x}^{(l+1)}\right] = \boldsymbol{f}\left[\boldsymbol{x}^{(l)}\right] + \frac{\partial \boldsymbol{f}}{\partial \boldsymbol{x}}(\boldsymbol{x}'), \tag{5.11}$$

where $\boldsymbol{x}' = \boldsymbol{x}^{(l+1)} - \boldsymbol{x}^{(l)}$ is an *increment* of $\boldsymbol{x}$, and $\partial\boldsymbol{f}/\partial\boldsymbol{x}$ is the *Jacobian matrix* of $\boldsymbol{f}$. It is possible to approximate $\partial \boldsymbol{f}/\partial \boldsymbol{x}$. In a similar way in ENDGame1D, the system to be solved is $(R_\rho, R_\Theta, R_w) = \mathbf{0}$.

The residuals are found by setting the superscript (l) to indicate the *best guess* for the $n+1$ term after l iterations, and then putting all terms in the discretised governing equations (5.8), (5.9) and (5.10) on the right hand side so that the residual is left on the left-hand side. The residuals are as follows:

$$R_\rho = \left\{\rho\left[1 - \frac{\beta_\rho \Delta t}{r^2}\frac{\partial(r^2 w)}{\partial r}\right]\right\}_D^{(n)} - \left\{\rho\left[1 + \frac{\alpha_\rho \Delta t}{r^2}\frac{\partial(r^2 w)}{\partial r}\right]\right\}^{(l)}, \tag{5.12}$$

$$R_w = \Big(\delta_V w + \beta_w \Delta t \Psi\Big)_D^{(n)} - \left\{(\delta_V + \nu\Delta t)w - \alpha_w \Delta t \Psi - \frac{\Delta t}{\overline{\rho}}\frac{\partial}{\partial r}\left[\frac{\mu}{r^2}\frac{\partial(r^2 w)}{\partial r}\right]\right\}^{(l)}, \tag{5.13}$$

$$R_\Theta = \Theta_D^{(n)} - \left\{\Theta - \frac{\Delta t}{C_p\overline{\rho\overline{\Pi}}}\left[\mu\left\{\overline{\frac{1}{r^2}\frac{\partial(r^2 w)}{\partial r}}\right\}^2 + \frac{1}{r^2}\frac{\partial}{\partial r}\left(r^2\lambda\frac{\partial T}{\partial r}\right)\right]\right\}^{(l)}. \tag{5.14}$$

The method for reducing the residuals used in this section mirrors that used in appendix A.5. The system of equations to be solved is given by (A.51), using the same equations and linearisation techniques. The same approximations are also made to calculate the right-hand side of (A.51) by differentiating the expressions for the residuals (5.12), (5.13), (5.14), along with the extra approximations:

- Perturbations to μ and λ are small and may be neglected.
- Approximate $1/\overline{\rho\Pi} \approx 1/\overline{\rho^*\Pi^*}$ in the Θ equation.

These approximations lead to the full set of viscous residuals and the equation of state: (5.15)- (5.18).

Full viscous residual and state equations

$$R_\rho \approx \rho' + \frac{\alpha\Delta t}{r^2}\frac{\partial}{\partial r}\left(r^2\overline{\rho}^* w'\right), \tag{5.15}$$

$$R_w \approx (\delta_V + \nu\Delta t)w' + \alpha_w \Delta t\, C_p\left(\Theta^*\frac{\partial \Pi'}{\partial r} + \frac{\partial \Pi^*}{\partial r}\Theta'\right) - \frac{\Delta t}{\overline{\rho}^*}\frac{\partial}{\partial r}\left[\frac{\mu}{r^2}\frac{\partial(r^2 w')}{\partial r}\right], \tag{5.16}$$

$$R_\Theta \approx \alpha_z \Delta t\overline{\frac{\partial \Theta^*}{\partial r}}w' + \Theta' - \frac{\Delta t}{C_p\overline{\rho^*\overline{\Pi^*}}}\frac{1}{r^2}\frac{\partial}{\partial r}\left[r^2\lambda\frac{\partial}{\partial r}\left(\overline{\Pi}^*\Theta' + \Theta^*\overline{\Pi}'\right)\right], \tag{5.17}$$

$$0 \approx \frac{\rho'}{\rho^*} + \overline{\frac{\Theta'}{\Theta^*}} - \frac{1-\kappa}{\kappa}\frac{\Pi'}{\Pi^*}. \tag{5.18}$$

5.5 Constructing the boundary value problems

The residual and state equations found in section 5.4: (5.15) - (5.18) form four sets of equations with four sets of unknowns ρ', Θ', w' and Π'. It would be preferable to obtain from these a single set of equations for a single set of unknowns. Trying to follow the same method as the one used in appendix A.6 does not produce a problem that can easily be solved (it becomes a high order problem with inverse differential operators), so a different approach is taken by exploiting one's physical knowledge of the problem, and considering the set of governing equations in the viscous region (at high altitudes) and the inviscid region (at low altitudes) separately.

In the viscous region, the terms containing μ and λ dominate and must be included. Other terms may be dropped as they will be relatively small, so the $\alpha_w \Delta t\, C_p(\Theta' \frac{\partial \Pi^*}{\partial r} + \Theta^* \frac{\partial \Pi'}{\partial r})$ term from the R_w equation (5.16), and the $\alpha \Delta t \frac{\partial \Theta^*}{\partial r} w'$ term from the R_Θ equation (5.17) are neglected. This leaves the set of residual and state equations in the viscous region (5.19)-(5.22). The $(\delta_V + \nu \Delta t) w'$ term in the R_w equation in the viscous region (5.20) need not be neglected as it is already an equation in terms of w' only.

Residual and state equations in the viscous region

$$R_\rho \approx \rho' + \frac{\alpha \Delta t}{r^2} \frac{\partial}{\partial r}\left(r^2 \overline{\rho}^* w'\right), \tag{5.19}$$

$$R_w \approx (\delta_V + \nu \Delta t) w' - \frac{\Delta t}{\overline{\rho}^*} \frac{\partial}{\partial r}\left[\frac{\mu}{r^2} \frac{\partial (r^2 w')}{\partial r}\right], \tag{5.20}$$

$$R_\Theta \approx \Theta' - \frac{\Delta t}{C_p \overline{\rho^* \Pi^*}} \frac{1}{r^2} \frac{\partial}{\partial r}\left[r^2 \lambda \frac{\partial}{\partial r}\left(\overline{\Pi}^* \Theta' + \Theta^* \overline{\Pi}'\right)\right], \tag{5.21}$$

$$0 \approx \frac{\rho'}{\rho^*} + \frac{\overline{\Theta'}}{\Theta^*} - \frac{1-\kappa}{\kappa} \frac{\Pi'}{\Pi^*}. \tag{5.22}$$

In the inviscid region, the set of equations is identical to that used in appendix A.5, where the viscous terms which contain μ and λ are neglected to be left with equations (5.23) - (5.26). In the viscous region, an equation for w' has been trivially obtained: the R_w equation (5.20). It therefore remains to obtain one for the inviscid region too, rather than an equation for Π' as in section A.6.

Residual and state equations in the inviscid region

$$R_\rho \approx \rho' + \frac{\alpha \Delta t}{r^2} \frac{\partial}{\partial r}\left(r^2 \overline{\rho}^* w'\right), \tag{5.23}$$

$$R_w \approx (\delta_V + \nu \Delta t) w' + \alpha_w \Delta t\, C_p \left(\Theta^* \frac{\partial \Pi'}{\partial r} + \frac{\partial \Pi^*}{\partial r} \Theta'\right), \tag{5.24}$$

$$R_\Theta \approx \alpha_z \Delta t \frac{\overline{\partial \Theta^*}}{\partial r} w' + \Theta', \tag{5.25}$$

$$0 \approx \frac{\rho'}{\rho^*} + \frac{\overline{\Theta'}}{\Theta^*} - \frac{1-\kappa}{\kappa} \frac{\Pi'}{\Pi^*}. \tag{5.26}$$

Equations for Π' and w' have been obtained from the inviscid equation set in appendix A.6, given by (A.66) and (A.70). Eliminate to get w' instead of Π' by substituting an expression for Π' from (A.70) into (A.66) to obtain

$$w' - D_1\left[\frac{\kappa\Pi^*}{1-\kappa}D_2(w')\right] \approx BR_w - D_1(\Pi^*)R_\Theta - D_1\left[\frac{\kappa\Pi^*}{1-\kappa}\left(\frac{R_\rho}{\rho^*} + \frac{\overline{R_\Theta}}{\Theta^*}\right)\right], \quad (5.27)$$

which is an equation in terms of w' only. This can be compared with the w' equation in the viscous region (5.20). By combining the terms that occur in both expressions for w' in each region, equation (5.28) can be obtained, which should work in both the viscous and inviscid regions. This is a single set of equations for a single set of unknowns w'. Equation (5.28) is a boundary value problem that can be solved to obtain w': this process is detailed in section 5.6. A scale analysis is performed in appendix E.6 to show that the method used to obtain the boundary value problem (5.28) will still give reasonably accurate solutions of an appropriate scale.

$$\boxed{\begin{aligned} & w' - D_1\left[\frac{\kappa\Pi^*}{1-\kappa}D_2(w')\right] - B\frac{\Delta t}{\overline{\rho^*}}\frac{\partial}{\partial r}\left[\frac{\mu}{r^2}\frac{\partial(r^2 w')}{\partial r}\right] \\ \approx \quad & BR_w - D_1(\Pi^*)R_\Theta - D_1\left[\frac{\kappa\Pi^*}{1-\kappa}\left(\frac{R_\rho}{\rho^*} + \frac{\overline{R_\Theta}}{\Theta^*}\right)\right]. \end{aligned}} \quad (5.28)$$

After obtaining w' by solving the above boundary value problem, the other increment terms ρ', Θ' and Π' are obtained by back-substitution. The back-substitutions must be made into the *full* equation set, rather than the viscous and inviscid equation sets. The above boundary value problem for w' only includes the viscous term μ, but does not include the diffusive term λ, so this term should be included in the back-substitution. Therefore the full equation for R_Θ (5.17) is used to obtain an equation for Θ', since this equation includes λ. The value for w' can be taken from the solution to the above boundary value problem. This will involve solving another boundary value problem for Θ'.

First, it can be noted that the diffusion of heat changes the temperature and pressure rather than moving mass around, since it does not act on the mass continuity equation. Then in the viscous region, it can be assumed that the ρ' term is small compared to the Θ' and Π' terms in the equation of state (5.18), so rearranging the remaining terms leaves

$$\Pi' = \frac{\kappa}{1-\kappa}\frac{\Pi^*}{\overline{\Theta}^*}\overline{\Theta}'. \quad (5.29)$$

This expression for Π' can be substituted into the R_Θ equation (5.17) to obtain

$$R_\Theta \approx \alpha_z \Delta t \frac{\partial \Theta^*}{\partial r} w' + \Theta' - \frac{\Delta t}{C_p \overline{\rho^* \Pi^*}} \frac{1}{r^2} \frac{\partial}{\partial r} \left[r^2 \lambda \frac{\partial}{\partial r} \left(\overline{\Pi}^* \Theta' + \Theta^* \overline{\frac{\kappa}{1-\kappa} \frac{\Pi^*}{\overline{\Theta}^*} \overline{\Theta}'} \right) \right]. \tag{5.30}$$

The double linear interpolation of Θ' here is not ideal. However, the contribution of this term is significantly smaller than the $\overline{\Pi}^* \Theta'$ term on its own, because of the $\kappa/(1-\kappa) \approx 2/5$ coefficient in the doubly averaged term. It should therefore be inconsequential to remove the double linear interpolation of Θ'/Θ^* and be left with

$$\left(1 + \frac{\kappa}{1-\kappa}\right) \overline{\Pi}^* \Theta' = \frac{1}{1-\kappa} \overline{\Pi}^* \Theta'. \tag{5.31}$$

Note that in the inviscid region, the diffusion term is small, so the approximations made here will have very little effect on the solution. Therefore, an equation for Θ' that should work in both the viscous and inviscid regions is obtained as follows:

$$\boxed{\Theta' - \frac{\Delta t}{C_p \overline{\rho^* \Pi^*}} \frac{1}{1-\kappa} \frac{1}{r^2} \frac{\partial}{\partial r} \left[r^2 \lambda \frac{\partial \left(\overline{\Pi}^* \Theta' \right)}{\partial r} \right] \approx R_\Theta - \alpha_z \Delta t \frac{\partial \Theta^*}{\partial r} w'.} \tag{5.32}$$

A single set of equations has been obtained for a single set of unknowns Θ', given w'. Equation (5.32) is a boundary value problem that can be solved to obtain Θ': this process is detailed in section 5.7.

After obtaining w' and Θ' by solving the two boundary value problems, the value for w' can be back-substituted into the R_ρ equation (5.15) to obtain ρ'.

Alternative routes for back-substitutions are possible, and provided that:

1. the boundary value problem is derived exactly from the linearised equations without further approximations, and
2. the boundary value problem is solved exactly,

then the choice of back-substitution does not matter. In ENDGame1D however, condition 1 does not hold as the equations need to be considered in the inviscid and viscous limits separately, and hence different back-substitutions may produce different errors. These effects should be minimal and have not been considered here.

5.6 Solving the boundary value problem for w'

In this section, the boundary value problem for w' (5.28) derived in section 5.5 is turned into a form suitable for programming into the ENDGame1D code. The mathematical detail of how it is set up as a tridiagonal system of equations and solved is set out in full.

5.6.1 Discretise the left-hand side of the boundary value problem for w'

The discretised form of the left-hand side of the w' boundary value problem (5.28) is derived in this section. The discretised forms of the D_1 and $\rho^* D_2$ operators and their associated coefficients $D^{(1)}_{i-1/2,j}$ and $D^{(2)}_{i,j-1/2}$ are derived in appendix A.7.1.

The discretised form of the third term of the w' boundary value problem (5.28) is as follows for $k \in [2, N]$ (the boundary conditions at $k = 1, N+1$ are found later):

$$\begin{aligned} -\left\{ \frac{\Delta t}{\rho^*} \frac{\partial}{\partial r} \left[\frac{\mu}{r^2} \frac{\partial (r^2 X)}{\partial r} \right] \right\}_{k-\frac{1}{2}} &= - \frac{\Delta t}{(\overline{\rho}^* \Delta r)_{k-\frac{1}{2}}} \left[\mu_k \frac{(AX)_{k+\frac{1}{2}} - (AX)_{k-\frac{1}{2}}}{V_k} \right. \\ &\quad \left. - \mu_{k-1} \frac{(AX)_{k-\frac{1}{2}} - (AX)_{k-\frac{3}{2}}}{V_{k-1}} \right]. \end{aligned} \tag{5.33}$$

where V_k denotes the volume of the current grid cell, $A_{k-1/2}$ denotes the area of the bottom cell face of grid cell k, and $A_{k+1/2}$ denotes the area of the top cell face, as in Figure A.4. In order to abbreviate this, define the following functions to obtain expressions for the coefficients of $X_{k-3/2}$, $X_{k-1/2}$ and $X_{k+1/2}$:

$$F^{\rho}_{k-\frac{1}{2}} = - \frac{\Delta t}{(\overline{\rho}^* \Delta r)_{k-\frac{1}{2}}}, \quad F^{\mu}_{k} = \left. \frac{\mu}{V} \right|_{k}, \tag{5.34}$$

so that (5.33) may be written as follows for $k \in [2, N]$:

$$- \frac{\Delta t}{\rho^*} \frac{\partial}{\partial r} \left[\frac{\mu}{r^2} \frac{\partial (r^2 X)}{\partial r} \right]_{k-\frac{1}{2}} = D^{\mu}_{k-\frac{1}{2},k-\frac{3}{2}} X_{k-\frac{3}{2}} + D^{\mu}_{k-\frac{1}{2},k-\frac{1}{2}} X_{k-\frac{1}{2}} + D^{\mu}_{k-\frac{1}{2},k+\frac{1}{2}} X_{k+\frac{1}{2}}, \tag{5.35}$$

where:

$$D^{\mu}_{k-\frac{1}{2},k-\frac{3}{2}} = F^{\rho}_{k-\frac{1}{2}} F^{\mu}_{k-1} A_{k-\frac{3}{2}}, \tag{5.36}$$

$$D^{\mu}_{k-\frac{1}{2},k-\frac{1}{2}} = - F^{\rho}_{k-\frac{1}{2}} \left[F^{\mu}_{k-1} + F^{\mu}_{k} \right] A_{k-\frac{1}{2}}, \tag{5.37}$$

$$D^{\mu}_{k-\frac{1}{2},k+\frac{1}{2}} = F^{\rho}_{k-\frac{1}{2}} F^{\mu}_{k} A_{k+\frac{1}{2}}. \tag{5.38}$$

Using these coefficients, the discretised form of the left-hand side of the w' boundary value problem (5.28) is as follows for $k \in [2, N]$ (the boundary conditions at $k = 1, N$ are found later):

$$\begin{aligned} &(B^{-1} w')_{k-\frac{1}{2}} - \left\{ B^{-1} D_1 \left[\frac{\kappa \Pi^*}{1-\kappa} D_2(w') \right] \right\}_{k-\frac{1}{2}} - \left\{ \frac{\Delta t}{\overline{\rho^*}} \frac{\partial}{\partial r} \left[\frac{\mu}{r^2} \frac{\partial (r^2 w')}{\partial r} \right] \right\}_{k-\frac{1}{2}} \\ &= B^{-1}_{k-\frac{1}{2}} w'_{k-\frac{1}{2}} - B^{-1}_{k-\frac{1}{2}} \left\{ D^{(1)}_{k-\frac{1}{2},k-1} \left. \frac{\kappa}{1-\kappa} \frac{\Pi^*}{\rho^*} \right|_{k-1} \left[D^{(2)}_{k-1,k-\frac{3}{2}} w'_{k-\frac{3}{2}} + D^{(2)}_{k-1,k-\frac{1}{2}} w'_{k-\frac{1}{2}} \right] \right. \end{aligned}$$

$$+ D^{(1)}_{k-\frac{1}{2},k}\frac{\kappa}{1-\kappa}\frac{\Pi^*}{\rho^*}\bigg|_{k}\left[D^{(2)}_{k,k-\frac{1}{2}}w'_{k-\frac{3}{2}} + D^{(2)}_{k,k+\frac{1}{2}}w'_{k+\frac{1}{2}}\right]\Bigg\}$$

$$+ D^{\mu}_{k-\frac{1}{2},k-\frac{3}{2}}w'_{k-\frac{3}{2}} + D^{\mu}_{k-\frac{1}{2},k-\frac{1}{2}}w'_{k-\frac{1}{2}} + D^{\mu}_{k-\frac{1}{2},k+\frac{1}{2}}w'_{k+\frac{1}{2}} \tag{5.39}$$

Define the operators $D^w_{i-1/2,j-1/2}$ to be the coefficients of $w'_{j-1/2}$ for the left-hand side of (5.28) evaluated at level $i-1/2$, in order to abbreviate this so that it becomes:

$$(B^{-1}w')_{k-\frac{1}{2}} - \left\{B^{-1}D_1\left[\frac{\kappa\Pi^*}{1-\kappa}D_2(w')\right]\right\}_{k-\frac{1}{2}} - \left\{\frac{\Delta t}{\overline{\overline{\rho^*}}}\frac{\partial}{\partial r}\left[\frac{\mu}{r^2}\frac{\partial(r^2w')}{\partial r}\right]\right\}_{k-\frac{1}{2}}$$

$$= D^w_{k-\frac{1}{2},k-\frac{3}{2}}w'_{k-\frac{3}{2}} + D^w_{k-\frac{1}{2},k-\frac{1}{2}}w'_{k-\frac{1}{2}} + D^w_{k-\frac{1}{2},k+\frac{1}{2}}w'_{k+\frac{1}{2}}, \tag{5.40}$$

where the $D^w_{i-1/2,j-1/2}$ operators are defined as follows:

$$D^w_{k-\frac{1}{2},k-\frac{3}{2}} = -B^{-1}_{k-\frac{1}{2}}D^{(1)}_{k-\frac{1}{2},k-1}\frac{\kappa}{1-\kappa}\frac{\Pi^*}{\rho^*}\bigg|_{k-1}D^{(2)}_{k-1,k-\frac{3}{2}} + D^{\mu}_{k-\frac{1}{2},k-\frac{3}{2}}, \tag{5.41}$$

$$\begin{aligned} D^w_{k-\frac{1}{2},k-\frac{1}{2}} &= B^{-1}_{k-\frac{1}{2}}\left[1 - D^{(1)}_{k-\frac{1}{2},k-1}\frac{\kappa}{1-\kappa}\frac{\Pi^*}{\rho^*}\bigg|_{k-1}D^{(2)}_{k-1,k-\frac{1}{2}} - D^{(1)}_{k-\frac{1}{2},k}\frac{\kappa}{1-\kappa}\frac{\Pi^*}{\rho^*}\bigg|_{k}D^{(2)}_{k,k-\frac{1}{2}}\right] \\ &\quad + D^w_{k-\frac{1}{2},k-\frac{1}{2}} \end{aligned} \tag{5.42}$$

$$D^w_{k-\frac{1}{2},k+\frac{1}{2}} = -B^{-1}_{k-\frac{1}{2}}D^{(1)}_{k-\frac{1}{2},k}\frac{\kappa}{1-\kappa}\frac{\Pi^*}{\rho^*}\bigg|_{k}D^{(2)}_{k,k+\frac{1}{2}} + D^{\mu}_{k-\frac{1}{2},k+\frac{1}{2}}. \tag{5.43}$$

5.6.2 Construct a matrix to solve

By adding together all of the discretised terms of the left-hand side of the boundary value problem for w' (5.28) and using the above abbreviations, a tridiagonal system of equations for w' is obtained for $k \in [2, N]$:

$$D^w_{k-\frac{1}{2},k-\frac{3}{2}}w'_{k-\frac{1}{2}} + D^w_{k-\frac{1}{2},k-\frac{1}{2}}w'_{k-\frac{1}{2}} + D^w_{k-\frac{1}{2},k+\frac{1}{2}}w'_{k+\frac{1}{2}} = R^w_{k-\frac{1}{2}}, \tag{5.44}$$

where $R^w_{k-1/2}$ is the right-hand side of (5.28) at level $k-1/2$.

5.6.3 Boundary conditions

The boundary conditions on w' (A.41) are enforced so that there are no vertical velocities at the surface or the top of the atmosphere, and so $w_{1/2} = w_{N+1/2} = 0$ and $w'_{1/2} = w'_{N+1/2} = 0$.

5.6.4 Tridiagonal system

With these boundary conditions, the matrix definitions given by (5.46) and (5.47) can be made, where $\boldsymbol{R}_w$ denotes the vector of values of the right-hand side of the w' boundary value problem (5.28) at each w-level, and is set to 0 at the top and bottom boundaries. Now equation (5.28) can be written as a tridiagonal system of equations

$$\boldsymbol{D}_w = \begin{bmatrix} 1 & 0 & 0 & \cdots & 0 \\ D^w_{\frac{3}{2},\frac{1}{2}} & D^w_{\frac{3}{2},\frac{3}{2}} & D^w_{\frac{3}{2},\frac{5}{2}} & & \vdots \\ \ddots & \ddots & \ddots & & \\ D^w_{k-\frac{1}{2},k-\frac{3}{2}} & D^w_{k-\frac{1}{2},k-\frac{1}{2}} & D^w_{k-\frac{1}{2},k+\frac{1}{2}} & & \\ & \ddots & \ddots & \ddots & \\ \vdots & D^w_{N-\frac{1}{2},N-\frac{3}{2}} & D^w_{N-\frac{1}{2},N-\frac{1}{2}} & D^w_{N-\frac{1}{2},N+\frac{1}{2}} & \\ 0 & \cdots & 0 & 0 & 1 \end{bmatrix} \tag{5.46}$$

$$\boldsymbol{w} \equiv \begin{bmatrix} w'_{1/2} \\ w'_{3/2} \\ \vdots \\ w'_{k-1/2} \\ \vdots \\ w'_{N-1/2} \\ w'_{N+1/2} \end{bmatrix} \qquad \boldsymbol{R}_w \equiv \begin{bmatrix} 0 \\ R^w_{\frac{3}{2}} \\ \vdots \\ R^w_{k-\frac{1}{2}} \\ \vdots \\ R^w_{N-\frac{1}{2}} \\ 0 \end{bmatrix} \tag{5.47}$$

---

for $w'_{k+1/2}$ as follows:

$$\boxed{\boldsymbol{D}_w \boldsymbol{w} = \boldsymbol{R}_w.} \tag{5.45}$$

This can be solved using a standard tridiagonal system solver [Press *et al.* , 1993].

5.7 Solving the boundary value problem for Θ'

In this section, the Θ' boundary value problem (5.32) derived in section 5.5 is set up as a tridiagonal system of equations to be solved. This section sets out the mathematical detail of this derivation in full.

5.7.1 Discretise the left-hand side of the boundary value problem for Θ'

The discretised form of the left-hand side of the Θ' boundary value problem (5.32) is as follows for $k \in [2, N]$ (the boundary conditions at $k = 1, N$ are found later):

$$\Theta'_{k-\frac{1}{2}} - \left\{ \frac{\Delta t}{C_p(\overline{\rho^* \Pi^*})} \frac{1}{1-\kappa} \frac{1}{r^2} \frac{\partial}{\partial r}\left[r^2 \lambda \frac{\partial \left(\overline{\Pi}^* \Theta'\right)}{\partial r} \right] \right\}_{k-\frac{1}{2}} \tag{5.48}$$

$$= \Theta'_{k-\frac{1}{2}} - \frac{\Delta t}{C_p(1-\kappa)(\overline{\rho^* \Pi^* r^2})_{k-\frac{1}{2}}} \left\{ \left.\frac{r^2\lambda}{\Delta r}\right|_k \left[\left(\overline{\Pi}^* \Theta'\right)_{k+\frac{1}{2}} - \left(\overline{\Pi}^* \Theta'\right)_{k-\frac{1}{2}} \right] \right.$$

$$\left. - \left.\frac{r^2\lambda}{\Delta r}\right|_{k-1} \left[\left(\overline{\Pi}^* \Theta'\right)_{k-\frac{1}{2}} - \left(\overline{\Pi}^* \Theta'\right)_{k-\frac{3}{2}} \right] \right\}, \tag{5.49}$$

Next, define the following function in order to abbreviate this:

$$F^C_{k-1/2} = - \frac{\Delta t}{C_p(1-\kappa)} \left. \frac{1}{\overline{\rho^* \Pi^* r^2}} \right|_{k-1/2}, \quad F^\lambda_k = \left. \frac{r^2 \lambda}{\Delta r} \right|_k \tag{5.50}$$

Define the operators $D^{\Theta}_{i-1/2,j-1/2}$ to be the coefficients of $\Theta'_{j-1/2}$ for the left-hand side of (5.32) evaluated at level $i-1/2$, in order to abbreviate this so that it becomes:

$$\begin{aligned}\Theta'_{k-\frac{1}{2}} - \left\{ \frac{\Delta t}{C_p(\overline{\rho^* \Pi^*})} \frac{1}{1-\kappa} \frac{1}{r^2} \frac{\partial}{\partial r}\left[r^2 \lambda \frac{\partial\left(\overline{\Pi}^* \Theta'\right)}{\partial r} \right] \right\}_{k-\frac{1}{2}} \\ = D^{\Theta}_{k-\frac{1}{2},k-\frac{3}{2}} \Theta'_{k-\frac{3}{2}} + D^{\Theta}_{k-\frac{1}{2},k-\frac{1}{2}} \Theta'_{k-\frac{1}{2}} + D^{\Theta}_{k-\frac{1}{2},k+\frac{1}{2}} \Theta'_{k+\frac{1}{2}},\end{aligned} \tag{5.51}$$

where the $D^{(\Theta)}_{i-1/2,j-1/2}$ operators are defined as follows:

$$D^{\Theta}_{k-\frac{1}{2},k-\frac{3}{2}} = F^{C}_{k-\frac{1}{2}} F^{\lambda}_{k-1} \overline{\Pi}^*_{k-\frac{3}{2}}, \tag{5.52}$$

$$D^{\Theta}_{k-\frac{1}{2},k-\frac{1}{2}} = 1 - F^{C}_{k-\frac{1}{2}} \left[F^{\lambda}_{k-1} + F^{\lambda}_{k} \right] \overline{\Pi}^*_{k-\frac{1}{2}}, \tag{5.53}$$

$$D^{\Theta}_{k-\frac{1}{2},k+\frac{1}{2}} = F^{C}_{k-\frac{1}{2}} F^{\lambda}_{k} \overline{\Pi}^*_{k+\frac{1}{2}}. \tag{5.54}$$

5.7.2 Construct a matrix to solve

By adding together all the discretised terms of the left hand side of the Θ boundary value problem (5.32) and using the above abbreviations, a tridiagonal system of equations is obtained for $k \in [2, N]$:

$$D^{\Theta}_{k-\frac{1}{2},k-\frac{3}{2}} \Theta'_{k-\frac{3}{2}} + D^{\Theta}_{k-\frac{1}{2},k-\frac{1}{2}} \Theta'_{k-1/2} + D^{\Theta}_{k-\frac{1}{2},k+\frac{1}{2}} \Theta'_{k+\frac{1}{2}} = R^{\Theta}_{k+\frac{1}{2}}, \tag{5.55}$$

where $R^{\Theta}_{k-1/2}$ is the right-hand side of equation (5.32) at level $k-1/2$.

5.7.3 Boundary conditions

At the surface, level 1/2, the boundary condition on w (A.41) is enforced so that there are no vertical velocities at the surface. Neglecting the viscous and diffusive terms in the energy equation (5.5), as these are insignificant at the surface, leaves

$$\left.\frac{D\Theta}{Dt}\right|_{1/2} = 0. \tag{5.56}$$

Expanding this using the definition for the material derivative (A.2) gives

$$0 = \left.\frac{\partial \Theta}{\partial t}\right|_{1/2} + w_{1/2} \left.\frac{\overline{\partial \Theta}}{\partial r}\right|_{1/2} = \left.\frac{\partial \Theta}{\partial t}\right|_{1/2}. \tag{5.57}$$

This implies that at the surface, $\Theta_{1/2}$ is fixed, and so $\Theta'_{1/2} = 0$.

At the top model boundary, level $N + 1/2$, it is assumed that the temperature is close to being isothermal (this should hold very well when the top boundary is set to be above 200 km in the US Standard Atmosphere). From this, the following

$$\boldsymbol{D}_\Theta = \begin{bmatrix} 1 & 0 & 0 & \cdots & & 0 \\ D^{(\Theta)}_{\frac{3}{2},\frac{1}{2}} & D^{(\Theta)}_{\frac{3}{2},\frac{3}{2}} & D^{(\Theta)}_{\frac{3}{2},\frac{5}{2}} & & & \vdots \\ & \ddots & \ddots & \ddots & & \\ & D^{(\Theta)}_{k-\frac{1}{2},k-\frac{3}{2}} & D^{(\Theta)}_{k-\frac{1}{2},k-\frac{1}{2}} & D^{(\Theta)}_{k-\frac{1}{2},k+\frac{1}{2}} & & \\ & & \ddots & \ddots & \ddots & \\ \vdots & & & D^{(\Theta)}_{N-\frac{1}{2},N-\frac{3}{2}} & D^{(\Theta)}_{N-\frac{1}{2},N-\frac{1}{2}} & D^{(\Theta)}_{N-\frac{1}{2},N+\frac{1}{2}} \\ 0 & \cdots & & 0 & -\frac{\overline{\Pi}^*_{N-1/2}}{\Delta r_N} & \frac{\overline{\Pi}^*_{N+1/2}}{\Delta r_N} \end{bmatrix} \tag{5.60}$$

$$\boldsymbol{\Theta} \equiv \begin{bmatrix} \Theta'_{1/2} \\ \Theta'_{3/2} \\ \vdots \\ \Theta'_{k-1/2} \\ \vdots \\ \Theta'_{N-1/2} \\ \Theta'_{N+1/2} \end{bmatrix} \qquad \boldsymbol{R}_\Theta \equiv \begin{bmatrix} R_\Theta \\ R^\Theta_{\frac{3}{2}} \\ \vdots \\ R^\Theta_{k-\frac{1}{2}} \\ \vdots \\ R^\Theta_{N-\frac{1}{2}} \\ -\frac{\partial T}{\partial r}\Big|_N \end{bmatrix} \tag{5.61}$$

---

is obtained (for some number of iterations l):

$$\begin{aligned} 0 &= \frac{\partial T}{\partial r}\bigg|_N^{(l+1)} \\ &= \frac{\partial(\overline{\Pi}^*\Theta)}{\partial r}\bigg|_N^{(l)} + \frac{\partial(\overline{\Pi}^*\Theta')}{\partial r}\bigg|_N \\ &= \frac{\partial T}{\partial r}\bigg|_N^{(l)} + \frac{\overline{\Pi}^*_{N+1/2}\Theta'_{N+1/2} - \overline{\Pi}^*_{N-1/2}\Theta'_{N-1/2}}{\Delta r_N} \end{aligned} \tag{5.58}$$

5.7.4 Tridiagonal system

With these boundary conditions, the matrix definitions given by (5.60) and (5.61) can be made, where $\boldsymbol{R}_\Theta$ denotes the vector of values of the right-hand side of the Θ' boundary value problem (5.32) at each w-level. Now equation (5.32) can be written as a tridiagonal system of equations for $\Theta'_{k-1/2}$ as follows:

$$\boxed{\boldsymbol{D}_\Theta \boldsymbol{\Theta} = \boldsymbol{R}_\Theta.} \tag{5.59}$$

This can be solved using a standard tridiagonal system solver [Press *et al.* , 1993].

5.8 Comparison to the non-viscous formulation

In this section, stability tests are performed (as in section 3.4) using the original inviscid formulation from appendix A and the formulation with vertical molecular

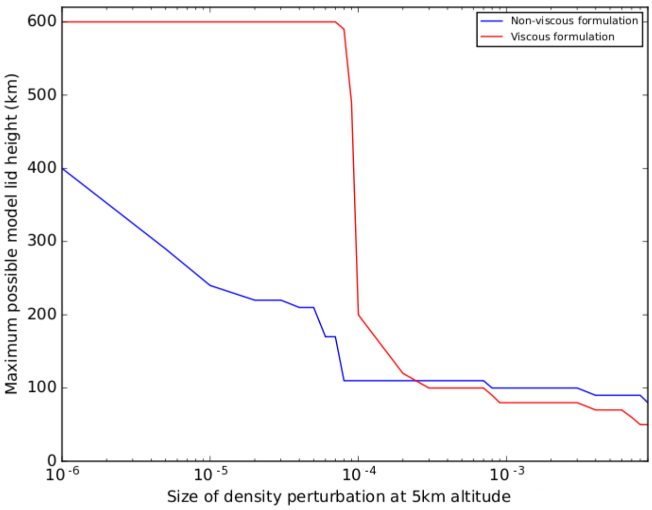

Figure 5.1: Stability tests of ENDGame1D comparing the viscous and non-viscous formulations. The lines on this stability test plot represent the maximum possible top boundary height for which a simulation with 5 minute time-steps remains stable for 4 weeks for different sized density perturbations.

viscosity and diffusion derived in this chapter. The results of the stability tests for the viscous and non-viscous formulations are shown in Figure 5.1.

Figure 5.2 shows the maximum velocities observed at each height throughout the whole simulation of the vertical propagation of an acoustic wave to the top boundary, which is a measure of the wave's amplitude as it propagates upwards. The relative density perturbation of 10^{-4} and model lid height of 300 km are chosen to illustrate the damping effect of vertical molecular viscosity and diffusion in the thermosphere for a case where the inviscid run remains stable. Vertical molecular viscosity and diffusion are seen to be damping the waves above ~130 km. This is as expected from the comparison of the acoustic wave growth rate time-scale and the diffusion time-scale performed in section 5.1. This damping of acoustic waves by molecular velocity and diffusion corresponds to a significant improvement in stability compared with the inviscid formulation for density perturbations less than 10^{-4}, shown in Figure 5.1.

The baroclinic wave tests mentioned in section 3.4 show that ENDGame simulations will typically generate relative density perturbations of orders 10^{-4} to 10^{-3}. However, the very sudden drop in maximum top boundary heights in Figure 5.1 occurs for relative density perturbations greater than 10^{-4}. This drop in stability occurs at the same point where the maximum top boundary for the non-viscous formulation goes below the molecularly diffusive region at 135 km. The key to im-

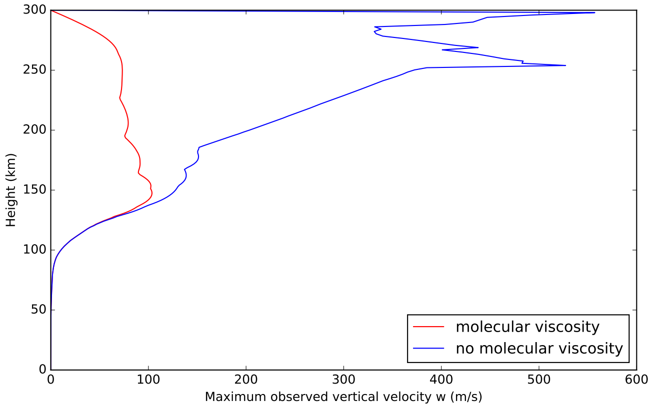

Figure 5.2: The maximum observed velocity at each height throughout the whole simulation of an acoustic wave propagating to the top model boundary at 300 km, with and without the implicit implementation of vertical molecular viscosity and diffusion. The acoustic wave was triggered with a relative density perturbation of 10^{-4} at 5 km altitude. This simulation used a 1 second time-step, the USSA temperature profile and a quadratically stretched grid.

proving stability for larger density perturbations therefore seems to be to get the top boundary to the molecularly diffused region so that vertical molecular viscosity and diffusion can then act to keep ENDGame stable up to an altitude of 600 km.

It may later be prudent to look into including other physical processes that may be significant at slightly lower levels such as ion drag [Medvedev *et al.* , 2017] in order to address the problem of stability for larger density perturbations. However, the most straightforward way of dealing with this is to add in a small amount of off-centring, as in section 3.4.3. Figure 5.3 shows the results of stability tests of the viscous formulation with different implicitness parameters α.

With vertical molecular viscosity and diffusion included, a smaller α may be used to obtain greater stability with higher top boundaries and larger density perturbations than without vertical molecular viscosity and diffusion (as in section 3.4.3). As small an α as possible should be chosen to reduce the artificial damping of high frequency waves. It should be noted that the results of similar stability tests may differ in ENDGame3D because of the introduction of horizontal effects like shear.

Table 5.2 shows the results of some convergence tests to compare the rate of convergence (i.e. the rate at which the residuals get smaller) between the viscous and non-viscous formulations. The R_ρ residual seems to converge faster in the viscous scheme than in the non-viscous scheme. The R_Θ residual initially gets larger, but after more iterations, it also seems to converge faster in the viscous scheme than in the non-viscous scheme. The convergence of R_w however seems to stall at some point. This is likely to be a result of the extra approximations that are made to

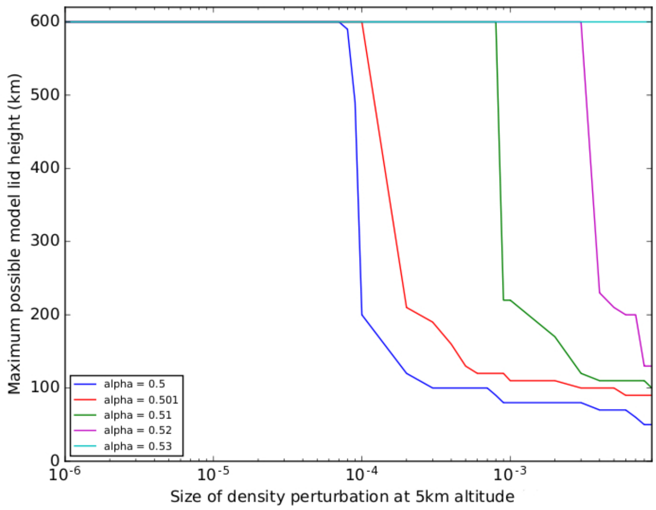

Figure 5.3: Stability tests of ENDGame1D comparing the use of different implicitness parameters with the viscous formulation. The lines on this stability test plot represent the maximum possible top boundary height for which a simulation with 5 minute time-steps remains stable for 4 weeks for different sized density perturbations.

Iter.	Inv. R_ρ	Vis. R_ρ	Inv. R_Θ	Vis. R_Θ	Inv. R_w	Vis. R_w
1	2.96E-004	2.96E-004	22750	2653	184.8	26.22
2	2.54E-007	7.11E-007	8250	8384	104.9	4.147
3	1.55E-008	1.54E-008	5477	8989	33.12	4.921
4	4.34E-011	5.83E-011	1050	2010	17.68	3.656
5	8.27E-012	3.17E-012	353.6	56.56	4.282	3.645
6	2.35E-012	2.69E-014	110.0	27.22	8.26E-001	3.676
7	4.75E-013	3.89E-015	47.20	2.226	2.26E-001	3.667
8	2.39E-013	6.83E-017	8.13	1.66E-001	7.99E-002	3.667
9	9.62E-014	4.19E-017	3.280	6.08E-002	1.83E-002	3.667
10	1.40E-014	3.15E-017	6.66E-001	1.06E-002	7.84E-003	3.667
11	5.58E-015	2.34E-017	1.31E-001	8.18E-004	2.29E-003	3.667
12	1.90E-015	2.41E-017	5.04E-002	2.71E-004	8.11E-004	3.667

Table 5.2: Convergence tests for ENDGame1D with and without vertical molecular viscosity and diffusion. A simulation is performed for 1 day with 12 iterations for each 5 minute time-step. The top boundary is set at 200 km, and $\alpha = 0.5$. The residuals are output at each iteration, and their rate of decrease illustrates the rate of convergence of the solver.

include vertical molecular viscosity and diffusion in the governing equations.

Figure 5.4 shows the results of some stability tests for a range of time-steps Δt, with the same off-centring parameter $\alpha = 0.51$ and density perturbation of 10^{-4}. The decaying effect of the off-centring parameter α is greater for larger Δt, as shown by the time-scale for the off-centring parameter (4.56). This is why the stability of the inviscid scheme increases as larger Δt are used. The stability of the viscous scheme seems to drop off for larger time-steps. This is also likely to be a result of the extra approximations that are made to include vertical molecular viscosity and diffusion in the governing equations.

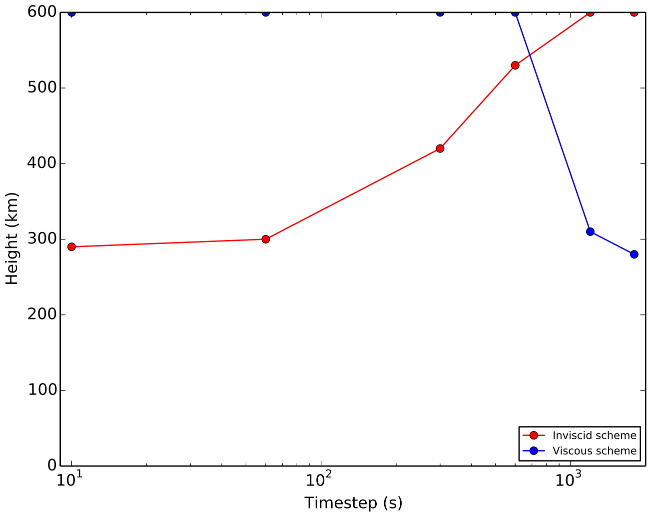

Figure 5.4: Stability tests of ENDGame1D comparing the use of different time-steps with the viscous and inviscid formulations. The lines on this stability plot represent the maximum possible top boundary height for which a simulation with a density perturbation of 10^{-4} and an off-centring parameter of $\alpha = 0.51$ remains stable for 4 weeks for different time-steps. The time-steps considered are $\Delta t \in [10\,\mathrm{s}, 1\,\mathrm{min}, 5\,\mathrm{min}, 10\,\mathrm{min}, 20\,\mathrm{min}, 30\,\mathrm{min}]$.

5.9 Summary

In this chapter, vertical molecular viscosity and diffusion is included in ENDGame1D in a fully coupled way to the dynamics in order to avoid time-splitting errors. It is handled fully-implicitly in time as it is expected to only have a damping effect in the upper atmosphere. The new equation set including vertical molecular viscosity and diffusion requires a completely new solution method compared to the original formulation. This involves considering the residual and state equation set in the viscous and and inviscid regions separately in order to derive a problem for w' that can be solved using a tridiagonal matrix algorithm. When back-substituting to obtain the other variable increments, another tridiagonal problem must be solved to obtain Θ', but the back-substitution to obtain the other variables is trivial.

The scheme performs remarkably well compared to the original formulation. If ENDGame1D can remain stable up to the molecularly diffused region at about 130 km, then molecular viscosity and diffusion act to prevent further acoustic wave growth above this altitude, keeping the dynamical core stable with a top boundary up to 600 km. Combined with a small amount of off-centring, ENDGame1D with vertical molecular viscosity and diffusion remains stable with a top boundary at 600 km for all of the kinds of waves that ENDGame1D is expected to be able to deal with.

Chapter 6

Vertical Molecular Viscosity and Diffusion in 3D

In chapter 5, it was found that the fully coupled implicit-in-time implementation of vertical molecular viscosity and diffusion together with a small amount of off-centring act to prevent wave amplitudes in ENDGame from growing excessively. The stability of ENDGame1D is greatly improved: it can be made stable with off-centring up to the molecularly diffused region, then vertical molecular viscosity and diffusion make it stable for top model boundaries up to 600 km.

In this chapter, the discretisation of the full 3D governing equations including vertical molecular viscosity and diffusion and their implementation into the ENDGame code is discussed. New solver technology must be developed to cope with the strong vertical molecular viscosity and diffusion in the thermosphere. The key novelty of this work is the fully-implicit treatment of vertical molecular viscosity and diffusion fully coupled to the semi-implicit (SI) treatment of the dynamics. In 3D, it is found that a small amount of off-centring of the SI scheme allows the dynamical core to remain stable with a top boundary up to 270 km under the baroclinic wave test.

6.1 Motivation

In this chapter, only the vertical contribution of molecular viscosity and diffusion is to be included. In this section, an expression for the decaying time-scale of horizontal diffusion is found and used to determine at what altitude it will have a significant effect on acoustic wave growth, and when it will be necessary for these terms to be included implicitly in time.

$r - r_{\text{Earth}}$ (km)	ρ ($\text{kg}\,\text{m}^{-3}$)	T (K)	g ($\text{m}\,\text{s}^{-2}$)	τ_{diff_H} (s)		τ_{growth} (s)
0	1.2×10^{0}	285	9.80	1×10^{16}	$>$	49
100	3×10^{-7}	196	9.50	4×10^{9}	$>$	42
200	7×10^{-11}	856	9.21	3×10^{5}	$>$	92
300	2×10^{-12}	976	8.94	8340	$>$	103
400	8×10^{-14}	996	8.68	327	$>$	108
420	4×10^{-14}	997	8.62	175	$>$	109
430	3×10^{-14}	998	8.60	128	$>$	110
440	2×10^{-14}	998	8.57	94	$<$	110
500	3×10^{-15}	999	8.43	15	$<$	113
600	2×10^{-16}	1000	8.19	0.78	$<$	117

Table 6.1: Comparison of the horizontal diffusion and acoustic wave growth time-scales at various altitudes with the USSA temperature profile and a uniform grid with a vertical length scale of $L_r = 1\,\text{km}$ and a horizontal length scale of $2\pi r_{\text{E}}/64 \approx 626\,\text{km}$.

The 3D linear diffusion equation (4.57) is:

$$\rho\, C_p \frac{\partial T}{\partial t} = \boldsymbol{\nabla} \cdot (\lambda \boldsymbol{\nabla} T), \tag{6.1}$$

where λ is the thermal conductivity (E.5) and μ is the coefficient of molecular viscosity (4.58). Let τ_{diff_H} be the horizontal diffusion time-scale. Considering the approximate magnitude of the individual horizontal terms in the linear diffusion equation (6.1) gives:

$$\frac{dT}{\tau_{\text{diff}_H}} \sim \frac{\mu}{\rho} \frac{dT}{L^2}, \tag{6.2}$$

where L is the horizontal length scale and it is assumed that $P_r \sim 1$. Rearranging this gives the following diffusion time-scale:

$$\frac{1}{\tau_{\text{diff}_H}} \sim \frac{\mu}{\rho L^2}. \tag{6.3}$$

Approximations for the horizontal diffusion time-scale τ_{diff_H} and the acoustic wave growth rate time-scale τ_{growth} at different levels of the atmosphere are shown in Table 6.1. For 430 km and below, it can be seen that the τ_{diff_H} is much larger than τ_{growth}, which means that the horizontal diffusion acts too slowly to have a significant damping effect on acoustic waves. However, by 440 km, τ_{diff_H} becomes smaller than τ_{growth}, getting smaller at higher latitudes, meaning that horizontal diffusion acts quickly enough to have a significant damping effect on acoustic waves. It should be noted that the precise values in Table 6.1 depend on the horizontal length scale considered.

If the horizontal diffusion time-scale τ_{diff_H} is less than the time-step Δt of the SI timestepping scheme, then the horizontal diffusion terms will need to be included implicitly in time rather than explicitly on the right-hand side (as shown in appendix E.5). This is indeed the case: from Table 6.1, if timesteps larger than 5 min are to be used above 400 km, then the horizontal diffusion will need to be included implicitly in time. The time-step typically used is 30 mins, but may be varied depending on the horizontal length scale L.

By comparing the horizontal diffusion time-scale τ_{diff_H} with the acoustic wave growth time-scale τ_{growth} in Table 6.1, it can be seen that horizontal diffusion begins to have a tangible effect on acoustic wave growth above 440 km. At this point, horizontal diffusion will need to be included fully implicitly. Therefore, including vertical diffusion only is a reasonable approximation up to about 440 km.

6.2 Continuous equations

The continuous equations in 3D with source terms, introduced fully in appendix A.1 and given by (A.1), (A.16), (A.18), (A.20) and (A.11) are as follows:

$$\begin{aligned}
\frac{D\boldsymbol{u}}{Dt} + 2\boldsymbol{\Omega}\times\boldsymbol{u} &= -\frac{1}{\rho}\boldsymbol{\nabla}p - \boldsymbol{\nabla}\boldsymbol{\phi} + \boldsymbol{S}^{\boldsymbol{u}}, && (6.4)\\
\frac{D\Theta}{Dt} &= S^{\Theta}, && (6.5)\\
\frac{D\rho}{Dt} + \rho\boldsymbol{\nabla}\cdot\boldsymbol{u} &= 0, && (6.6)\\
\frac{D\boldsymbol{r}}{Dt} &= \boldsymbol{u}, && (6.7)\\
\Pi^{\frac{1-\kappa}{\kappa}} &= \frac{R}{p_e}\rho\Theta, && (6.8)
\end{aligned}$$

The pressure gradient term in the momentum equation (6.4) may be replaced using the difference between the pressure p and the *equilibrium pressure* p_e (E.1):

$$p - p_e = -\widetilde{\kappa}\boldsymbol{\nabla}\cdot\boldsymbol{u}, \tag{6.9}$$

where $\widetilde{\kappa}$ is the bulk viscosity. In this chapter, it is useful to set $p_e = p$ and $p = p_{\mathrm{tot}}$ for simplicity of notation. The pressure gradient term (A.12) is then:

$$-\frac{1}{\rho}\boldsymbol{\nabla}p = -C_p\Theta\boldsymbol{\nabla}\Pi. \tag{6.10}$$

Together, these give:

$$\frac{1}{\rho}\boldsymbol{\nabla}p_{\mathrm{tot}} = \frac{1}{\rho}\boldsymbol{\nabla}p - \frac{1}{\rho}\boldsymbol{\nabla}(\widetilde{\kappa}\boldsymbol{\nabla}\cdot\boldsymbol{u}) \tag{6.11}$$

Define the variable $\boldsymbol{\Psi}$ as follows:

$$\boldsymbol{\Psi} = -\big(C_p\Theta\boldsymbol{\nabla}\Pi + \boldsymbol{\nabla}\phi + 2\boldsymbol{\Omega}\times\boldsymbol{u}\big). \tag{6.12}$$

There are two types of stress tensor to consider in this section:

1. The *deviatoric stress tensor* which has no trace, so the pressure is not included:

$$\boldsymbol{\tau} = \mu\left[\boldsymbol{\nabla u} + (\boldsymbol{\nabla u})^T - \frac{2}{3}(\boldsymbol{\nabla}\cdot\boldsymbol{u})\boldsymbol{I}\right], \tag{6.13}$$

   where $\boldsymbol{I}$ is the identity matrix and $\cdot^T$ denotes a transpose matrix.

2. The *full/ total stress tensor*, defined to be:

$$\begin{aligned}\boldsymbol{\sigma} &= \boldsymbol{\tau} - p_{\text{tot}}\boldsymbol{I}\\ &= \boldsymbol{\tau} - p\boldsymbol{I} + (\widetilde{\kappa}\boldsymbol{\nabla}\cdot\boldsymbol{u})\boldsymbol{I}\end{aligned} \tag{6.14}$$

[Batchelor, 2000; Chapman & Cowling, 1970]. The components of the stress tensors $\boldsymbol{\tau}$ and $\boldsymbol{\sigma}$ are expressed fully in appendix F.2.

Batchelor [2000] shows the 3D momentum equation with the *full* stress tensor: first use (6.12) to consolidate a number of terms of (6.4) into $\boldsymbol{\Psi}$, and use (6.11) to express the pressure gradient fully:

$$\frac{D\boldsymbol{u}}{Dt} - \boldsymbol{\Psi} - \frac{1}{\rho}\boldsymbol{\nabla}(\widetilde{\kappa}\boldsymbol{\nabla}\cdot\boldsymbol{u}) = \boldsymbol{S}^{\boldsymbol{u}}. \tag{6.15}$$

Now the source term should be replaced with the full stress tensor (6.14), but:

1. The $\frac{1}{\rho}\boldsymbol{\nabla}p$ term is already in $\boldsymbol{\Psi}$, and
2. The $\frac{1}{\rho}\boldsymbol{\nabla}(\widetilde{\kappa}\boldsymbol{\nabla}\cdot\boldsymbol{u})$ term is already on the left-hand side.

All that remains is the deviatoric stress tensor term $\frac{1}{\rho}\boldsymbol{\nabla}\cdot\boldsymbol{\tau}$. Note that here, terms that describe momentum exchange between separate gas species will be neglected. Expand out Ψ and use the expression for the full stress tensor (6.14) to obtain the 3D momentum equation with vertical molecular viscosity and diffusion:

$$\frac{D\boldsymbol{u}}{Dt} + 2\boldsymbol{\Omega}\times\boldsymbol{u} + \boldsymbol{\nabla}\phi - \frac{1}{\rho}\boldsymbol{\nabla}\cdot\boldsymbol{\sigma} = \boldsymbol{0}. \tag{6.16}$$

A full expression for $\boldsymbol{\nabla}\cdot\boldsymbol{\sigma}$ in meteorological spherical polar coordinates is found in appendix F.2.1.

The 3D energy equation with vertical molecular viscosity and diffusion, also derived in appendix E.1 and given by (E.13) :

$$C_v\rho\frac{DT}{Dt} + p\boldsymbol{\nabla}\cdot\boldsymbol{u} - \boldsymbol{\tau} : \boldsymbol{\nabla}\boldsymbol{u} = \widetilde{\kappa}(\boldsymbol{\nabla}\cdot\boldsymbol{u})^2 - \boldsymbol{\nabla}\cdot\boldsymbol{q}, \tag{6.17}$$

where $\boldsymbol{q} = -\lambda\boldsymbol{\nabla}T$ is the diffusive heat flux, and

$$\boldsymbol{\tau} : \boldsymbol{\nabla}\cdot\boldsymbol{u} = \boldsymbol{\sigma} : \boldsymbol{\nabla}\cdot\boldsymbol{u} + p\boldsymbol{\nabla}\cdot\boldsymbol{u} + \widetilde{\kappa}\,\boldsymbol{\nabla}\cdot\boldsymbol{u} \tag{6.18}$$

where:

$$\boldsymbol{\sigma} : \boldsymbol{\nabla}\boldsymbol{u} = \boldsymbol{\nabla}\cdot(\boldsymbol{\sigma}\cdot\boldsymbol{u}) - \boldsymbol{u}\cdot(\boldsymbol{\nabla}\cdot\boldsymbol{\sigma}), \tag{6.19}$$

where $\boldsymbol{\sigma}\cdot\boldsymbol{u} = (\boldsymbol{\sigma}_r\cdot\boldsymbol{u}, \boldsymbol{\sigma}_\theta\cdot\boldsymbol{u}, \boldsymbol{\sigma}_\phi\cdot\boldsymbol{u})^T$. A full expression for $\boldsymbol{\sigma} : \boldsymbol{\nabla}\boldsymbol{u}$ in meteorological spherical polar coordinates is found in appendix F.2.1.

From appendix E.1, it is possible to obtain from the energy equation (6.17) an equation with terms that can be resolved in ENDGame, which is as follows:

$$C_p\Pi\rho\frac{D\Theta}{Dt} - \boldsymbol{\tau} : \boldsymbol{\nabla}\boldsymbol{u} = \widetilde{\kappa}(\boldsymbol{\nabla}\cdot\boldsymbol{u})^2 + \boldsymbol{\nabla}\cdot(\lambda\boldsymbol{\nabla}T). \tag{6.20}$$

So the full set of continuous governing equations in 3D spherical polar coordinates including vertical molecular viscosity and diffusion is given by (6.21)- (6.26).

$$\frac{Du}{Dt} + 2(\Omega_\phi w - \Omega_r v) + C_p\Theta\frac{1}{r\cos\phi}\frac{\partial\Pi}{\partial\theta} - \frac{1}{\rho}(\boldsymbol{\nabla}\cdot\boldsymbol{\sigma})_\theta = 0, \tag{6.21}$$

$$\frac{Dv}{Dt} + 2(\Omega_r u - \Omega_\theta w) + C_p\Theta\frac{1}{r}\frac{\partial\Pi}{\partial\phi} - \frac{1}{\rho}(\boldsymbol{\nabla}\cdot\boldsymbol{\sigma})_\phi = 0, \tag{6.22}$$

$$\frac{Dw}{Dt} + 2(\Omega_\theta v - \Omega_\phi u) + C_p\Theta\frac{\partial\Pi}{\partial r} + \frac{\partial\Phi}{\partial r} - \frac{1}{\rho}(\boldsymbol{\nabla}\cdot\boldsymbol{\sigma})_r = 0, \tag{6.23}$$

$$\frac{D\rho}{Dt} + \rho\boldsymbol{\nabla}\cdot\boldsymbol{u} = 0, \tag{6.24}$$

$$C_p\Pi\rho\frac{D\Theta}{Dt} - \boldsymbol{\tau} : \boldsymbol{\nabla}\boldsymbol{u} = \widetilde{\kappa}(\boldsymbol{\nabla}\cdot\boldsymbol{u})^2 + \boldsymbol{\nabla}\cdot(\lambda\boldsymbol{\nabla}T), \tag{6.25}$$

$$\rho = \left(\frac{p}{R}\right)\frac{\Pi^{\frac{1-\kappa}{\kappa}}}{\Theta}. \tag{6.26}$$

6.3 Semi-implicit semi-Lagrangian discretisation

In this section, the continuous 3D governing equations in spherical polar coordinates with vertical molecular viscosity and diffusion are discretised. First, the SISL discretisation is applied to each of the continuous governing equations, in the same way as in section 5.3, although the placement of variables within grid cells must be

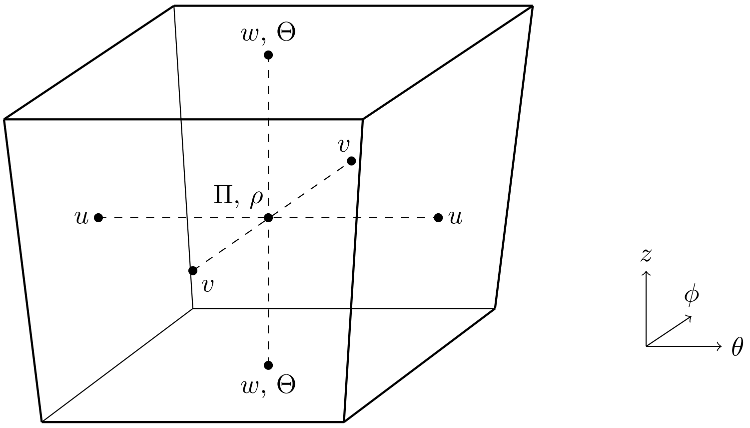

Figure 6.1: Illustration of a grid cell in ENDGame3D, with the Charney-Phillips vertical configuration of model variables and the Arakawa C-grid horizontal staggering of variables. Π and ρ are stored at the centre of each grid cell, w and Θ are stored at the top and bottom grid faces, u is stored at the east and west grid faces and v is stored at the north and south grid faces.

considered. These are illustrated in Figure 6.1.

The 3D discretised governing equations including the temporally implicit treatment of the vertical molecular viscosity and diffusion terms are now given by equations (6.27) - (6.31), where 'rhs' denotes the right-hand side/ explicit part of the discretisation of each equation. Note that here, the vertical diffusion terms, i.e. terms with two $\frac{\partial}{\partial r}$ components or $\frac{\partial}{\partial r}(\mu\ldots)$ and $\frac{\partial}{\partial r}(\lambda\ldots)$, are treated fully implicitly, The horizontal diffusion terms are currently neglected, as they only become significant above an altitude of 440 km (as shown in section 6.1), at which point, they need to be treated fully implicitly in time. The full expression of the stress tensor derivatives is detailed in appendix F.2.2. These terms are expanded fully, and the vertical diffusion terms that arise are treated implicitly. For simplicity, only the terms treated implicitly are written out in full here. Also note that $\overline{(\ldots)}^r$, $\overline{(\ldots)}^\theta$ and $\overline{(\ldots)}^\phi$ denote linear interpolation in the vertical r, horizontal θ and horizontal ϕ directions, respectively. Finally, note that for brevity, continuous notation is used for the spherical spatial derivatives.

6.4 Residual estimation

The discretised governing equations (6.27) - (6.31) form a coupled non-linear system. The approximate Newton's Method (5.11) can be used to find successively better approximations for the solution to this system of equations. This system of equations will not be satisfied after any number of iterations, so these equations will have some residuals R_u, R_v, R_w, R_ρ and R_Θ, which should be as small as possible.

The residuals are found by setting the superscript (l) to indicate the best guess

$$\left\{u - \alpha_u \Delta t \Psi_u - \frac{\Delta t}{\overline{\rho}^{\theta}} \frac{1}{r^2} \frac{\partial}{\partial r}\left[r^2 \mu r \frac{\partial}{\partial r}\left(\frac{u}{r}\right)\right]\right\}^{(n+1)} = (\mathrm{rhs}_u)_D^{(n)}, \tag{6.27}$$

$$\left\{v - \alpha_v \Delta t \Psi_v - \frac{\Delta t}{\overline{\rho}^{\phi}} \frac{1}{r^2} \frac{\partial}{\partial r}\left[r^2 \mu r \frac{\partial}{\partial r}\left(\frac{v}{r}\right)\right]\right\}^{(n+1)} = (\mathrm{rhs}_v)_D^{(n)}, \tag{6.28}$$

$$\begin{aligned}\Bigg\{(\delta_V + \nu \Delta t) w - \alpha_w \Delta t \Psi_w - \frac{\Delta t}{\overline{\rho}^{r}} \frac{1}{r^2} \frac{\partial}{\partial r}\Bigg[r^2 \Big\{2\mu \frac{\partial w}{\partial r} & \\ + \Big(\widetilde{\kappa} - \frac{2\mu}{3}\Big) \frac{1}{r^2} \frac{\partial (r^2 w)}{\partial r}\Big\}\Bigg]\Bigg\}^{(n+1)} & = (\mathrm{rhs}_w)_D^{(n)},\end{aligned} \tag{6.29}$$

$$\big[\rho(1 + \alpha_\rho \Delta t \boldsymbol{\nabla} \cdot \boldsymbol{u})\big]^{(n+1)} = (\mathrm{rhs}_\rho)_D^{(n)}, \tag{6.30}$$

$$\begin{aligned}\Bigg\{\Theta - \frac{\Delta t}{C_p \overline{\rho \Pi}^{r}} \Bigg[\kappa \Big\{\overline{\frac{1}{r^2} \frac{\partial (r^2 w)}{\partial r}}^{r}\Big\}^2 + \frac{1}{r^2} \frac{\partial}{\partial r}\left(r^2 \lambda \frac{\partial T}{\partial r}\right) & \\ - \overline{\frac{1}{r^2} \frac{\partial (r^2 w)}{\partial r}}^{r} \Big\{2\mu \overline{\frac{\partial w}{\partial r}}^{r} + \Big(\widetilde{\kappa} - \frac{2\mu}{3}\Big) \overline{\frac{1}{r^2} \frac{\partial (r^2 w)}{\partial r}}^{r}\Big\} & \\ - \overline{\frac{1}{r^2} \frac{\partial (r^2 u)}{\partial r}}^{\theta} \mu r \overline{\frac{\partial}{\partial r}\left(\frac{u}{r}\right)}^{\theta} - \overline{\frac{1}{r^2} \frac{\partial (r^2 v)}{\partial r}}^{\phi} \mu r \overline{\frac{\partial}{\partial r}\left(\frac{v}{r}\right)}^{\phi}\Bigg]\Bigg\}^{(n+1)} & = (\mathrm{rhs}_\Theta)_D^{(n)}.\end{aligned} \tag{6.31}$$

for the $n+1$ term after l iterations, and then putting all terms in the discretised governing equations (6.27) - (6.31) on the right-hand side so that the residual is left on the left-hand side. The residuals are as follows:

$$R_u = (\mathrm{rhs}_u)_D^{(n)} - \left\{u - \alpha_u \Delta t \Psi_u - \frac{\Delta t}{\overline{\rho}^{\theta}} \frac{1}{r^2} \frac{\partial}{\partial r}\left[r^2 \mu r \frac{\partial}{\partial r}\left(\frac{u}{r}\right)\right]\right\}^{(l)}, \tag{6.32}$$

$$R_v = (\mathrm{rhs}_v)_D^{(n)} - \left\{v - \alpha_v \Delta t \Psi_v - \frac{\Delta t}{\overline{\rho}^{\phi}} \frac{1}{r^2} \frac{\partial}{\partial r}\left[r^2 \mu r \frac{\partial}{\partial r}\left(\frac{v}{r}\right)\right]\right\}^{(l)}, \tag{6.33}$$

$$\begin{aligned}R_w = {} & (\mathrm{rhs}_w)_D^{(n)} - \Bigg\{(\delta_V + \nu \Delta t) w - \alpha_w \Delta t\, \Psi_w \\ & - \frac{\Delta t}{\overline{\rho}^{r}} \frac{1}{r^2} \frac{\partial}{\partial r}\Bigg[r^2 \Big\{2\mu \frac{\partial w}{\partial r} + \Big(\widetilde{\kappa} - \frac{2\mu}{3}\Big) \frac{1}{r^2} \frac{\partial (r^2 w)}{\partial r}\Big\}\Bigg]\Bigg\}^{(l)},\end{aligned} \tag{6.34}$$

$$R_\rho = (\mathrm{rhs}_\rho)_D^{(n)} - \big[\rho(1 + \alpha_\rho \Delta t\, \boldsymbol{\nabla} \cdot \boldsymbol{u})\big]^{(l)}, \tag{6.35}$$

$$\begin{aligned}R_\Theta = {} & (\mathrm{rhs}_\Theta)_D^{(n)} - \Bigg\{\Theta - \frac{\Delta t}{C_p \overline{\rho \Pi}^{r}} \Bigg[\widetilde{\kappa} \Big\{\overline{\frac{1}{r^2} \frac{\partial (r^2 w)}{\partial r}}^{r}\Big\}^2 + \frac{1}{r^2} \frac{\partial}{\partial r}\left(r^2 \lambda \frac{\partial T}{\partial r}\right) \\ & - \frac{1}{r^2} \frac{\partial (r^2 w)}{\partial r} \Big\{2\mu \frac{\partial w}{\partial r} + \Big(\widetilde{\kappa} - \frac{2\mu}{3}\Big) \frac{1}{r^2} \frac{\partial (r^2 w)}{\partial r}\Big\} \\ & - \frac{1}{r^2} \frac{\partial (r^2 u)}{\partial r} \mu r \frac{\partial}{\partial r}\left(\frac{u}{r}\right) - \frac{1}{r^2} \frac{\partial (r^2 v)}{\partial r} \mu r \frac{\partial}{\partial r}\left(\frac{v}{r}\right)\Bigg]\Bigg\}^{(l)}.\end{aligned} \tag{6.36}$$

Details on how to calculate the departure points $r_D^{(n)}$ are given in appendix A.4, and the method for reducing the residuals used in this section mirrors the method used in appendix A.5. The system of equations to be solved resembles (A.51), but it is now a larger system that includes the R_u and R_v residuals, given by (6.37), where $\partial_\varphi \equiv \partial / \partial \varphi$.

$$\begin{bmatrix} R_u \\ R_v \\ R_w \\ R_\Theta \\ R_\rho \end{bmatrix} = - \begin{bmatrix} \partial_u R_u & \partial_v R_u & \partial_w R_u & \partial_\Theta R_u & \partial_\rho R_u \\ \partial_u R_v & \partial_v R_v & \partial_w R_v & \partial_\Theta R_v & \partial_\rho R_v \\ \partial_u R_w & \partial_v R_w & \partial_w R_w & \partial_\Theta R_w & \partial_\rho R_w \\ \partial_u R_\Theta & \partial_v R_\Theta & \partial_w R_\Theta & \partial_\Theta R_\Theta & \partial_\rho R_\Theta \\ \partial_u R_\rho & \partial_v R_\rho & \partial_w R_\rho & \partial_\Theta R_\rho & \partial_\rho R_\rho \end{bmatrix} \begin{bmatrix} u' \\ v' \\ w' \\ \Theta' \\ \rho' \end{bmatrix} \tag{6.37}$$

Each term in the Jacobian of (6.37) is found by differentiating the residual equations (6.32) - (6.36), making the same approximations as in appendix A.5 and regarding perturbations to the scalar coefficient of molecular viscosity μ and the coefficient of molecular thermal conductivity λ as negligible, as in section 5.4. In 3D, a few extra approximations are made to obtain a new equation set:

- Neglect Θ' in the horizontal direction, i.e. the u and v equations.
- The Coriolis terms in $\boldsymbol{\Psi}$ are handled explicitly on the right-hand side.
- Similarly to how equation (A.54) is derived in 1D, it can also be obtained that

$$\frac{\partial [\ldots]_D^{(n)}}{\partial \boldsymbol{u}} \approx -\alpha_z \Delta t \frac{\partial [\ldots]_D^{(n)}}{\partial \boldsymbol{r}}. \tag{6.38}$$

Using these approximations leads to the equations for the residuals and the equation of state given by (6.39) - (6.44).

Full 3D viscous residual and state equations

$$R_u \approx u' - \frac{\Delta t}{\overline{\rho^*}^\theta} \frac{1}{r^2} \frac{\partial}{\partial r}\left[r^2 \mu r \frac{\partial}{\partial r}\left(\frac{u'}{r}\right)\right] + \alpha_u \Delta t \, C_p \overline{\Theta^*}^{\theta r} \frac{1}{r\cos\phi} \frac{\partial \Pi'}{\partial \theta}, \tag{6.39}$$

$$R_v \approx v' - \frac{\Delta t}{\overline{\rho^*}^\phi} \frac{1}{r^2} \frac{\partial}{\partial r}\left[r^2 \mu r \frac{\partial}{\partial r}\left(\frac{v'}{r}\right)\right] + \alpha_v \Delta t \, C_p \overline{\Theta^*}^{\phi r} \frac{1}{r} \frac{\partial \Pi'}{\partial \phi}, \tag{6.40}$$

$$\begin{aligned} R_w \approx\ & (\delta_V + \nu \Delta t) w' - \frac{\Delta t}{\overline{\rho^*}^r} \frac{1}{r^2} \frac{\partial}{\partial r}\left\{ r^2 \left[2\mu \frac{\partial w'}{\partial r} + \left(\widetilde{\kappa} - \frac{2\mu}{3}\right) \frac{1}{r^2} \frac{\partial (r^2 w')}{\partial r} \right]\right\} \\ & + \alpha_w \Delta t \, C_p \left(\Theta^* \frac{\partial \Pi'}{\partial r} + \frac{\partial \Pi^*}{\partial r} \Theta' \right), \end{aligned} \tag{6.41}$$

$$R_\rho \approx \rho' + \alpha \Delta t \boldsymbol{\nabla} \cdot (\overline{\rho^*} \boldsymbol{u}'), \tag{6.42}$$

$$R_\Theta \approx \alpha_z \Delta t \overline{\frac{\partial \Theta^*}{\partial r}}^r w' + \Theta' - \frac{\Delta t}{C_p \overline{\rho^* \Pi^*}^r} \frac{1}{r^2} \frac{\partial}{\partial r}\left[r^2 \lambda \frac{\partial}{\partial r}\left(\overline{\Pi^*}^r \Theta' + \Theta^* \overline{\Pi'}^r \right)\right], \tag{6.43}$$

$$0 \approx \frac{\rho'}{\rho^*} + \overline{\frac{\Theta'}{\Theta^*}}^r - \frac{1-\kappa}{\kappa} \frac{\Pi'}{\Pi^*}. \tag{6.44}$$

6.5 Constructing the elliptic problems

The residual and state equations found in section 6.3: (6.39) - (6.44) form six sets of equations with six sets of unknowns u', v', w', ρ', Θ' and Π'.

At this point, it is worth noting that the solver from the stand-alone version of the ENDGame dynamical core differs from the solver used currently in the operational version of the dynamical core used in the Met Office UM. The stand-alone version of ENDGame uses an adaptive multigrid method, which solves the problem on a coarse grid, and uses this to approximate solutions on ever finer grids to narrow down on the solution quickly. The Met Office UM dynamical core, however, uses a Krylov subspace method: a method for finding eigenvalues of large sparse matrices. The Krylov subspace generated by an $n \times n$ matrix A and a vector b of dimension n is the linear subspace spanned by $\{b, Ab, A^2b, \ldots, A^{r-1}b\}$ for some $r \in [1, 2, \ldots)$, and is able to solve systems quite effectively if it has a good preconditioner.

For the stand-alone version of ENDGame3D, it would be preferable to obtain from these a single set of equations for a single set of unknowns. However, trying to follow the same method as that used in 1D in section 5.5 gives a high order problem that has inverse differential operators. There are techniques for solving big linear systems. But by aiming for a single set of equations for a single set of unknowns, a well-posed problem may be obtained that can be solved quickly. It is hoped that these same benefits can be acquired in the viscous case. Solving an elliptic problem at w-grid points would also require significant development of ENDGame's multigrid solver, which is designed around solving for a value at ρ-levels. Instead, a different approach is taken which leads to an elliptic problem for Π'. It is shown in appendix E.7 that the approximations made are equivalent to those used by the 1D problem, but an elliptic problem for Π is more practical to implement.

To abbreviate the equation set, neglect the Π' term in the R_Θ equation (6.43) (it is shown in appendix E.7 that the approximations made here lead to the same problem as derived in 1D in section 5.5, which is valid in both the viscous and inviscid regions), and make the following substitutions:

$$Q(X) = X - \frac{\Delta t}{C_p \overline{\rho^* \Pi^*}^r} \frac{1}{r^2} \frac{\partial}{\partial r}\left[r^2 \lambda \frac{\partial}{\partial r}(\overline{\Pi^*}^r X)\right], \tag{6.45}$$

$$T_\theta(X) = X - \frac{\Delta t}{\overline{\rho^*}^\theta} \frac{1}{r^2} \frac{\partial}{\partial r}\left[r^2 \mu r \frac{\partial}{\partial r}\left(\frac{X}{r}\right)\right], \tag{6.46}$$

$$T_\phi(X) = X - \frac{\Delta t}{\overline{\rho^*}^\phi} \frac{1}{r^2} \frac{\partial}{\partial r}\left[r^2 \mu r \frac{\partial}{\partial r}\left(\frac{X}{r}\right)\right], \tag{6.47}$$

$$T_r(X) = (\delta_V + \nu \Delta t)X - \frac{\Delta t}{\overline{\rho^*}^r} \frac{1}{r^2} \frac{\partial}{\partial r}\left\{r^2\left[2\mu \frac{\partial X}{\partial r} + \left(\widetilde{\kappa} - \frac{2\mu}{3}\right)\frac{1}{r^2}\frac{\partial (r^2 X)}{\partial r}\right]\right\}, \tag{6.48}$$

where Q, T_θ, T_ϕ and T_r are all tridiagonal operators. With these expressions, the residual and state equations can be rewritten as:

$$\begin{aligned}
R_u &\approx T_\theta(u') + \alpha_u \Delta t\, C_p \overline{\Theta^*}^{\theta r} \frac{1}{r\cos\phi}\frac{\partial \Pi'}{\partial \theta}, && (6.49)\\
R_v &\approx T_\phi(v') + \alpha_v \Delta t\, C_p \overline{\Theta^*}^{\phi r} \frac{1}{r}\frac{\partial \Pi'}{\partial \phi}, && (6.50)\\
R_w &\approx T_r(w') + \alpha_w \Delta t\, C_p \left(\Theta^* \frac{\partial \Pi'}{\partial r} + \frac{\partial \Pi^*}{\partial r}\Theta' \right), && (6.51)\\
R_\rho &\approx \rho' + \alpha \Delta t \boldsymbol{\nabla} \cdot \left(\overline{\rho^*} \boldsymbol{u}' \right), && (6.52)\\
R_\Theta &\approx Q(\Theta') + \alpha_z \Delta t \overline{\frac{\partial \Theta^*}{\partial r}}^r w', && (6.53)\\
0 &\approx \frac{\rho'}{\rho^*} + \frac{\overline{\Theta'}^r}{\Theta^*} - \frac{1-\kappa}{\kappa}\frac{\Pi'}{\Pi^*}. && (6.54)
\end{aligned}$$

Begin by eliminating ρ' by taking (6.54) - (6.52)$/\rho^*$:

$$-\frac{R_\rho}{\rho^*} = \frac{\overline{\Theta'}^r}{\Theta^*} - \frac{1-\kappa}{\kappa}\frac{\Pi'}{\Pi^*} - \frac{\alpha \Delta t}{\rho^*} \boldsymbol{\nabla} \cdot (\overline{\rho^*} \boldsymbol{u}'). \tag{6.55}$$

Next, eliminate u' and v' by substituting rearranged expressions for u' and v' from the R_u and R_v equations (6.49), (6.50) into (6.55) to obtain:

$$\begin{aligned}
\frac{\overline{\Theta'}^r}{\Theta^*} - \frac{1-\kappa}{\kappa}\frac{\Pi'}{\Pi^*} + \frac{\alpha\Delta t}{\rho^*} \Bigg\{ & \frac{1}{r\cos\phi}\frac{\partial}{\partial\theta}\left[\overline{\rho^*}^\theta T_\theta^{-1}\left(\alpha_u \Delta t\, C_p \overline{\Theta^*}^{\theta r} \frac{1}{r\cos\phi}\frac{\partial \Pi'}{\partial\theta} \right)\right] \\
& + \frac{1}{r\cos\phi}\frac{\partial}{\partial\phi}\left[\overline{\rho^*}^\phi T_\phi^{-1}\left(\alpha_v \Delta t\, C_p \overline{\Theta^*}^{\phi r} \frac{1}{r}\frac{\partial \Pi'}{\partial\phi} \right) \cos\phi \right] \\
& - \frac{1}{r^2}\frac{\partial}{\partial r}\left(r^2 \overline{\rho^*}^r w' \right) \Bigg\} \\
= -\frac{R_\rho}{\rho^*} + \frac{\alpha\Delta t}{\rho^*} \Bigg\{ & \frac{1}{r\cos\phi}\frac{\partial}{\partial\theta}\left[\overline{\rho^*}^\theta T_\theta^{-1}(R_u) \right] + \frac{1}{r\cos\phi}\frac{\partial}{\partial\phi}\left[\overline{\rho^*}^\phi T_\phi^{-1}(R_v)\cos\phi \right] \Bigg\}. \qquad (6.56)
\end{aligned}$$

Next, make the approximation that $Q(\Theta') \approx \Theta'$ in order to eliminate Θ' in equations (6.51) and (6.53). In the inviscid region, it is clear that $Q(\Theta') \approx \Theta'$. In the viscous region, Q acts as a diffusive operator, amplifying small vertical scales. Therefore, Q^{-1} acts as a smoothing operator, capturing large scales, meaning that T_r will become more significant than Q^{-1}, so it is expected that the effect of T_r will dominate over Q in equation (6.51). It is shown in appendix E.7 that this assumption will lead to a problem that is valid in both viscous and inviscid regions. First, take (6.51)$-\alpha_w \Delta t\, C_p \frac{\partial \Pi^*}{\partial r}$ (6.53), and use the coefficient B (A.64), the operator D_1 (A.65) and the following expression for the Brunt Väisälä frequency N^2 in a non-hydrostatic atmosphere:

$$N^2 = -C_p \frac{\partial \Pi^*}{\partial r} \overline{\frac{\partial \Theta^*}{\partial r}}^r, \tag{6.57}$$

to obtain:

$$T_r(w') + B^{-1}D_1(\Pi') + \alpha_w\alpha_z\Delta t^2 N^2 w' = R_w - \alpha_w \Delta t\, C_p \frac{\partial \Pi^*}{\partial r} R_\Theta. \tag{6.58}$$

Define the following substitution for (6.58):

$$\widehat{T}(X) = T_r(X) + \alpha_w\alpha_z\Delta t^2 N^2 X, \tag{6.59}$$

so that it can be abbreviated as follows:

$$\widehat{T}(w') + B^{-1}D_1(\Pi') = R_w - \alpha_w \Delta t\, C_p \frac{\partial \Pi^*}{\partial r} R_\Theta. \tag{6.60}$$

Next, take (6.56) - $\overline{(6.53)/\Theta^*}^{r}$ and use the D_2 operator (A.69). Define $\boldsymbol{\nabla}_H$ to represent the horizontal part of the gradient operator in spherical coordinates as in appendix (F.1), $\overline{\rho^*}^{H}$ to represent ρ^* linearly interpolated in one horizontal direction corresponding to the components of $\boldsymbol{\nabla}_H$, and $\overline{\Theta^*}^{Hr}$ to represent Θ^* linearly interpolated in the vertical direction r as well as a single horizontal direction. It is also assumed that due to the second order vertical derivative in T_θ and T_ϕ, they vary only weakly in the horizontal direction, and that $\boldsymbol{\nabla}_H$ varies only in the horizontal. It is therefore a reasonable approximation that T_θ and T_ϕ, and their inverses, commute with $\boldsymbol{\nabla}_H$, as long as the background varies smoothly enough. Then T_θ^{-1} and T_ϕ^{-1} may be brought outside the $\boldsymbol{\nabla}_H \cdot \boldsymbol{\nabla}_H$ operator in (6.56) to ρ-points. Also, T_H may be defined at ρ-points, and compared with T_θ (6.46) and T_ϕ (6.47), as follows:

$$T_H(X) = X - \frac{\Delta t}{\rho^*}\frac{1}{r^2}\frac{\partial}{\partial r}\left[r^2 \mu r \frac{\partial}{\partial r}\left(\frac{X}{r}\right)\right], \tag{6.61}$$

and so the following may be obtained

$$\begin{aligned} &-\frac{1-\kappa}{\kappa}\frac{\Pi'}{\Pi^*} + \frac{\alpha^2\Delta t^2}{\rho^*} T_H^{-1}\big[\boldsymbol{\nabla}_H \cdot \big(C_p \overline{\rho^*}^{H}\overline{\Theta^*}^{Hr}\boldsymbol{\nabla}_H \Pi'\big)\big] - D_2(w') \\ &= -\frac{R_\rho}{\rho^*} - \overline{\frac{R_\Theta}{\Theta^*}}^{r} + \frac{\alpha\Delta t}{\rho^*} T_H^{-1}\big[\boldsymbol{\nabla}_H \cdot (\overline{\rho^*}^{H}\boldsymbol{R}_{\boldsymbol{u}_H})\big]. \end{aligned} \tag{6.62}$$

Lastly, eliminate w' by taking (6.62) + $D_2[\widehat{T}^{-1}(6.60)]$ and take T_H of both sides to obtain:

$$\begin{aligned} &-\frac{1-\kappa}{\kappa} T_H\left(\frac{\Pi'}{\Pi^*}\right) + \frac{\alpha^2\Delta t^2}{\rho^*}\boldsymbol{\nabla}_H \cdot (C_p \overline{\rho^*}^{H}\overline{\Theta^*}^{Hr}\boldsymbol{\nabla}_H \Pi') + T_H\Big[D_2\big\{\widehat{T}^{-1}\big[B^{-1}D_1(\Pi')\big]\big\}\Big] \\ &= -T_H\left(\frac{R_\rho}{\rho^*} + \overline{\frac{R_\Theta}{\Theta^*}}^{r}\right) + \frac{\alpha\Delta t}{\rho^*}\boldsymbol{\nabla}_H \cdot (\overline{\rho^*}^{H}\boldsymbol{R}_{\boldsymbol{u}_H}) + T_H\left\{D_2\left[\widehat{T}^{-1}\left(R_w - \alpha_w\Delta t\, C_p \frac{\partial \Pi^*}{\partial r} R_\Theta\right)\right]\right\} \end{aligned} \tag{6.63}$$

6.5.1 Obtaining a simpler Π' problem with a columnwise Jacobi iteration

The problem for Π' (6.63) is a big linear problem that would be expensive to solve, but it may be simplified by approximating it using columnwise Jacobi iterations. The strongest couplings occur in the vertical direction, so the Jacobi iteration simplifies the system by only considering components of the system that are in the same column. In this section, a new problem is set up where the components of the system in the vertical direction are solved columnwise while the horizontal components are put on the right-hand side, which leads to a problem that can be solved. These mathematical details would only be required to recreate the precise experiments performed in this chapter.

Define $H(\Pi')$ to be the problem for Π' and $\mathcal{R}$ to be the right-hand side of (6.63), so that $H(\Pi') = \mathcal{R}$. After l_N Newton iterations and l_J Jacobi iterations, equation (6.63) looks like

$$H\left[\Pi'^{(l_J)}\right] - \mathcal{R}^{(l_N)} \approx \mathcal{R}^{(l_J)}, \tag{6.64}$$

where $\mathcal{R}^{(l_N)}$ is the right-hand side of (6.63). The aim now is to find an increment to the Π increment Π': denoted by Π'', that reduces $\mathcal{R}^{(l_J)}$ to zero. Assume that the error is negligible after $l_J + 1$ Jacobi iterations, so $\mathcal{R}^{(l_J+1)} \approx 0$, and also that $\Pi'^{(l_J+1)} = \Pi'^{(l_J)} + \Pi''$. By considering equation (6.64) after $l_J + 1$ Jacobi iterations, it can be obtained that

$$H(\Pi'') \approx -\mathcal{R}^{(l_J)}. \tag{6.65}$$

The system given by equation (6.65) can be approximated with a columnwise Jacobi method: begin by separating $H(\Pi'')$ as follows:

$$H_S(\Pi'') + H_N(\Pi'') = -\mathcal{R}^{(l_J)}, \tag{6.66}$$

where $H_S(\Pi'')$ represents terms that are evaluated in the same column and which are updated in columnwise Jacobi iterations (from Jacobi iteration l_J to $l_J + 1$), and $H_N(\Pi'')$ represents terms in neighbouring columns and which are not updated in columnwise Jacobi iterations. These end up on the right-hand side and are evaluated at Jacobi iteration l_J.

Define the following coefficients which come from the $\boldsymbol{\nabla}_H \cdot \boldsymbol{\nabla}_H$ term in (6.63):

$$c_1 = \alpha_\rho \alpha_u \Delta t^2 \, C_p, \tag{6.67}$$

$$r^{\text{west}}_{i-\frac{1}{2},k} = \left.\frac{c_1 A^{\text{west}}\overline{\rho^*}^{\theta}\overline{\Theta^*}^{\theta r}}{\overline{r}^{\theta}}\right|_{i-\frac{1}{2},k}, \tag{6.68}$$

$$r^{\text{south}}_{j-\frac{1}{2},k} = \left.\frac{c_1 A^{\text{south}}\overline{\rho^*}^{\phi}\overline{\Theta^*}^{\phi r}}{\overline{r}^{\phi}}\right|_{j-\frac{1}{2},k}, \tag{6.69}$$

where A^{west}_k is the area of the west face of cell k, and A^{south}_k is the area of the south face of cell k. The $r^{\text{west}}_{i-\frac{1}{2},k}$ and $r^{\text{south}}_{j-\frac{1}{2},k}$ coefficients come from the term with two $\boldsymbol{\nabla}_H$ operators on the left-hand side of equation (6.63). Each component of $H(\Pi''_{i,j})$ (where i is in the θ direction and j is in the ϕ direction) is considered at positions (i,j) separately, and the parts that include $\Pi''_{i,j}$ terms are included in $H_S(\Pi''_{i,j})$ as follows:

$$\begin{aligned} H_S(\Pi''_{i,j}) &= -\frac{1-\kappa}{\kappa}T_H\left(\frac{\Pi''_{i,j}}{\Pi^*_{i,j}}\right) + T_H\Big[D_2\big\{\widehat{T}^{-1}\big[B^{-1}D_1(\Pi''_{i,j})\big)\big]\big\}\Big] \\ &\quad - \frac{1}{(\rho^* V)_k}\left(\frac{r^{\text{west}}_{i-\frac{1}{2}} + r^{\text{west}}_{i+\frac{1}{2}}}{\Delta\theta_i\cos\phi_j} + \frac{r^{\text{south}}_{j-\frac{1}{2}} + r^{\text{south}}_{j+\frac{1}{2}}}{\Delta\phi_j}\right)\Pi''_{i,j}. \end{aligned} \tag{6.70}$$

The high order and inverse operators in equation (6.70) will produce a dense matrix that will be tough and expensive to solve. By reducing it to a sparse matrix system, a well-posed problem can be obtained that can be solved much more effectively.

Now, equation (6.66) can be approximated with a columnwise Jacobi method: this is set up by just solving for Π'' in one column at a time, and so neglecting the terms in neighbouring columns given by $H_N(\Pi'')$, to obtain

$$\boxed{H_S(\Pi'') \approx -\mathcal{R}^{(l_J)}.} \tag{6.71}$$

So a single set of equations for a single set of unknowns Π'' has been obtained. Equation (6.71) is a problem that can be solved to obtain Π'': this process is detailed in section 6.6. Then using $\Pi'^{(l_J+1)} = \Pi'^{(l_J)} + \Pi''$, the Π' increment can be obtained. More increments may need to be found based on the number of multigrid operations. The scale analysis performed in appendix E.6 also applies to this problem (6.71) derived from the 3D viscous equations, and verifies that the method used to obtain this problem will still give reasonably accurate solutions of an appropriate scale.

The right-hand side of the problem (6.71) includes the right-hand side of (6.63) $\mathcal{R}$, which includes the following $\widehat{T}^{-1}$ term that cannot be evaluated in its current form:

$$\widehat{T}^{-1}\widetilde{R} = \widehat{T}^{-1}\left(R_w - \alpha_w\Delta t\, C_p\frac{\partial\Pi^*}{\partial r}R_\Theta\right). \tag{6.72}$$

This can be rearranged to obtain an elliptic problem that can be solved to obtain $X = \widehat{T}^{-1}\widetilde{R}$:

$$\boxed{\widehat{T}X = \widetilde{R}.} \tag{6.73}$$

6.5.2 Backsubstituting for other elliptic problems

After obtaining Π' by solving the problem (6.71), back-substitution is performed to obtain the other increment terms ρ', Θ', u', v' and w'. First, w' may be easily obtained by substituting the value for Π' in (6.60).

The remaining back-substitutions are made into the *full* set of equations (6.39) - (6.44) in order to capture the effects of the diffusive term λ. The R_Θ equation (6.43) can be rearranged to obtain an elliptic problem that can be solved to obtain Θ' by putting the known terms including Π' and w' on the right-hand side:

$$\boxed{Q(\Theta') = R_\Theta - \alpha_z \Delta t \frac{\overline{\partial \Theta^*}^r}{\partial r} w' + \frac{\Delta t}{C_p \rho^* \overline{\Pi^*}^r} \frac{1}{r^2}\frac{\partial}{\partial r}\left[r^2 \lambda \frac{\partial}{\partial r}\left(\Theta^* \overline{\Pi'}^r\right)\right].} \tag{6.74}$$

Similarly, equations (6.39) and (6.40) can be rearranged to obtain elliptic problems that can be solved to obtain u' and v' by putting the known terms including Π' on the right-hand side to obtain equations (6.75) and (6.76).

$$T_\theta(u') = R_u - \alpha_u \Delta t\, C_p \overline{\Theta^*}^{\theta r} \frac{1}{r\cos\phi}\frac{\partial \Pi'}{\partial \theta}, \tag{6.75}$$

$$T_\phi(v') = R_v - \alpha_v \Delta t\, C_p \overline{\Theta^*}^{\phi r} \frac{1}{r}\frac{\partial \Pi'}{\partial \phi}. \tag{6.76}$$

Lastly, ρ' may be obtained by substituting the values for Π' and Θ' into the equation of state (6.44).

6.6 Solving the problem for Π'

In this section, the problem for Π' (6.71) derived in section 6.5 is turned into a form suitable for programming into the ENDGame code. The mathematical detail of how this is set up and solved is set out in full. This is accomplished by setting up another variable to obtain two elliptic problems of two variables, that can be solved together by setting up a heptadiagonal system.

Define the variable q' as follows:

$$\boxed{\widehat{T}(q') \equiv \alpha_w \Delta t\, C_p \Theta^* \frac{\partial \Pi'}{\partial r}.} \tag{6.77}$$

Then it can be noted that:

$$D_1(\Pi') = B\alpha_w \Delta t\, C_p \Theta^* \frac{\partial \Pi'}{\partial r} = B\widehat{T}(q'). \tag{6.78}$$

Also define the following:

$$\begin{aligned} E &\equiv \frac{1}{(\rho^* V)_k}\left(\frac{r^{\text{west}}_{i-\frac{1}{2}} + r^{\text{west}}_{i+\frac{1}{2}}}{\Delta\theta_i \cos\phi_j} + \frac{r^{\text{south}}_{j-\frac{1}{2}} + r^{\text{south}}_{j+\frac{1}{2}}}{\Delta\phi_j}\right), & (6.79)\\ S(X) &\equiv -\frac{1-\kappa}{\kappa} T_H\left(\frac{X}{\Pi^*}\right) - EX. & (6.80) \end{aligned}$$

then the elliptic problem for Π' (6.71) may be expressed as:

$$\boxed{H_S(\Pi') = S(\Pi') + T_H[D_2(q')] \;\approx\; -\mathcal{R}^{(l_J)}.} \tag{6.81}$$

Equations (6.77) and (6.81) form a system of two equations with two unknowns to find: Π' and q. Expressions for B, D_1 and D_2 are given by equations (A.64), (A.65) and (A.69) respectively. The expressions for T_H, $\widetilde{T}$, $\widehat{T}$, Q, E and S are given by equations (6.61) (6.48) (6.59) (6.45), (6.79), and (6.81), respectively.

Equations (6.77) and (6.81) are an improvement over the initial Π' problem (6.71). This is because there are no inverse operators, which means these equations will lead a well-posed problem and a sparse matrix system that will be able to be inverted and solved much more efficiently.

Each term of the systems of equations to be solved, (6.77) and (6.81), must be expanded and discretised in order to set up a matrix system that can be solved. This mathematical detail is set out in the following subsections.

6.6.1 Discretise $\widehat{T}(q')$

The term $\widehat{T}(q')$ appears in (6.77), and is given by (6.59). Its discretised form is as follows for $k \in [2, N]$ (the boundary conditions at $k = 1, N+1$ are found later):

$$\begin{aligned} \widehat{T}(q')_{k-\frac{1}{2}} &= (\delta_V + \nu\Delta t) q'_{k-\frac{1}{2}} + \alpha_w \alpha_z \Delta t^2 N^2 q'_{k-\frac{1}{2}} \\ &\quad - \frac{\Delta t}{(\overline{\rho^*}^r r^2 \Delta r)_{k-\frac{1}{2}}}\left[2(r^2\mu)_k \frac{q'_{k+\frac{1}{2}} - q'_{k-\frac{1}{2}}}{\Delta r_k} - 2(r^2\mu)_{k-1}\frac{q'_{k-\frac{1}{2}} - q'_{k-\frac{3}{2}}}{\Delta r_{k-1}}\right] \\ &\quad - \frac{\Delta t}{(\overline{\rho^*}^r \Delta r)_{k-\frac{1}{2}}}\left[\left(\widetilde{\kappa} - \frac{2\mu_k}{3}\right)\frac{(Aq')_{k+\frac{1}{2}} - (Aq')_{k-\frac{1}{2}}}{V_k} - \left(\widetilde{\kappa} - \frac{2\mu_{k-1}}{3}\right)\frac{(Aq')_{k-\frac{1}{2}} - (Aq')_{k-\frac{3}{2}}}{V_{k-1}}\right]. \end{aligned} \tag{6.82}$$

Define the operators $\widehat{T}_{i-1/2,j-1/2}$ to be the coefficients of $q'_{j-1/2}$ for $\widehat{T}(q')_{i-1/2}$, in order to abbreviate this so that it becomes:

$$\widehat{T}(q')_{k-\frac{1}{2}} = \widehat{T}_{k-\frac{1}{2},k-\frac{3}{2}}q'_{k-\frac{3}{2}} + \widehat{T}_{k-\frac{1}{2},k-\frac{1}{2}}q'_{k-\frac{1}{2}} + \widehat{T}_{k-\frac{1}{2},k+\frac{1}{2}}q'_{k+\frac{1}{2}}. \tag{6.83}$$

The $\widehat{T}_{i-1/2,j-1/2}$ operators are defined fully in appendix E.9.

6.6.2 Discretise $\Theta^*\frac{\partial\Pi'}{\partial r}$

The term $\Theta^*\frac{\partial\Pi'}{\partial r}$ appears in equation (6.77). Its discretised form is as follows for $k \in [2, N-1]$ (the boundary values at $k = 1, N+1$ are not used):

$$\left(\Theta^*\frac{\partial\Pi'}{\partial r}\right)_{k-\frac{1}{2}} = \Theta^*_{k-\frac{1}{2}}\frac{\Pi'_k - \Pi'_{k-1}}{\Delta r_{k-\frac{1}{2}}}. \tag{6.84}$$

Define the constant C_2 and the operators $D^{(1)}_{i-1/2,j}$ to be the coefficients of Π_j for $(\Theta^*\frac{\partial\Pi'}{\partial r})_{i-1/2}$:

$$C_2 \;=\; \alpha_w\Delta t\, C_p, \quad D^{(1)}_{k-\frac{1}{2},k} = \frac{C_2\Theta^*_{k-\frac{1}{2}}}{\Delta r_{k-\frac{1}{2}}}, \quad D^{(1)}_{k-\frac{1}{2},k-1} = -\frac{C_2\Theta^*_{k-\frac{1}{2}}}{\Delta r_{k-\frac{1}{2}}}, \tag{6.85}$$

so that this becomes:

$$\alpha_w\Delta t\, C_p\left(\Theta^*\frac{\partial\Pi'}{\partial r}\right)_{k-\frac{1}{2}} = D^{(1)}_{k-\frac{1}{2},k}\Pi'_k + D^{(1)}_{k-\frac{1}{2},k-1}\Pi'_{k-1}. \tag{6.86}$$

6.6.3 Discretise $T_H[D_2(q')]$

The term $T_H[D_2(q')]$ appears in (6.81), and the operators D_2 and T_H are given by (A.69) and (6.61) respectively. The components of ρ^*D_2 operator are discretised fully in appendix A.7.1, and the coefficients $D^{(2)}_{i,j-1/2}$ are defined. Here, these act as the coefficients of $q'_{j-1/2}$ for $D_2(q')_i$.

The discretised form of $T_H(X/\rho^*)$ (where $1/\rho^*$ is used to cancel the ρ^* that is included in the ρ^*D_2 operator from appendix A.7.1) is as follows for $k \in [2, N-1]$ (the boundary conditions at $k = 1, N$ are found later):

$$T_H\left(\frac{X}{\rho^*}\right)_k = X_k - \frac{\Delta t}{(\rho^*V)_k}\left[\frac{A\mu r}{\Delta r}\bigg|_{k+\frac{1}{2}}\left(\frac{X}{\rho^*r}\bigg|_{k+1} - \frac{X}{\rho^*r}\bigg|_k\right) - \frac{A\mu r}{\Delta r}\bigg|_{k-\frac{1}{2}}\left(\frac{X}{\rho^*r}\bigg|_k - \frac{X}{\rho^*r}\bigg|_{k-1}\right)\right]. \tag{6.87}$$

Define the operators $T_{i,j}$ to be the coefficients of X_j for $T_H(X/\rho^*)_i$, in order to abbreviate this so that it becomes:

$$T_H(X)_k = T_{k,k-1}X_{k-1} + T_{k,k}X_k + T_{k,k+1}X_{k+1}. \tag{6.88}$$

The $T_{i,j}$ operators are defined fully in appendix E.9.

Using the $T_{i,j}$ and $D^{(2)}_{i,j-1/2}$ coefficients, the discretised form of $T_H[D_2(q')]$ is as follows for $k \in [2, N-1]$ (the boundary conditions at $k = 1, N$ are found later):

$$\begin{aligned} T_H[D_2(q')]_k \ &= T_{k,k-1}D^{(2)}_{k-1,k-\frac{3}{2}}q'_{k-\frac{3}{2}} + \left[T_{k,k-1}D^{(2)}_{k-1,k-\frac{1}{2}} + T_{k,k}D^{(2)}_{k,k-\frac{1}{2}}\right]q'_{k-\frac{1}{2}} \\ &\quad + \left[T_{k,k}D^{(2)}_{k,k+\frac{1}{2}} + T_{k,k+1}D^{(2)}_{k+1,k+\frac{1}{2}}\right]q'_{k-\frac{1}{2}} + T_{k,k+1}D^{(2)}_{k+1,k+\frac{3}{2}}q'_{k+\frac{3}{2}}. \end{aligned} \tag{6.89}$$

Define the operators $(TD)_{i,j-1/2}$ to be the coefficients of $q_{j-1/2}$ for $T_H[D_2(q')]_i$, in order to abbreviate this so that it becomes:

$$\begin{aligned} T_H[D_2(q')]_k \ &= (TD)_{k,k-\frac{3}{2}}q'_{k-\frac{3}{2}} + (TD)_{k,k-\frac{1}{2}}q'_{k-\frac{1}{2}} \\ &\quad + (TD)_{k,k+\frac{1}{2}}q'_{k+\frac{1}{2}} + (TD)_{k,k+\frac{3}{2}}q'_{k+\frac{3}{2}}. \end{aligned} \tag{6.90}$$

The $(TD)_{i,j-1/2}$ operators are defined fully in appendix E.9.

6.6.4 Discretise $S(\Pi')$

The term $S(\Pi')$ appears in (6.81), and is given by (6.80). Its discretised form is expressed with the $T_{i,j}$ operators and is as follows for $k \in [2, N-1]$ (the boundary conditions at $k = 1, N$ are found later):

$$S(\Pi')_k \ = \ -\frac{1-\kappa}{\kappa}\left(T_{k,k-1}\frac{\Pi'}{\Pi^*}\bigg|_{k-1} + T_{k,k}\frac{\Pi'}{\Pi^*}\bigg|_{k} + T_{k,k+1}\frac{\Pi'}{\Pi^*}\bigg|_{k+1}\right) - E. \tag{6.91}$$

Define the operators $S_{i,j}$ to be the coefficients of Π_j for $S(\Pi')_i$ in order to abbreviate this so that it becomes:

$$S(\Pi')_k = S_{k,k-1}\Pi'_{k-1} + S_{k,k}\Pi'_k + S_{k,k+1}\Pi'_{k+1}. \tag{6.92}$$

The $S_{i,j}$ operators are defined fully in appendix E.9.

6.6.5 Construct a matrix system to solve

By adding together all of the discretised terms on the left-hand side of equations (6.77) and (6.81), and using the above abbreviations, a heptadiagonal system of equations is obtained for $k \in [2, N-1]$:

$$\begin{aligned} &(TD)_{k,k-\frac{3}{2}}q'_{k-\frac{3}{2}} + S_{k,k-1}\Pi'_{k-1} + (TD)_{k,k-\frac{1}{2}}q'_{k-\frac{1}{2}} + S_{k,k}\Pi'_k \\ &\quad +(TD)_{k,k+\frac{1}{2}}q'_{k+\frac{1}{2}} + S_{k,k+1}\Pi'_{k+1} + (TD)_{k,k+\frac{3}{2}}q'_{k+\frac{3}{2}} \ = \ -\widehat{\mathcal{R}}^{(l_J)}_k, \end{aligned} \tag{6.93}$$

$$\widehat{T}_{k-\frac{1}{2},k-\frac{3}{2}}q'_{k-\frac{3}{2}} + D^{(1)}_{k-\frac{1}{2},k-1}\Pi'_{k-1} + \widehat{T}_{k-\frac{1}{2},k-\frac{1}{2}}q'_{k-\frac{1}{2}} + D^{(1)}_{k-\frac{1}{2},k} + \widehat{T}_{k-\frac{1}{2},k+\frac{1}{2}}q'_{k+\frac{1}{2}} \ = 0. \tag{6.94}$$

6.6.6 Boundary conditions

The boundary conditions on Π' at the surface and the top of the atmosphere at vertical levels 1 and N respectively, and the boundary conditions on q' at levels $1/2$ and $N+1/2$ need to be included.

At levels $1/2$ and $N+1/2$, the boundary conditions on w (A.41) are enforced so that there are no vertical velocities at the surface or at the top boundary of the model, so $w_{1/2} = w_{N+1/2} = 0$, and $w'_{1/2} = w'_{N+1/2} = 0$. Now consider equation (6.60), but using the expression for q', this may be written:

$$\widehat{T}(w') + \widehat{T}(q') = R_w - \alpha_w \Delta t\, C_p \frac{\partial \Pi^*}{\partial r} R_\Theta. \tag{6.95}$$

It can be seen here that q' is analogous to w', as rearranging this for q' in terms of w' would leave a constant factor of w' and the remaining right-hand side terms. Therefore, the boundary conditions that apply to w' at levels $1/2$ and $N+1/2$ also apply to q', so $q'_{1/2} = q'_{N+1/2} = 0$.

For levels 1 and N, no-stress boundary conditions are applied, so that terms involving $\mu_{1/2}$ and $\mu_{N+1/2}$ may be neglected. At the surface, this is justified because the effect of molecular viscosity is very small, so $\mu_{1/2}$ is negligible. At the top of the atmosphere, this boundary condition is applied because there is *no top boundary* at the top of the real atmosphere to cause any stress. This means that at level 1, the $(TD)_{1,-1/2}$ and $S_{1,0}$ terms vanish from equation (6.93), and the $T_{1,0}$ term vanishes from $(TD)_{1,1/2}$, and the $\widetilde{A}_{1/2}$ term vanishes from $S_{1,1}$ and $T_{1,1}$ leaving:

$$T^{\dagger}_{1,1} = 1 - \frac{F_1^{\rho V}\widetilde{A}_{\frac{3}{2}}}{r_1}, \qquad (TD)^{\dagger}_{1,\frac{1}{2}} = T^{\dagger}_{1,1} D^{(2)}_{1,\frac{1}{2}}, \qquad S^{\dagger}_{1,1} = -\frac{1-\kappa}{\kappa}\frac{T^{\dagger}_{1,1}}{\Pi^*} - E. \tag{6.96}$$

At level N, the $S_{N,N+1}$ and $(TD)_{N,N+1}$ terms vanish, and the $T_{N,N+3/2}$ term vanishes from $(TD)_{N,N+1/2}$ and the $\widetilde{A}_{N+1/2}$ term vanishes from $S_{N,N}$ and $T_{N,N}$ leaving:

$$T^{\dagger}_{N,N} = 1 - \frac{F_N^{\rho V}\widetilde{A}_{N-\frac{1}{2}}}{r_N}, \qquad (TD)^{\dagger}_{N,N+\frac{1}{2}} = T^{\dagger}_{N,N} D^{(2)}_{N,N+\frac{1}{2}}, \qquad S^{\dagger}_{N,N} = -\frac{1-\kappa}{\kappa}\frac{T^{\dagger}_{N,N}}{\Pi^*} - E. \tag{6.97}$$

6.6.7 Heptadiagonal system

With the boundary conditions, the matrix definitions given by (6.99) and (6.100) can be made, where $\boldsymbol{R}_\Pi$ denotes the vector of values of the right-hand sides of equations (6.77) and (6.81). Now equations (6.77) and (6.81) can be written as a heptadiagonal system of equations as follows:

$$\boxed{\boldsymbol{D}_{\Pi,q}\boldsymbol{Q} = \boldsymbol{R}.} \tag{6.98}$$

This is a heptadiagonal system of equations for $q'_{k+1/2}$ and Π'_k, that is solved using techniques for dealing with banded diagonal matrices [Press *et al.* , 1993].

6.6.8 Solving the elliptic problem on the right-hand side of the elliptic problem for Π'

Equation (6.73) is the elliptic problem that is solved to find an expression for the $\widehat{T}^{-1}$ term on the right-hand side of the Π' elliptic problem. The discretised form for $k \in [2, N]$ of $\widehat{T}$ has already been found in section 6.6.1.

Using the expression for the discretised form of $\widehat{T}$ (6.83), it can be seen that no contribution to the system is made by $\widehat{T}_{3/2,1/2}$ and $\widehat{T}_{N-1/2,N+1/2}$, because they are only applied to the boundary values of w' and q' that equal 0, as found in section 6.6.6. Similarly, they will make no contribution to this system because $\widehat{T}X$ in the elliptic problem (6.73) is analogous to $\widehat{T}(w') + \alpha_w \Delta t\, C_p \widehat{T}(q')$ in (6.95). So to enforce $\widehat{T}_{3/2,1/2} = \widehat{T}_{N-1/2,N+1/2} = 0$, set $X_{1/2} = X_{N+1/2} = 0$.

With the boundary conditions, the matrix definitions given by (6.102) and (6.103) can be made, where $\widetilde{\boldsymbol{R}}$ denotes the vector of values of the right-hand side of the elliptic problem (6.73). Now equation (6.73) can be written as a tridiagonal system of equations for $X = \widehat{T}^{-1}\widetilde{R}$ as follows:

$$\boxed{\boldsymbol{D}_R \boldsymbol{X} = \widetilde{\boldsymbol{R}}.} \tag{6.101}$$

This can be solved using a standard tridiagonal system solver [Press *et al.* , 1993].

6.7 Solving the elliptic problem for Θ'

In this section, the elliptic problem for Θ' (6.74) derived in section 6.5 is turned into a form suitable for programming into the ENDGame code, by setting it up as a tridiagonal system of equations and solving it.

6.7.1 Discretise $Q(\Theta')$

The term $Q(\Theta')$ appears in (6.74) and is given by (6.45). Its discretised form is as follows for $k \in [2, N]$ (the boundary conditions at $k = 1, N+1$ are found later):

$$
\boldsymbol{D}_{\mathrm{II},q} =
\left[
\begin{array}{ccccccccc}
1 & 0 & 0 & 0 & 0 & 0 & 0 & \cdots & 0 \\
(TD)^{\dagger}_{1,\frac{1}{2}} & S^{\dagger}_{1,1} & (TD)_{1,\frac{3}{2}} & S_{1,2} & (TD)_{1,\frac{5}{2}} & 0 & 0 & & 0 \\
\widehat{T}_{\frac{3}{2},\frac{1}{2}} & -D^{(1)}_{\frac{3}{2},1} & \widehat{T}_{\frac{3}{2},\frac{3}{2}} & -D^{(1)}_{\frac{3}{2},2} & \widehat{T}_{\frac{3}{2},\frac{5}{2}} & 0 & 0 & & \vdots \\
\ddots & \ddots & \ddots & \ddots & \ddots & \ddots & \ddots & \ddots & \\
 & \widehat{T}_{k-\frac{1}{2},k-\frac{3}{2}} & -D^{(1)}_{k-\frac{1}{2},k-1} & \widehat{T}_{k-\frac{1}{2},k-\frac{1}{2}} & -D^{(1)}_{k-\frac{1}{2},k} & \widehat{T}_{k-\frac{1}{2},k+\frac{1}{2}} & 0 & 0 & \\
 & (TD)_{k,k-\frac{3}{2}} & S_{k,k-1} & (TD)_{k,k-\frac{1}{2}} & S_{k,k} & (TD)_{k,k+\frac{1}{2}} & S_{k,k+1} & (TD)_{k,k+\frac{3}{2}} & \\
 & 0 & 0 & \widehat{T}_{k+\frac{1}{2},k-\frac{1}{2}} & -D^{(1)}_{k+\frac{1}{2},k} & \widehat{T}_{k+\frac{1}{2},k+\frac{1}{2}} & -D^{(1)}_{k+\frac{1}{2},k+1} & \widehat{T}_{k+\frac{1}{2},k+\frac{3}{2}} & \\
 & \ddots & \ddots & \ddots & \ddots & \ddots & \ddots & \ddots & \ddots \\
\vdots & & 0 & 0 & \widehat{T}_{N-\frac{1}{2},N-\frac{3}{2}} & -D^{(1)}_{N-\frac{1}{2},N-1} & \widehat{T}_{N-\frac{1}{2},N-\frac{1}{2}} & -D^{(1)}_{N-\frac{1}{2},N} & \widehat{T}_{N-\frac{1}{2},N+\frac{1}{2}} \\
0 & & 0 & 0 & (TD)_{N,N-\frac{3}{2}} & S_{N,N-1} & (TD)_{N,N-\frac{1}{2}} & S^{\dagger}_{N,N} & (TD)^{\dagger}_{N,N+\frac{1}{2}} \\
0 & \cdots & 0 & 0 & 0 & 0 & 0 & 0 & 1
\end{array}
\right]
\qquad (6.99)
$$

$$\boldsymbol{Q} = \begin{bmatrix} q'_{\frac{1}{2}} \\ \Pi'_1 \\ q'_{\frac{3}{2}} \\ \vdots \\ q'_{k-\frac{3}{2}} \\ \Pi'_{k-1} \\ q'_{k-\frac{1}{2}} \\ \Pi'_k \\ q'_{k+\frac{1}{2}} \\ \Pi'_{k+1} \\ q'_{k+\frac{3}{2}} \\ \vdots \\ q'_{N-\frac{1}{2}} \\ \Pi'_N \\ q'_{N+\frac{1}{2}} \end{bmatrix}, \quad \boldsymbol{R}_\Pi \equiv \begin{bmatrix} 0 \\ -\widehat{\mathcal{R}}_1^{(l_J)} \\ 0 \\ \vdots \\ 0 \\ -\widehat{\mathcal{R}}_{k-1}^{(l_J)} \\ 0 \\ -\widehat{\mathcal{R}}_k^{(l_J)} \\ 0 \\ -\widehat{\mathcal{R}}_{k+1}^{(l_J)} \\ 0 \\ \vdots \\ 0 \\ -\widehat{\mathcal{R}}_N^{(l_J)} \end{bmatrix}, \tag{6.100}$$

$$\boldsymbol{D}_{\mathrm{R}} = \begin{bmatrix} 1 & 0 & 0 & \cdots & 0 & \\ \widehat{T}_{\frac{3}{2},\frac{1}{2}} & \widehat{T}_{\frac{3}{2},\frac{3}{2}} & \widehat{T}_{\frac{3}{2},\frac{5}{2}} & & \vdots & \\ & \ddots & \ddots & \ddots & & \\ & \widehat{T}_{k-\frac{1}{2},k-\frac{3}{2}} & \widehat{T}_{k-\frac{1}{2},k-\frac{1}{2}} & \widehat{T}_{k-\frac{1}{2},k+\frac{1}{2}} & & \\ & & \ddots & \ddots & \ddots & \\ \vdots & & \widehat{T}_{N-\frac{1}{2},N-\frac{3}{2}} & \widehat{T}_{N-\frac{1}{2},N-\frac{1}{2}} & \widehat{T}_{N-\frac{1}{2},N+\frac{1}{2}} & \\ 0 & \cdots & 0 & 0 & 1 & \end{bmatrix} \tag{6.102}$$

$$\boldsymbol{X} \equiv \begin{bmatrix} X_{1/2} \\ X_{3/2} \\ \vdots \\ X_{k-1/2} \\ \vdots \\ X_{N-1/2} \\ X_{N+1/2} \end{bmatrix} \quad \widetilde{\boldsymbol{R}} \equiv \begin{bmatrix} 0 \\ \widetilde{R}_{\frac{3}{2}} \\ \vdots \\ \widetilde{R}_{k-\frac{1}{2}} \\ \vdots \\ \widetilde{R}_{N-\frac{1}{2}} \\ 0 \end{bmatrix} \tag{6.103}$$

$$\begin{aligned} Q(\Theta')_{k-\frac{1}{2}} &= \Theta'_{k-\frac{1}{2}} - \frac{\Delta t}{C_p(\overline{\rho^*\Pi^*}^r r^2\Delta r)_{k-\frac{1}{2}}} \left\{ \frac{r^2\lambda}{\Delta r}\bigg|_k \left[\left(\overline{\Pi^*}^r\Theta'\right)_{k+\frac{1}{2}} - \left(\overline{\Pi^*}^r\Theta'\right)_{k-\frac{1}{2}} \right] \right. \\ &\qquad \left. - \frac{r^2\lambda}{\Delta r}\bigg|_{k-1} \left[\left(\overline{\Pi^*}^r\Theta'\right)_{k-\frac{1}{2}} - \left(\overline{\Pi^*}^r\Theta'\right)_{k-\frac{3}{2}} \right] \right\}. \end{aligned} \tag{6.104}$$

Define the operators $Q_{i-1/2,j-1/2}$ to be the coefficients of $\Theta'_{j-1/2}$ for $Q(\Theta')_{i-1/2}$, in order to abbreviate this so that it becomes:

$$Q(\Theta')_{k-\frac{1}{2}} = Q_{k-\frac{1}{2},k-\frac{3}{2}}\Theta'_{k-\frac{3}{2}} + Q_{k-\frac{1}{2},k-\frac{1}{2}}\Theta'_{k-\frac{1}{2}} + Q_{k-\frac{1}{2},k+\frac{1}{2}}\Theta'_{k+\frac{1}{2}}. \tag{6.105}$$

The $Q_{i-1/2,j-1/2}$ operators are defined fully in appendix E.9.

6.7.2 Construct a matrix problem to solve

By adding together all of the discretised terms on the left-hand side of the elliptic problem for Θ' (6.74) and using the above abbreviations, a tridiagonal system of equations is obtained for $k \in [2, N]$:

$$Q_{k-\frac{1}{2},k-\frac{3}{2}}\Theta'_{k-\frac{3}{2}} + Q_{k-\frac{1}{2},k-\frac{1}{2}}\Theta'_{k-\frac{1}{2}} + Q_{k-\frac{1}{2},k+\frac{1}{2}}\Theta'_{k+\frac{1}{2}} = R^{\Theta}_{k-\frac{1}{2}}, \tag{6.106}$$

where $R^{\Theta}_{k-1/2}$ is the right-hand side of equation (6.74) at level $k - 1/2$.

6.7.3 Boundary conditions

The boundary conditions on Θ' at the surface and the top of the atmosphere at vertical levels $1/2$ and $N + 1/2$ respectively need to be included.

At level $1/2$, the boundary conditions on w (A.41) are enforced so that there are no vertical velocities at the surface, so $w_{1/2} = 0$, and $w'_{1/2} = 0$. Next, consider the R_{Θ} equation (6.43): at level $1/2$, the coefficient of thermal diffusivity λ is negligible and $w'_{1/2} = 0$, which leaves $\Theta'_{1/2} = R_{\Theta}$.

At level $N + 1/2$, the $Q_{N+1/2,N+3/2}$ term vanishes, and the F^{λ}_{N+1} term vanishes from $Q_{N+1/2,N+1/2}$, leaving:

$$Q^{\dagger}_{N+\frac{1}{2},N+\frac{1}{2}} = 1 - F^{Q}_{N+\frac{1}{2}} F^{\lambda}_{N} \overline{\Pi^{*}}^{r}_{N+\frac{1}{2}}. \tag{6.107}$$

6.7.4 Tridiagonal system

With the boundary conditions, the matrix definitions given by (6.109) and (6.110) can be made, where $\boldsymbol{R}_{\Theta}$ denotes the vector of values of the right-hand sides of the elliptic problem for Θ' (6.74). Now equation (6.74) can be written as a tridiagonal system of equations for $\Theta'_{k+1/2}$, given Π'_{k}, as follows:

$$\boxed{\boldsymbol{D}_{\Theta}\boldsymbol{\Theta} = \boldsymbol{R}_{\Theta}.} \tag{6.108}$$

This can be solved using a standard tridiagonal system solver [Press *et al.* , 1993].

6.8 Solving the elliptic problems for u' and v'

In this section, the elliptic problems for u' (6.75) and v' (6.76) derived in section 6.5 are turned into a form suitable for programming into the ENDGame code, by setting them up as tridiagonal systems of equations to be solved.

$$\boldsymbol{D}_\Theta = \begin{bmatrix} 1 & 0 & 0 & \cdots & & & 0 \\ Q_{\frac{3}{2},\frac{1}{2}} & Q_{\frac{3}{2},\frac{3}{2}} & Q_{\frac{3}{2},\frac{5}{2}} & & & & \vdots \\ \ddots & \ddots & \ddots & & & & \\ & Q_{k-\frac{1}{2},k-\frac{3}{2}} & Q_{k-\frac{1}{2},k-\frac{1}{2}} & Q_{k-\frac{1}{2},k+\frac{1}{2}} & & & \\ & & \ddots & \ddots & \ddots & & \\ \vdots & & & & Q_{N-\frac{1}{2},N-\frac{3}{2}} & Q_{N-\frac{1}{2},N-\frac{1}{2}} & Q_{N-\frac{1}{2},N+\frac{1}{2}} \\ 0 & \cdots & & & 0 & Q_{N+\frac{1}{2},N-\frac{1}{2}} & Q^\dagger_{N+\frac{1}{2},N+\frac{1}{2}} \end{bmatrix} \tag{6.109}$$

$$\boldsymbol{\Theta} \equiv \begin{bmatrix} \Theta'_{1/2} \\ \Theta'_{3/2} \\ \vdots \\ \Theta'_{k-1/2} \\ \vdots \\ \Theta'_{N-1/2} \\ \Theta'_{N+1/2} \end{bmatrix}, \quad \boldsymbol{R}_\Theta \equiv \begin{bmatrix} R_\Theta \\ R^\Theta_{\frac{3}{2}} \\ \vdots \\ R^\Theta_{k-\frac{1}{2}} \\ \vdots \\ R^\Theta_{N-\frac{1}{2}} \\ R^\Theta_{N+\frac{1}{2}} \end{bmatrix}, \tag{6.110}$$

6.8.1 Discretise the left-hand side of the elliptic problem for u' and v'

The discretised forms of the left-hand sides of the elliptic problems for u' (6.75) and v' (6.76) are found simply by linearly interpolating the $T_{i,j}$ operators (defined fully in appendix E.9) to u or v points. The discretised forms of the elliptic problems for u' and v' are then:

$$T_\theta(u')_{i+\frac{1}{2},k} = \overline{T}^\theta_{k,k-1} u'_{i+\frac{1}{2},k-1} + \overline{T}^\theta_{k,k} u'_{i+\frac{1}{2},k} + \overline{T}^\theta_{k,k+1} u'_{i+\frac{1}{2},k+1}, \tag{6.111}$$

$$T_\phi(v')_{i+\frac{1}{2},k} = \overline{T}^\phi_{k,k-1} v'_{j+\frac{1}{2},k-1} + \overline{T}^\phi_{k,k} v'_{j+\frac{1}{2},k} + \overline{T}^\phi_{k,k+1} v'_{j+\frac{1}{2},k+1}. \tag{6.112}$$

6.8.2 Construct a matrix problem to solve

By adding together all of the discretised terms on the left-hand side of the elliptic problem for u' (6.75) (or v' (6.76)) and using the above abbreviations, a tridiagonal system of equations is obtained for $k \in [2, N-1]$:

$$\overline{T}^\theta_{k,k-1} u'_{i+\frac{1}{2},k-1} + \overline{T}^\theta_{k,k} u'_{i+\frac{1}{2},k} + \overline{T}^\theta_{k,k+1} u'_{i+\frac{1}{2},k+1} = R^u_{i+\frac{1}{2},k}, \tag{6.113}$$

$$\overline{T}^\phi_{k,k-1} v'_{j+\frac{1}{2},k-1} + \overline{T}^\phi_{k,k} v'_{j+\frac{1}{2},k} + \overline{T}^\phi_{k,k+1} v'_{j+\frac{1}{2},k+1} = R^v_{j+\frac{1}{2},k}. \tag{6.114}$$

where $R^u_{i+1/2,k}$ is the right-hand side of equation (6.75) at level k, and $R^v_{j+1/2,k}$ is the right-hand side of equation (6.76) at level k.

6.8.3 Tridiagonal system

With the boundary conditions for $T_{i,j}$, the matrix definitions given by (6.117) and (6.118) can be made, where $\boldsymbol{R}_u$ denotes the vector of values of the right-hand sides of the elliptic problem for u' (6.75) and $\boldsymbol{R}_u$ denotes the vector of values of the right-hand sides of the elliptic problem for v' (6.76). Now equations (6.75) and (6.76) can be written as tridiagonal systems of equations as in (6.115) and (6.116).

$$\boxed{\begin{aligned} \boldsymbol{D}_u\boldsymbol{u} &= \boldsymbol{R}_u, \\ \boldsymbol{D}_v\boldsymbol{v} &= \boldsymbol{R}_u. \end{aligned}} \qquad \begin{aligned} &(6.115) \\ &(6.116) \end{aligned}$$

Equations (6.115) and (6.116) are now in the form of a tridiagonal system of equations for u'_k and v'_k, given Π'_k, that can be solved using a standard tridiagonal matrix algorithm [Press *et al.* , 1993].

$$\boldsymbol{D}_u = \begin{bmatrix} \overline{T}^{\theta\,\dagger}_{1,1} & \overline{T}^{\theta}_{1,2} & 0 & \cdots & & 0 \\ \overline{T}^{\theta}_{2,1} & \overline{T}^{\theta}_{2,2} & \overline{T}^{\theta}_{2,3} & & & \vdots \\ \ddots & \ddots & \ddots & \ddots & & \\ & \overline{T}^{\theta}_{k,k-1} & \overline{T}^{\theta}_{k,k} & \overline{T}^{\theta}_{k,k+1} & & \\ & & \ddots & \ddots & \ddots & \\ \vdots & & \overline{T}^{\theta}_{N-1,N-2} & \overline{T}^{\theta}_{N-1,N-1} & \overline{T}^{\theta}_{N-1,N} & \\ 0 & \cdots & 0 & \overline{T}^{\theta}_{N,N-1} & \overline{T}^{\theta\,\dagger}_{N,N} & \end{bmatrix} \qquad (6.117)$$

$$\boldsymbol{u} \equiv \begin{bmatrix} u_{i+\frac{1}{2},1} \\ \vdots \\ u_{i+\frac{1}{2},k} \\ \vdots \\ u_{i+\frac{1}{2},N} \end{bmatrix}, \quad \boldsymbol{v} \equiv \begin{bmatrix} v_{j+\frac{1}{2},1} \\ \vdots \\ v_{j+\frac{1}{2},k} \\ \vdots \\ v_{j+\frac{1}{2},N} \end{bmatrix}, \quad \boldsymbol{R}_u \equiv \begin{bmatrix} R^u_{i+\frac{1}{2},1} \\ \vdots \\ R^u_{i+\frac{1}{2},k} \\ \vdots \\ R^u_{i+\frac{1}{2},N} \end{bmatrix}, \quad \boldsymbol{R}_v \equiv \begin{bmatrix} R^v_{j+\frac{1}{2},1} \\ \vdots \\ R^v_{j+\frac{1}{2},k} \\ \vdots \\ R^v_{j+\frac{1}{2},N} \end{bmatrix}. \qquad (6.118)$$

6.9 Comparison to the non-viscous formulation

In this section, stability tests are performed in ENDGame3D using the implicit formulation with vertical molecular viscosity and diffusion derived in this chapter. The results of the stability tests for the viscous and non-viscous formulations are shown in Figure 6.2. Here, ENDGame3D is run with $\Delta x \approx 300\,\mathrm{km}$, $\Delta t = 30\,\mathrm{min}$, and is initiated with a baroclinic wave, although the initial condition for the temperature profile needed to be modified as the basic state described by Ullrich *et al.* [2013] is only valid up to 15 km. Above this altitude, this temperature profile is merged with

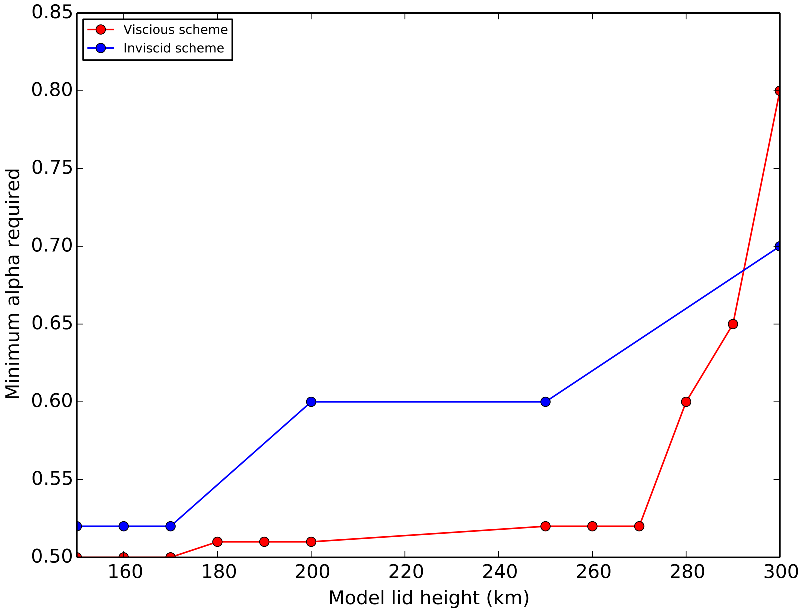

Figure 6.2: Stability tests of ENDGame3D comparing the viscous and non-viscous formulations. The lines on this stability test plot represent the minimum off-centring parameter α required for a simulation with 30 minute time-steps to remain stable for 10 days for different model lid heights under the baroclinic wave test.

the USSA temperature profile: this is described in appendix E.10.

Recall that the off-centring parameter α acts to artificially damp the dynamical core which improves its stability, but reduces its accuracy: it is therefore preferable to use as low a value of α as possible. It can be seen that the inviscid scheme requires a value of $\alpha = 0.6$ above 200 km, whereas the new scheme with vertical molecular viscosity and diffusion only requires $\alpha = 0.52$ up to 270 km. The viscous scheme is therefore demonstrably more stable, since it doesn't need as much off-centring as the inviscid scheme to be able to run simulations with higher top boundaries.

Recall Figure 5.4 in which the stability of ENDGame1D is tested for different time-steps. This suggests that the stability of ENDGame3D with vertical molecular viscosity and diffusion may be further improved with smaller time-steps, although this becomes more prohibitively expensive to perform stability tests with. Therefore, only 30 min time-steps are considered here.

The inviscid scheme appears to still be performing remarkably well compared to the stability tests of ENDGame1D in section 3.4. The main reason for this is the larger time-step being used in these experiments: here, $\Delta t = 30\,\text{min}$. The decaying time-scale of the off-centring parameter α (4.56) depends on the time-step used, and has a larger effect for bigger time-steps. This also means that smaller α are required

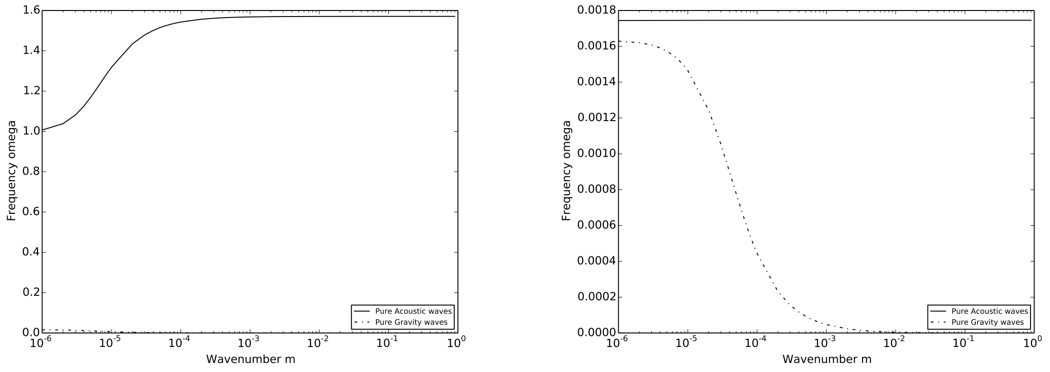

Figure 6.3: The temporally-discrete frequencies using the pure acoustic wave dispersion relation (4.35) and the pure gravity wave dispersion relation (4.36) with (left) $\Delta t = 3\,\mathrm{s}$ and (right) $\Delta t = 30\,\mathrm{min}$. Estimates for wavenumbers are taken from ENDGame3D simulations at 140 km: $k = 4 \times 10^{-6}$ and $l = 5 \times 10^{-6}$, and a range of values for the vertical wavenumber m.

for the viscous scheme to get the top boundary to the molecularly diffused region.

Above an altitude of 270 km, the stability of both schemes decreases significantly. For the viscous scheme, this is most likey related to the extra approximations that are made in order to reach an easily solvable elliptic problem in 3D with vertical molecular viscosity and diffusion. These extra approximations together with the huge range of orders of magnitude of density values at these altitudes act to keep the solver from being able to converge to a solution very well this high up.

Figure 6.3 shows the frequencies calculated using the pure temporally-discrete acoustic wave and gravity wave dispersion relations (4.35) and (4.36) respectively, for different timesteps, and for horizontal wavenumbers estimated from ENDGame at 140 km. From this, it can be seen that for larger timesteps ($\Delta t = 30\,\mathrm{min}$), the acoustic wave and gravity wave frequencies are of the same order of magnitude for smaller vertical wavenumbers m. High frequency acoustic waves are damped heavily by ENDGame's SI timestepping scheme, and so the acoustic wave frequency collapses to the same frequency as gravity waves for smaller vertical wavenumbers, and for large Δt. For smaller timesteps ($\Delta t = 3\,\mathrm{s}$), there is a large difference between acoustic wave and gravity wave frequencies for all vertical wavenumbers, so acoustic waves should be distinguishable from gravity waves in ENDGame3D simulations.

When the vertical velocity is plotted, as in Figures 6.4 and 6.6, the wavelike patterns that can be observed near the top boundary of the dynamical core are both gravity waves and acoustic waves being slowed by ENDGame's SI timestepping scheme. The left-hand plots of these figures show the wave amplitudes observed in the inviscid version without vertical molecular viscosity and diffusion. Lighter colours in these plots indicate small wave amplitudes, while darker colours indicate

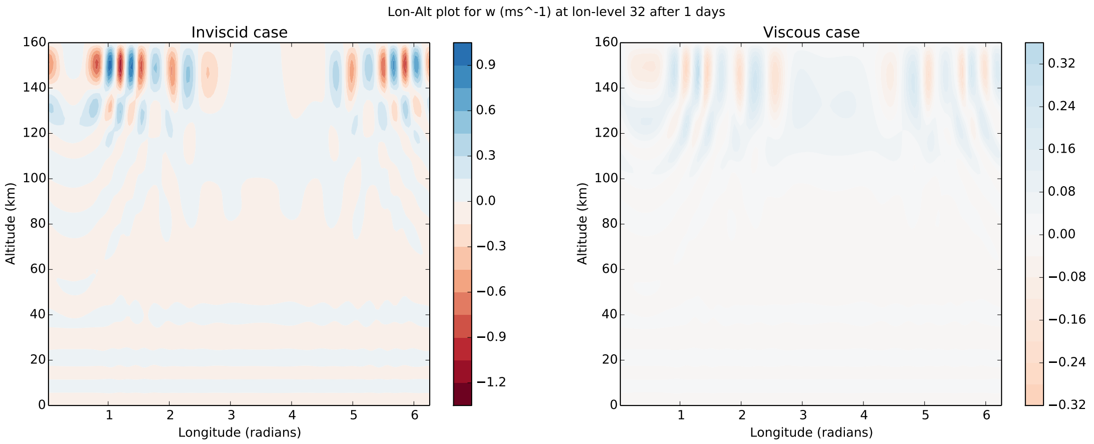

Figure 6.4: Longitude-altitude plots at the equator of vertical velocity w after 1 day for a baroclinic wave test with (left) the original inviscid formulation and (right) the new formulation with vertical molecular viscosity and diffusion with $\Delta t = 30\,\text{min}$, up to 160 km.

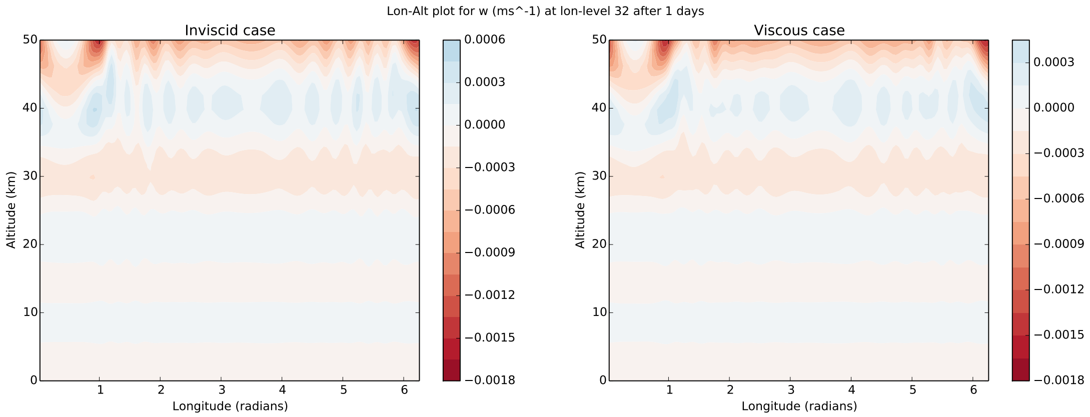

Figure 6.5: Longitude-altitude plots at the equator of vertical velocity w after 1 day for a baroclinic wave test with (left) the original inviscid formulation and (right) the new formulation with vertical molecular viscosity and diffusion, with $\Delta t = 30\,\text{min}$, up to 50 km. 12 iterations per step are used to remove numerical artefacts.

much larger wave amplitudes. It can be seen that without vertical molecular viscosity and diffusion, wave amplitudes begin to get significantly bigger above 120 km and continue to grow.

The right-hand plots of Figures 6.4 and 6.6 show the wave amplitudes observed in ENDGame3D with vertical molecular viscosity and diffusion: the muted colours in the thermosphere show that when the waves reach the molecularly diffused region above 130 km, the wave amplitudes are prevented from growing as much by the vertical molecular viscosity and diffusion.

Figure 6.5 zooms in on the lower 50 km of Figure 6.4. From this, it can be verified that vertical molecular viscosity and diffusion has very little effect on the state of the lower atmosphere. These plots are not identical however, and these slight differences are not due to numerical artefacts (even with 12 iterations per

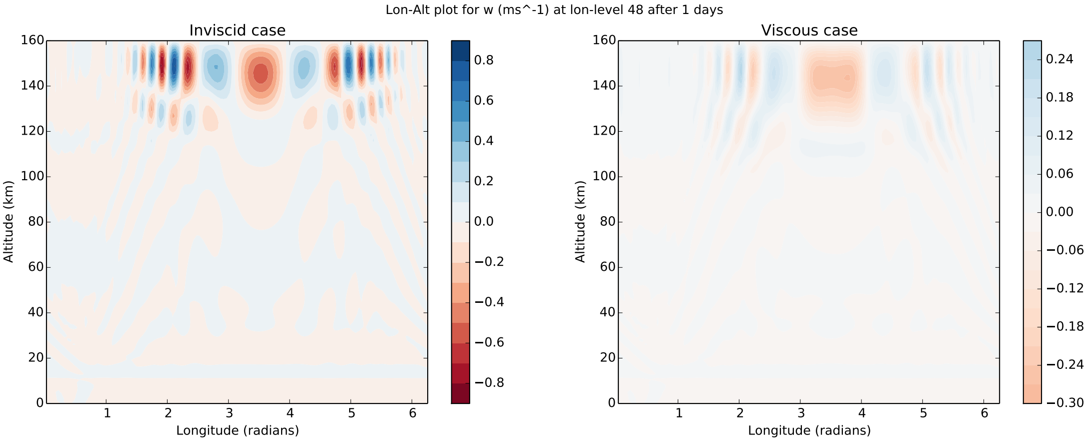

Figure 6.6: Longitude-altitude plots at 45^o latitude of vertical velocity w after 1 day for a baroclinic wave test with (left) the original inviscid formulation and (right) the new formulation with vertical molecular viscosity and diffusion with $\Delta t = 30\,\text{min}$, up to 160 km.

step rather than the usual 4, the solution is not quite the same). They are most likely related to waves propagating up into the upper atmosphere, reflecting off the top boundary and back down again: this causes some differences in the lower atmosphere depending on whether or not molecular viscosity and diffusion are acting in the upper atmosphere.

Figure 6.7 shows vertical velocity plots from ENDGame3D with vertical molecular viscosity and diffusion with a higher top boundary at 250 km. Some bigger vertical structures can be seen here that can't be seen with the lower top boundary, but the smaller scale horizontal structure can still be seen. The wave amplitudes still get larger by 120 km altitude, but they do not get any larger at higher altitudes: the vertical molecular viscosity and diffusion act to prevent the further growth of vertically propagating waves in the thermosphere. Some of the differences between these plots with Figures 6.4 and 6.6 can be attributed to the waves bouncing off the lower top boundary in Figures 6.4 and 6.6.

Figure 6.8 shows vertical velocity plots from ENDGame3D with vertical molecular viscosity and diffusion simulated with a small 3 s time-step, in order to compare the hydrostatic and non-hydrostatic formulations. Recall that from Figure 6.3, it can be shown that the use of a smaller time-step theoretically allows acoustic wave frequencies to be distinguishable from gravity wave frequencies in ENDGame. However, acoustic waves can only be represented in non-hydrostatic dynamics

Table 6.2 shows the results of some convergence tests to compare the rate of convergence (i.e. the rate at which the residuals get smaller) between the viscous and non-viscous formulations. It can be seen that most of the residuals converge

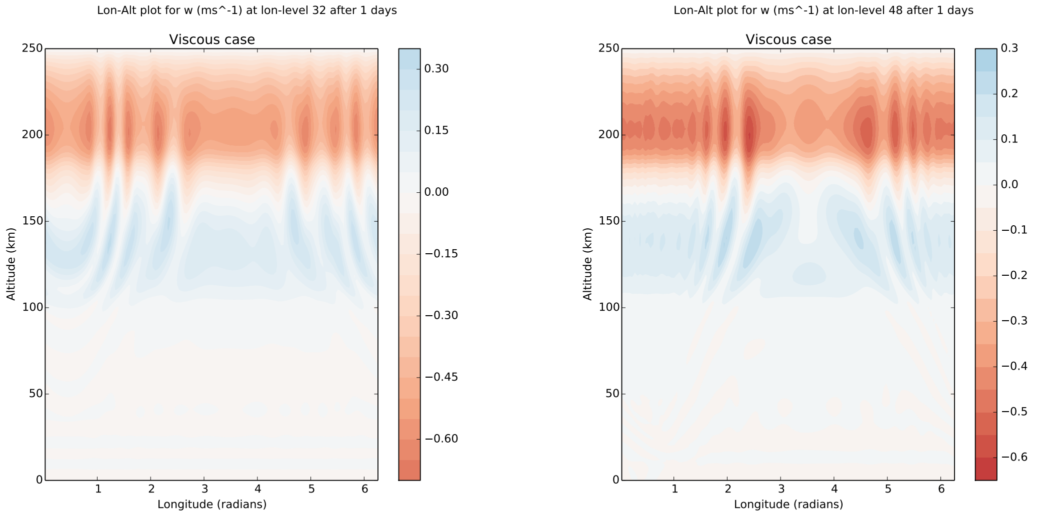

Figure 6.7: Longitude-altitude plots (left) at the equator and (right) at 45^o latitude, of vertical velocity w after 1 day for a baroclinic wave test with the new formulation with vertical molecular viscosity and diffusion with $\Delta t = 30\,\text{min}$, up to $250\,\text{km}$.

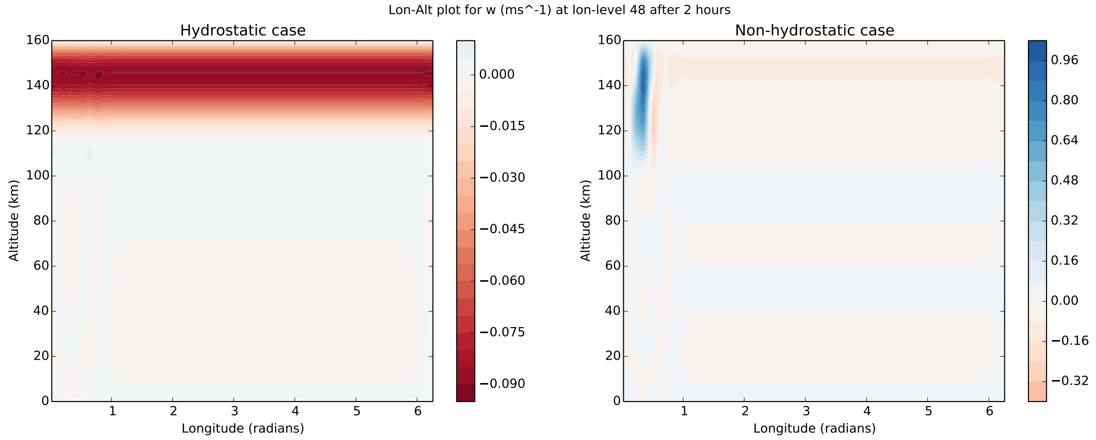

Figure 6.8: Longitude-altitude plots at 45^o latitude of vertical velocity after 2 hours for a baroclinic wave test with the (left) hydrostatic and (right) non-hydrostatic formulation with vertical molecular viscosity and diffusion, with $\Delta t = 3\,\text{s}$, up to $160\,\text{km}$. Note that the colour scale does not match across these two plots.

faster in the inviscid case than in the viscous case. For R_Θ, the residual even gets larger at the first iteration before reducing thereafter. The convergence of R_w seems to stall at some point. As in ENDGame1D, this is likely to be a result of the extra approximations that are made in order to include vertical molecular viscosity and diffusion in the governing equations. Despite this lack of convergence, Figures 6.4 and 6.5 demonstrate that the fully coupled viscous solver represents the lower atmosphere well, while having the expected damping effect on acoustic waves in the thermosphere.

Iter.	Inv. R_ρ	Vis. R_ρ	Inv. R_Θ	Vis. R_Θ	Inv. R_u	Vis. R_u	Inv. R_v	Vis. R_v	Inv. R_w	Vis. R_w
1	3.72E-006	3.73E-006	1433	412.9	3.188	1.387	3.780	1.954	0.2164	36.67
2	3.55E-009	1.76E-008	112.4	536.1	0.3404	0.3329	0.3624	0.4575	4.639	19.07
3	7.50E-011	9.89E-010	8.262	25.06	3.15E-002	0.3034	3.45E-002	0.4186	0.9874	19.05
4	1.86E-012	6.81E-011	1.396	4.803	3.91E-003	0.2785	4.26E-003	0.3851	9.38E-002	19.06
5	4.48E-014	6.00E-011	0.2677	4.293	5.26E-004	0.2555	6.04E-004	0.3542	8.98E-003	19.05
6	1.28E-015	6.00E-011	6.96E-002	3.928	9.14E-005	0.2344	1.10E-004	0.3257	1.92E-003	19.05
7	6.10E-016	6.00E-011	2.12E-002	3.592	1.96E-005	0.2151	2.37E-005	0.2995	4.19E-004	19.04
8	5.15E-016	6.00E-011	7.81E-003	3.284	5.21E-006	0.1975	6.80E-006	0.2755	1.22E-004	19.04
9	5.09E-016	6.00E-011	3.67E-003	3.003	1.75E-006	0.1812	1.75E-006	0.2534	3.72E-005	19.04
10	5.05E-016	6.00E-011	2.12E-003	2.747	7.31E-007	0.1664	1.22E-006	0.2331	1.19E-005	19.03
11	5.27E-016	6.00E-011	1.36E-003	2.512	3.74E-007	0.1527	7.09E-007	0.2145	4.03E-006	19.03
12	5.02E-016	6.00E-011	9.04E-004	2.298	2.16E-007	0.1402	4.50E-007	0.1973	1.53E-006	19.03

Table 6.2: Convergence tests for ENDGame3D with and without vertical molecular viscosity and diffusion. A simulation is performed for 1 day with 12 iterations for each 30 minute time-step. The top boundary is set at 180 km, and $\alpha = 0.52$. The residuals are output at each iteration, and their rate of decrease illustrates the rate of convergence of the solver. For reference, 4 iterations is usually used, but here, more iterations are used to analyse the rate of convergence.

6.10 Summary

In this chapter, vertical molecular viscosity and diffusion is included in ENDGame3D in a fully-coupled way to the dynamics. The real challenge in this work was in formulating a completely new solution method to include vertical molecular viscosity and diffusion. This involved utilising a columnwise Jacobi iteration to be able to neglect terms in neighbouring columns from the one currently being considered. A few additional, reasonable approximations were also needed to obtain a heptadiagonal matrix system that can easily be inverted and solved. Scale analyses were performed to verify that the additional assumptions made were reasonable. When back-substituting to obtain the other variable increments, more tridiagonal problems must be solved to obtain Θ', u' and v', but the back-substitution to obtain the other variables is trivial.

The scheme still performs remarkably well compared to the original formulation in 3D. With a small amount of off-centring ($\alpha = 0.52$), the viscous scheme is able to remain stable for 10 days subject to the baroclinic wave test with a top model boundary set up to 270 km, whereas the inviscid scheme requires $\alpha = 0.6$ to get the top model boundary above 200 km. The other results shown in this chapter are just a confirmation that the viscous scheme is behaving as expected: the vertical molecular viscosity and diffusion has very little impact in the lower atmosphere, but prevents the excessive growth of wave amplitudes above 130 km.

Chapter 7

Conclusions

7.1 Summary

The results of the stability tests performed in section 3.4 confirmed the need for the development of ENDGame to be able to remain stable with high top boundaries, to improve the accuracy of the dissipation of fast acoustic waves and to introduce physical effects that are more important in the thermosphere.

The ray-tracing experiments performed in chapter 4 provided insight into how waves propagate differently depending on whether they are governed by the analytical or numerical governing equations. From this, it was possible to see the strong damping effect that molecular viscosity and diffusion have in the thermosphere.

The next aim was therefore to include a vertical molecular viscosity and diffusion in ENDGame1D in chapter 5. It is a realistic physical damping mechanism that has a significant effect in the thermosphere. When it is combined with a small amount of off-centring, vertical molecular viscosity and diffusion allows the top boundary of ENDGame1D to be able to be lifted to the top of the thermosphere when dealing with realistic density perturbations and acoustic waves.

After this, vertical molecular viscosity and diffusion was included in ENDGame3D in chapter 6, which added complexity due to the new interactions between the vertical diffusion and the horizontal components of the governing equations. This improved ENDGame's stability greatly with higher top model boundaries when subjected to the baroclinic wave test.

7.2 Future Research

The beginnings of a non-hydrostatic whole-atmosphere dynamical core that includes vertical molecular viscosity and diffusion have been developed in this thesis. It does not yet model a complex thermosphere, but it is able to stand up with a complex troposphere that generates baroclinic waves. More improvements can be made to further improve its accuracy and stability when simulating the whole atmosphere.

- ENDGame3D should be tested for its response to thermospheric forcing.
- Only vertical diffusion has been included in this work, but horizontal diffusion becomes significant above an altitude of 440 km. These terms would need to be included fully implicitly in time, which would involve further significant development to the numerical solver.
- Molecular viscosity and diffusive separation of multiple gas species has not been considered in this thesis, but its inclusion would improve ENDGame's accuracy. Above altitudes of 120 km, turbulent mixing is no longer a dominant factor, and the atmosphere strictly ought not to be treated as well mixed above this height. Therefore, individual constituent transport should be represented by separate governing equations.
- Ion drag refers to the effect of collisions of charged particles (ions) and other gas species, which becomes important in the thermosphere [Akmaev, 2011]. While molecular viscosity and diffusion are the dominant gravity wave damping mechanisms in the thermosphere, exceeding the effects of ion friction by several orders of magnitude, its effects are not completely negligible and seem to become significant at an altitude just below 100 km [Medvedev *et al.* , 2017].
- There may be further developments that can be made to the physics and chemistry in ENDGame and the UM, and the feasibility of incorporating new processes in ENDGame can be verified by first testing them in ENDGame1D.

As well as a number of potential developments to consider related to the ENDGame dynamical core, more practical applications of this work within the Met Office could also be considered:

- The implicit implementation of vertical molecular viscosity and diffusion could be developed and included within the dynamical core in the Met Office UM, as opposed to the stand-alone version used for the results obtained in this thesis.
- The sponge layer currently incorporated in the operational version of the UM could be replaced with vertical molecular viscosity and diffusion above 130 km.
- The Met Office is already developing a dynamical core, GungHo, for its next generation model: LFRic. The implicit implementation of vertical molecular viscosity and diffusion should be carried forward to these too.
- The whole atmosphere model could be developed for use in an operational capacity in space weather forecasting.

Appendix A

ENDGame1D Formulation

In this appendix, the equations that ENDGame solves in order to simulate the fluid dynamics of the atmosphere are derived. To begin with, only the vertical component of the governing equations is considered so that they can be applied to the one-dimensional (1D) vertical column version of ENDGame: ENDGame1D. ENDGame1D is heavily based on the full three-dimensional version of ENDGame for which detailed documentation already exists [Wood *et al.* , 2014a].

A reference list of all notation that is used throughout this thesis can be found in the Mathematical Notation section.

A.1 Continuous equations

For the sake of setting up the dynamical core, the Earth's atmosphere can be thought of very simply as a body of gas subjected to heating and cooling from solar energy and other sources, being absorbed, emitted and reabsorbed at rates that vary in time and space. These variations in temperature then cause changes in pressure and density, which drives winds and changes velocities. A more detailed view could be considered by including the presence of different states of water, surface emissions and chemical reactions. The way that the gas responds to this heating and cooling can be described by Newton's second law of motion, together with the first law of thermodynamics and conservation of mass: the *governing equations* [Batchelor, 2000]. These governing equations for ENDGame1D are presented in this section.

First, consider Newton's second law applied to fluid motion expressed as the vector form of the Navier-Stokes *momentum conservation equation*,

$$\frac{D\boldsymbol{u}}{Dt} + 2\boldsymbol{\Omega} \times \boldsymbol{u} = -\frac{\boldsymbol{\nabla} p}{\rho} - \boldsymbol{g} + \boldsymbol{S}^{\boldsymbol{u}}, \tag{A.1}$$

based on the Navier-Stokes equation of motion found in Batchelor [2000]. From this, the 1D version can later be extracted. Here,

$$\frac{D}{Dt} \equiv \frac{\partial}{\partial t} + \boldsymbol{u} \cdot \boldsymbol{\nabla}, \tag{A.2}$$

is the *material derivative* (also referred to as the *Lagrangian derivative* or the *substance derivative*). $\boldsymbol{u} = (u, v, w)$ is the *velocity vector*, so the $D\boldsymbol{u}/Dt$ term represents the rate of change of velocity as it moves along the trajectory of a Lagrangian parcel of air. Next, $\boldsymbol{\Omega} = (\Omega_1, \Omega_2, \Omega_3)$ is Earth's rotation vector, and so $2\boldsymbol{\Omega} \times \boldsymbol{u}$ represents the planet's *Coriolis forces.*

On the right hand side, p represents *pressure* and ρ represents *density*, so the $-\boldsymbol{\nabla}p/\rho$ term represents the *pressure gradient.* The next term, $-\boldsymbol{g}$ is the *apparent gravitational vector*: the sum of actual gravity and the centrifugal force. This may also be expressed in terms of the *geopotential* Φ, which is defined by $\boldsymbol{g} = \boldsymbol{\nabla}\Phi$.

Lastly, the *source term* $\boldsymbol{S^u}$ represents the effects of *physical parametrisations* on $\boldsymbol{u}$ [Wood *et al.* , 2014b]: processes that are difficult to resolve and are of too small a scale compared to the model's resolution to be represented in the dynamical core (e.g. radiation and chemistry cannot be represented by the Navier-Stokes equations, and must be represented by separate models). Regardless, they do have some effect on the equations. The source term also includes physical processes that are not currently included in the momentum equation, such as ion drag, molecular viscosity and diffusion, or the inter-species drag term when multiple gas species are included.

In ENDGame1D, the pressure gradient term is set up so that the properties of different gas species may be considered. *Mixing ratios* m_X are the ratio of the mass of some gas species X to the mass of *dry air*: air that does not contain water vapour, and ρ_X is the density of the gas species X. These two quantities are related as $\rho_X \equiv m_X \rho_d$, where the subscript d indicates dry quantities. The *total density* is then given by

$$\rho \equiv \rho_d \left(1 + \sum_{X=v,cl,cf,\ldots} m_X \right), \tag{A.3}$$

where it is assumed that cloud liquid (cl) and cloud frozen (cf) and other (rain, graupel, etc) water species have the same velocity as the dry air (d) and water vapour (v) [Wood *et al.* , 2014b]. Also, C_{pd} is the *specific heat capacity at constant pressure for dry air*, and C_{vd} is the *specific heat capacity at constant volume for dry air.* Note that R_d is the *gas constant per unit mass for dry air*, $\kappa_d \equiv R_d/C_{pd}$, and $R_d \equiv \kappa_d C_{pd} \equiv C_{pd} - C_{vd}$. Then the *Exner pressure* Π is given by

$$\Pi \equiv \left(\frac{p}{p_e}\right)^{\kappa_d}, \tag{A.4}$$

[Vallis, 2006], where p_e is the equilibrium pressure. Π is the pressure variable that is used in place of p in ENDGame1D.

Now, the equation for the pressure gradient for multiple gas species is derived. For an ideal gas, the usual form of the *equation of state*, i.e. the ideal gas law, is

$$p = R\rho T, \tag{A.5}$$

where T denotes *temperature*. In a mixture of gases, each gas has a partial pressure, and the total pressure of an ideal gas mixture is simply the sum of the partial pressures of each individual ideal gas in the mixture. Here, group all non-dry quantities together with the water vapour subscript (v), as liquid and ice produce a negligible contribution to p [Wood *et al.* , 2014a], and assume that the ideal gas law applies for both the dry and moist components of the mixture. Therefore, using the total density (A.3) with the ideal gas law (A.5), gives

$$\begin{aligned} p &= \big[R_d\rho_d + R_v(\rho_d m_v)\big]T \\ &= \left[R_d\rho_d\left(1 + \frac{m_v}{\epsilon}\right)\right]T, \end{aligned} \tag{A.6}$$

where $\epsilon \equiv R_d/R_v$. Now, the *virtual temperature* T_v may be constructed as follows:

$$T_v \equiv T\left(1 + \frac{m_v}{\epsilon}\right), \tag{A.7}$$

which is the temperature needed to satisfy the ideal gas law for the dry quantities ρ_d and R_d. Next consider the relation between temperature, Exner pressure and the *potential temperature* Θ: $\Pi \equiv T/\Theta$. In conjunction with the virtual temperature T_v, this gives the following equation for the *virtual potential temperature* Θ_{vd}:

$$\Theta_{vd} = \frac{T_v}{\Pi} = T_v\left(\frac{p_e}{p}\right)^{\kappa_d}. \tag{A.8}$$

Equation (A.4) for the Exner pressure can be rearranged to get

$$p = p_e\Pi^{1/\kappa_d}. \tag{A.9}$$

Now the equation of state (A.5) is rearranged and the dry quantities R_d, ρ_d and the virtual temperature T_v are used to derive a new equation of state as follows:

$$\rho_d = \frac{p}{R_d T_v} = \frac{p_e \Pi^{1/\kappa_d}}{R_d T_v} = \frac{p_e \Pi^{1/\kappa_d}}{R_d \Theta_{vd} \Pi}, \tag{A.10}$$

so the equation of state is now given by

$$\boxed{\rho_d = \left(\frac{p_e}{R_d}\right) \frac{\Pi^{\frac{1-\kappa_d}{\kappa_d}}}{\Theta_{vd}}.} \tag{A.11}$$

Now a new pressure gradient term for the momentum equation (A.1) can be obtained in terms of the Exner pressure Π. Substituting for p using the expression for the Exner pressure (A.9), using the total density equation (A.3), the equation of state (A.11), and the relation $\kappa_d \equiv R_d / C_{pd}$, gives the following expression for the pressure gradient:

$$-\frac{\boldsymbol{\nabla} p}{\rho} = -\frac{C_{pd}\Theta_{vd}}{\left(1 + \sum_{X=v,cl,cf,\ldots} m_X\right)} \boldsymbol{\nabla}\Pi. \tag{A.12}$$

With this new pressure gradient term, a new vector form for the Navier-Stokes momentum conservation equation is obtained:

$$\frac{D\boldsymbol{u}}{Dt} + 2\boldsymbol{\Omega} \times \boldsymbol{u} = -\frac{C_{pd}\Theta_{vd}}{\left(1 + \sum_{X=v,cl,cf,\ldots} m_X\right)} \boldsymbol{\nabla}\Pi - \boldsymbol{g} + \boldsymbol{S}^{\boldsymbol{u}}. \tag{A.13}$$

The momentum equation for ENDGame1D can be extracted from its vector form (A.13). Note that the vertical component of $2\boldsymbol{\Omega} \times \boldsymbol{u}$ is given by $2(\Omega_1 v - \Omega_2 u)$, where u and v are the horizontal components of the velocity vector $\boldsymbol{u} = (u, v, w)$, and where w is the vertical component of $\boldsymbol{u}$. Hence, the vertical component of the momentum equation is as follows:

$$\frac{Dw}{Dt} + 2(\Omega_1 v - \Omega_2 u) = -\frac{C_{pd}\Theta_{vd}}{\left(1 + \sum_{X=v,cl,cf,\ldots} m_X\right)} \frac{\partial \Pi}{\partial r} - g + S^w, \tag{A.14}$$

where in 1D,

$$\frac{D}{Dt} = \frac{\partial}{\partial t} + w\frac{\partial}{\partial r}.$$

In ENDGame1D, further simplifications will be made to the momentum equation. Note that the parts that are removed may be re-introduced later in future experiments. All terms that contain the horizontal velocities u and v will be neglected, and a dry atmosphere will be considered, neglecting terms that include the mixing ratio. The spherical height coordinate r is used in order to preserve the distinction between the gradient ($\boldsymbol{\nabla}$) and divergence ($\boldsymbol{\nabla}\cdot$) operators. The subscripts v and d are removed for clarity, so that $T_v = T$, $\Theta_{vd} = \Theta$ and $C_{pd} = C_p$. With these changes, the momentum equation becomes:

$$\boxed{\frac{Dw}{Dt} + C_p\Theta\frac{\partial\Pi}{\partial r} + \frac{\partial\Phi}{\partial r} = S^w.} \tag{A.15}$$

The equation for the *first law of thermodynamics* in 3D is unchanged from Wood *et al.* [2014a], and is as follows:

$$\frac{D\Theta_{vd}}{Dt} = S^{\Theta_{vd}}. \tag{A.16}$$

In ENDGame1D, the source term and the subscripts v and d are neglected, leaving:

$$\boxed{\frac{D\Theta}{Dt} = 0.} \tag{A.17}$$

The vector form of the Navier-Stokes *mass conservation equation*, or *continuity equation*, is given by

$$\frac{D\rho_d}{Dt} + \rho_d\boldsymbol{\nabla}\cdot\boldsymbol{u} = 0, \tag{A.18}$$

[Wood *et al.* , 2014b]. The continuity equation in 1D is also unchanged: considering only the vertical part of the vector form of the continuity equation (A.18) and neglecting the subscript d, so that $\rho_d = \rho$, gives

$$\boxed{\frac{D\rho}{Dt} + \frac{\rho}{r^2}\frac{\partial(r^2 w)}{\partial r} = 0.} \tag{A.19}$$

The vector form of the *kinematic equation* is included in anticipation of the semi-Lagrangian discretisation, and is given by

$$\frac{D\boldsymbol{r}}{Dt} = \boldsymbol{u}, \tag{A.20}$$

where $\boldsymbol{r} = (r, \theta, \phi)$ is the *position vector* [Wood *et al.* , 2014b]. The vertical component of the kinematic equation (A.20) is given by

$$\boxed{\frac{Dr}{Dt} = w.} \tag{A.21}$$

The set of simplified continuous governing equations: (A.15), (A.17), (A.19), and (A.21) together with the equation of state (A.11) form the basis of ENDGame1D.

A.2 Semi-implicit semi-Lagrangian discretisation

The governing equations found in appendix A.1 are theoretically able to provide all of the information about the motion of the gas in the Earth's atmosphere. However, they are not solvable analytically and must be solved numerically. In order to set up a scheme that is able to achieve this, the equations are discretised over relatively large time-steps and grid spaces.

With *semi-Lagrangian* (SL) schemes, the material derivative is discretised as follows (for some arbitrary $\varphi(r)$):

$$\frac{D\varphi}{Dt} = \frac{\varphi^{(n+1)} - \varphi_D^{(n)}}{\Delta t} = f\left[\varphi_D^{(n)}, \varphi^{(n+1)}\right], \tag{A.22}$$

where $\varphi_D^{(n)}$ denotes the variable φ evaluated explicitly at the current time-step n, and at the *departure point* r_D corresponding to the position r, given by

$$r_D = r - \int_t^{t+\Delta t} w\Delta t, \tag{A.23}$$

(appendix A.4 covers how to obtain r and w for the departure point) and $\varphi^{(n+1)}$ denotes the variable φ evaluated implicitly at the next time-step $n+1$ and position r. The approximation is not made at a fixed point in space, but works by tracing back along the trajectory of a parcel of air, and evaluating its properties at the departure point by interpolation. ENDGame uses cubic-Lagrange interpolation [Wood *et al.* , 2014b] (this technique is detailed in Press *et al.* [1993]).

As shown in Figure A.1, $\varphi^{(n+1)}$ is evaluated at the new time-step at position r, where $r = r_k$ for some grid level k, and $\varphi_D^{(n)}$ is evaluated at the current time-step and at the corresponding departure point r_D. The grid in a SL scheme is therefore a grid of arrival points of Lagrangian particles/ parcels of air. This method's downside is that the quantity being transported is not exactly conserved because accuracy is lost in the interpolation performed in order to obtain r_D.

The remaining terms of the governing equations (i.e. not D/Dt terms: terms that are not associated with transport of parcels of air) describe the various wavelike motions of the atmosphere, including planetary waves, gravity waves and acoustic waves. Some of these have a more significant effect than others, but they all need to be well handled by the numerical scheme. Acoustic waves, for example, play a very small role in the behaviour of the weather and climate, but they are also the

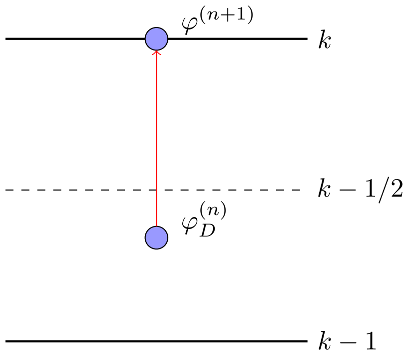

Figure A.1: Illustration of a semi-Lagrangian scheme: an arbitrary variable φ is evaluated at the departure point D at time-step n, and evaluated at level k at time-step $n+1$.

fastest type of propagating wave, and if they were modelled fully explicitly, it would greatly increase the time it takes for the simulation to run.

This problem is dealt with by using a *semi-implicit* (SI) scheme. This involves averaging each term over the time-step. This technique allows the stable simulation of all of the waves without being restricted to very small time-steps [Wood *et al.* , 2014b]. The drawback however, is that while slow low frequency waves (like gravity waves) are handled accurately enough, the fast high frequency acoustic waves end up being damped by the implicit part of the scheme (This effect is explained and described in detail in section 3.3). The SI scheme controls the amount of damping of high frequency through off-centring.

The *semi-implicit semi-Lagrangian* (SISL) discretisation of some equation:

$$\frac{D\varphi}{Dt} = f(r), \tag{A.24}$$

looks like

$$\frac{\varphi^{(n+1)} - \varphi_D^{(n)}}{\Delta t} = \alpha f\left[\varphi^{(n+1)}\right] + \beta f\left[\varphi_D^{(n)}\right], \tag{A.25}$$

where $\beta \equiv 1 - \alpha$ [Payne, 2008]. The *implicitness parameter*: $\alpha \in [0, 1]$ is used to set the implicitness of the scheme and control damping. The scheme is unstable for $\alpha \in [0.0, 0.5)$. For $\alpha = 0.5$, the scheme has no damping, and for larger values of $\alpha \in (0.5, 1.0]$, the scheme becomes more stable, but has an increased amount of artificial damping, and at $\alpha = 1$, the scheme is fully implicit-in-time [Payne, 2008].

Using this combination of techniques, the simplified assumed continuous governing equations (A.15), (A.17), (A.19), and (A.21) can be discretised to obtain a

SISL scheme. First define a variable Ψ as follows:

$$\Psi \equiv -\left(C_p\Theta\frac{\partial\Pi}{\partial r}+\frac{\partial\Phi}{\partial r}\right). \tag{A.26}$$

Next, replace the source term in the momentum equation (A.15) with the *Rayleigh damping term* applied only to the vertical velocity w, $-\nu(r)$ [Klemp *et al.* , 2008], and include a *hydrostatic switch* δ_V [Wood *et al.* , 2014b]. Setting $\delta_V \equiv 1$ makes the (deep-atmosphere) equation set fully non-hydrostatic, whereas setting $\delta_V \equiv 0$ reduces it to the quasi-hydrostatic set. Note that ENDGame1D does not include the Rayleigh damping term, so terms including ν are omitted from the code. With these additions, and by using Ψ (A.26), the momentum equation (A.15) becomes

$$\delta_V\frac{Dw}{Dt}-\Psi=-\nu w. \tag{A.27}$$

Note that the Rayleigh damping term νw is discretised fully implicitly-in-time, while the rest of the terms are handled semi-implicitly. Discretising the momentum equation (A.27) gives

$$\delta_V\left[\frac{w^{(n+1)}-w_D^{(n)}}{\Delta t}\right]-\left[\alpha_w\Psi^{(n+1)}+\beta_w\Psi_D^{(n)}\right]=-\nu w^{(n+1)}. \tag{A.28}$$

Rearranging this gives the discretised momentum equation:

$$\boxed{\left[(\delta_V+\nu\Delta t)w-\alpha_w\Delta t\Psi\right]^{(n+1)}=\left(\delta_V w+\beta_w\Delta t\Psi\right)_D^{(n)}.} \tag{A.29}$$

Next, the thermodynamic equation (A.17), the continuity equation (A.19) and the kinematic equation (A.21) are all discretised to obtain the following:

$$\frac{\Theta^{(n+1)}-\Theta_D^{(n)}}{\Delta t}=0, \tag{A.30}$$

$$\frac{\rho^{(n+1)}-\rho_D^{(n)}}{\Delta t}+\left\{\alpha_\rho\left[\frac{\rho}{r^2}\frac{\partial(r^2w)}{\partial r}\right]^{(n+1)}+\beta_\rho\left[\frac{\rho}{r^2}\frac{\partial(r^2w)}{\partial r}\right]_D^{(n)}\right\}=0, \tag{A.31}$$

$$\frac{r^{(n+1)}-r_D^{(n)}}{\Delta t}-\alpha_z w^{(n+1)}-\beta_z w_D^{(n)}=0. \tag{A.32}$$

Rearranging these gives the discretised thermodynamic, continuity and kinematic equations given by (A.33), (A.34) and (A.35), respectively. Equations (A.29), (A.34) and (A.35) all have separate implicitness parameters: α_w, α_ρ and α_z. However, the linear stability analysis of the SISL discretisation of the fully-compressible equations performed by Payne [2008] shows that the scheme is stable as long as each of $\alpha_w, \alpha_\rho, \alpha_z \in (0.5, 1.0]$, and they do not necessarily have to be equal.

$$\boxed{\begin{aligned} \Theta^{(n+1)} &= \Theta_D^{(n)}, \\ \left\{\rho\left[1+\frac{\alpha_\rho \Delta t}{r^2}\frac{\partial(r^2 w)}{\partial r}\right]\right\}^{(n+1)} &= \left\{\rho\left[1-\frac{\beta_\rho \Delta t}{r^2}\frac{\partial(r^2 w)}{\partial r}\right]\right\}_D^{(n)}, \\ \big(r-\alpha_z \Delta t w\big)^{(n+1)} &= \big(r+\beta_z \Delta t w\big)_D^{(n)}. \end{aligned}} \qquad \begin{aligned} &(A.33) \\ &(A.34) \\ &(A.35) \end{aligned}$$

A.3 Spatial discretisation

In this section, the discretisation of the state equation and terms that include spatial derivatives ($\partial/\partial r$) within the continuous governing equations, are considered. In ENDGame1D, the atmosphere has N vertical levels, which are illustrated in Figure A.2. A staggered grid is implemented using the Charney-Phillips configuration of model variables [Holdaway *et al.* , 2012], so that for $k \in [1, N]$, the values of scalar variables are stored at levels k (Π, ρ and Φ), and for $k \in [0, N]$ values of momentum and thermodynamic variables are stored at levels $k+1/2$ (w, Θ and Ψ). Note that k-levels are referred to as ρ-levels, and $k+1/2$ -levels as w-levels. Staggering the grid in this way allows derivatives to be approximated more accurately, as they will use values that are only one level apart in their calculations.

First, the state equation (A.11) is rearranged and discretised to obtain an equation for the Exner pressure at level k, Π_k:

$$\boxed{\Pi_k = \left(\frac{R}{p_e}\rho_k \overline{\Theta}_k^r\right)^{\frac{\kappa}{1-\kappa}},} \tag{A.36}$$

where $\overline{(\cdots)}^r$ denotes linear interpolation in the vertical r direction, so an estimated value of Θ at level k: $\overline{\Theta}_k^\rho$ is given by

$$\overline{\Theta}_k^r = a_k \Theta_{k+1/2} + b_k \Theta_{k-1/2}, \tag{A.37}$$

where

$$a_k = \frac{r_k - r_{k-1/2}}{r_{k+1/2} - r_{k-1/2}}, \; b_k = \frac{r_{k+1/2} - r_k}{r_{k+1/2} - r_{k-1/2}}, \tag{A.38}$$

are weighting terms for linearly interpolating an estimated value of a variable at ρ-level k between the levels $k-1/2$ and $k+1/2$: the two adjacent w-levels.

Next, the Ψ equation (A.26), which comes from the momentum equation, is

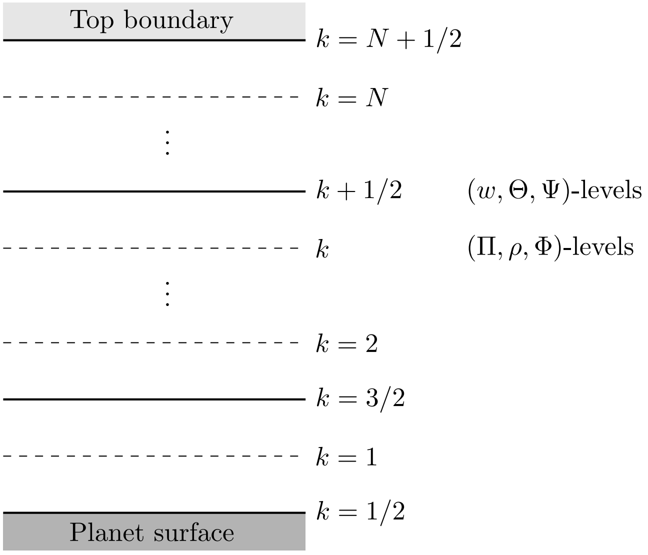

Figure A.2: Illustration of the vertical staggered grid used in ENDGame1D, using the Charney-Phillips configuration of model variables.

discretised as follows:

$$\Psi_{k+1/2} = -C_p \Theta_{k+1/2} \frac{\Pi_{k+1} - \Pi_k}{\Delta r_{k+1/2}} - \frac{\Phi_{k+1} - \Phi_k}{\Delta r_{k+1/2}}, \tag{A.39}$$

where $\Delta r_{k+1/2} = r_{k+1} - r_k$.

Lastly, the following expression from the continuity equation is discretised:

$$\left[\frac{1}{r^2}\frac{\partial(r^2 w)}{\partial r}\right]_k = \frac{1}{r_k^2}\frac{(r^2 w)_{k+1/2} - (r^2 w)_{k-1/2}}{\Delta r_k}. \tag{A.40}$$

In order to prevent the atmosphere in the simulation from disappearing into space or into the ground, the following boundary conditions are used to ensure that there is no vertical flow at the base or the top boundary of the model:

$$w_{1/2} = 0, \;\; w_{N+1/2} = 0. \tag{A.41}$$

A.4 Finding departure points

Earlier, the departure point (A.23) was defined as $r_D = r - w\Delta t$. It was noted how approximations of material derivatives are not made at fixed points in space, but along the trajectory of the parcel of air, evaluated at the departure point. In this section, the procedure for obtaining these departure points is discussed.

As w varies in space and time, departure points are computed approximately by an iterative method. Rearranging the discretised kinematic equation (A.35) gives:

$$r_D^{(n)} = r - \left[\alpha_z \Delta t w^{(n+1)} + \beta_z \Delta t w_D^{(n)}\right], \qquad \text{(A.42)}$$

where r is written rather than $r^{(n+1)}$, since the grid in an SL scheme is a grid of arrival points of Lagrangian parcels of air and does not change with time; whereas the departure points may change at each time-step. However, ρ values are stored on k-levels rather than $k + 1/2$ -levels, so for ρ and Π levels, the rearranged discrete kinematic equation (A.42) is modified slightly:

$$r_D^{(n)} = r - \left[\alpha_z \Delta t \overline{w}^{(n+1)} + \beta_z \Delta t \overline{w}_D^{(n)}\right], \qquad \text{(A.43)}$$

where $\overline{w}$ is the *linear interpolation* of w from w-levels to ρ-levels. The rearranged discrete kinematic equations (A.42) and (A.43) must be solved iteratively to find departure points for w and Θ, since $w_D^{(n)} = w[r_D^{(n)}]$ by the kinematic equation (A.21). The superscript $\cdot^{(d)}$ denotes the *departure* point iteration count. Then

$$r_D^{(n,d+1)} = r - \left[\alpha_z \Delta t w^{(n+1)} + \beta_z \Delta t w_D^{(n,d)}\right]. \qquad \text{(A.44)}$$

To find the next departure point estimate $r_D^{(n,d+1)}$ using (A.44), the value for w at the current departure point estimate $r_D^{(n,d)}$ needs to be evaluated using $w_D^{(n,d)} = w[r_D^{(n,d)}]$.

This process is illustrated in Figure A.3. Consider estimating the location of the departure point of a Lagrangian parcel of air arriving at grid level $k + 1/2$, so $r = r_{k+1/2}$. Find some $j \in [0, N]$ such that the new estimate for the location of the departure point $r_D^{(n,d)}$ lies somewhere between $r_{j-1/2}$ and $r_{j+1/2}$. If the departure point is higher (lower) than the arrival point, then *search* above (below) the arrival level $k + 1/2$, by checking whether $r_{j-1/2} < r_D^{(n,d)} < r_{j+1/2}$ for each interval.

Once an appropriate j has been obtained, use linear interpolation to approximate a value for $w_D^{(n,d)}$ as follows:

$$w[r_D^{(n,d)}] = w(r_{j+1/2}) \left[\frac{r_D^{(n,d)} - r_{j-1/2}}{\Delta r_j}\right] + w(r_{j-1/2}) \left[\frac{r_{j+1/2} - r_D^{(n,d)}}{\Delta r_j}\right]. \qquad \text{(A.45)}$$

This value for $w_D^{(n,d)}$ can then be substituted into equation (A.44) to find the next estimation for the departure point $r_D^{(n,d+1)}$.

The techniques for locating departure points $r_D^{(n,d+1)}$ described in this section must be used to interpolate the variables on the right hand side of the time discretised governing equations (A.29), (A.33), (A.34) and (A.35), to the departure

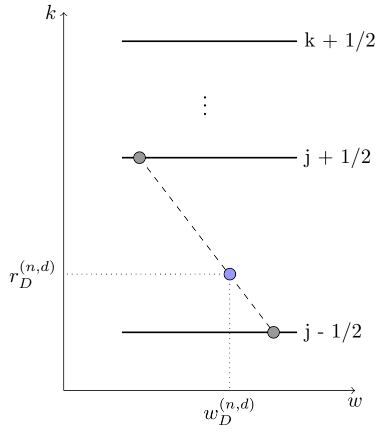

Figure A.3: Illustration of the linear interpolation technique being used to estimate $w_D^{(n,d)}$. First, search for the levels $j+1/2$ and $j-1/2$ which bracket the departure point (these are not necessarily close to the arrival level $k+1/2$). Then perform a linear interpolation for w between these two levels to find an approximation for w at the departure point.

points $r_D^{(n)}$. In ENDGame, this is done by cubic Lagrange interpolation with linear interpolation at the top and bottom intervals, or constant extrapolation if needed.

A.5 Residual estimation

The discretised governing equations (A.29), (A.33) and (A.34), together with the departure point equation (A.44), form a coupled non-linear system. The approximate Newton's method can be used to find successively better approximations for the solution to this system of equations. This system will not be satisfied exactly after any number of iterations, so the equations will have some *residuals* R_w, R_Θ and R_ρ respectively, which should be as small as possible.

Newton's method for finding successively better roots to a function in multiple dimensions, i.e. to estimate $\boldsymbol{x}$ such that $\boldsymbol{f}(\boldsymbol{x}) = \boldsymbol{0}$, may be written:

$$\boldsymbol{0} \approx \boldsymbol{f}[\boldsymbol{x}^{(l+1)}] = \boldsymbol{f}[\boldsymbol{x}^{(l)}] + \frac{\partial \boldsymbol{f}}{\partial \boldsymbol{x}}(\boldsymbol{x}'), \tag{A.46}$$

where $\boldsymbol{x}' = \boldsymbol{x}^{(l+1)} - \boldsymbol{x}^{(l)}$ is an *increment* of $\boldsymbol{x}$, and $\partial \boldsymbol{f}/\partial \boldsymbol{x}$ is the *Jacobian matrix* of $\boldsymbol{f}$. It is possible to approximate $\partial \boldsymbol{f}/\partial \boldsymbol{x}$. In a similar way in ENDGame1D, the system to be solved is $(R_\rho, R_\Theta, R_w) = \boldsymbol{0}$.

The residuals are found by setting the superscript (l) to indicate a *best guess* for the $n+1$ term after l iterations, and then putting all terms in the discretised governing equations (A.29), (A.33) and (A.34) on the right hand side so that the residual is left on the left hand side. The residuals are as follows:

$$R_w = \left(\delta_V w + \beta_w \Delta t \Psi\right)_D^{(n)} - \left[(\delta_V + \nu \Delta t) w - \alpha_w \Delta t \Psi\right]^{(l)}, \tag{A.47}$$

$$R_\Theta = \Theta_D^{(n)} - \Theta^{(l)}, \tag{A.48}$$

$$R_\rho = \left\{\rho\left[1 - \frac{\beta_\rho \Delta t}{r^2}\frac{\partial(r^2 w)}{\partial r}\right]\right\}_D^{(n)} - \left\{\rho\left[1 + \frac{\alpha_\rho \Delta t}{r^2}\frac{\partial(r^2 w)}{\partial r}\right]\right\}^{(l)}. \tag{A.49}$$

When computing R_ρ, note that the latest estimate for w should be used. Using the rearranged discrete kinematic equation (A.42), and setting the (l) superscript to indicate the *best guess* for the $n+1$ term after l iterations, the following is obtained:

$$r - (\alpha_z \Delta t w)^{(l)} = (r + \beta_z \Delta t w)_D^{(n)}, \tag{A.50}$$

noting that $r^{(n+1)} = r$ since the grid of arrival points in the SL scheme is fixed.

Increments w', Θ' and ρ' are to be found that will reduce the residuals R_w, R_Θ and R_ρ. To begin with, in a similar way to Newton's method (A.46), the system to be solved is given by (A.51), where $\partial_\varphi \equiv \partial/\partial_\varphi$.

$$\begin{bmatrix} R_w \\ R_\Theta \\ R_\rho \end{bmatrix} = - \begin{bmatrix} \partial_w R_w & \partial_\Theta R_w & \partial_\rho R_w \\ \partial_w R_\Theta & \partial_\Theta R_\Theta & \partial_\rho R_\Theta \\ \partial_w R_\rho & \partial_\Theta R_\rho & \partial_\rho R_\rho \end{bmatrix} \begin{bmatrix} w' \\ \Theta' \\ \rho' \end{bmatrix} \tag{A.51}$$

Next, the Jacobian of the right-hand side of (A.51) is approximated. First, rearranging the discrete kinematic equation (A.50) gives

$$r_D^{(n)} = r - \left[\alpha_z \Delta t w^{(l)} + \beta_z \Delta t w_D^{(n)}\right]. \tag{A.52}$$

Differentiating this with respect to w gives

$$\frac{\partial r_D^{(n)}}{\partial w} = -\alpha_z \Delta t. \tag{A.53}$$

Using this, it is then useful to note that

$$\begin{aligned} \frac{\partial[\ldots]_D^{(n)}}{\partial w} &= \frac{\partial[\ldots]_D^{(n)}}{\partial r}\frac{\partial r_D^{(n)}}{\partial w} \\ &= -\alpha_z \Delta t \frac{\partial[\ldots]_D^{(n)}}{\partial r}. \end{aligned} \tag{A.54}$$

It is also useful to linearise the equation of state (A.36). Taking logarithms of both sides, and rearranging the result gives the following:

$$\frac{1-\kappa}{\kappa}\log \Pi_k = \log\left(\frac{R}{p_e}\right) + \log \rho_k + \log \overline{\Theta}_k. \tag{A.55}$$

Next, express Π_k, ρ_k and $\overline{\Theta}_k$ as the sums of their reference profiles and their increments. The *reference profile* of a variable is denoted by $\cdot^*$. This is calculated once per step and is expected to remain a good approximation. Therefore, $\Pi_k = \Pi^* + \Pi'$, $\rho_k = \rho^* + \rho'$ and $\overline{\Theta}_k^r = \overline{\Theta^*}^r + \overline{\Theta'}^r$. Taking the Taylor expansion of the logarithm of a variable x_k, where $x_k = \Pi_k$, ρ_k or $\overline{\Theta}_k^r$, about its reference profile, and then linearising it, gives the following:

$$\log x_k = \log x^* + \frac{x'}{x^*} + \mathcal{O}(x'^{\,2}) \approx \log x^* + \frac{x'}{x^*}. \tag{A.56}$$

The reference profiles Π^*, ρ^* and $\overline{\Theta^*}^r$ satisfy the log of the state equation (A.55), so

$$\frac{1-\kappa}{\kappa}\log \Pi^* = \log\left(\frac{R}{p_e}\right) + \log\rho^* + \log\overline{\Theta^*}^r. \tag{A.57}$$

Then this may be used with the linearised Taylor series expansions of $\log \Pi_k$, $\log \rho_k$ and $\log \overline{\Theta}_k^r$ as for the linearised Taylor expansion of x_k (A.56), to get the linearised equation of state from equation (A.55) as follows:

$$\boxed{\frac{1-\kappa}{\kappa}\frac{\Pi'}{\Pi^*} \approx \frac{\rho'}{\rho^*} + \frac{\overline{\Theta'}^r}{\Theta^*}.} \tag{A.58}$$

The Jacobian on the right-hand side of equation (A.51) can now be approximated to obtain expressions for the residuals R_w, R_Θ and R_ρ. To calculate the entries of the Jacobian by differentiating the residual equations (A.47), (A.48) and (A.49), the following approximations are made:

- Approximate $\partial[\ldots]_D^{(n)}/\partial r$ in the ρ equation by $\partial\rho^*/\partial r$, and $\partial[\ldots]_D^{(n)}/\partial r$ in the Θ equation by $\partial\Theta^*/\partial r$.
- Neglect $\partial[\ldots]_D^{(n)}/\partial r$ in the w equation by taking $w^* = 0$.
- Approximate $\rho^{(l)}$ by ρ^* in $\partial R_\rho/\partial w$.
- Use the approximation that $\alpha_\rho \approx \alpha_z = \alpha$.
- Use equations (A.54) and the linearised equation of state (A.58).

Using these approximations leads to the residual equations (A.59)-(A.61).

$$\boxed{\begin{aligned}
R_w &\approx (\delta_V + \nu\Delta t)w' + \alpha_w \Delta t\, C_p\left(\Theta^*\frac{\partial\Pi'}{\partial r} + \frac{\partial\Pi^*}{\partial r}\Theta'\right), && \text{(A.59)}\\
R_\Theta &\approx \Theta' + \alpha_z\Delta t\frac{\overline{\partial\Theta^*}^r}{\partial r}\,w', && \text{(A.60)}\\
R_\rho &\approx \rho' + \frac{\alpha\Delta t}{r^2}\frac{\partial}{\partial r}\left(r^2\overline{\rho^*}^r w'\right). && \text{(A.61)}
\end{aligned}}$$

A.6 Constructing the boundary value problem

The linearised state equation (A.58) and the approximated residuals (A.59), (A.60) and (A.61), form four sets of equations with four sets of unknowns ρ', Θ', w' and Π'. It would be preferable to obtain from these a single set of equations for a single set of unknowns in the form of an value that can be solved.

Begin by rearranging the Θ residual approximation R_Θ (A.60), as follows:

$$\Theta' = R_\Theta - \alpha_z \Delta t \frac{\overline{\partial \Theta^*}^r}{\partial r} w'. \tag{A.62}$$

Then substitute equation (A.62) for Θ' into the w residual approximation (A.59):

$$\left[(\delta_V + \nu\Delta t) - \alpha_w \alpha_z \Delta t^2 C_p \frac{\overline{\partial \Theta^*}^r}{\partial r}\frac{\partial \Pi^*}{\partial r}\right] w' + \alpha_w \Delta t\, C_p \Theta^* \frac{\partial \Pi'}{\partial r} = R_w - \alpha_w \Delta t\, C_p \frac{\partial \Pi^*}{\partial r} R_\Theta. \tag{A.63}$$

The expression of equation (A.63) can be abbreviated by defining the coefficient B:

$$B \equiv \left[(\delta_V + \nu\Delta t) - \alpha_w \alpha_z \Delta t^2 C_p \frac{\overline{\partial \Theta^*}^r}{\partial r}\frac{\partial \Pi^*}{\partial r}\right]^{-1}, \tag{A.64}$$

and the operator D_1 (for an arbitrary X):

$$D_1(X) \equiv B \alpha_w \Delta t\, C_p \Theta^* \frac{\partial X}{\partial r}. \tag{A.65}$$

Then equation (A.63) becomes:

$$w' + D_1(\Pi') = B R_w - D_1(\Pi^*) R_\Theta. \tag{A.66}$$

Now take $\overline{(\text{A.62})/\Theta^*}^r$ and substitute it for $\overline{\Theta'/\Theta^*}^r$ in equation (A.58):

$$\frac{1-\kappa}{\kappa}\frac{\Pi'}{\Pi^*} = \frac{\rho'}{\rho^*} - \alpha_z \Delta t \overline{\frac{1}{\Theta^*}\frac{\overline{\partial \Theta^*}^r}{\partial r} w'}^r + \overline{\frac{R_\Theta}{\Theta^*}}^r. \tag{A.67}$$

Next, ρ'/ρ^* is eliminated in equation (A.67) by taking (A.67) - (A.61)/ρ^*:

$$\frac{1-\kappa}{\kappa}\frac{\Pi'}{\Pi^*} = \frac{R_\rho}{\rho^*} - \frac{\alpha\Delta t}{\rho^*}\frac{1}{r^2}\frac{\partial}{\partial r}\left(r^2 \overline{\rho^*}^r w'\right) - \alpha_z \Delta t \overline{\frac{1}{\Theta^*}\frac{\overline{\partial \Theta^*}^r}{\partial r} w'}^r + \overline{\frac{R_\Theta}{\Theta^*}}^r. \tag{A.68}$$

Equation (A.68) can be abbreviated by defining the operator D_2 (for an arbitrary X):

$$D_2(X) \equiv \frac{\alpha\Delta t}{\rho^*}\frac{1}{r^2}\frac{\partial}{\partial r}\left(r^2 \overline{\rho^*}^r X\right) + \alpha_z \Delta t \overline{\frac{1}{\Theta^*}\frac{\overline{\partial \Theta^*}^r}{\partial r} X}^r. \tag{A.69}$$

Then equation (A.68) becomes:

$$\frac{1-\kappa}{\kappa}\frac{\Pi'}{\Pi^*} + D_2(w') = \frac{R_\rho}{\rho^*} + \frac{\overline{R_\Theta}^r}{\Theta^*}\,. \tag{A.70}$$

Lastly, w' can be eliminated from equation (A.70) by taking D_2 [(A.66)] - (A.70):

$$\boxed{D_2[D_1(\Pi')] - \frac{1-\kappa}{\kappa}\frac{\Pi'}{\Pi^*} = D_2[BR_w - D_1(\Pi^*)R_\Theta] - \frac{R_\rho}{\rho^*} - \frac{\overline{R_\Theta}^r}{\Theta^*}\,.} \tag{A.71}$$

Equation (A.71) is an boundary value problem that can be solved to obtain Π': this process is detailed in appendix A.7. After this, the value for Π' is back-substituted into equation (A.66) to obtain w'. The value for w' is then back-substituted into equation (A.62) to obtain Θ', and ρ' can be obtained by substituting the values for Π' and Θ' into equation (A.58).

A.7 Solving the boundary value problem

In this section, the boundary value problem for Π' (A.71) is turned into a form suitable for programming in the ENDGame1D code: by setting it up as a tridiagonal system of equations and solving it. Each term of equation (A.71) must be expanded and discretised in order to set up a matrix system of equations that can be solved. This is done in the following subsection.

First, note that divergence operators need to be calculated slightly differently to gradient operators. The divergence measures the volume density of the outward flux of a vector field from a volume around a given point. Despite being a 1D column dynamical core, volumes and areas are introduced in order to calculate the divergence. The divergence is as follows:

$$\left.\frac{1}{r^2}\frac{\partial[r^2(\cdots)]}{\partial r}\right|_k = \frac{A_{k+1/2}(\cdots)_{k+1/2} - A_{k-1/2}(\cdots)_{k-1/2}}{V_k} \tag{A.72}$$

The *column* in ENDGame1D will *spread out* with height so that the volume of each cell gets larger with altitude. An illustration of a grid cell in ENDGame1D is given in Figure A.4. Let V_k denote the volume of the current grid cell, $A_{k-1/2}$ denote the area of the bottom cell face of grid cell k, and $A_{k+1/2}$ denote the area of the top cell face. The lowest grid cell can just have a unit area: $A_{1/2} = 1$.

Next, recall from appendix A.3 that Π' is stored at ρ-levels. Therefore, the operator $D_1(\Pi')$ is stored at w-levels and $D_2[D_1(\Pi')]$ is stored at ρ-levels. B is

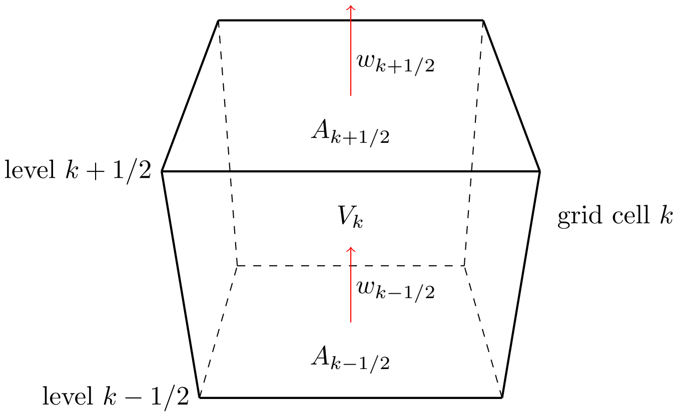

Figure A.4: Illustration of a grid cell in ENDGame1D, with the volume of the cell given by V_k, the area of the bottom cell face given by $A_{k-1/2}$ and of the top cell face given by $A_{k+1/2}$, and the velocities at the bottom and the top of the cell given by $w_{k-1/2}$ and $w_{k+1/2}$ respectively.

included in the expression for D_1, so B is calculated at w-levels. The $\partial\Theta^*/\partial r$ and $\partial\Pi^*/\partial r$ terms in the expression for B (A.64) are calculated at w-levels as follows:

$$\left.\frac{\partial \Pi^*}{\partial r}\right|_{k+1/2} = \frac{\Pi^*_{k+1} - \Pi^*_k}{\Delta r_{k+1/2}}, \quad \left.\frac{\partial \overline{\Theta^*}^r}{\partial r}\right|_{k+1/2} = \frac{\overline{\Theta^*}^r_{k+1} - \overline{\Theta^*}^r_k}{\Delta r_{k+1/2}}. \tag{A.73}$$

With these expressions, the B coefficient can be easily calculated.

A.7.1 Discretise the left-hand side of the boundary value problem

To obtain the discretised form of the left-hand side of (A.71), first obtain discretised forms of the operators D_1 and D_2, given by equations (A.65) and (A.69) respectively.

The discretised form of D_1 is as follows for $k \in [2, N-1]$:

$$D_1(X)_{k-\frac{1}{2}} = B_{k-\frac{1}{2}} \alpha_w \Delta t \, C_p \Theta^*_{k-\frac{1}{2}} \frac{X_k - X_{k-1}}{\Delta r_{k-\frac{1}{2}}}. \tag{A.74}$$

Define the following function:

$$F^{(1)}_{k-\frac{1}{2}} = \alpha_w \Delta t \left.\frac{B\Theta^*}{\Delta r}\right|_{k-\frac{1}{2}}. \tag{A.75}$$

Define the operators $D^{(1)}_{i-\frac{1}{2},j}$ to be the coefficients of X_j for $D^{(1)}(X)_{i-\frac{1}{2}}$ in order to abbreviate $D_1(X)_k$ so that it becomes:

$$D_1(X)_{k-\frac{1}{2}} = D^{(1)}_{k-\frac{1}{2},k} X_k + D^{(1)}_{k-\frac{1}{2},k-1} X_{k-1}, \tag{A.76}$$

where the $D^{(1)}_{i-\frac{1}{2},j}$ operators are:

$$D^{(1)}_{k-\frac{1}{2},k} = F^{(1)}_{k-\frac{1}{2}}, \quad D^{(1)}_{k-\frac{1}{2},k-1} = -F^{(1)}_{k-\frac{1}{2}}. \tag{A.77}$$

The operator D_2 (A.69) can be rewritten using linear interpolation to ensure that all terms are at ρ-levels, and multiplying through by ρ^*:

$$\rho^* D_2(X) \equiv \alpha\Delta t\rho^* \frac{1}{r^2}\frac{\partial(r^2 X)}{\partial r} + \alpha\Delta t\overline{\frac{\partial\rho^*}{\partial r}X}^r + \alpha_z\Delta t\rho^*\overline{\frac{1}{\Theta^*}\overline{\frac{\partial\Theta^*}{\partial r}}^r X}^r . \tag{A.78}$$

Note here that the first two terms of (A.78) cannot be combined using the product rule because the two terms come from different grid levels.

Each term of $\rho^* D_2$ (A.78) is now expanded fully for $k \in [1, N]$. First, expand the divergence part of $\rho^* D_2[D_1(\Pi')]$ as follows:

$$\left[\alpha\Delta t\rho^*\frac{1}{r^2}\frac{\partial}{\partial r}(r^2 X)\right]_k = \alpha\Delta t\rho^*_k\frac{(AX)_{k+1/2} - (AX)_{k-1/2}}{V_k}. \tag{A.79}$$

As X is stored at w-levels, the second term of $\rho^* D_2[X]$ (A.78) is linearly interpolated:

$$\alpha\Delta t\left(\overline{\frac{\partial\rho^*}{\partial r}X}^r\right)_k = \alpha\Delta t\overline{\frac{\partial\rho^*}{\partial r}}^r\Bigg|_k\Big[a_k X_{k+1/2} + b_k X_{k-1/2}\Big]. \tag{A.80}$$

where a_k and b_k (A.38) are coefficients for linearly interpolating values from w-levels to ρ-levels. The last term of $\rho^* D_2$ (A.78) is linearly interpolated in the same way:

$$\alpha_z\Delta t\left(\rho^*\overline{\frac{1}{\Theta^*}\overline{\frac{\partial\Theta^*}{\partial r}}^r X}^r\right)_k = \alpha_z\Delta t\left(\rho^*\overline{\frac{1}{\Theta^*}\overline{\frac{\partial\Theta^*}{\partial r}}^r}^r\right)_k\Big[a_k X_{k+1/2} + b_k X_{k-1/2}\Big]. \tag{A.81}$$

Next, define the following functions in order to find expressions for the coefficients of $X_{k-1/2}$ and $X_{k+1/2}$ for $\rho^* D_2(X)_k$ (A.69):

$$F_k^{D1} \equiv \alpha\Delta t\frac{\rho^*}{V}\bigg|_k, \quad F_k^{D2} = \alpha\Delta t\overline{\frac{\partial\rho^*}{\partial r}}^r\bigg|_k, \quad F_k^{D3} = \alpha_z\Delta t\frac{\rho^*}{\overline{\Theta^*}^r}\bigg|_k, \tag{A.82}$$

so that $D_2(X)_k$ may be written as follows for $k \in [1, N]$:

$$D_2(X)_k = D^{(2)}_{k,k-\frac{1}{2}}X_{k-\frac{1}{2}} + D^{(2)}_{k,k+\frac{1}{2}}X_{k+\frac{1}{2}}, \tag{A.83}$$

where:

$$D^{(2)}_{k,k-\frac{1}{2}} = -F_k^{D1}A_{k-\frac{1}{2}} + F_k^{D2}b_k + F_k^{D3}b_k\overline{\frac{\partial\Theta^*}{\partial r}}^r\bigg|_{k-\frac{1}{2}}, \tag{A.84}$$

$$D^{(2)}_{k,k+\frac{1}{2}} = F_k^{D1}A_{k+\frac{1}{2}} + F_k^{D2}a_k + F_k^{D3}a_k\overline{\frac{\partial\Theta^*}{\partial r}}^r\bigg|_{k+\frac{1}{2}}. \tag{A.85}$$

Using the $D^{(1)}_{i-1/2,j}$ and $D^{(2)}_{i,j-1/2}$ coefficients, the discretised form of the left-hand side of the boundary value problem for Π' (A.71) is as follows for $k \in [2, N-1]$ (the boundary conditions at $k = 1, N$ are found later):

$$\left\{\rho^* D_2[D_1(\Pi')]\right\}_k - \frac{1-\kappa}{\kappa}\frac{\rho^*\Pi'}{\Pi^*}\bigg|_k = D^{(2)}_{k,k-\frac{1}{2}}\left[D^{(1)}_{k-\frac{1}{2},k-1}\Pi'_{k-1} + D^{(1)}_{k-\frac{1}{2},k}\Pi'_k\right] + D^{(2)}_{k,k+\frac{1}{2}}\left[D^{(1)}_{k+\frac{1}{2},k}\Pi'_k + D^{(1)}_{k+\frac{1}{2},k+1}\Pi'_{k+1}\right] - \frac{1-\kappa}{\kappa}\frac{\rho^*\Pi'}{\Pi^*}\bigg|_k . \tag{A.86}$$

A combination of the D_1 and D_2 operators may then be built up out of the $D^{(1)}_{i-1/2,j}$ and $D^{(2)}_{i,j-1/2}$ coefficients as follows:

$$D^{(2,1)}_{k,k-1} = D^{(2)}_{k,k-\frac{1}{2}} D^{(1)}_{k-\frac{1}{2},k-1}, \tag{A.87}$$

$$D^{(2,1)}_{k,k} = D^{(2)}_{k,k-\frac{1}{2}} D^{(1)}_{k-\frac{1}{2},k} - \frac{1-\kappa}{\kappa}\frac{\rho^*}{\Pi^*}\bigg|_k + D^{(2)}_{k,k+\frac{1}{2}} D^{(1)}_{k+\frac{1}{2},k}, \tag{A.88}$$

$$D^{(2,1)}_{k,k+1} = D^{(2)}_{k,k+\frac{1}{2}} D^{(1)}_{k+\frac{1}{2},k+1}, \tag{A.89}$$

in order to abbreviate this so that it becomes:

$$\left\{\rho^* D_2[D_1(\Pi')]\right\}_k - \frac{1-\kappa}{\kappa}\frac{\rho^*\Pi'}{\Pi^*}\bigg|_k = D^{(2,1)}_{k,k-1}\Pi'_{k-1} + D^{(2,1)}_{k,k}\Pi'_k + D^{(2,1)}_{k,k+1}\Pi'_{k+1}. \tag{A.90}$$

A.7.2 Construct a matrix system to solve

By adding together all of the discretised terms on the left-hand side of the boundary value problem for Π' (A.71) and using the above abbreviations, a tridiagonal system of equations is obtained for $k \in [2, N-1]$:

$$D^{2,1}_{k,k-1}\Pi'_{k-1} + D^{(2,1)}_{k,k}\Pi'_k + D^{(k,k+1)}\Pi'_{k+1} = R^{\Pi}_k, \tag{A.91}$$

where R^{Π}_k is the right-hand side of equation (A.71) at level k.

A.7.3 Boundary conditions

The boundary conditions on Π' at the surface and the top of the atmosphere at levels 1 and N respectively need to be included.

At levels 1 and N, there are no vertical velocities at the boundaries (A.41): so $w_{1/2} = 0$ and $w_{N+1/2} = 0$, and hence $w'_{1/2} = 0$ and $w'_{N+1/2} = 0$. Evaluating the R_Θ equation (A.60) at levels 1 and N gives $\Theta'_{1/2} = \Theta'_{N+1/2} = 0$. Using these boundary conditions in the R_w equation (A.59) gives $\Theta^*_{1/2}\,\frac{\partial\Pi'}{\partial r}\big|_{1/2} = \Theta^*_{N+1/2}\,\frac{\partial\Pi'}{\partial r}\big|_{N+1/2} = 0$. Lastly, including these boundary conditions in (A.63) leaves $\frac{\partial\Pi^*}{\partial r}\big|_{1/2} = \frac{\partial\Pi^*}{\partial r}\big|_{N+1/2} = 0$. Hence using (A.64), it can be obtained that $B_{1/2} = B_{N+1/2} = 0$, and so $D_1(\Pi')_{1/2} = 0$, and $D_1(\Pi)_{N+1/2} = 0$. This means that at level 1, the $D^{(2,1)}_{1,0}$ term vanishes from equation (A.91) and the $D^{(1)}_{1/2,1}$ term vanishes from $D^{(2,1)}_{1,1}$, leaving:

$$D^{(2,1)\dagger}_{1,1} = -\frac{1-\kappa}{\kappa}\frac{\rho^*}{\Pi^*}\bigg|_1 + D^{(2)}_{1,\frac{3}{2}}D^{(1)}_{\frac{3}{2},1}. \tag{A.92}$$

At level N, the $D^{(2,1)}_{N,N+1}$ term, and the $D^{(1)}_{N+1/2,N}$ term from $D^{(2,1)}_{N,N}$ both vanish, leaving:

$$D^{(2,1)\dagger}_{N,N} = D^{(2)}_{N,N-\frac{1}{2}}D^{(1)}_{N-\frac{1}{2},N} - \frac{1-\kappa}{\kappa}\frac{\rho^*}{\Pi^*}\bigg|_N. \tag{A.93}$$

A.7.4 Tridiagonal system

With the boundary conditions, the matrix definitions given by (A.95) and (A.96) can be made, where $\boldsymbol{R}$ denotes the vector of values of the right hand side of the boundary value problem for Π' (A.71) at each k-level. Now the boundary value problem for Π' (A.71) can be written as a tridiagonal system of equations for Π'_k as follows:

$$\boxed{\boldsymbol{D\Pi} = \boldsymbol{R}.} \tag{A.94}$$

This can be solved using a standard tridiagonal system solver [Press *et al.* , 1993].

$$\boldsymbol{D} = \begin{bmatrix} D^{(2,1)\dagger}_{1,1} & D^{(2,1)}_{1,2} & 0 & \cdots & & 0 \\ D^{(2,1)}_{2,1} & D^{(2,1)}_{2,2} & D^{(2,3)} & & & \vdots \\ \ddots & \ddots & \ddots & & & \\ & D^{(2,1)}_{k,k-1} & D^{(2,1)}_{k,k} & D^{(2,1)}_{k,k+1} & & \\ & & \ddots & \ddots & \ddots & \\ \vdots & & & D^{(2,1)}_{N-1,N-2} & D^{(2,1)}_{N-1,N-1} & D^{(2,1)}_{N-1,N} \\ 0 & \cdots & & 0 & D^{(2,1)}_{N,N-1} & D^{(2,1)\dagger}_{N,N} \end{bmatrix} \tag{A.95}$$

$$\boldsymbol{\Pi} \equiv \begin{bmatrix} \Pi'_1 \\ \Pi'_2 \\ \vdots \\ \Pi'_k \\ \vdots \\ \Pi'_{N-1} \\ \Pi'_N \end{bmatrix}, \quad \boldsymbol{R} \equiv \begin{bmatrix} R^{\Pi}_1 \\ R^{\Pi}_2 \\ \vdots \\ R^{\Pi}_k \\ \vdots \\ R^{\Pi}_{N-1} \\ R^{\Pi}_N \end{bmatrix}, \tag{A.96}$$

Appendix B

ENDGame code details

In this appendix, some details are given about aspects of the ENDGame code that are not necessarily new, but the details of which are useful to understand.

B.1 Initialising the dynamical core

Within the initialisation subroutine in ENDGame, a few equations are used for setting up the Exner pressure Π and potential temperature Θ, that do not depend on other variables ρ and w. These are not derived in the formulation of ENDGame1D in appendix A, so these equations are derived in this section.

Begin with the simplified continuous momentum equation (A.15). Neglect the source term and Dw/Dt, since $t = 0$ when the dynamical core is being initialised. This leaves

$$C_p \Theta \frac{\partial \Pi}{\partial r} + \frac{\partial \Phi}{\partial r} = 0. \tag{B.1}$$

Using the relation $\Theta\Pi = T$, this becomes

$$0 = C_p T \frac{\partial}{\partial r}(\log \Pi) + \frac{\partial \Phi}{\partial r}, \tag{B.2}$$

This can now be integrated with respect to r as follows:

$$C_p T \log \Pi = -\Phi + C_p T \log \Pi_0, \tag{B.3}$$

where $C_p T \log \Pi_0$ is a constant of integration. This can be rearranged to obtain the following expression for the Exner pressure:

$$\Pi = \Pi_0 \exp\left(- \frac{\Phi}{C_p T} \right). \tag{B.4}$$

At level $k = 1$, take $\Pi \equiv (p/p_e)^\kappa$, and p_e to be the equilibrium pressure. Then the reference Exner pressure near the surface can be taken to be $\Pi_0 \approx 1$. This gives an equation for the initial Exner pressure at level $k = 1$:

$$\Pi_{k=1} \approx \exp\bigg(- \frac{\Phi}{C_p T} \bigg). \tag{B.5}$$

For calculating the Exner pressure Π at higher levels, return to the momentum equation (B.1), multiply through by ∂z and rearrange as follows:

$$\partial \Pi = -\frac{\partial \Phi}{C_p \Theta}. \tag{B.6}$$

From this, the difference in Exner pressure between two levels k and $k+1$ can be seen to be given by

$$\Pi_{k+1} \ = \Pi_k - \frac{\Phi_{k+1} - \Phi_k}{C_p \Theta}. \tag{B.7}$$

Using $\Pi_{k=1}$ (B.5) as a starting point, the rest of the initial Π_k can be found.

Using the definition for the potential temperature: $\Theta = T(p_e/p)^\kappa$, the potential temperature Θ at the surface is then given to be

$$\Theta_{k=1/2} = T_{k=1/2}, \tag{B.8}$$

where $T_{k=1/2}$ can be obtained from the initial temperature profile. The potential temperature variable Θ is stored at levels $k + 1/2$ for $k \in [0, N]$. Therefore, at k-levels, $\overline{\Theta}$ is approximated using linear interpolation as in (A.37):

$$\overline{\Theta}_k = a\Theta_{k+1/2} + b\Theta_{k-1/2}. \tag{B.9}$$

Using the relation $\Theta = T/\Pi$, an expression for $\overline{\Theta}$ at k-levels can be obtained using the Exner pressures that have already been found: $\overline{\Theta}_k = T_k/\Pi_k$. Then by rearranging the expression for $\overline{\Theta}_k$ (B.9), an equation for Θ at the next $(k + 1/2)$-level is:

$$\Theta_{k+1/2} = \frac{T_k/\Pi_k - b_k \Theta_{k-1/2}}{a_k}. \tag{B.10}$$

Using $\Theta_{k=1/2}$ (B.8) as a starting point, the rest of the initial $\Theta_{k+1/2}$ can be found.

B.2 Inner and outer loops

ENDGame is set up to solve a non-linear system of equations at each time-step. A quasi-Newton method is used to solve the elliptic problem, as in section A.6. If the elliptic problem for Π' (A.71) had been solved perfectly, then its residuals would all be 0. However, an analytic solution to the problem cannot be found, so the residuals are non-zero and so increments are found that make these residuals smaller.

For a normal Newton method, residuals would be found, and then increments would be obtained to reduce these residuals, before repeating these processes in a loop. However, a complication arises due to the location of some of the terms needed to calculate the residual being at the departure points: calculating departure points is a very expensive process, especially in ENDGame3D, so it would be preferable to avoid doing this at every time-step.

For this reason, the *step* subroutine in ENDGame is set up with an outer loop and an inner loop within the outer loop. In the outer loop, the departure points and trajectories are recalculated and the values for all of the right-hand side terms of the discretised governing equations (A.29), (A.33), (A.34), are cubic-Lagrange interpolated to these new departure points. Then in the inner loop, best guesses for the left-hand side of the discretised governing equations are found, and so the residuals (A.47), (A.48), (A.49), are able to be calculated. The elliptic problem is then set up and solved, and the increments that reduce the residuals can be found. Then the current state of the system is updated by adding these increments to all of the variables, and are able to be used in the next loop or time-step.

The inner loop can be run multiple times independently of the outer loop. However, the inner loop does not include a recalculation of the departure points and the residuals. Recalculating the residual without updating the departure points would give the wrong answer for the residual, and hence the inner loop would end up trying to correct the wrong estimate of the error.

Instead, the residuals are estimated as if the departure points had been updated at the end of the inner loop. As R_Θ is calculated in the outer loop, rather than leaving it unchanged, it is assumed that the first loop will have done a reasonable job of updating all of the variables so that the residual will be close to zero, i.e. $R_\Theta \approx 0$. Also, the right-hand side term of the discretised continuity equation (A.34) is corrected to simulate the vertical change in departure points. Let D_1 be the original departure point and D_2 be the estimate of the new departure point. The Lagrangian parcel of air moves at velocity w, and its density will change by $\partial[\rho^*]^{(n)}_{D_2}/\partial w$ between the two departure points. Then using equation (A.54):

$$\begin{aligned}\left\{\rho\left[1-\frac{\beta_\rho \Delta t}{r^2}\frac{\partial(r^2 w)}{\partial r}\right]\right\}^{(n)}_{D_2} &\approx \left\{\rho\left[1-\frac{\beta_\rho \Delta t}{r^2}\frac{\partial(r^2 w)}{\partial r}\right]\right\}^{(n)}_{D_1} + w\frac{\partial[\rho^*]^{(n)}_{D_2}}{\partial w} \\ &\approx \left\{\rho\left[1-\frac{\beta_\rho \Delta t}{r^2}\frac{\partial(r^2 w)}{\partial r}\right]\right\}^{(n)}_{D_1} - \alpha_z \Delta t w\frac{\partial \rho^*}{\partial r}. \qquad \text{(B.11)}\end{aligned}$$

Top model boundary height $r - r_{\text{Earth}}$ (km)	Vertical grid level number N	Flattening Parameter φ
100	100	1
	50	15
200	200	1
	100	5
300	150	1
400	200	1
500	250	1
600	300	1

Table B.1: This table shows the minimum value for the flattening parameter φ such that the grid level thickness found using (B.12) is always less than $H_\rho/2$ found using (B.13), so that there are at least two grid levels per scale height, allowing the accurate calculation of vertical derivatives.

This can be used to get a reasonable estimate for what R_ρ would be, whilst avoiding the expensive departure point calculation that is left in the outer loop. This option can be used to reduce integration times, although the simulations in this thesis have only used four outer loops for each time-step with no extra inner loops.

B.3 Grid settings in ENDGame3D

ENDGame3D currently uses the following equation for the grid level height at level k:

$$r_{k-1/2} = r_{N+\frac{1}{2}} \frac{\{\varphi[(k-\frac{1}{2})/(N+\frac{1}{2})]^2 + 1\}^{1/2} - 1}{(\varphi+1)^{1/2} - 1} \tag{B.12}$$

[Ullrich *et al.* , 2013] where φ is a *flattening parameter* that controls the resolution near the surface. When vertically extending ENDGame3D, the number of vertical levels N has the potential to get so large that ENDGame may become computationally expensive to run. It is prudent therefore to reduce the number of vertical grid levels in the upper atmosphere if there is no detriment to model accuracy.

Here the *density scale height*:

$$\frac{1}{H_\rho} = \frac{RT(r)}{g(r)}, \tag{B.13}$$

is calculated at all altitudes, where $T = T(r)$ is given by the USSA temperature profile and $g = g(r)$ is a function of height. It should be noted that in ENDGame3D, R is set to be the gas constant for dry air, while in reality, it varies depending on the constituent gas species of the atmosphere at that altitude. The inclusion of multiple gas species is outside the scope of this project.

Table B.1 shows the minimum flattening parameter φ required in order to ensure that there are at least two grid level heights per scale height.

Appendix C

Acoustic Waves

In this appendix, the dispersion relation for acoustic waves is derived, and other theoretical properties of acoustic waves are considered.

C.1 1D Acoustic wave theory

Consider the Navier-Stokes momentum equation (A.1), but take the vertical component and neglect the Coriolis, gravity and viscosity terms, to obtain

$$\frac{Dw}{Dt} = \frac{\partial w}{\partial t} + w\frac{\partial w}{\partial r} = -\frac{1}{\rho}\frac{\partial p}{\partial r}. \tag{C.1}$$

The continuity equation (A.19) can be expressed as follows by using the material derivative (A.2) and the product rule:

$$0 = \frac{\partial \rho}{\partial t} + \frac{1}{r^2}\frac{\partial (r^2 w \rho)}{\partial r}. \tag{C.2}$$

These equations will later be linearised. First, split the *current state* of the system (w, p, ρ, Θ) into a *basic state* $(w_0, p_0, \rho_0, \Theta_0)$, that satisfies both of the governing equations (C.1) and (C.2), and a *small perturbation term* (w', p', ρ', Θ'), as follows:

$$w = w_0 + w',\ p = p_0 + p',\ \rho = \rho_0 + \rho',\ \Theta = \Theta_0 + \Theta'.$$

The perturbation terms are small, so products of perturbation terms may be neglected. Assuming that the system is initialised from a resting basic state, then $w_0 = 0$, and so $w = w'$. Here, the isothermal approximation is used, so that $T = T_0$, where T_0 is a constant. In this case, let $p = p(\rho, \Theta)$, where Θ is given by

$$\Theta = T\left(\frac{p_e}{p}\right)^{\kappa}, \tag{C.3}$$

where $\kappa \equiv R/C_p$. Equation (C.3) for Θ may be rearranged to obtain the equation of state for this system. First, rearrange the ideal gas law (A.5) to obtain:

$$\left(\frac{p}{p_e}\right)^{1-\kappa} = \frac{R\Theta\rho}{p_e}. \tag{C.4}$$

Next take the logarithm of both sides of (C.4), expand and differentiate to obtain:

$$(1-\kappa)\frac{1}{p}dp = \frac{1}{\Theta}d\Theta + \frac{1}{\rho}d\rho. \tag{C.5}$$

Note that as p', ρ' and Θ' are small, then $1/p_0 \approx 1/p$, $1/\rho_0 \approx 1/\rho$ and $1/\Theta_0 \approx 1/\Theta$. Also note that $dp \approx p'$, $d\rho \approx \rho'$ and $d\Theta \approx \Theta'$. Then rearrange (C.5) to get an expression for p':

$$p' \approx \frac{p_0}{1-\kappa}\left(\frac{\Theta'}{\Theta_0} + \frac{\rho'}{\rho_0}\right). \tag{C.6}$$

As an isothermal basic state is assumed, then $T = T_0$, so $T' = 0$, and hence $\Theta' = 0$. Therefore, (C.6) becomes

$$p' \approx \frac{p_0}{1-\kappa}\frac{\rho'}{\rho_0}. \tag{C.7}$$

By using partial differentiation, the assumption that $d\rho \approx \rho'$, and the ideal gas law (A.5), the following expression for $p' = p'(\rho, \Theta)$ may be found:

$$\begin{aligned} p' &\approx \left.\frac{\partial p'}{\partial \rho'}\right|_{\Theta'} d\rho + \left.\frac{\partial p'}{\partial \Theta'}\right|_{\rho'} d\Theta \\ &\approx \frac{p_0}{\rho_0}\frac{1}{1-\kappa}\rho' + 0, \\ &\approx \frac{RT_0}{1-\kappa}\rho'. \end{aligned} \tag{C.8}$$

Note that the speed of the propagation of sound waves is given by

$$c_s^2 = \frac{\partial p}{\partial \rho}, \tag{C.9}$$

Batchelor [2000], and so using the assumptions that $\partial p \approx p'$ and $\partial \rho \approx \rho'$, and p' (C.8), an expression for the speed of sound for acoustic waves can be obtained:

$$c_s^2 \approx \frac{p'}{\rho'} \approx \frac{RT_0}{1-\kappa}, \tag{C.10}$$

For a dry, isothermal atmosphere with a temperature of 250 K, the speed of sound can be found using (C.10) to be approximately $300\,\mathrm{m\,s^{-1}}$. It is worth noting that the speed of sound increases in the thermosphere if the USSA temperature profile initial condition is used, since the temperature increases greatly above an altitude of 100 km when using the USSA temperature profile, as can be seen in Figure 3.1.

The momentum and continuity equations, given by (C.1) and (C.2) respectively, may now be linearised. Linearising the momentum equation (C.1) and using the speed of sound (C.10) gives

$$\rho_0 \frac{\partial w'}{\partial t} + c_s^2 \frac{\partial \rho'}{\partial r} = 0. \tag{C.11}$$

Next, in a similar way, linearise the continuity equation (C.2) so it becomes:

$$\frac{\partial \rho'}{\partial t} + \frac{1}{r^2}\frac{\partial (r^2 \rho_0 w')}{\partial r} = 0. \tag{C.12}$$

So together, equations (C.11) and (C.12) give the linearised governing equations. Eliminate w' by taking $\frac{\partial}{\partial t}$ (C.12) - $\frac{1}{r^2}\frac{\partial}{\partial r}[r^2$(C.11)] and note that the basic state ρ_0 is independent of time, to obtain the acoustic wave equation:

$$0 = \frac{\partial^2 \rho'}{\partial t^2} - \frac{c_s^2}{r^2}\frac{\partial}{\partial r}\left(r^2 \frac{\partial \rho'}{\partial r}\right). \tag{C.13}$$

Wavelike solutions of the acoustic wave equation (C.13) for ρ' are required, that are proportional to $\exp[\mathrm{i}(mr - \omega t)]$, for vertical wavenumber m and frequency ω. Putting a solution of this form into the acoustic wave equation (C.13) gives the dispersion equation for 1D linear acoustic waves:

$$\omega^2 = c_s^2 m^2. \tag{C.14}$$

Using the acoustic wave dispersion relation (C.14), the phase velocity of 1D linear acoustic waves is found to be

$$c_p = \frac{\omega}{m} = c_s, \tag{C.15}$$

and the group velocity of 1D linear acoustic waves is found to be

$$c_g = \frac{\partial \omega}{\partial m} = c_s, \tag{C.16}$$

Salby [1996].

C.2 Growth rate of acoustic waves

In this section, the variation of density and pressure perturbations with altitude are shown, and hence, how waves grow with altitude. This is useful for approximate or order-of-magnitude calculations. Consider the 1D momentum equation (A.15), but consider the case where it has a resting basic state, so $w = 0$, and use $\Theta \equiv T/\Pi$ and it becomes

$$C_pT\frac{\partial}{\partial r}(\log\Pi) = -\frac{\partial\Phi}{\partial r}. \tag{C.17}$$

Next, integrate (C.17) with respect to r, and set the constant of integration to be $C_pT\log\Pi_0$, for some constant reference Exner pressure Π_0, to obtain

$$C_pT\log\Pi = -gr + C_pT\log\Pi_0. \tag{C.18}$$

Rearrange this to obtain an expression for $\log\Pi$:

$$\log\Pi = -\frac{\Phi}{C_pT} + \log\Pi_0. \tag{C.19}$$

Take the exponential of both sides of this equation and use the definition $\kappa \equiv R/C_p$ to get an expression for Π:

$$\Pi = \Pi_0\exp\left(-\frac{\kappa}{H_\rho}r\right), \tag{C.20}$$

where

$$H_\rho = \frac{RT}{g}, \tag{C.21}$$

is the *density scale height*. Now, use the growth rate of Π (C.20) and the definition: $\Theta \equiv T/\Pi$, with the equation of state (A.11) to obtain an expression for ρ:

$$\rho = \left(\frac{p_0}{RT}\right)\Pi_0^{1/\kappa}\exp\left(-\frac{r}{H_\rho}\right). \tag{C.22}$$

The growth rate of density with height can also be expressed as

$$\rho \propto \exp\left(-\frac{r}{H_\rho}\right). \tag{C.23}$$

For quadratic quantities, like the *kinetic energy density* ρu^2, to remain constant following a wave packet, the perturbation terms for velocity w', pressure p' and density ρ' must all vary like

$$\rho_0^{-1/2} \propto \exp\left(\frac{r}{2H_\rho}\right), \tag{C.24}$$

[Salby, 1996].

Appendix D

Ray-Tracing

In this appendix, some extra equations that are needed for implementing the ray-tracing techniques from chapter 4 are detailed. These include techniques for smoothing the temperature profile and finding expressions for its derivatives, and finding expressions for the derivatives of N^2, c_s^2 and Γ.

D.1 Smooth temperature profile

In order for the WKB approximation to be satisfied, the properties of the atmosphere must vary gradually [Gill, 1982], so the background temperature profile should be smooth. The definition of the USSA temperature profile introduced in section (3.2) is piecewise linear up to an altitude of 91 km. Therefore, Hermite cubic interpolation is used near the discontinuities in the temperature profile to obtain a smooth temperature profile for which first and second derivatives can be found [Boor, 1978]. Above 91 km, first and second derivatives for T are also derived.

As $T(z)$ and $T'(z) = \partial T/\partial z$ are known up to 91 km as defined by United States Committee on Extension to the Standard Atmosphere (COESA) [1976], a cubic polynomial can be applied to fit through a number of points z_i for $i \in \{1, 2, \ldots\}$. The position of the points can be changed to alter the amount of smoothing. Let $T_i = T(z_i)$ and $T_i' = T'(z_i)$. Then the *Hermite cubic polynomial* $\widehat{T}$ that passes through (z_i, T_i) and (z_{i+1}, T_{i+1}) with derivative T_i' at z_i and T_{i+1}' at z_{i+1} is:

$$\begin{aligned}\widehat{T}(z) \;&= \frac{(z-z_i)^2}{(z_{i+1}-z_i)^2}\left[\left(T_{i+1}' - \frac{2T_{i+1}}{z_{i+1}-z_i}\right)(z - z_{i+1}) + T_{i+1}\right] \\ &\quad + \frac{(z-z_{i+1})^2}{(z_{i+1}-z_i)^2}\left[\left(T_i' - \frac{2T_i}{z_i - z_{i+1}}\right)(z - z_i) + T_i\right]. \qquad \text{(D.1)}\end{aligned}$$

The first and second derivatives of the Hermite cubic polynomial are as follows:

$$
\begin{aligned}
\widehat{T}'(z) \;=\;& \frac{2(z-z_i)}{(z_{i+1}-z_i)^2}\left[\left(T'_{i+1}-\frac{2T_{i+1}}{z_{i+1}-z_i}\right)(z-z_{i+1})+T_{i+1}\right]+\frac{(z-z_i)^2}{(z_{i+1}-z_i)^2}\left(T'_{i+1}-\frac{2T_{i+1}}{z_{i+1}-z_i}\right)\\
&+\frac{2(z-z_{i+1})}{(z_{i+1}-z_i)^2}\left[\left(T'_i-\frac{2T_i}{z_i-z_{i+1}}\right)(z-z_i)+T_i\right]+\frac{(z-z_{i+1})^2}{(z_{i+1}-z_i)^2}\left(T'_i-\frac{2T_i}{z_i-z_{i+1}}\right), \qquad \text{(D.2)}\\
\widehat{T}''(z) \;=\;& \frac{2}{(z_{i+1}-z_i)^2}\left[\left(T'_{i+1}-\frac{2T_{i+1}}{z_{i+1}-z_i}\right)(z-z_{i+1})+T_{i+1}\right]+\frac{4(z-z_i)}{(z_{i+1}-z_i)^2}\left(T'_{i+1}-\frac{2T_{i+1}}{z_{i+1}-z_i}\right)\\
&+\frac{2}{(z_{i+1}-z_i)^2}\left[\left(T'_i-\frac{2T_i}{z_i-z_{i+1}}\right)(z-z_i)+T_i\right]+\frac{4(z-z_i)}{(z_{i+1}-z_i)^2}\left(T'_i-\frac{2T_i}{z_i-z_{i+1}}\right). \qquad \text{(D.3)}
\end{aligned}
$$

Above 91 km, the temperature profile is defined by a smooth function that can be differentiated to obtain $T'(z)$ and $T''(z)$. For $z \in [91\,\mathrm{km}, 110\,\mathrm{km}]$, $\widehat{T}$ is:

$$
\widehat{T}(z) = T(91\,\mathrm{km}) + A\left[1-\left(\frac{z-91\,\mathrm{km}}{a}\right)^2\right]^{1/2}, \qquad \text{(D.4)}
$$

where $A = -76.3232\,\mathrm{K}$, $a = -19.9429\,\mathrm{km}$, and its derivatives are given by:

$$
\begin{aligned}
\widehat{T}'(z) \;=\;& -\frac{A}{a}\left(\frac{z-91\,\mathrm{km}}{a}\right)\left[1-\left(\frac{z-91\,\mathrm{km}}{a}\right)^2\right]^{-1/2}, \qquad \text{(D.5)}\\
\widehat{T}''(z) \;=\;& -\frac{A}{a^2}\left[1-\left(\frac{z-91\,\mathrm{km}}{a}\right)^2\right]^{-1/2}\left\{1+\left(\frac{z-91\,\mathrm{km}}{a}\right)^2\left[1-\left(\frac{z-91\,\mathrm{km}}{a}\right)^2\right]^{-1}\right\}. \qquad \text{(D.6)}
\end{aligned}
$$

T is linear between 110 km and 120 km, and is smooth at 110 km and 120 km. For $z \in [120\,\mathrm{km}, 1000\,\mathrm{km}]$, $\widehat{T}$ is given by

$$
\widehat{T}(z) \;= T_{\mathrm{exo}} - [T_{\mathrm{exo}} - T(120\,\mathrm{km})]\exp(-\lambda\xi), \qquad \text{(D.7)}
$$

where T_{exo} is the exospheric temperature and

$$
\lambda \;= \frac{12\,\mathrm{K\,km^{-1}}}{T_{\mathrm{exo}} - T(120\,\mathrm{km})}, \quad \xi(z) = \frac{(z-120\,\mathrm{km})(r_E+120\,\mathrm{km})}{r_E+z}, \qquad \text{(D.8)}
$$

where r_E is the radius of the Earth. $\widehat{T}'(z)$ and $\widehat{T}''(z)$ are given by

$$
\begin{aligned}
\widehat{T}'(z) \;=\;& \lambda[T_{\mathrm{exo}} - T(120\,\mathrm{km})]\left(\frac{r_E+120\,\mathrm{km}}{r_E+z}\right)^2\exp(-\lambda\xi), \qquad \text{(D.9)}\\
\widehat{T}''(z) \;=\;& \lambda[T_{\mathrm{exo}} - T(120\,\mathrm{km})]\left(\frac{r_E+120\,\mathrm{km}}{r_E+z}\right)^2\left\{-\frac{2}{r_E+z}-\lambda\left(\frac{r_E+120\,\mathrm{km}}{r_E+z}\right)^2\right\}\exp(-\lambda\xi). \qquad \text{(D.10)}
\end{aligned}
$$

D.2 Terms for $\partial\widehat{\omega}/\partial z$

Equation (4.43) for $\partial\widehat{\omega}/\partial z$ requires expressions for $\partial(N^2)/\partial z$, $\partial(c_s^2)/\partial z$ and $\partial\Gamma/\partial z$. These are found in this section. To begin, the geopotential Φ that accounts for

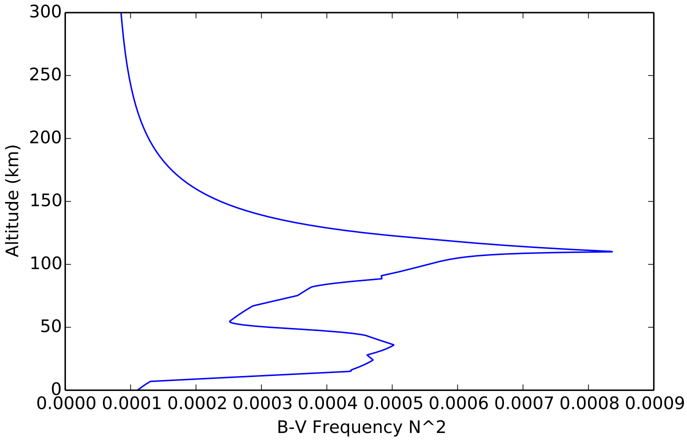

Figure D.1: Brunt Väisälä frequency N^2 at each height calculated using equation (D.16) with the USSA temperature profile.

gravity varying with distance from the Earth's surface, and its derivatives are:

$$\frac{\partial\Phi}{\partial z} = \Phi_z = g\left(\frac{r_E}{r_E+z}\right)^2, \tag{D.11}$$

$$\frac{\partial^2\Phi}{\partial z^2} = \Phi_{zz} = -2g\frac{r_E^2}{(r_E+z)^3}. \tag{D.12}$$

Using the hydrostatic form of the vertical 2D momentum equation (4.8) and equation (A.8) for Θ, the following result can be obtained:

$$\frac{\partial\Pi}{\partial z} = \Pi_z = -\frac{\Phi_z\Pi}{C_pT}, \tag{D.13}$$

$$\frac{1}{\Pi}\frac{\partial^2\Pi}{\partial z^2} = \frac{\Pi_{zz}}{\Pi} = \frac{1}{C_pT}\left(\frac{\Phi_z^2}{C_pT} + \frac{\Phi_zT_z}{T} - \Phi_{zz}\right). \tag{D.14}$$

Using these, new expressions for the Brunt Väisälä frequency N^2 and its derivative can be found:

$$N^2 = \frac{\Phi_z}{\Theta}\frac{\partial\Theta}{\partial z} = \Phi_z\left(\frac{T_z}{T} + \frac{\Phi_z}{C_pT}\right), \tag{D.15}$$

$$\frac{\partial(N^2)}{\partial z} = \Phi_{zz}\left(\frac{T_z}{T} + \frac{2\Phi_z}{C_pT}\right) + \Phi_z\left[\frac{T_{zz}}{T} - \left(\frac{T_z}{T}\right)^2 - \frac{\Phi_zT_z}{C_pT^2}\right]. \tag{D.16}$$

A plot of N^2 against altitude is shown in Figure D.1 to illustrate the peak of N^2 that arises at 110 km. The combination of the low values for T and the large values for $\partial T/\partial z$ that occur around the thermopause between 100 and 110 km cause N^2 to become very large. It should be noted that this is not an artefact of the USSA temperature profile in particular, as similar values for N^2 can be obtained using, for example, the MSIS-90 model [Hedin, 1991].

The derivative of the expression for the speed of sound (C.10) is:

$$\frac{\partial(c_s^2)}{\partial z} = \frac{RT_z}{1-\kappa}. \tag{D.17}$$

The derivative of the inverse height scale Γ (4.26) is:

$$\frac{\partial \Gamma}{\partial z} = \frac{1}{2}\left[\frac{\Phi_{zz}}{c_s^2} - \frac{\Phi_z}{c_s^4}\frac{\partial(c_s^2)}{\partial z} - \frac{1}{\Phi_z}\frac{\partial(N^2)}{\partial z} + \frac{N^2\Phi_{zz}}{\Phi_z^2}\right]. \tag{D.18}$$

D.3 Conservation of frequency along the ray

A useful result that can be obtained from the ray-tracing equations (4.1) and (4.2) is that the frequency ω is conserved along the ray trajectory, i.e. that $D_{\boldsymbol{c}_g}\omega/dt = 0$ provided that $\partial\Omega/\partial t = 0$, i.e. provided the background is steady [Lighthill, 1978]. To show this, first $\partial\omega/\partial x|_z$ and $\partial\omega/\partial z|_x$ are found:

$$\begin{aligned} \left.\frac{\partial \omega}{\partial x}\right|_z &= \frac{\partial\Omega}{\partial k}\frac{\partial k}{\partial x} + \frac{\partial\Omega}{\partial m}\frac{\partial m}{\partial x} + \left.\frac{\partial\Omega}{\partial x}\right|_{k,m}, && \text{(D.19)}\\ \left.\frac{\partial \omega}{\partial z}\right|_x &= \frac{\partial\Omega}{\partial k}\frac{\partial k}{\partial z} + \frac{\partial\Omega}{\partial m}\frac{\partial m}{\partial z} + \left.\frac{\partial\Omega}{\partial z}\right|_{k,m}. && \text{(D.20)} \end{aligned}$$

Equation (4.2) may also be expressed as follows:

$$\begin{aligned} \frac{\partial k}{\partial t} + \boldsymbol{c}_g\cdot\boldsymbol{\nabla}_{\boldsymbol{x}}k &= \frac{\partial k}{\partial t} + \frac{\partial\Omega}{\partial k}\frac{\partial k}{\partial x} + \frac{\partial\Omega}{\partial m}\frac{\partial k}{\partial z} = -\left.\frac{\partial\Omega}{\partial x}\right|_{k,m}, && \text{(D.21)}\\ \frac{\partial m}{\partial t} + \boldsymbol{c}_g\cdot\boldsymbol{\nabla}_{\boldsymbol{x}}m &= \frac{\partial m}{\partial t} + \frac{\partial\Omega}{\partial k}\frac{\partial m}{\partial x} + \frac{\partial\Omega}{\partial m}\frac{\partial m}{\partial z} = -\left.\frac{\partial\Omega}{\partial z}\right|_{k,m}. && \text{(D.22)} \end{aligned}$$

Using these expressions, we can obtain $D_{\boldsymbol{c_g}}\omega/Dt \equiv 0$ as required:

$$\begin{aligned} \frac{D_{\boldsymbol{c_g}}\omega}{Dt} &= \frac{\partial\Omega}{\partial t} + \boldsymbol{c}_g\cdot\boldsymbol{\nabla}_{\boldsymbol{x}}\omega \\ &= \frac{\partial\Omega}{\partial t} + \frac{\partial\Omega}{\partial k}\left.\frac{\partial\omega}{\partial x}\right|_z + \frac{\partial\Omega}{\partial m}\left.\frac{\partial\omega}{\partial z}\right|_x \\ &= 0. && \text{(D.23)} \end{aligned}$$

D.4 The WKB approximation

In section 4.5, some of the experiments performed are outside the limit of WKB theory. In this appendix, the assertion is made and justified that WKB theory can still be used to describe the behaviour of wave propagation outside this limit.

Dingle [1973] discusses the WKB approximation, and states that the accuracy of solutions obtained through this approximation are high when either

1. the wavevector $\boldsymbol{k}$ is slowly varying, or
2. $\boldsymbol{k}$ is large in magnitude.

In section 4.3.4, it is assumed that $\boldsymbol{k}$ varies slowly with height z, but $\boldsymbol{k}$ is not large enough in magnitude for the wavelength to be significantly shorter than the background length scale. To confirm whether changes in the wavenumber and wave amplitude agree with the WKB theory, experiments have been performed to compare the wavenumbers and wave amplitudes produced by the ray-tracing scheme with those obtained in ENDGame1D.

Vertically propagating waves are simulated in ENDGame1D by forcing an oscillation at the bottom boundary. Once it reaches a steady state, the wave amplitudes at each height level i of ENDGame1D from (4.27), accounting for temperature variations, can be recorded as

$$q_i = \rho_0^{1/2}\overline{\Theta}_0^r \Pi'. \tag{D.24}$$

The local wave amplitude q_{0i}, wavenumber m_i and phase ϕ_i can be estimated by fitting a function

$$q_i = q_{0i}\cos(m_i z_i + \phi_i) \tag{D.25}$$

to the data over a set of $2n+1$ grid points near level i ($n = 2$ was found to be sufficient). The fits for q_{0i}, m_i and ϕ_i are found by minimising the mean square error (MSE$_i$) given by

$$\mathrm{MSE}_i = \frac{1}{2N+1}\sum_{j=i-n}^{i+n}\big[q_j - q_{0i}\cos(m_i z_j + \phi_i)\big], \tag{D.26}$$

using a minimisation scheme such as the downhill simplex method [Nelder & Mead, 1965]. The wavenumbers m_i and wave amplitudes q_{0i} can then be compared with outputs from the ray-tracing scheme, to determine whether changes in the wavenumber and wave amplitudes indeed agree with WKB theory.

The results of this experiment are shown in Figures D.2 and D.3. Figure D.2 shows a comparison of the wave amplitudes q_i from ENDGame1D to the wave energy W from the ray-tracing scheme, for an acoustic wave in cases where the wavenumbers and frequency being used are outside the limit of validity of WKB theory according to Figure 4.4. The two measures of the wave amplitude match up quite well in this plot, although the vertical molecular viscosity and diffusion appears to take slightly longer to reduce the wave amplitude in the thermosphere in ENDGame1D.

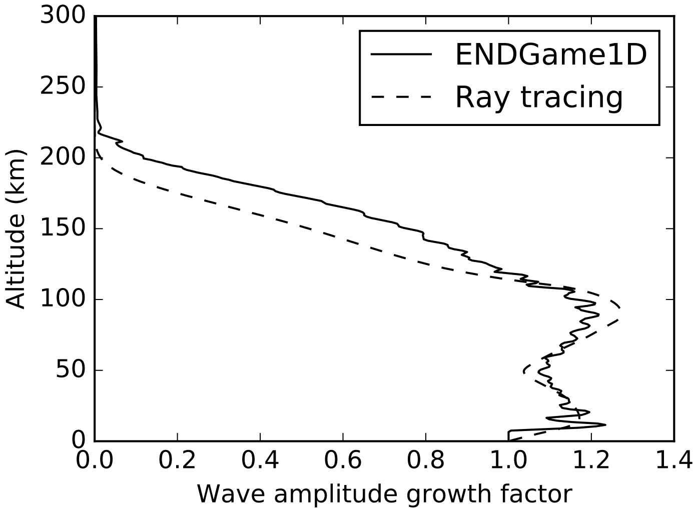

Figure D.2: A comparison of the relative wave amplitudes q_0 from ENDGame1D and the wave energy W from the ray-tracing scheme. In ENDGame1D, there is a continuous oscillation to Θ at the bottom boundary with a frequency of $\omega = 0.2$ from which the wave amplitude is measured. In both cases, a uniform grid with $\Delta z = 500\,\mathrm{m}$ and a centred time-step is used with $\Delta t = 1\,\mathrm{s}$.

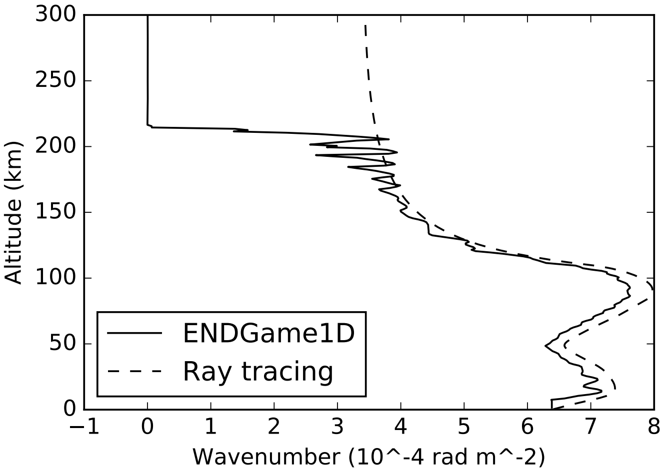

Figure D.3: A comparison of the wavenumbers m from ENDGame1D and the ray-tracing scheme. In ENDGame1D, there is a continuous oscillation to Θ at the bottom boundary with a frequency of $\omega = 0.2$ from which the wavenumber is measured. In both cases, a uniform grid with $\Delta z = 500\,\mathrm{m}$ and a centred time-step is used with $\Delta t = 1\,\mathrm{s}$

Figure D.3 shows a comparison of the wavenumbers in ENDGame1D and the ray-tracing scheme. The wavenumbers produced by both models are very similar, up to an altitude of 200 km. At this point, the wave amplitudes in ENDGame become smaller than the drift in the background and the wavenumber quickly falls to 0. However, the lines in Figures D.2 and D.3 are very similar, and it can be concluded that WKB theory can still be used to describe the behaviour of wave propagation for the small wavenumbers that are dealt with here.

Appendix E

Vertical molecular viscosity and diffusion

In this appendix, the theory of the governing equations including molecular viscosity and diffusion is derived and is used in sections 5 and 6.

E.1 Derivation of continuous equations for ENDGame1D

Usually pressure p is well approximated by $p = p_e(\rho, e)$, where p_e is the *equilibrium pressure*: the value of p given by the equation of state, and e is the *specific internal energy.* However, this approximation does not necessarily hold when there is relative motion. In this case, the difference between p and p_e is given by

$$p - p_e = -\tilde{\kappa} \boldsymbol{\nabla} \cdot \boldsymbol{u}, \tag{E.1}$$

where $\tilde{\kappa}$ is a scalar coefficient dependent on the local state of the fluid, and $\boldsymbol{\nabla} \cdot \boldsymbol{u}$ represents the rate of expansion [Batchelor, 2000]. Since $\boldsymbol{\nabla} \cdot \boldsymbol{u}$ is usually small, the expansion damping effect is widely omitted from the continuous governing equations, except in extreme situations like shocks.

The *scalar coefficient of molecular viscosity* μ may be given as

$$\mu = 3.34 \times 10^{-7} T^{0.71} \,\mathrm{kg\,m^{-1}\,s^{-1}}, \tag{E.2}$$

where T is the given temperature profile [Vadas, 2007]. The *kinematic viscosity* is:

$$\tilde{\nu} = \frac{\mu}{\rho}, \tag{E.3}$$

where $\overline{\rho}$ is the *mean density*, and hence, the *bulk viscosity* is given by

$$\tilde{\kappa} = \frac{\tilde{\nu}}{\mathrm{Pr}}, \tag{E.4}$$

where $\mathrm{Pr} \approx 0.7$ is the *Prandtl number* (Pr can vary slightly with temperature, but this may be neglected for now) [Vadas, 2007]. Lastly, the *coefficient of molecular thermal conductivity* λ is given by

$$\lambda = \overline{\rho} C_v \tilde{\kappa}, \tag{E.5}$$

[Chapman & Cowling, 1970].

Next, the momentum, continuity and energy conservation equations including vertical molecular viscosity and diffusion are obtained. The continuity equation (A.19) is unchanged. With the original pressure gradient term (A.12), and by neglecting Coriolis forces and the source term, the momentum equation (A.14) becomes:

$$\frac{Dw}{Dt} + \frac{1}{\rho}\frac{\partial p}{\partial r} + \frac{\partial \Phi}{\partial r} = 0. \tag{E.6}$$

The pressure gradient term here needs to be replaced so that it is in terms of variables that are stored in ENDGame1D: w, ρ, Θ and Π, but not p. Express $\tilde{\kappa}$ in terms of μ using the kinematic (E.3) and bulk viscosity equations (E.4), and using the pressure gradient (E.1), the pressure gradient term in the momentum equation (E.6) becomes

$$\begin{aligned} \frac{1}{\rho}\frac{\partial p}{\partial r} &= \frac{1}{\rho}\frac{\partial}{\partial r}\left(p_e - \tilde{\kappa}\boldsymbol{\nabla}\cdot\boldsymbol{u}\right) \\ &= \frac{1}{\rho}\frac{\partial p_e}{\partial r} - \frac{1}{\rho}\frac{\partial}{\partial r}\left[\frac{\mu}{\mathrm{Pr}\overline{\rho}}\frac{1}{r^2}\frac{\partial(r^2 w)}{\partial r}\right]. \end{aligned} \tag{E.7}$$

From experiments and observations of the attenuation of high frequency sound waves, the value of $\mu/\tilde{\kappa}$ is found to be a constant of order unity for a polyatomic perfect gas (i.e. a theoretical charged chemical gas species with no intermolecular forces) [Batchelor, 2000]. This implies the following relationship between μ and $\tilde{\kappa}$:

$$\frac{\mu}{\tilde{\kappa}} = \mathrm{Pr}\overline{\rho} \sim 1. \tag{E.8}$$

Hence, using μ/κ (E.8), the pressure gradient term from (E.7) becomes

$$\frac{1}{\rho}\frac{\partial p}{\partial r} = \frac{1}{\rho}\frac{\partial p_e}{\partial r} - \frac{1}{\rho}\frac{\partial}{\partial r}\left[\frac{\mu}{r^2}\frac{\partial(r^2 w)}{\partial r}\right]. \tag{E.9}$$

Substituting this expression for the pressure gradient (E.9) into the momentum equation (E.6) gives

$$\frac{Dw}{Dt} + \frac{1}{\rho}\frac{\partial p_e}{\partial r} + \frac{\partial \Phi}{\partial r} = \frac{1}{\rho}\frac{\partial}{\partial r}\left[\frac{\mu}{r^2}\frac{\partial (r^2 w)}{\partial r}\right]. \tag{E.10}$$

Using the ENDGame pressure gradient (A.12), the equilibrium pressure gradient term can be replaced with an expression for Exner pressure, to obtain

$$\frac{Dw}{Dt} + C_p\Theta\frac{\partial \Pi}{\partial r} + \frac{\partial \Phi}{\partial r} = \frac{1}{\rho}\frac{\partial}{\partial r}\left[\frac{\mu}{r^2}\frac{\partial (r^2 w)}{\partial r}\right]. \tag{E.11}$$

Lastly, make a substitution for Ψ (A.26) to obtain the required form of the momentum equation as follows:

$$\boxed{\frac{Dw}{Dt} - \Psi = \frac{1}{\rho}\frac{\partial}{\partial r}\left[\frac{\mu}{r^2}\frac{\partial (r^2 w)}{\partial r}\right].} \tag{E.12}$$

Next, consider the following vector form of the *energy conservation equation* which is based on the same equation from Batchelor [2000] that includes additional terms describing the heat exchange of multiple gas species which are neglected here:

$$C_v\rho\frac{DT}{Dt} + p_e\boldsymbol{\nabla}\cdot\boldsymbol{u} + \boldsymbol{\nabla}\cdot\boldsymbol{q} = \boldsymbol{\tau} : \boldsymbol{\nabla}\boldsymbol{u} + \widetilde{\kappa}(\boldsymbol{\nabla}\cdot\boldsymbol{u})^2, \tag{E.13}$$

where $\boldsymbol{\tau}$ is the deviatoric stress tensor (6.13) and $\mathbf{q} = -\lambda\boldsymbol{\nabla}T$ is the *diffusive heat flux*. Note that other sources, such as Chapman & Cowling [1970], use a different sign convention for the stress tensor term here. The continuous 3D energy equation with vertical molecular viscosity and diffusion is found here, and the 1D version is then extracted from this.

Using the difference between p and p_e (E.1), $\mu/\widetilde{\kappa}$ (E.8) and equation (A.9) for the Exner pressure, the energy conservation equation (E.13) becomes

$$C_v\rho\frac{DT}{Dt} + p_e\Pi^{\frac{1}{\kappa}}\boldsymbol{\nabla}\cdot\boldsymbol{u} - \boldsymbol{\tau} : \boldsymbol{\nabla}\boldsymbol{u} = \widetilde{\kappa}(\boldsymbol{\nabla}\cdot\boldsymbol{u})^2 + \boldsymbol{\nabla}\cdot(\lambda\boldsymbol{\nabla}\cdot T). \tag{E.14}$$

In this form, the left-hand side of the energy equation includes the term DT/Dt, which is not in terms of the variables that are stored in ENDGame at each time-step: $\boldsymbol{u}$, ρ, Θ and Π. Use $\Theta = T/\Pi$, substitute for Π from the equation of state (A.11) and multiply through by $\Theta^{\kappa/1-\kappa}$ to obtain

$$\Theta^{\frac{1}{1-\kappa}} = T\left(\frac{R}{p_e}\rho\right)^{-\frac{\kappa}{1-\kappa}}. \tag{E.15}$$

Next, take the logarithm of both sides to obtain

$$\frac{1}{1-\kappa}\log\Theta = \log T - \frac{\kappa}{1-\kappa}\left[\log\left(\frac{R}{p_e}\right) + \log\rho\right]. \tag{E.16}$$

Take the material derivative of both sides to obtain

$$\frac{1}{1-\kappa}\frac{1}{\Theta}\frac{D\Theta}{Dt} = \frac{1}{T}\frac{DT}{Dt} - \frac{\kappa}{1-\kappa}\frac{1}{\rho}\frac{D\rho}{Dt}. \tag{E.17}$$

Note that $1-\kappa = C_v/C_p$ and $\kappa = R/C_p$. Rearranging this expression and using the continuity equation (A.18) and the equation of state (A.11) gives a new expression for the left-hand side of the energy equation (E.14)

$$C_p\Pi\rho\frac{D\Theta}{Dt} = C_v\rho\frac{DT}{Dt} + \frac{p_e\Pi^{1/\kappa}}{r^2}\boldsymbol{\nabla}\cdot\boldsymbol{u}. \tag{E.18}$$

This gives a new form of the energy equation:

$$C_p\rho\Pi\frac{D\Theta}{Dt} - \boldsymbol{\tau} : \boldsymbol{\nabla}\boldsymbol{u} = \widetilde{\kappa}(\boldsymbol{\nabla}\cdot\boldsymbol{u})^2 + \frac{1}{r^2}\frac{\partial}{\partial r}\left(r^2\lambda\frac{\partial T}{\partial r}\right). \tag{E.19}$$

For ENDGame1D, without horizontal and stress tensor terms, this reduces to:

$$\boxed{C_p\rho\Pi\frac{D\Theta}{Dt} = \widetilde{\kappa}\left[\frac{1}{r^2}\frac{\partial(r^2w)}{\partial r}\right]^2 + \frac{1}{r^2}\frac{\partial}{\partial r}\left(r^2\lambda\frac{\partial T}{\partial r}\right).} \tag{E.20}$$

E.2 Explicit-in-time vertical molecular viscosity and diffusion

In this section, the 1D continuous equations including the vertical molecular viscosity and diffusion terms are discretised, but the viscous and diffusive terms are added to the momentum equation (5.4) and energy equation (5.5) explicitly in time. The dynamics terms will all be handled in the same way as in appendices A.2 and A.3.

In section 5.3, these terms are added fully implicitly with respect to time, since the explicit scheme is unstable if the time-scale of molecular diffusion τ_{diff} is much smaller than the time-step Δt used in ENDGame1D (as shown in appendix E.5). However, it is much more straightforward to first implement them explicitly. It will also be useful for performing a *reference run*, where by using a much smaller time-step and grid spacing than is used operationally, the dynamical core can be run so that its performance is driven primarily by vertical molecular viscosity and diffusion and is not restricted by the numerics: to test if vertical molecular viscosity and diffusion can control the wave growth enough to increase the ENDGame1D's stability.

The continuity, momentum and energy equations including vertical molecular viscosity and diffusion, (5.3), (5.4) and (5.5) respectively, are discretised in the same way as in section A.2, before adding the diffusion terms located at the arrival points to obtain the $n+1$ step. The discretised governing equations including vertical molecular viscosity and diffusion are given by (E.21) - (E.23), where $\cdot^{(n+1)}$ denotes a variable being evaluated implicitly at the next time-step $n+1$ and at position r, and $\cdot_D^{(n)}$ denotes a variable being evaluated explicitly at the current time-step n, and at the departure point corresponding to r: r_D. The $\cdot^\dagger$ terms represent the viscous terms, and are evaluated at the current time-step n at the arrival point.

$$\boxed{\begin{aligned}
\left\{\rho\left[1+\frac{\alpha_\rho\Delta t}{r^2}\frac{\partial(r^2w)}{\partial r}\right]\right\}^{(n+1)} &= \left\{\rho\left[1-\frac{\beta_\rho\Delta t}{r^2}\frac{\partial(r^2w)}{\partial r}\right]\right\}_D^{(n)}, && \text{(E.21)}\\
\left[(\delta_V+\nu\Delta t)w-\alpha_w\Delta t\Psi\right]^{(n+1)} &= \left(\delta_V w+\beta_w\Delta t\Psi\right)_D^{(n)}+\Delta t\left\{\frac{1}{\rho}\frac{\partial}{\partial r}\left[\frac{\mu}{r^2}\frac{\partial(r^2w)}{\partial r}\right]\right\}^\dagger, && \text{(E.22)}\\
\left(C_p\rho\Pi\Theta\right)^{(n+1)} &= \left(C_p\rho\Pi\Theta\right)_D^{(n)}+\Delta t\left\{\mu\left[\frac{1}{r^2}\frac{\partial(r^2w)}{\partial r}\right]^2+\frac{1}{r^2}\frac{\partial}{\partial r}\left(r^2\lambda\frac{\partial T}{\partial r}\right)\right\}^\dagger. && \text{(E.23)}
\end{aligned}}$$

The spatial discretisation of the viscous and diffusion terms must be considered. Begin with the viscous term added explicitly to the momentum equation (E.22):

$$\left\{\frac{1}{\rho}\frac{\partial}{\partial r}\left[\frac{\mu}{r^2}\frac{\partial(r^2w)}{\partial r}\right]\right\}^\dagger. \tag{E.24}$$

Discretising this gives an expression for the viscous term at level $k+1/2$:

$$\left\{\frac{1}{\rho}\frac{\partial}{\partial r}\left[\frac{\mu}{r^2}\frac{\partial(r^2w)}{\partial r}\right]\right\}_{k+1/2} = \frac{1}{(\overline{\rho}^r\Delta r)_{k+1/2}}\left\{\left[\frac{\mu}{r}\frac{\partial(r^2w)}{\partial r}\right]_{k+1}-\left[\frac{\mu}{r}\frac{\partial(r^2w)}{\partial r}\right]_k\right\}, \tag{E.25}$$

where an estimated value of ρ at level $k+1/2$: $\overline{\rho}^r$ is given by

$$\overline{\rho}^r_{k+1/2} = \overline{\rho}_{k+1/2} = a_{k+1/2}\rho_{k+1}+b_{k+1/2}\rho_k, \tag{E.26}$$

(the r superscript may be dropped) where

$$a_{k+1/2} = \frac{r_{k+1/2}-r_k}{r_{k+1}-r_k},\quad b_{k+1/2} = \frac{r_{k+1}-r_{k+1/2}}{r_{k+1}-r_k}, \tag{E.27}$$

are weighting terms for interpolating a variable stored at w-level $k+1/2$ between the two adjacent ρ-levels k and $k+1$. Note that these interpolate to w-levels, whereas the weighting terms given by equation (A.38) interpolate to ρ-levels. Also note that $\Delta r_{j+1/2} = r_{j+1} - r_j$, and $\partial(r^2 w)/\partial r$ at ρ-levels is given by equation (A.40) with boundary condition (A.41).

Next, consider the viscous term added explicitly to the energy equation (E.23):

$$\left\{\mu\left[\frac{1}{r^2}\frac{\partial(r^2 w)}{\partial r}\right]^2\right\}^\dagger. \tag{E.28}$$

Discretising this gives an expression for the viscous term at level $k+1/2$:

$$\left\{\mu\left[\frac{1}{r^2}\frac{\partial(r^2 w)}{\partial r}\right]^2\right\}_{k+\frac{1}{2}} = (\mu a)_{k+\frac{1}{2}}\left\{\left[\frac{1}{r^2}\frac{\partial(r^2 w)}{\partial r}\right]^2_{k+1}\right\} + (\mu b)_{k+\frac{1}{2}}\left\{\left[\frac{1}{r^2}\frac{\partial(r^2 w)}{\partial r}\right]^2_{k}\right\}. \tag{E.29}$$

Finally, consider the diffusion term added explicitly to the energy equation (E.23):

$$\left[\frac{1}{r^2}\frac{\partial}{\partial r}\left(r^2\lambda\frac{\partial T}{\partial r}\right)\right]^\dagger. \tag{E.30}$$

Discretising this gives an expression for the diffusion term at level $k+1/2$:

$$\left[\frac{1}{r^2}\frac{\partial}{\partial r}\left(r^2\lambda\frac{\partial T}{\partial r}\right)\right]_{k+1/2} = \frac{1}{(r^2\Delta r)_{k+1/2}}\left[\left(r^2\,\lambda\frac{\partial T}{\partial r}\right)_{k+1} - \left(r^2\lambda\frac{\partial T}{\partial r}\right)_{k}\right], \tag{E.31}$$

where $\partial T/\partial r$ at k-levels is given by

$$\left.\frac{\partial T}{\partial r}\right|_k = \frac{T_{k+1/2} - T_{k-1/2}}{\Delta r_k}. \tag{E.32}$$

Here, T_k is found by rearranging the equation of state (A.11) and using $T = \Theta\Pi$:

$$T_{k+1/2} = \Theta_{k+1/2}^{\frac{1}{1-\kappa}}\left(\frac{R}{p_0}\overline{\rho}_{k+1/2}\right)^{\frac{\kappa}{1-\kappa}}. \tag{E.33}$$

E.3 Testing the explicit scheme

In this section, ENDGame1D is run using the temporally explicit scheme derived in appendix E.2 to determine whether vertical molecular viscosity and diffusion in ENDGame1D has a significant enough damping effect on vertically propagating waves that the implicit-in-time scheme for vertical molecular viscosity and diffusion should be developed.

Figure E.1 shows an example of a plot of the maximum velocities observed at each height throughout the whole simulation of the vertical propagation of an acoustic wave to the top boundary with and without the implementation of vertical molecular viscosity and diffusion. This is a useful measure of the wave amplitudes that occur at different altitudes throughout the simulation. Fast, vertically propagating

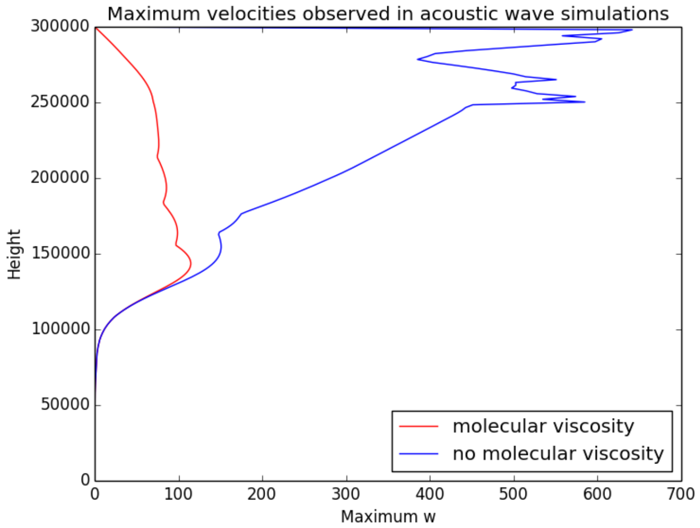

Figure E.1: The maximum velocity observed at each height throughout the whole simulation of an acoustic wave propagating to a top model boundary at 300 km, with and without the explicit implementation of vertical molecular viscosity and diffusion. The acoustic wave was triggered with a relative density perturbation of 10^{-4} at 5 km altitude. This simulation used the USSA temperature profile and a quadratically stretched grid.

acoustic waves are thought to be a cause of the large vertical winds that are observed in the thermosphere [Hickey *et al.* , 2001], and the large velocity values w that are observed above 100 km in this plot are indicative of this.

In ENDGame1D, without any numerical damping or viscosity present in the thermosphere, an excessive amount of wave energy is channelled upwards, producing overly large density perturbations that cause it to become unstable. Including vertical molecular viscosity and diffusion in the governing equations should have the effect of dissipating acoustic waves more realistically in the thermosphere, reducing the vertical velocities observed in the thermosphere, as shown in section 5.1.

Indeed, the difference that the inclusion of vertical molecular viscosity and diffusion makes can be clearly seen in Figure E.1: above 100 km, the maximum observed w values increase hugely without viscosity. With the inclusion of vertical molecular viscosity and diffusion, the w values still increase above 100 km, but at about 135 km where the two lines diverge, the viscosity acts to limit the speed that the vertical winds are able to reach, as expected from the scale analysis performed in section 5.1. This effect would be even more apparent with higher top model boundaries, but the required time-steps for the explicit scheme are too small.

In appendix C.1, it is shown that the vertical velocity w of acoustic waves varies like $\rho^{1/2}$. Therefore, in Figure E.2, $w_0(\rho_s/\rho)^{1/2}$ is plotted, where ρ_s is the *surface density* and w_0 is a constant that depends on the strength of the acoustic wave. This

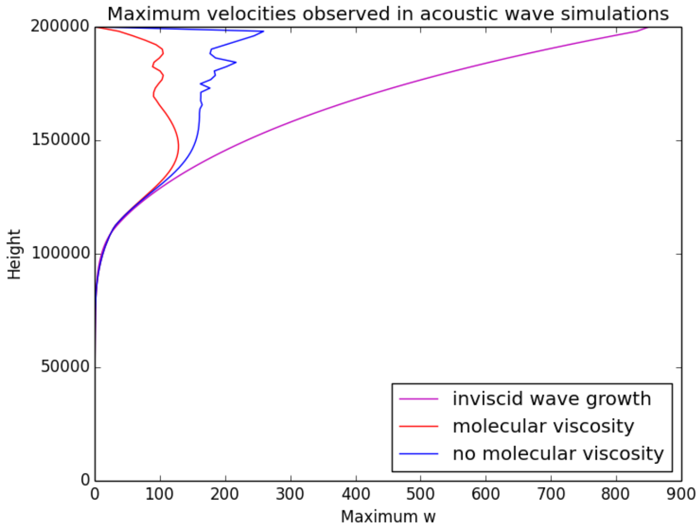

Figure E.2: The maximum velocity observed at each height throughout the whole simulation of an acoustic wave propagating to a top model boundary at 200 km, with and without vertical molecular viscosity and diffusion, and a theoretical plot of the maximum velocity that would be observed in an inviscid atmosphere without the numerics slowing down the high frequency waves. This simulation used the USSA temperature profile and a quadratically stretched grid.

line shows the maximum velocity that would be observed in an inviscid atmosphere. Due to the SISL nature of ENDGame's formulation, the maximum group velocities output by ENDGame1D are limited by its highest resolvable frequency (this concept is explained further in section 3.2), and so are much lower than the acoustic wave velocity in an inviscid atmosphere.

It seems that vertical molecular viscosity and diffusion is less effective at damping the acoustic wave if the amplitude of the wave is too large to begin with. This is likely to be because the wave amplitudes get too big before they reach the molecularly diffused region above 130 km. Further experiments will be performed with the implicit scheme to determine whether this is likely to be a problem for the kinds of acoustic waves that ENDGame will be expected to handle in realistic simulations. Overall, the plots shown so far demonstrate that vertical molecular viscosity and diffusion have the potential to damp fast waves in the thermosphere.

Next, the potential effects of vertical molecular viscosity and diffusion on ENDGame1D's stability is shown by performing stability tests. The settings are chosen to minimise the simulation run time of the explicit scheme while still allowing vertical molecular viscosity and diffusion to have a demonstrable damping effect on the acoustic waves. The top model boundary must be high enough for the diffusion time-scale to be shorter than the acoustic wave growth time-scale (so from Table 5.1, at least 150 km high).

The time-step used is limited not only by the stability criterion (E.41), but also by the diffusion time-scales given in Table 5.1. In particular, the diffusion time-scales become very small as the top model boundary is lifted up to 600 km. Runs with time-steps this small would take an excessively long time just to simulate an acoustic wave propagating from the surface to the top boundary.

An experiment was therefore performed using the following settings: a 0.01 s time-step and a relative density perturbation of 4×10^{-3} at 5 km high was used to initiate an acoustic wave, with the simulation being considered stable if it ran without crashing for 6 hours. Without vertical molecular viscosity and diffusion, the dynamical core is only able to remain stable with a top model boundary of up to 140 km. With vertical molecular viscosity and diffusion switched on however, the top model boundary can be lifted up to 220 km and remains stable. This demonstrates that vertical molecular viscosity and diffusion have the potential to improve ENDGame1D's stability and reduce vertical velocities in the thermosphere. Overall, implementing the implicit scheme for vertical molecular viscosity and diffusion should be beneficial based on this analysis.

E.4 Separate viscous timestep

In this section, a scheme is tested whereby the dynamics components of the continuous governing equations in 1D (that includes the molecular viscosity and diffusion terms) are dealt with in a separate time-step to the viscous and diffusive terms. In section 5, it is asserted that because molecular viscosity is a fast acting process in the thermosphere, it must be combined with the rest of the dynamics in a fully coupled way, because solving for the viscosity in a separate time-step would generate big time-splitting errors. Here, it is verified whether handling molecular viscosity and diffusion in a separate time-step is viable.

Developing a scheme specifically designed to solve just for the viscous terms in their own time-step would be more straightforward than the development of the fully-coupled viscous scheme developed in section 5. If the errors are not significant for large time-steps, it would be preferable to just use a split-viscous scheme.

Since the fully-coupled viscous scheme has already been developed and tested, this is used after the dynamics step is completed, but the dynamics terms are removed so that it essentially solves for the viscous terms only. Using this implementation of a split-viscous scheme, some stability tests are performed and their results shown in Figure E.3.

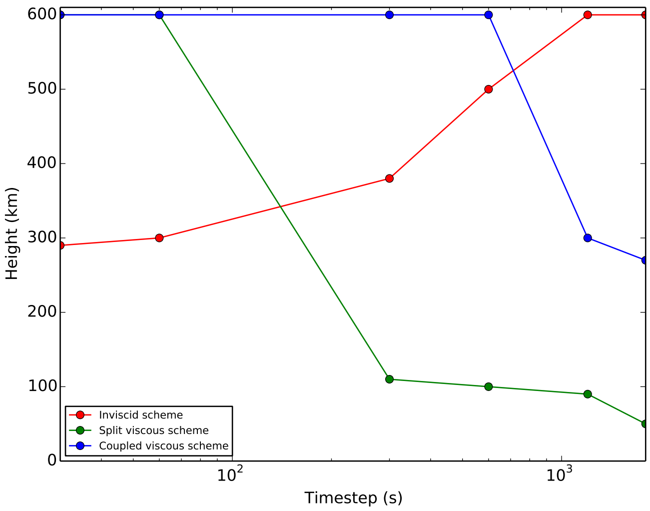

Figure E.3: Stability tests of ENDGame1D comparing the use of different time-steps with the split-viscous, coupled-viscous and inviscid formulations. The lines on this stability plot represent the maximum possible top boundary height for which a simulation with a density perturbation of 10^{-4} and an off-centring parameter of $\alpha = 0.51$ remains stable for 4 weeks for different time-steps. The time-steps considered are $\Delta t \in [30\,\mathrm{s}, 1\,\mathrm{min}, 5\,\mathrm{min}, 10\,\mathrm{min}, 20\,\mathrm{min}, 30\,\mathrm{min}]$.

Figure E.3 shows the results of stability tests for the split-viscous scheme for a range values of Δt with the off-centring parameter $\alpha = 0.51$. It can be seen that as the decaying effect of α is greater for larger Δt, as shown by the time-scale for the off-centring parameter (4.56), increasing the stability of the inviscid scheme as larger Δt are used. The stability of the coupled viscous scheme seems to drop off for larger time-steps, likely as a result of some approximations that are made in coupling the viscous terms to the dynamics equations.

However, the coupled viscous scheme is far more stable than the split-viscous scheme for timesteps larger than 1 min. The time-splitting errors are caused by finding one solution for the dynamics terms, and then using this to find another solution that includes the effects of molecular viscosity and diffusion as well. These two solutions may be quite different in the thermosphere where molecular viscosity and diffusion has a more significant effect, and the errors generated by alternating between these two solutions ends up becoming quite large, particularly for these larger time-steps.

The smaller the timesteps that are used, the more that the solutions generated by the split-viscous scheme match the solutions from the fully-coupled viscous scheme, although using such small values for Δt is not viable for practical use. The fully-coupled viscous scheme is therefore necessary to keep ENDGame1D stable as it is vertically extended.

E.5 Stability analysis of the diffusion equation

The linear diffusion equation is given by

$$\frac{\partial T}{\partial t} = \tilde{\kappa}\frac{\partial^2 T}{\partial z^2}, \tag{E.34}$$

where $T = T(z,t)$ and $\tilde{\kappa}$ (> 0) is the bulk viscosity, given by E.4 [Garcia, 1994].

In section E.2, the viscous and diffusive terms were added to the momentum equation (5.4) and energy equation (5.5) explicitly in time. This means that rather than using the same SISL scheme as with the dynamics terms in section A.2, the diffusion terms are essentially treated using a *Forward-in-Time and Centred-in-Space* (FTCS) timestepping scheme that discretises the diffusion equation as follows:

$$\frac{T_j^{(n+1)} - T_j^{(n)}}{\Delta t} = \tilde{\kappa}\left(\frac{T_{j+1}^{(n)} - 2T_j^{(n)} + T_{j-1}^{(n)}}{\Delta z^2}\right). \tag{E.35}$$

Then wavelike solutions of this are of the form:

$$T_j^{(n)} = A^n \exp(\mathrm{i}kj\Delta z), \tag{E.36}$$

where $A \in \mathbb{C}$ is the *amplification factor*, which is constant. If it is found that $|A| > 1$, then the numerical solution of T is growing with time and is unstable. Here, the condition that guarantees a stable solution is found. Begin by substituting equation (E.36) into equation (E.35):

$$\frac{A^{n+1}\mathrm{e}^{\mathrm{i}kj\Delta z} - A^n\mathrm{e}^{\mathrm{i}kj\Delta z}}{\Delta t} = \tilde{\kappa}\left(\frac{A^n\mathrm{e}^{\mathrm{i}k(j+1)\Delta z} - 2A^n\mathrm{e}^{\mathrm{i}kj\Delta z} + A^n\mathrm{e}^{\mathrm{i}k(j-1)\Delta z}}{\Delta z^2}\right). \tag{E.37}$$

By dividing through by $A^n\mathrm{e}^{\mathrm{i}kj\Delta z}$, this simplifies to:

$$\frac{A-1}{\Delta t} - = \tilde{\kappa}\left(\frac{\mathrm{e}^{\mathrm{i}k\Delta z} - 2 + \mathrm{e}^{-\mathrm{i}k\Delta z}}{\Delta z^2}\right). \tag{E.38}$$

By noting that $\mathrm{e}^{\mathrm{i}k\Delta z} + \mathrm{e}^{-\mathrm{i}k\Delta z} = 2\cos k\Delta z$ and rearranging this expression, an equation for the amplification factor A is obtained as follows:

$$A = 1 - \frac{2\tilde{\kappa}\Delta t}{\Delta z^2}\left(1 - \cos k\Delta z\right). \tag{E.39}$$

Note that $0 \leq 1 - \cos k\Delta z \leq 2$. If it is supposed that $2\tilde{\kappa}\Delta t/\Delta z^2 \leq 1$, then

$$1 \ \geq A = 1 - \frac{2\tilde{\kappa}\Delta t}{\Delta z^2}(1 - \cos k\Delta z) \geq 1 - (1 - \cos k\Delta z) = \cos k\Delta z \ \geq \ -1, \tag{E.40}$$

So $-1 \leq A \leq 1$. Therefore, the scheme is conditionally stable, since $|A| \leq 1$ as long as $2\tilde{\kappa}\Delta t/\Delta z^2 \leq 1$. By rearranging this, and using the diffusion time-scale (4.60), the condition on the time-step Δt for stability becomes:

$$\Delta t \leq \frac{\Delta z^2}{2\tilde{\kappa}} = \frac{\tau_{\text{diff}}}{2}, \tag{E.41}$$

or in other words, if $\tau_{\text{diff}} < 2\Delta t$, then this explicit scheme is unstable.

E.6 Scale analysis of the elliptic problem for the viscous scheme

The aim of the exercise detailed in this section is to check that the boundary value problem for the fully coupled implicit viscous scheme in 1D (5.28) and the elliptic problem in 3D (6.63) gives accurate solutions without the terms that are neglected in order to obtain a solvable elliptic problem. A scaling argument is used to estimate the size of these neglected terms and show that they do not have a significant effect on the solution in the viscous and inviscid regions.

It can be seen that the boundary problem for the viscous scheme (5.28) is also the correct equation to use in the inviscid region as all of the terms from the boundary value problem in the inviscid region (5.27) are included in equation (5.28). The extra viscous terms in (5.28) are negligible in the inviscid region. Therefore, it just needs to be considered whether this equation is valid in the viscous and intermediate cases.

First, make the following definitions: separate the variable increments/ perturbation terms $(u', v', w', \rho', \Pi', \Theta')$ into their reference profiles $(u^*, v^*, w^*, \rho^*, \Pi^*, \Theta^*)$ and some dimensionless variables $(\widehat{u}, \widehat{v}, \widehat{w}, \widehat{\rho}, \widehat{\Pi}, \widehat{\Theta})$ such that any variable increment φ' can be expressed as $\varphi' = \varphi^* \widehat{\varphi}$. Also, recall the density scale height given by (C.21): $H_\rho = RT/g$, which is obtained by making the isothermal approximation. This approximation is fine for order-of-magnitude calculations such as those used in this scale analysis. From the growth rate for Π (C.20), note that

$$\frac{1}{\Pi^*}\frac{\partial \Pi^*}{\partial r} \approx \frac{\kappa}{H_\rho}. \tag{E.42}$$

Using $T^* \equiv \Theta^*\Pi^*$, it can be seen that as T is approximately linear, then $\Theta^* \sim (\Pi^*)^{-1}$

Note that all the perturbation fields have the same vertical scale height H, the scale height of a disturbance with a small wavelike structure. Therefore:

$$\frac{1}{w'}\frac{\partial(w')}{\partial r} \approx \frac{1}{H}, \quad \frac{1}{\Pi'}\frac{\partial \Pi'}{\partial r} \approx \frac{1}{H}, \quad \frac{1}{\Theta'}\frac{\partial \Theta'}{\partial r} \approx \frac{1}{H}. \tag{E.43}$$

This is reasonable if $H < H_\rho$, and if $H > H_\rho$, then other terms in the solution will dominate anyway.

Suppose the diffusion terms (with λ) dominate the other terms (including the viscous terms, with μ) in the full viscous equation for R_Θ: (5.17). The λ terms are the main concern because the elliptic problem for w' (5.28) does not include any diffusion terms; only the second elliptic problem for Θ' (5.32) does. Consider the full viscous equation for R_Θ (5.17) and assume that the λ term dominates, leaving:

$$R_\Theta \sim \frac{\Delta t}{C_p \overline{\rho^* \Pi^*}} \frac{1}{r^2} \frac{\partial}{\partial r} \left\{ r^2 \lambda \frac{\partial}{\partial r} \left[\overline{\Pi}^* \Theta^* (\widehat{\Theta} + \widehat{\Pi}) \right] \right\}. \tag{E.44}$$

Using the above approximations for estimating derivatives using the scale heights H and H_ρ, simplifying further by letting

$$\frac{1}{\widetilde{H}} = \max \left| \frac{1}{H}, \frac{\kappa}{H_\rho} \right|, \tag{E.45}$$

and by neglecting dimensionless variables, the following can be obtained:

$$R_\Theta \sim \frac{\Delta t \lambda \Theta'}{C_p \overline{\rho}^* \widetilde{H}^2}. \tag{E.46}$$

Define C_Θ to be the dominant term of R_Θ in the viscous and intermediate cases:

$$C_\Theta = \frac{\Delta t \lambda}{C_p \overline{\rho}^* \widetilde{H}^2}, \tag{E.47}$$

so that $R_\Theta \sim C_\Theta \Theta'$. Then the full viscous equation for R_Θ (5.17) becomes

$$R_\Theta \approx (1 + C_\Theta)\Theta' + \alpha_z \Delta t \frac{\overline{\partial \Theta^*}}{\partial r} w'. \tag{E.48}$$

If next, Θ' is eliminated from the full viscous equation for w' (5.16), then

$$R_w - \frac{\alpha_w \Delta t\, C_p}{1 + C_\Theta} R_\Theta \approx \left(\delta_V + \nu \Delta t - \frac{\alpha_w \alpha_z \Delta t^2 C_p}{1 + C_\Theta} \frac{\partial \Pi^*}{\partial r} \frac{\overline{\partial \Theta^*}}{\partial r} \right) w' + \alpha_w \Delta t\, C_p \Theta^* \frac{\partial \Pi'}{\partial r}. \tag{E.49}$$

The w' coefficient resembles the B coefficient (A.64), but has an extra $1/(1 + C_\Theta)$ factor. This means that B^{-1} is small in the viscous case where C_Θ is large.

Similarly Θ' may be eliminated from the linearised state equation (5.18):

$$\frac{1-\kappa}{\kappa}\frac{\Pi'}{\Pi^*} = \frac{\rho'}{\rho^*} - \frac{\alpha_z \Delta t}{1+C_\Theta}\overline{\frac{1}{\Theta^*}\frac{\overline{\partial\Theta^*}}{\partial r}}w' + \frac{1}{1+C_\Theta}\frac{\overline{R_\Theta}}{\Theta^*}. \tag{E.50}$$

This is then substituted into the full viscous equation for ρ' (5.15) to eliminate ρ', which gives $D_2(w')$, as given by equation (A.69), but with an extra $1/(1+C_\Theta)$ factor. This means that $D_2(w')$ is small in the viscous case where C_Θ is large.

If the λ terms were able to be fully incorporated into an elliptic problem for w' (5.28), then they would have the effect of making the B^{-1} and $D_2(w')$ terms smaller. But when the μ term is large, the terms with B^{-1} and $D_2(w')$ are small compared to the viscous terms. This suggests that the elliptic problem for w' (5.28) is indeed a good approximation across all levels of diffusion.

E.7 1D and 3D approximation comparison

In chapter 6 on the 3D formulation including vertical molecular viscosity and diffusion, it becomes necessary to derive a different elliptic problem to that obtained in chapter 5 on the 1D formulation. Here it is shown that the approximations made in the derivation of the elliptic problem in 3D lead to an equivalent problem to that which was used in 1D, and is valid in both the inviscid and viscous regions.

The 1D residual and state equations (5.15) - (5.18) are abbreviated by neglecting the Π' term in the R_Θ equation (5.17) and making the following substitutions:

$$Q(X) = X - \frac{\Delta t}{C_p\overline{\overline{\rho^*\Pi^*}}}\frac{1}{r^2}\frac{\partial}{\partial r}\left[r^2\lambda\frac{\partial}{\partial r}\left(\overline{\Pi}^*\Theta'\right)\right], \tag{E.51}$$

$$T(X) = (\delta_V + \nu\Delta t)X - \frac{\Delta t}{\overline{\rho}^*}\frac{\partial}{\partial r}\left[\frac{\mu}{r^2}\frac{\partial(r^2 X)}{\partial r}\right]. \tag{E.52}$$

Then the residual and state equations may be rewritten as:

$$R_\rho \approx \rho' + \frac{\alpha\Delta t}{r^2}\frac{\partial}{\partial r}\left(r^2\overline{\rho}^* w'\right), \tag{E.53}$$

$$R_w \approx T(w') + \alpha_w \Delta t\, C_p\left(\Theta^*\frac{\partial\Pi'}{\partial r} + \frac{\partial\Pi^*}{\partial r}\Theta'\right), \tag{E.54}$$

$$R_\Theta \approx Q(\Theta') + \alpha_z\Delta t\overline{\frac{\partial\Theta^*}{\partial r}}w', \tag{E.55}$$

$$0 \approx \frac{\rho'}{\rho^*} + \frac{\overline{\Theta'}}{\Theta^*} - \frac{1-\kappa}{\kappa}\frac{\Pi'}{\Pi^*}. \tag{E.56}$$

Begin by eliminating ρ' by taking (E.56) - (E.53)/ρ^*:

$$-\frac{R_\rho}{\rho^*} = \frac{\overline{\Theta'}}{\Theta^*} - \frac{1-\kappa}{\kappa}\frac{\Pi'}{\Pi^*} - \frac{\alpha\Delta t}{\rho^*}\frac{1}{r^2}\frac{\partial}{\partial r}(r^2\overline{\rho}^* w'). \tag{E.57}$$

Next, assume that $Q(\Theta') \approx \Theta'$ in order to eliminate Θ' by taking (E.54) - $\alpha_w \Delta t\, C_p \frac{\partial \Pi^*}{\partial r}$ (E.55), and use the coefficient B (A.64), the operator D_1 (A.65) and the non-hydrostatic form of the Brunt Väisälä frequency N^2 (6.57) to obtain:

$$T(w') + B^{-1}D_1(\Pi') + \alpha_w\alpha_z\Delta t^2 N^2 w' = R_w - B^{-1}D_1(\Pi^*)R_\Theta, \tag{E.58}$$

and by taking (E.57) - (E.55)/Θ^* and using the D_2 operator (A.69):

$$-\frac{R_\rho}{\rho^*} - \frac{\overline{R_\Theta}}{\Theta^*} = -\frac{1-\kappa}{\kappa}\frac{\Pi'}{\Pi^*} - D_2(w'). \tag{E.59}$$

Finally, eliminate Π' by taking (E.59) + $B^{-1}D_1[\frac{\kappa\Pi^*}{1-\kappa}$(E.58)] and rearrange:

$$\begin{aligned} & w' - B\frac{\Delta t}{\overline{\rho}^*}\frac{\partial}{\partial r}\left[\frac{\mu}{r^2}\frac{\partial(r^2 w')}{\partial r}\right] - D_1\left[\frac{\kappa\Pi^*}{1-\kappa}D_2(w')\right] \\ & = BR_w - D_1(\Pi^*)R_\Theta - D_1\left[\frac{\kappa\Pi^*}{1-\kappa}\left(\frac{R_\rho}{\rho^*} + \frac{\overline{R_\Theta}}{\Theta^*}\right)\right], \end{aligned} \tag{E.60}$$

which is identical to the elliptic problem for w' obtained in chapter 5: (5.28). This means that neglecting the Π' term in the R_Θ equation (5.17), and assuming $Q(\Theta') \approx \Theta'$ are equivalent assumptions to those made in 1D to obtain an elliptic problem that is valid in both inviscid and viscous regions. This means that making these same approximations will lead to an elliptic problem in 3D that is valid in both the inviscid and viscous regions.

E.8 Comparison of the 1D and 3D problems

Here, it is verified that the system of equations obtained in chapter 6 on the 3D formulation including vertical molecular viscosity and diffusion, is equivalent to the system of equations obtained in chapter 5 on the 1D formulation. Whereas the aim of section E.7 was to derive an elliptic problem from the 1D equation set using the same assumptions as made in 3D, here the aim is to directly compare the 1D equation set with the vertical component of the 3D equation set.

By neglecting terms with horizontal derivatives in equation (6.62) for w' and Π', then the equations for w' and Π' (6.58) and (6.62) are as follows:

$$T_r(w') + B^{-1}D_1(\Pi') + \alpha_w\alpha_z\Delta t^2 N^2 w' = R_w - \alpha_w\Delta t\, C_p\frac{\partial \Pi^*}{\partial r}R_\Theta, \tag{E.61}$$

$$-\frac{1-\kappa}{\kappa}\frac{\Pi'}{\Pi^*} + D_2(w') \;=\; -\frac{R_\rho}{\rho^*} - \overline{\frac{R_\Theta}{\Theta^*}}^r . \tag{E.62}$$

In chapter 6, w' is eliminated to obtain an elliptic problem for Π'. Here, Π' is eliminated to get an elliptic problem for w' instead that can be compared with the 1D elliptic problems (5.28) by taking (E.61) + $B^{-1}D_1(\frac{\kappa\Pi^*}{1-\kappa}$E.62) to obtain:

$$\begin{aligned} &T_r(w') + \alpha_w\alpha_z\Delta t^2 N^2 w' + B^{-1}D_1\left[\frac{\kappa\Pi^*}{1-\kappa}D_2(w')\right] \\ &= R_w - \alpha_w\Delta t\, C_p\frac{\partial\Pi^*}{\partial r}R_\Theta - B^{-1}D_1\left[\frac{\kappa\Pi^*}{1-\kappa}\left(\frac{R_\rho}{\rho^*} + \overline{\frac{R_\Theta}{\Theta^*}}^r\right)\right] \end{aligned} \tag{E.63}$$

Take B(E.63), expand the $T_r(w')$ expression (6.48), and use the expression for B (A.64) to simplify the resulting expression to obtain:

$$\begin{aligned} &w' - B\frac{\Delta t}{\overline{\rho^*}}\frac{\partial}{\partial r}\left[\frac{\mu}{r^2}\frac{\partial(r^2 w')}{\partial r}\right] - D_1\left[\frac{\kappa\Pi^*}{1-\kappa}D_2(w')\right] \\ &= BR_w - D_1(\Pi^*)R_\Theta - D_1\left[\frac{\kappa\Pi^*}{1-\kappa}\left(\frac{R_\rho}{\rho^*} + \overline{\frac{R_\Theta}{\Theta^*}}^r\right)\right] \end{aligned} \tag{E.64}$$

which is equal to the elliptic problem for w' (5.28) obtained in chapter 5 on the 1D formulation. This confirms that the vertical component of the 3D formulation including vertical molecular viscosity and diffusion is indeed equivalent to the 1D formulation.

E.9 Full coefficient definitions

In this appendix, the various coefficients defined in section 6.6 are written out fully.

E.9.1 $\widehat{T}(q')$ coefficients

Define the following expressions for the coefficients used in equation (6.83):

$$C_1 \equiv (\delta_V + \nu\Delta t) + \alpha_w\alpha_z\Delta t^2 N^2, \qquad F^{\mu 1}_k \equiv \left.\frac{2r^2\mu}{\Delta r}\right|_k \tag{E.65}$$

$$F^{\mu 2}_k \equiv \left[\left(\widetilde{\kappa} - \frac{2\mu}{3}\right)\frac{1}{V}\right]_k, \qquad F^{r0}_{k-\frac{1}{2}} \equiv -\frac{\Delta t}{(\overline{\rho^*}^r\Delta r)_{k-\frac{1}{2}}}, \qquad F^{r}_{k-\frac{1}{2}} \equiv \left.\frac{F^{r0}}{r^2}\right|_{k-\frac{1}{2}} \tag{E.66}$$

so the coefficients from (6.83) are as follows:

$$\widehat{T}_{k-\frac{1}{2},k-\frac{3}{2}} = F^{r}_{k-\frac{1}{2}}F^{\mu 1}_{k-1} + F^{r0}_{k-\frac{1}{2}}F^{\mu 2}_{k-1}A_{k-\frac{3}{2}}, \tag{E.67}$$

$$\widehat{T}_{k-\frac{1}{2},k-\frac{1}{2}} = C_1 - F^{r}_{k-\frac{1}{2}}\left(F^{\mu 1}_{k} + F^{\mu 1}_{k-1}\right) + F^{r0}_{k-\frac{1}{2}}\left(F^{\mu 2}_{k} + F^{\mu 2}_{k-1}\right)A_{k-\frac{1}{2}}, \tag{E.68}$$

$$\widehat{T}_{k-\frac{1}{2},k+\frac{1}{2}} = F^{r}_{k-\frac{1}{2}}F^{\mu 1}_{k} + F^{r0}_{k-\frac{1}{2}}F^{\mu 2}_{k}A_{k+\frac{1}{2}}. \tag{E.69}$$

E.9.2 $T_H[D_2(q')]$ coefficients

Define the following expressions for the coefficients used in equation (6.88):

$$F_k^{\rho V} = -\frac{\Delta t}{(\rho^* V)_k}, \qquad \widetilde{A}_{k-\frac{1}{2}} \equiv \left.\frac{A\mu r}{\Delta r}\right|_{k-\frac{1}{2}} \tag{E.70}$$

so the coefficients from (6.88) are as follows:

$$T_{k,k-1} = \frac{F_k^{\rho V}\widetilde{A}_{k-\frac{1}{2}}}{r_{k-1}}, \; T_{k,k} = 1 - \frac{F_k^{\rho V}\big(\widetilde{A}_{k+\frac{1}{2}} + \widetilde{A}_{k-\frac{1}{2}}\big)}{r_k}, \; T_{k,k+1} = \frac{F_k^{\rho V}\widetilde{A}_{k+\frac{1}{2}}}{r_{k+1}}. \tag{E.71}$$

A combination of the T_H and D_2 operators may then be built to obtain the coefficients used in (6.90) as follows:

$$(TD)_{k,k-\frac{3}{2}} = T_{k,k-1}D^{(2)}_{k-1,k-\frac{3}{2}}, \tag{E.72}$$

$$(TD)_{k,k-\frac{1}{2}} = T_{k,k-1}D^{(2)}_{k-1,k-\frac{1}{2}} + T_{k,k}D^{(2)}_{k,k-\frac{1}{2}}, \tag{E.73}$$

$$(TD)_{k,k+\frac{1}{2}} = T_{k,k}D^{(2)}_{k,k+\frac{1}{2}} + T_{k,k+1}D^{(2)}_{k+1,k+\frac{1}{2}}, \tag{E.74}$$

$$(TD)_{k,k+\frac{3}{2}} = T_{k,k+1}D^{(2)}_{k+1,k+\frac{3}{2}}. \tag{E.75}$$

E.9.3 $S(\Pi')$ coefficients

The coefficients from (6.92) may be defined in terms of the T coefficients given by (E.71), as follows:

$$S_{k,k-1} = -\frac{1-\kappa}{\kappa}\frac{T_{k,k-1}}{\Pi^*_{k-1}}, \tag{E.76}$$

$$S_{k,k} = -\frac{1-\kappa}{\kappa}\frac{T_{k,k}}{\Pi^*_{k}} - E, \tag{E.77}$$

$$S_{k,k+1} = -\frac{1-\kappa}{\kappa}\frac{T_{k,k+1}}{\Pi^*_{k+1}}. \tag{E.78}$$

E.9.4 $Q(\Theta')$ coefficients

Define the following expressions for the coefficients used in equation (6.105):

$$F^Q_{k+\frac{1}{2}} \equiv -\frac{\Delta t}{C_p(\rho^*\overline{\Pi^*}^r r^2\Delta r)_{k+\frac{1}{2}}}, \quad F^\lambda_k \equiv \left.\frac{r^2\lambda}{\Delta r}\right|_k, \tag{E.79}$$

so the coefficients from (6.105) are as follows:

$$Q_{k-\frac{1}{2},k-\frac{3}{2}} \equiv F^Q_{k-\frac{1}{2}}F^\lambda_{k-1}\overline{\Pi^*}^r_{k-\frac{3}{2}}, \tag{E.80}$$

$$Q_{k-\frac{1}{2},k-\frac{1}{2}} \equiv 1 - F^Q_{k-\frac{1}{2}}\big(F^\lambda_k + F^\lambda_{k-1}\big)\overline{\Pi^*}^r_{k-\frac{1}{2}}, \tag{E.81}$$

$$Q_{k-\frac{1}{2},k+\frac{1}{2}} \equiv F^{Q}_{k-\frac{1}{2}} F^{\lambda}_{k} \overline{\Pi^{*}}_{k+\frac{1}{2}}. \tag{E.82}$$

E.10 Smooth temperature profiles in ENDGame3D

ENDGame3D currently uses the basic state for the temperature profile described in Ullrich *et al.* [2013], which decreases with altitude. It is a good approximation of the temperature profile up to 15 km, but above this altitude, this temperature profile should be merged with the USSA temperature profile that is used in 1D as in section 3.2.

Define T_{UMJS} to be the basic state for the temperature profile described in Ullrich *et al.* [2013], $\overline{T}$ to be the horizontal mean of all values of T_{UMJS} at each height r, and T_{USSA} to be the USSA temperature profile. Then the temperature profile that gradually merges T_{UMJS} with T_{UMJS}, defined to be $\widetilde{T}_{\mathrm{USSA}}$ is as follows:

$$\widetilde{T}_{\mathrm{USSA}} = T_{\mathrm{UMJS}} + aT_{\mathrm{USSA}} - a\overline{T}, \tag{E.83}$$

where $a \in [0,1]$ varies between 0 and 1 from 0 km to 30 km.

Appendix F

Spherical Polar Coordinates

In this appendix, various vector calculus identities in meteorological spherical polar coordinates are derived and used in section 6.

F.1 Vector calculus identities

In meteorology and in ENDGame, the following spherical coordinates are used: the radius r, the longitude θ and the latitude ϕ. These have the corresponding unit vectors $\widehat{\boldsymbol{r}}$, $\widehat{\boldsymbol{\theta}}$ and $\widehat{\boldsymbol{\phi}}$. In terms of Cartesian coordinates, they are

$$r = \sqrt{x^2 + y^2 + z^2},\ \theta = \tan^{-1}\left(\frac{y}{x}\right),\ \phi = \sin^{-1}\left(\frac{z}{r}\right). \tag{F.1}$$

The Cartesian coordinates in terms of spherical coordinates are:

$$x = r\cos\theta\cos\phi,\ y = r\sin\theta\cos\phi,\ z = r\sin\phi. \tag{F.2}$$

The scale factors are:

$$h_r = 1,\ h_\theta = r\cos\phi,\ h_\phi = r. \tag{F.3}$$

The vector calculus identities are as follows:

$$\begin{aligned}
\boldsymbol{\nabla} V &= \widehat{\boldsymbol{r}}\frac{\partial V}{\partial r} + \widehat{\boldsymbol{\theta}}\frac{1}{r\cos\phi}\frac{\partial V}{\partial\theta} + \widehat{\boldsymbol{\phi}}\frac{1}{r}\frac{\partial V}{\partial\phi}, && \text{(F.4)}\\
\boldsymbol{\nabla}\cdot\boldsymbol{F} &= \frac{1}{r^2}\frac{\partial(r^2F_r)}{\partial r} + \frac{1}{r\cos\phi}\frac{\partial F_\theta}{\partial\theta} + \frac{1}{r\cos\phi}\frac{\partial}{\partial\phi}(F_\phi\cos\phi), && \text{(F.5)}\\
\nabla^2 V &= \frac{1}{r^2}\frac{\partial}{\partial r}\left(r^2\frac{\partial V}{\partial r}\right) + \frac{1}{r^2\cos^2\phi}\frac{\partial^2 V}{\partial\theta^2} + \frac{1}{r^2\cos\phi}\frac{\partial}{\partial\phi}\left(\frac{\partial V}{\partial\phi}\cos\phi\right), && \text{(F.6)}\\
\boldsymbol{n}\cdot\boldsymbol{\nabla} V &= n_r\frac{\partial V}{\partial r} + \frac{n_\theta}{r\cos\phi}\frac{\partial V}{\partial\theta} + \frac{n_\phi}{r}\frac{\partial V}{\partial\phi}, && \text{(F.7)}\\
\boldsymbol{n}\cdot\boldsymbol{\nabla}\boldsymbol{F} &= \widehat{\boldsymbol{r}}\left(\boldsymbol{n}\cdot\boldsymbol{\nabla}F_r - \frac{n_\theta F_\theta}{r} - \frac{n_\phi F_\phi}{r}\right)
\end{aligned}$$

$$
\begin{aligned}
&+\widehat{\boldsymbol{\theta}}\left(\boldsymbol{n}\cdot\boldsymbol{\nabla}F_\theta-\frac{n_\theta F_\phi}{r}\tan\phi+\frac{n_\theta F_r}{r}\right)\\
&+\widehat{\boldsymbol{\phi}}\left(\boldsymbol{n}\cdot\boldsymbol{\nabla}F_\phi+\frac{n_\phi F_r}{r}+\frac{n_\theta F_\theta}{r}\tan\phi\right),
\end{aligned}
\tag{F.8}
$$

where V is a scalar, and $\boldsymbol{n}=(n_r,n_\theta,n_\phi)$ and $\boldsymbol{F}=(F_r,F_\theta,F_\phi)$ are vectors. Using (F.8), the following identities involving the unit vectors $\widehat{\boldsymbol{r}}$, $\widehat{\boldsymbol{\theta}}$ and $\widehat{\boldsymbol{\phi}}$ are found:

$$
\begin{aligned}
\widehat{\boldsymbol{r}}\cdot\boldsymbol{\nabla}\widehat{\boldsymbol{r}} &= \boldsymbol{0}, & \widehat{\boldsymbol{r}}\cdot\boldsymbol{\nabla}\widehat{\boldsymbol{\theta}} &= \boldsymbol{0}, & \widehat{\boldsymbol{r}}\cdot\boldsymbol{\nabla}\widehat{\boldsymbol{\phi}} &= \boldsymbol{0},\\
\widehat{\boldsymbol{\theta}}\cdot\boldsymbol{\nabla}\widehat{\boldsymbol{r}} &= \frac{\widehat{\boldsymbol{\theta}}}{r}, & \widehat{\boldsymbol{\theta}}\cdot\boldsymbol{\nabla}\widehat{\boldsymbol{\theta}} &= -\frac{\widehat{\boldsymbol{r}}}{r}+\frac{\tan\phi}{r}\widehat{\boldsymbol{\phi}}, & \widehat{\boldsymbol{\theta}}\cdot\boldsymbol{\nabla}\widehat{\boldsymbol{\phi}} &= -\frac{\tan\phi}{r}\widehat{\boldsymbol{\theta}},\\
\widehat{\boldsymbol{\phi}}\cdot\boldsymbol{\nabla}\widehat{\boldsymbol{r}} &= \frac{\widehat{\boldsymbol{\phi}}}{r}, & \widehat{\boldsymbol{\phi}}\cdot\boldsymbol{\nabla}\widehat{\boldsymbol{\theta}} &= 0, & \widehat{\boldsymbol{\phi}}\cdot\boldsymbol{\nabla}\widehat{\boldsymbol{\phi}} &= -\frac{\widehat{\boldsymbol{r}}}{r}.
\end{aligned}
\tag{F.9}
$$

F.2 The rate-of-strain tensor and stress tensor

F.2.1 Spherical polar coordinates

The full stress tensor in spherical polar coordinates is given by:

$$
\boldsymbol{\sigma}=(\boldsymbol{\sigma}_r,\boldsymbol{\sigma}_\theta,\boldsymbol{\sigma}_\phi)^T,
\tag{F.10}
$$

where

$$
\boldsymbol{\sigma}_r = (\sigma_{rr},\sigma_{r\theta},\sigma_{r\phi}),
\tag{F.11}
$$

$$
\boldsymbol{\sigma}_\theta = (\sigma_{\theta r},\sigma_{\theta\theta},\sigma_{\theta\phi}),
\tag{F.12}
$$

$$
\boldsymbol{\sigma}_\phi = (\sigma_{\phi r},\sigma_{\phi\theta},\sigma_{\phi\phi}).
\tag{F.13}
$$

From Batchelor [2000], the expression for the full stress tensor in a fully compressible fluid can be found to be

$$
\boldsymbol{\sigma}=\boldsymbol{\tau}-p\boldsymbol{I},
\tag{F.14}
$$

where $\boldsymbol{\tau}$ is the deviatoric stress tensor: the trace-free part of the rate-of-strain tensor $\boldsymbol{e}$, i.e. $\mathrm{Tr}(\tau)=0$, and p is the pressure given by equation (E.1). The components of the rate-of-strain tensor are found as in Batchelor [2000] using the vector calculus identities introduced in appendix F.1, and are as follows:

$$
e_{rr} = \widehat{\boldsymbol{r}}\cdot(\widehat{\boldsymbol{r}}\cdot\boldsymbol{\nabla}\boldsymbol{u}) = \frac{\partial w}{\partial r},
\tag{F.15}
$$

$$\begin{aligned}
e_{\theta\theta} &= \qquad \widehat{\boldsymbol{\theta}} \cdot (\widehat{\boldsymbol{\theta}} \cdot \boldsymbol{\nabla u}) &&= \frac{1}{r\cos\phi}\frac{\partial u}{\partial \theta} - \frac{v}{r}\tan\phi + \frac{w}{r}, && \text{(F.16)}\\
e_{\phi\phi} &= \qquad \widehat{\boldsymbol{\phi}} \cdot (\widehat{\boldsymbol{\phi}} \cdot \boldsymbol{\nabla u}) &&= \frac{1}{r}\frac{\partial v}{\partial \phi} + \frac{w}{r}, && \text{(F.17)}\\
e_{r\theta} &= \frac{1}{2}\widehat{\boldsymbol{r}} \cdot (\widehat{\boldsymbol{\theta}} \cdot \boldsymbol{\nabla u}) + \frac{1}{2}\widehat{\boldsymbol{\theta}} \cdot (\widehat{\boldsymbol{r}} \cdot \boldsymbol{\nabla u}) &&= \frac{1}{2}\left[r\frac{\partial}{\partial r}\left(\frac{u}{r}\right) + \frac{1}{r\cos\phi}\frac{\partial w}{\partial \theta}\right], && \text{(F.18)}\\
e_{r\phi} &= \frac{1}{2}\widehat{\boldsymbol{r}} \cdot (\widehat{\boldsymbol{\phi}} \cdot \boldsymbol{\nabla u}) + \frac{1}{2}\widehat{\boldsymbol{\phi}} \cdot (\widehat{\boldsymbol{r}} \cdot \boldsymbol{\nabla u}) &&= \frac{1}{2}\left[r\frac{\partial}{\partial r}\left(\frac{v}{r}\right) + \frac{1}{r}\frac{\partial w}{\partial \phi}\right], && \text{(F.19)}\\
e_{\theta\phi} &= \frac{1}{2}\widehat{\boldsymbol{\theta}} \cdot (\widehat{\boldsymbol{\phi}} \cdot \boldsymbol{\nabla u}) + \frac{1}{2}\widehat{\boldsymbol{\phi}} \cdot (\widehat{\boldsymbol{\theta}} \cdot \boldsymbol{\nabla u}) &&= \frac{1}{2}\left[\frac{1}{r\cos\phi}\frac{\partial v}{\partial \theta} + \cos\phi\frac{\partial}{\partial \phi}\left(\frac{u}{r\cos\phi}\right)\right]. && \text{(F.20)}
\end{aligned}$$

Chapman & Cowling [1970] defines a trace-free tensor, defined here as the deviatoric stress tensor, given by

$$\boldsymbol{\tau} = 2\mu\boldsymbol{e} - \frac{2}{3}\mu(\boldsymbol{\nabla}\cdot\boldsymbol{u})\boldsymbol{I} = \mu\left[\boldsymbol{\nabla u} + (\boldsymbol{\nabla u})^T - \frac{2}{3}(\boldsymbol{\nabla}\cdot\boldsymbol{u})\boldsymbol{I}\right], \qquad \text{(F.21)}$$

The components of the full stress tensor $\boldsymbol{\sigma}$ are therefore as follows:

$$\begin{aligned}
\sigma_{rr} &= \tau_{rr} - p_e + \widetilde{\kappa}\boldsymbol{\nabla}\cdot\boldsymbol{u} &&= 2\mu\frac{\partial w}{\partial r} - p_e + \left(\widetilde{\kappa} - \frac{2\mu}{3}\right)\boldsymbol{\nabla}\cdot\boldsymbol{u} && \text{(F.22)}\\
\sigma_{\theta\theta} &= \tau_{\theta\theta} - p_e + \widetilde{\kappa}\boldsymbol{\nabla}\cdot\boldsymbol{u} &&= 2\mu\left(\frac{1}{r\cos\phi}\frac{\partial u}{\partial \theta} - \frac{v}{r}\tan\phi + \frac{w}{r}\right) - p_e + \left(\widetilde{\kappa} - \frac{2\mu}{3}\right)\boldsymbol{\nabla}\cdot\boldsymbol{u} && \text{(F.23)}\\
\sigma_{\phi\phi} &= \tau_{\phi\phi} - p_e + \widetilde{\kappa}\boldsymbol{\nabla}\cdot\boldsymbol{u} &&= 2\mu\left(\frac{1}{r}\frac{\partial v}{\partial \phi} + \frac{w}{r}\right) - p_e + \left(\widetilde{\kappa} - \frac{2\mu}{3}\right)\boldsymbol{\nabla}\cdot\boldsymbol{u} && \text{(F.24)}\\
\sigma_{r\theta} &= \tau_{r\theta} &&= \mu\left[r\frac{\partial}{\partial r}\left(\frac{u}{r}\right) + \frac{1}{r\cos\phi}\frac{\partial w}{\partial \phi}\right], && \text{(F.25)}\\
\sigma_{r\phi} &= \tau_{r\phi} &&= \mu\left[r\frac{\partial}{\partial r}\left(\frac{v}{r}\right) + \frac{1}{r}\frac{\partial w}{\partial \phi}\right], && \text{(F.26)}\\
\sigma_{\theta\phi} &= \tau_{\theta\phi} &&= \mu\left[\frac{1}{r\cos\phi}\frac{\partial v}{\partial \theta} + \cos\phi\frac{\partial}{\partial \phi}\left(\frac{u}{r\cos\phi}\right)\right]. && \text{(F.27)}
\end{aligned}$$

F.2.2 Evaluation of the stress tensor derivatives

In this section, the divergence of the stress tensors are found in meteorological spherical polar coordinates. A second order tensor can be built up from vectors $\boldsymbol{a}$, $\boldsymbol{b}$ as follows:

$$\boldsymbol{\nabla}\cdot(\boldsymbol{a}\boldsymbol{b}^T) = \boldsymbol{b}\boldsymbol{\nabla}\cdot\boldsymbol{a} + \boldsymbol{a}\cdot\boldsymbol{\nabla b}, \qquad \text{(F.28)}$$

where $\cdot^T$ denotes the transpose of a vector. Also, note that the full stress tensor $\boldsymbol{\sigma}$ (F.14) may be expressed in terms of the rate-of-strain tensor F.21 as follows:

$$\boldsymbol{\sigma} = 2\mu\boldsymbol{e} + \left[-p_e + \left(\widetilde{\kappa} - \frac{2\mu}{3}\right)\boldsymbol{\nabla}\cdot\boldsymbol{u}\right](\widehat{\boldsymbol{r}}\widehat{\boldsymbol{r}}^T + \widehat{\boldsymbol{\theta}}\widehat{\boldsymbol{\theta}}^T + \widehat{\boldsymbol{\phi}}\widehat{\boldsymbol{\phi}}^T), \qquad \text{(F.29)}$$

where $\boldsymbol{\nabla}\cdot\boldsymbol{u}$ is found using the vector calculus identities from appendix F.1:

$$\boldsymbol{\nabla}\cdot\boldsymbol{u}=\frac{1}{r^2}\frac{\partial}{\partial r}(r^2 w)+\frac{1}{\cos\phi}\frac{\partial u}{\partial\theta}+\frac{1}{\cos\phi}\frac{\partial}{\partial\phi}(v\cos\phi).\tag{F.30}$$

The separate components of $\boldsymbol{\nabla}\cdot\boldsymbol{\sigma}$ are as follows, found using (F.28) and (F.9):

$$\boldsymbol{\nabla}\cdot(\sigma_{rr}\,\widehat{\boldsymbol{r}}\widehat{\boldsymbol{r}}^T)=\frac{\widehat{\boldsymbol{r}}}{r^2}\frac{\partial}{\partial r}(r^2\sigma_{rr}),\tag{F.31}$$

$$\boldsymbol{\nabla}\cdot(\sigma_{r\theta}\,\widehat{\boldsymbol{r}}\widehat{\boldsymbol{\theta}}^T)=\frac{\widehat{\boldsymbol{\theta}}}{r^2}\frac{\partial}{\partial r}(r^2\sigma_{r\theta}),\tag{F.32}$$

$$\boldsymbol{\nabla}\cdot(\sigma_{r\phi}\,\widehat{\boldsymbol{r}}\widehat{\boldsymbol{\phi}}^T)=\frac{\widehat{\boldsymbol{\phi}}}{r^2}\frac{\partial}{\partial r}(r^2\sigma_{r\phi}),\tag{F.33}$$

$$\boldsymbol{\nabla}\cdot(\sigma_{\theta r}\,\widehat{\boldsymbol{\theta}}\widehat{\boldsymbol{r}}^T)=\frac{\widehat{\boldsymbol{r}}}{r\cos\phi}\frac{\partial\sigma_{\theta r}}{\partial\theta}+\frac{\sigma_{\theta r}}{r}\widehat{\boldsymbol{\theta}},\tag{F.34}$$

$$\boldsymbol{\nabla}\cdot(\sigma_{\theta\theta}\,\widehat{\boldsymbol{\theta}}\widehat{\boldsymbol{\theta}}^T)=\frac{\widehat{\boldsymbol{\theta}}}{r\cos\phi}\frac{\partial\sigma_{\theta\theta}}{\partial\theta}+\frac{\sigma_{\theta\theta}}{r}(-\widehat{\boldsymbol{r}}+\tan\phi\,\widehat{\boldsymbol{\phi}}),\tag{F.35}$$

$$\boldsymbol{\nabla}\cdot(\sigma_{\theta\phi}\,\widehat{\boldsymbol{\theta}}\widehat{\boldsymbol{\phi}}^T)=\frac{\widehat{\boldsymbol{\phi}}}{r\cos\phi}\frac{\partial\sigma_{\theta\phi}}{\partial\theta}-\frac{\sigma_{\theta\phi}}{r}\tan\phi\,\widehat{\boldsymbol{\theta}},\tag{F.36}$$

$$\boldsymbol{\nabla}\cdot(\sigma_{\phi r}\,\widehat{\boldsymbol{\phi}}\widehat{\boldsymbol{r}}^T)=\frac{\widehat{\boldsymbol{r}}}{r\cos\phi}\frac{\partial}{\partial\phi}(\sigma_{\phi r}\cos\phi)+\frac{\sigma_{\phi r}}{r}\widehat{\boldsymbol{\phi}},\tag{F.37}$$

$$\boldsymbol{\nabla}\cdot(\sigma_{\phi\theta}\,\widehat{\boldsymbol{\phi}}\widehat{\boldsymbol{\theta}}^T)=\frac{\widehat{\boldsymbol{\theta}}}{r\cos\phi}\frac{\partial}{\partial\phi}(\sigma_{\phi\theta}\cos\phi),\tag{F.38}$$

$$\boldsymbol{\nabla}\cdot(\sigma_{\phi\phi}\,\widehat{\boldsymbol{\phi}}\widehat{\boldsymbol{\phi}}^T)=\frac{\widehat{\boldsymbol{\phi}}}{r\cos\phi}\frac{\partial}{\partial\phi}(\sigma_{\phi\phi}\cos\phi)-\frac{\sigma_{\phi\phi}}{r}\widehat{\boldsymbol{r}}.\tag{F.39}$$

Hence, the divergence of the full stress tensor is given as follows:

$$\begin{aligned}\boldsymbol{\nabla}\cdot\boldsymbol{\sigma}\;=\;&\widehat{\boldsymbol{r}}\left[\frac{1}{r^2}\frac{\partial}{\partial r}(r^2\sigma_{rr})+\frac{1}{r\cos\phi}\frac{\partial\sigma_{\theta r}}{\partial\theta}-\frac{\sigma_{\theta\theta}}{r}+\frac{1}{r\cos\phi}\frac{\partial}{\partial\phi}(\sigma_{\phi r}\cos\phi)-\frac{\sigma_{\phi\phi}}{r}\right]\\&+\widehat{\boldsymbol{\theta}}\left[\frac{1}{r^2}\frac{\partial}{\partial r}(r^2\sigma_{r\theta})+\frac{\sigma_{\theta r}}{r}+\frac{1}{r\cos\phi}\frac{\partial\sigma_{\theta\theta}}{\partial\theta}-\frac{\sigma_{\theta\phi}}{r}\tan\phi+\frac{1}{r\cos\phi}\frac{\partial}{\partial\phi}(\sigma_{\phi\theta}\cos\phi)\right]\\&+\widehat{\boldsymbol{\phi}}\left[\frac{1}{r^2}\frac{\partial}{\partial r}(r^2\sigma_{r\phi})+\frac{\sigma_{\theta\theta}}{r}\tan\phi+\frac{1}{r\cos\phi}\frac{\partial\sigma_{\theta\phi}}{\partial\theta}+\frac{\sigma_{\phi r}}{r}+\frac{1}{r\cos\phi}\frac{\partial}{\partial\phi}(\sigma_{\phi\phi}\cos\phi)\right].\end{aligned}\tag{F.40}$$

Note that so far, the components of $\boldsymbol{\sigma}$ have not yet been evaluated.

First, consider the second term of the full stress tensor $\boldsymbol{\sigma}$ (F.29): abbreviate this as q and use the difference between p and p_e to note that:

$$q=p+\frac{2}{3}\mu\boldsymbol{\nabla}\cdot\boldsymbol{u}=p_e+\left(\frac{2}{3}\mu-\widetilde{\kappa}\right)\boldsymbol{\nabla}\cdot\boldsymbol{u}.\tag{F.41}$$

Using the vector calculus identities from appendix F.1, it can be found that:

$$\boldsymbol{\nabla}\cdot\left[q(\widehat{\boldsymbol{r}}\widehat{\boldsymbol{r}}^T+\widehat{\boldsymbol{\theta}}\widehat{\boldsymbol{\theta}}^T+\widehat{\boldsymbol{\phi}}\widehat{\boldsymbol{\phi}}^T)\right]=\widehat{\boldsymbol{r}}\frac{\partial q}{\partial r}+\frac{\widehat{\boldsymbol{\theta}}}{r\cos\phi}\frac{\partial q}{\partial\theta}+\frac{\widehat{\boldsymbol{\phi}}}{r}\frac{\partial q}{\partial\phi}=\boldsymbol{\nabla}q.\tag{F.42}$$

The divergence of the rate-of-strain tensor $2\mu\boldsymbol{e}$ may next be evaluated using the components of $\boldsymbol{e}$ given by equations (F.15)-(F.20) together with the expression for the stress tensor divergence (F.40). By noting the following results:

$$\frac{1}{r\cos^2\phi}\frac{\partial}{\partial\phi}(\cos^2\phi X) = \frac{1}{r\cos\phi}\frac{\partial}{\partial\phi}(\cos\phi X) - \frac{1}{r}\tan\phi\, X, \tag{F.43}$$

$$\frac{1}{r^3}\frac{\partial}{\partial r}(r^3 X) = \frac{1}{r}X + \frac{1}{r^2}\frac{\partial}{\partial r}(r^2 X), \tag{F.44}$$

then $\boldsymbol{\nabla}\cdot(2\mu\boldsymbol{e})$ may be expressed as follows:

$$\begin{aligned}
\boldsymbol{\nabla}\cdot(2\mu\boldsymbol{e}) = \; & \widehat{\boldsymbol{r}}\bigg\{-\frac{2\mu}{r}\left(\frac{2w}{r}+\frac{1}{r\cos\phi}\frac{\partial u}{\partial\theta}-\frac{v}{r}\tan\phi+\frac{1}{r}\frac{\partial v}{\partial\phi}\right)\\
&+\frac{2}{r^2}\frac{\partial}{\partial r}\left(\mu r^2\frac{\partial w}{\partial r}\right)\\
&+\frac{1}{r\cos\phi}\frac{\partial}{\partial\theta}\left[\mu\left(\frac{1}{r\cos\phi}\frac{\partial w}{\partial\theta}-\frac{u}{r}+\frac{\partial u}{\partial r}\right)\right]\\
&+\frac{1}{r\cos\phi}\frac{\partial}{\partial\phi}\left[\mu\cos\phi\left(\frac{1}{r}\frac{\partial w}{\partial\phi}-\frac{v}{r}+\frac{\partial v}{\partial r}\right)\right]\bigg\}\\
&+\widehat{\boldsymbol{\theta}}\bigg\{\frac{1}{r^3}\frac{\partial}{\partial r}\left[\mu r^3\left(\frac{1}{r}\frac{\partial w}{\partial\phi}-\frac{v}{r}+\frac{\partial v}{\partial r}\right)\right]\\
&+\frac{2}{r\cos\phi}\frac{\partial}{\partial\theta}\left[\mu\left(\frac{w}{r}+\frac{1}{r\cos\phi}\frac{\partial u}{\partial\theta}-\frac{v}{r}\tan\phi\right)\right]\\
&+\frac{1}{r\cos^2\phi}\frac{\partial}{\partial\phi}\left[\mu\cos^2\phi\left(\frac{u}{r}\tan\phi+\frac{1}{r}\frac{\partial u}{\partial\phi}+\frac{1}{r\cos\phi}\frac{\partial v}{\partial\theta}\right)\right]\bigg\}\\
&+\widehat{\boldsymbol{\phi}}\bigg\{\frac{2\tan\phi}{r}\left[\mu\left(\frac{w}{r}+\frac{1}{r\cos\phi}\frac{\partial u}{\partial\theta}-\frac{v}{r}\tan\phi\right)\right]\\
&+\frac{1}{r^3}\frac{\partial}{\partial r}\left[\mu r^3\left(\frac{1}{r}\frac{\partial w}{\partial\phi}-\frac{v}{r}+\frac{\partial v}{\partial r}\right)\right]\\
&+\frac{1}{r\cos\phi}\frac{\partial}{\partial\theta}\left[\mu\left(\frac{u}{r}\tan\phi+\frac{1}{r}\frac{\partial u}{\partial\phi}+\frac{1}{r\cos\phi}\frac{\partial v}{\partial\theta}\right)\right]\\
&+\frac{2}{r\cos\phi}\frac{\partial}{\partial\phi}\left[\mu\cos\phi\left(\frac{w}{r}+\frac{1}{r}\frac{\partial v}{\partial\phi}\right)\right]\bigg\}.
\end{aligned} \tag{F.45}$$

The divergence of the full stress tensor $\boldsymbol{\sigma}$ can then be obtained by taking:

$$\boldsymbol{\nabla}\cdot\boldsymbol{\sigma} = \boldsymbol{\nabla}\cdot(2\mu\boldsymbol{e}) - \boldsymbol{\nabla}q, \tag{F.46}$$

and the divergence of the deviatoric stress tensor is just:

$$\boldsymbol{\nabla}\cdot\boldsymbol{\tau} = \boldsymbol{\nabla}\cdot\boldsymbol{\sigma} - \boldsymbol{\nabla}p \tag{F.47}$$

Lastly, $\boldsymbol{\sigma}:\boldsymbol{\nabla}\boldsymbol{u}$ is expressed as follows:

$$\boldsymbol{\sigma}:\boldsymbol{\nabla}\boldsymbol{u} = \boldsymbol{\nabla}\cdot(\boldsymbol{\sigma}\cdot\boldsymbol{u}) - \boldsymbol{u}\cdot(\boldsymbol{\nabla}\cdot\boldsymbol{\sigma}), \tag{F.48}$$

where $\boldsymbol{\sigma} \cdot \boldsymbol{u} = (\boldsymbol{\sigma}_r \cdot \boldsymbol{u}, \boldsymbol{\sigma}_\theta \cdot \boldsymbol{u}, \boldsymbol{\sigma}_\phi \cdot \boldsymbol{u})^T$. The $\boldsymbol{u} \cdot (\boldsymbol{\nabla} \cdot \boldsymbol{\sigma})$ term is just found using (F.46), and the $\boldsymbol{\nabla} \cdot (\boldsymbol{\sigma} \cdot \boldsymbol{u})$ term is found using the vector calculus identities from appendix F.1 with equations (F.22)-(F.27) for the components of $\boldsymbol{\sigma}$. Many of the terms end up concatenating together to give a much more succinct expression for $\boldsymbol{\sigma} : \boldsymbol{\nabla u}$ as follows:

$$
\begin{aligned}
\boldsymbol{\sigma} : \boldsymbol{\nabla u} \;=\; & \frac{1}{r^2}\frac{\partial(r^2 w)}{\partial r}\Bigg\{ -p_e + 2\mu\frac{\partial w}{\partial r} \\
& \qquad + \left(\widetilde{\kappa} - \frac{2\mu}{3}\right)\left[\frac{1}{r^2}\frac{\partial(r^2 w)}{\partial r} + \frac{1}{r\cos\phi}\frac{\partial u}{\partial\theta} + \frac{1}{r\cos\phi}\frac{\partial}{\partial\phi}(v\cos\phi)\right]\Bigg\} \\
+ \; & \frac{1}{r^2}\frac{\partial(r^2 u)}{\partial r}\mu\left[\frac{1}{r\cos\phi}\frac{\partial w}{\partial\theta} + r\frac{\partial}{\partial r}\left(\frac{u}{r}\right)\right] \\
+ \; & \frac{1}{r^2}\frac{\partial(r^2 v)}{\partial r}\mu\left[\frac{1}{r}\frac{\partial w}{\partial\phi} + r\frac{\partial}{\partial r}\left(\frac{v}{r}\right)\right] \\
+ \; & \frac{1}{r\cos\phi}\frac{\partial w}{\partial\theta}\mu\left[\frac{1}{r\cos\phi}\frac{\partial w}{\partial\phi} + r\frac{\partial}{\partial r}\left(\frac{u}{r}\right)\right] \\
+ \; & \frac{1}{r\cos\phi}\frac{\partial u}{\partial\theta}\Bigg\{2\mu\left[-p_e + \frac{w}{r} + \frac{1}{r\cos\phi}\frac{\partial u}{\partial\theta} - \tan\phi\;\frac{v}{r}\right] \\
& \qquad + \left(\widetilde{\kappa} - \frac{2\mu}{3}\right)\left[\frac{1}{r^2}\frac{\partial(r^2 w)}{\partial r} + \frac{1}{r\cos\phi}\frac{\partial u}{\partial\theta} + \frac{1}{r\cos\phi}\frac{\partial}{\partial\phi}(v\cos\phi)\right]\Bigg\} \\
+ \; & \frac{1}{r\cos\phi}\frac{\partial v}{\partial\theta}\mu\left[\frac{\partial}{\partial\phi}\left(\frac{u}{r\cos\phi}\right)\cos\phi + \frac{1}{r\cos\phi}\frac{\partial v}{\partial\theta}\right] \\
+ \; & \frac{1}{r\cos\phi}\frac{\partial}{\partial\phi}(w\cos\phi)\mu\left[\frac{1}{r}\frac{\partial w}{\partial\phi} + r\frac{\partial}{\partial r}\left(\frac{v}{r}\right)\right] \\
+ \; & \frac{1}{r\cos\phi}\frac{\partial}{\partial\phi}(u\cos\phi)\mu\left[\frac{1}{r\cos\phi}\frac{\partial v}{\partial\theta} + \frac{\partial}{\partial\theta}\left(\frac{u}{r\cos\phi}\right)\cos\phi\right] \\
+ \; & \frac{1}{r\cos\phi}\frac{\partial}{\partial\phi}(v\cos\phi)\Bigg\{-p_e + 2\mu\left[\frac{w}{r} + \frac{1}{r}\frac{\partial v}{\partial\phi}\right] \\
& \qquad + \left(\widetilde{\kappa} - \frac{2\mu}{3}\right)\left[\frac{1}{r^2}\frac{\partial(r^2 w)}{\partial r} + \frac{1}{r\cos\phi}\frac{\partial u}{\partial\theta} + \frac{1}{r\cos\phi}\frac{\partial}{\partial\phi}(v\cos\phi)\right]\Bigg\},
\end{aligned}
\tag{F.49}
$$

which reduces to:

$$
\boldsymbol{\sigma} : \boldsymbol{\nabla u} = \boldsymbol{\tau} : \boldsymbol{\nabla u} - p_e \boldsymbol{\nabla} \cdot \boldsymbol{u} + \widetilde{\kappa}\, \boldsymbol{\nabla} \cdot \boldsymbol{u} \tag{F.50}
$$

Acronyms

CME	Coronal Mass Ejection
COSMIC	Constellation Observing System for Meteorology, Ionosphere and Climate
D-RAP	D-Region Absorption model
EIA	Equatorial Ionospheric Anomaly
ENDGame	Even Newer Dynamics for the General atmospheric modelling of the environment
EUV	Extreme Ultraviolet radiation
FTCS	Forward-in-Time and Centred-in-Space
FUV	Far Ultraviolet radiation
GAIA	Ground to topside model of Atmosphere and Ionosphere for Aeronomy
GCM	General Circulation Model
GITM	Global Ionosphere-Thermosphere Model
GPS	Global Positioning System
GRACE	Gravity Recovery And Climate Experiment
GungHo	Globally Uniform Next Generation Highly Optimized
IMAGE	Imager for Magnetopause-to-Aurora Global Exploration
LFRic	Name given to next generation model to replace the UM. Named in recognition of L.F. Richardson.
MOSWOC	Met Office Space Weather Operations Centre
MSIS-83	Mass Spectrometer/ Incoherent Scatter empirical model
ND	New Dynamics
REFM	Relativistic Electron Forecast Model
SABER	SAtellite Broadband for European Regions
SI	Semi-Implicit
SISL	Semi-Implicit and Semi-Lagrangian
SL	Semi-Lagrangian

SSW	Stratospheric Sudden Warming
SWPC	Space Weather Prediction Center
TEC	Total Electron Count
TIDI	TIMED Doppler Interferometer
TIMED	Thermosphere, Ionosphere, Mesosphere, Energetics and Dynamics satellite
UM	Unified Model
US COESA	United States Committee on Extension to the Standard Atmosphere
USSA	US Standard Atmosphere
UV	Ultraviolet radiation
WACCM-X	Whole Atmosphere Community Climate Model eXtension
WAM	Whole Atmosphere Model
WSA Enlil	Wang-Sheeley-Arge Enlil CME and solar wind model

Mathematical Notation

Definition	**Symbol**	**Unit**
basic state of variable	$\cdot_0$	
best guess for next timestep	$(\ldots)^{(l)}$	
bulk viscosity	$\widetilde{\kappa}$	$\mathrm{kg\,m^{-1}\,s^{-1}}$
Buoyancy frequency	N^2	$\mathrm{s^{-1}}$
cell height	Δr_k	m
cell width (ϕ direction)	$\Delta\phi_j$	m
cell width (θ direction)	$\Delta\theta_i$	m
cloud frozen water variable	$\cdot_{cf}$	
cloud liquid water variable	$\cdot_{cl}$	
coefficient of molecular thermal conductivity	λ	$\mathrm{kg\,m\,K^{-1}\,s^{-3}}$
coefficient of molecular viscosity	μ	$\mathrm{kg\,m^{-1}\,s^{-1}}$
current timestep	n	
Del operator	$\boldsymbol{\nabla}$	
density	ρ	$\mathrm{kg\,m^{-3}}$
density of gas species X	ρ_X	$\mathrm{kg\,m^{-3}}$
departure point	r_D	m
departure point iteration count	$.^{(d)}$	
deviatoric stress tensor	d_{ij}	

Definition	**Symbol**	**Unit**
diffusive heat flux	$\boldsymbol{q}$	
dry air variable	$\cdot_d$	
Earth's rotation vector	$\boldsymbol{\Omega}$	
effective frequency	$\widehat{\omega}$	s^{-1}
effective wavenumber in the x or θ direction	$\widehat{k}$	m^{-1}
effective wavenumber in the z or r direction	$\widehat{m}$	m^{-1}
equilibrium pressure	p_e	$\mathrm{kg\,m^{-1}\,s^{-2}}$
Exner pressure	Π	
exospheric temperature	T_{exo}	K
explicitly treated variable	$(\ldots)_D^{(n)}$	
explicitness parameter	β	
frequency	ω	s^{-1}
full stress tensor	$\boldsymbol{\sigma}$	
gas constant	R	
gas constant ratio	ϵ	
geopotential	Φ	
Gradient with respect to the wavevector	$\boldsymbol{\nabla_k}$	
gravitational acceleration	g	$\mathrm{m\,s^{-1}}$
gravitational vector	$\boldsymbol{g}$	
group velocity (vertical direction)	c_g	$\mathrm{m\,s^{-1}}$
group velocity vector	$\boldsymbol{c}_g$	
hydrostatic switch	δ_V	
implicitly treated variable	$(\ldots)^{(n+1)}$	
implicitness parameter	α	
increment term	$\cdot'$	
interpolated ρ variables	$\overline{(\ldots)}^{w}$	
interpolated w variables	$\overline{(\ldots)}^{\rho}$	
inverse height scale	Γ	m
isentropic exponent	κ	
kinematic viscosity	$\tilde{\nu}$	$\mathrm{kg\,m^{-1}\,s^{-1}}$
Lagrangian derivative	$\frac{D}{Dt}$	
length scale	L	m
mean quantity	$\overline{(\ldots)}$	

Definition	**Symbol**	**Unit**
mixing ratio of gas species X	m_X	
perturbed variable	$\cdot'$	
phase velocity	$\boldsymbol{c_p}$	ms^{-1}
phase velocity (vertical direction)	c_p	$\mathrm{m\,s}^{-1}$
position in Cartesian coordinates: horizontal direction 1	x	m
position in Cartesian coordinates: horizontal direction 2	y	m
position in Cartesian coordinates: vertical direction	z	m
position in spherical polar coordinates: altitude	r	m
position in spherical polar coordinates: latitude angle	ϕ	rad
position in spherical polar coordinates: longitude angle	θ	rad
position vector in spherical polar coordinates	$\boldsymbol{r}$	
potential temperature	Θ	K
Prandtl number	Pr	
pressure	p	$\mathrm{kg\,m}^{-1}\,\mathrm{s}^{-2}$
pressure gradient and gravity terms	Ψ	
Rayleigh viscosity	ν	
reference profile term	$\cdot^*$	
residual for ρ equation	R_ρ	
residual for ρ equation (alternative)	$\widehat{R}_\rho$	
residual for Θ equation	R_Θ	
residual for u equation	R_u	
residual for v equation	R_v	
residual for w equation	R_w	
scale height	H	m
source term for the momentum equation	$\boldsymbol{S^u}$	
source term for the thermodynamic equation	$\boldsymbol{S}^\Theta$	
specific heat capacity at constant pressure	C_p	$\mathrm{kg\,m}^2\,\mathrm{K}^{-1}\,\mathrm{s}^{-2}$
specific heat capacity at constant volume	C_v	$\mathrm{kg\,m}^2\,\mathrm{K}^{-1}\,\mathrm{s}^{-2}$
specific internal energy	e	
speed of sound	c_s	$\mathrm{m\,s}^{-1}$
temperature	T	K
time-scale for acoustic wave growth	τ_{growth}	s
time-scale for decay due to off-centring of the SI scheme	τ_α	s
time-scale for diffusion	τ_{diff}	s
time-scale for horizontal diffusion	τ_{diff_H}	s
timestep	Δt	s

Definition	**Symbol**	**Unit**
variable stored at the current ρ-level	$\cdot_k$	
variable stored at the current w-level	$\cdot_{k+1/2}$	
velocity in the x or θ direction	u	$\mathrm{m\,s^{-1}}$
velocity in the y or ϕ direction	v	$\mathrm{m\,s^{-1}}$
velocity in the z or r direction	w	$\mathrm{m\,s^{-1}}$
velocity vector	$\boldsymbol{u}$	
virtual potential temperature	Θ_v	K
virtual temperature	T_v	K
viscous step terms	$\cdot^{\dagger}$	
vorticity	$\boldsymbol{\omega}$	
water vapour variable	$\cdot_v$	
wave amplification factor	W	
wavenumber in the x or θ direction	k	$\mathrm{m^{-1}}$
wavenumber in the y or ϕ direction	l	$\mathrm{m^{-1}}$
wavenumber in the z or r direction	m	$\mathrm{m^{-1}}$
wavevector	$\boldsymbol{k}$	
weighting terms (from ρ-levels to w-levels)	$a_{k+1/2},\ b_{k+1/2}$	
weighting terms (from w-levels to ρ-levels)	$a_k,\ b_k$	

Bibliography

Afraimovich, E. L., Kosogorov, E. A., Perevalova, N. P., & Plotnikov, A. V. 2001. The use of GPS arrays in detecting shock-acoustic waves generated during rocket launchings. *Journal of Atmospheric and Solar-Terrestrial Physics*, **63**(18), 1941 – 1957.

Akmaev, R. A. 2011. Whole Atmosphere Modelling: Connecting Terrestrial and Space Weather. *Reviews of Geophysics*, **49**(4).

Akmaev, R. A., Fuller-Rowell, T. J., Wu, F., Forbes, J. M., Zhang, X., Anghel, A. F., Iredell, M. D., Moorthi, S., & Juang, H. M. 2008. Tidal variability in the lower thermosphere: Comparison of Whole Atmosphere Model (WAM) simulations with observations from TIMED. *Geophysical Research Letters*, **35**(3).

Arakawa, A., & Lamb, V. R. 1977. A Potential Enstrophy and Energy Conserving Scheme for the Shallow Water Equations. *Monthly Weather Review*, **109**(1), 18 – 36.

Baker, D. N., McPherron, R. L., Cayton, T. E., & Klebesadel, R. W. 1990. Linear prediction filter analysis of relativistic electron properties at 6.6 R_E. *Journal of Geophysical Research*, **95**(A9), 15133 – 15140.

Batchelor, G. K. 2000. *An Introduction to Fluid Dynamics.* Cambridge: Cambridge University Press.

Boor, C. De. 1978. *A Practical Guide to Splines.* First edn. Applied Mathematical Sciences, vol. 27, no. 1. Springer-Verlag New York.

Brown, A., Milton, S., Cullen, M., Golding, B., Mitchell, J., & Shelly, A. 2012. Unified Modeling and Prediction of Weather and Climate: A 25-Year Journey. *American Meteorological Society Journals*, **93**(12), 1865 – 1877.

Bush, M., Bornemann, J., Earnshaw, P., Heming, J., Smith, C., & Wilson, C. 2014 (May). ENDGame: The next Met Office atmospheric dynamical core. *Page 5732 of: EGU General Assembly Conference Abstracts.* EGU General Assembly Conference Abstracts, vol. 16.

Cannon, P. S., Angling, M., Barclay, L., Curry, C., Dyer, C., Edwards, R., Greene, G., Hapgood, M., Horne, R., Jackson, D., Mitchell, C., Owen, J., Richards, A., Rogers, C., Ryden, K., Saunders, S., Sweeting, M., Tanner, R., Thomson, A., & Underwood, C. 2013. Extreme Space Weather - A Report Published by the UK Royal Academy of Engineering. *Space Weather*, **11**(4), 138 – 139.

Chapman, S., & Cowling, T. G. 1970. *The Mathematical Theory of Non-Uniform Gases: An Account of the Kinetic Theory of Viscosity, Thermal Conduction and Diffusion in Gases.* Third edn. Cambridge Mathematical Library. Cambridge University Press.

Charney, J. G., & Phillips, N. A. 1953. Numerical integration of the Quasi-Geostropgic Equations for Barotropic and Simple Baroclinic Flows. *Journal of Meteorology*, **10**(2), 71–99.

Cullen, M. J. P., & Davies, T. 1991. A conservative split-explicit integration scheme with fourth-order horizontal advection. *Quarterly Journal for the Royal Meteorological Society*, **117**(501), 993 – 1002.

Curry, J. A., & Webster, P. J. 1998. *Thermodynamics of Atmospheres & Oceans.* International Geophysics Series, vol. 65. London: Academic Press.

Daley, R. 1998. The normal modes of the spherical non-hydrostatic equations with applications to the filtering of acoustic modes. *Tellus*, **40**(A), 96 – 106.

Davies, T., Cullen, M. J., Malcolm, A. J., Mawson, M. H., Staniforth, A., White, A. A., & Wood, N. 2005. A new dynamical core for the Met Office's global and regional modelling of the atmosphere. *Quarterly Journal of the Royal Meteorological Society*, **131**(608), 1759 – 1782.

Deng, Y., Richmond, A. D., Ridley, A. J., & Liu, H.-L. 2008. Assessment of the non-hydrostatic effect on the upper atmosphere using a general circulation model (GCM). *Geophysical Research Letters*, **35**(1).

Dingle, R. B. 1973. *Asymptotic Expansions: Their Derivation and Interpretation.* London: Academic Press.

Durran, D. R. 1999. *Numerical Methods for Wave Equations in Geophysical Fluid Dynamics.* 1 edn. Texts in Applied Mathematics, vol. 32. New York: Springer-Verlag.

Fuller-Rowell, T. J., Akmaev, R. A., Wu, F., Anghel, A., Maruyama, N., Anderson, D. N., Codrescu, M. V., Iredell, M., Moorthi, S., Juang, H.-M., Hou, Y.-T., & Millward, G. 2008. Impact of terrestrial weather on the upper atmosphere. *Geophysical Research Letters*, **35**(9).

Garcia, A. L. 1994. *Numerical Methods for Physicists.* First edn. New Jersey: Prentice-Hall.

Gill, A. E. 1982. *Atmosphere-Ocean Dynamics.* International Geophysics, vol. 30. Academic Press.

Goncharenko, L. P., Chau, J. L., Liu, H. L., & Coster, A. J. 2010. Unexpected connections between the stratosphere and ionosphere. *Geophysical Research Letters*, **37**(10).

Griffin, D. J., & Thuburn, J. 2018. Numerical effects on vertical wave propagation in deep-atmosphere models. *Quarterly Journal of the Royal Meteorological Society*, **144**(711), 567 – 580.

Hedin, A. E. 1991. Extension of the MSIS Thermospheric Model into the Middle and Lower Atmosphere. *Journal of Geophysical Research*, **96**(A2), 1159 – 1172.

Hickey, M. P., Schubert, G., & Walterscheid, R. L. 2001. Acoustic wave heating of the thermosphere. *Journal of Geophysical Reseach: Space Physics*, **106**(A10), 21543 – 21548.

Holdaway, D., Thuburn, J., & Wood, N. 2012. Comparison of Lorenz and Charney-Phillips vertical discretisations for dynamics–boundary layer coupling. Part I: Steady states. *Quarterly Journal of the Royal Meteorological Society*, **139**(673), 1073 – 1086.

Howison, S. 2005. *Practical Applied Mathematics: Modelling, Analysis, Approximation.* Cambridge Texts in Applied Mathematics. Oxford Centre for Industrial and Applied Mathematics , Mathematical Institute , Oxford University: Cambridge University Press.

Immel, T. J., Sagawa, E., England, S. L., Henderson, S. B., Hagan, M. E., Mende, S. B., Frey, H. U., Swenson, C. M., & Paxton, L. J. 2006. Control of equatorial ionospheric morphology by atmospheric tides. *Geophysical Research Letters*, **33**(15).

Ineson, S., Scaife, A. A., Knight, J. R., Manners, J. C., Dunstone, N. J., Gray, L. J., & Haigh, J. D. 2011. Solar forcing of winter climate variability in the Northern Hemisphere. *Nature Geoscience*, **4**(11), 753 – 757.

Jablonowski, C., & Williamson, D. L. 2006. A baroclinic instability test case for atmospheric model dynamical cores. *Quarterly Journal of the Royal Meteorological Society*, **132**(621C), 2943 – 2975.

Jin, H., Miyoshi, Y., Fujiwara, H., & Sinagawa, H. 2008. Electrodynamics of the formation of ionospheric wave number 4 longitudinal structure. *Journal of Geophysical Research*, **113**(September).

Jin, H., Miyoshi, Y., Fujiwara, H., Shinagawa, H., Terada, K., Terada, N., Ishii, M., Otsuka, Y., & Saito, A. 2011. Vertical connection from the tropospheric activities to the ionospheric longitudinal structure simulated by a new Earth's whole atmosphere-ionosphere coupled model. *Journal of Geophysical Reseach: Space Physics*, **116**(A1).

Kelley, M. C. 2009. *The Earth's Ionosphere: Plasma Physics and Electrodynamics.* 2 edn. International Geophysics, vol. 96. Academic Press.

Klemp, J. B., Dudhia, J., & Hassiotis, A. D. 2008. An Upper Gravity-Wave Absorbing Layer for NWP Applications. *American Meteorological Society Journals*, **136**(10), 3987 – 4004.

Krauss, S., Temmer, M., Veronig, A., Baur, O., & Lammer, H. 2015. Thermospheric and geomagnetic responses to interplanetary coronal mass ejections observed by ACE and GRACE: Statistical results. *Journal of Geophysical Research: Space Physics*, **120**(10), 8848 – 8860.

Larsen, M. F., & Meriwether, J. W. 2012. Vertical winds in the thermosphere. *Journal of Geophysical Reseach: Space Physics*, **117**(A9).

Lighthill, J. 1978. *Waves in Fluids.* Cambridge: Cambridge University Press.

Lin, C. H., Wang, W., Hagan, M. E., Hsiao, C. C., Immel, T. J., Hsu, M. L., Liu, J. Y., Paxton, L. J., Fang, T. W., & Liu, C. H. 2007. Plausible effect of atmospheric tides on the equatorial ionosphere observed by the FORMOSAT-3/COSMIC: Three-dimensional electron density structures. *Geophysical Research Letters*, **34**(11).

Liu, H.-L., Foster, B. T., Hagan, M. E., McInerney, J. M., Maute, A., Qian, L., Richmond, A. D., Roble, R. G., Solomon, S. C., Garcia, R. R., Kinnison, D., Marsh, D. R., Smith, A. K., Richter, J., Sassi, F., & Oberheide, J. 2010. Thermosphere extension of the Whole Atmosphere Community Climate Model. *Journal of Geophysical Reseach: Space Physics*, **115**(A12).

Lockwood, M., Harrison, R. G., Woollings, T., & Solanki, S. K. 2010. Are cold winters in Europe associated with low solar activity? *Environmental Research Letters*, **5**(2).

Long, D., & Thuburn, J. 2011. Numerical wave propagation on non-uniform one-dimensional staggered grids. *Journal of Computational Physics*, **230**(7), 2643 – 2659.

Medvedev, A. S., Yiğit, E., & Hartogh, Paul. 2017. Ion Friction and Quantification of the Geomagnetic Influence on Gravity Wave Propagation and Dissipation in the Thermosphere-Ionosphere. *Journal of Geophysical Research: Space Physics*, **122**(12), 21464 – 21475.

Miyoshi, Y., Fujiwara, H., Jin, H., & Shinagawa, H. 2014. A global view of gravity waves in the thermosphere simulated by a general circulation model. *Journal of Geophysical Research*, **119**(7), 5807 – 5820.

Mohebalhojeh, A. R., & Dritschel, D. G. 2000. On the representation of gravity waves in numerical models of the shallow-water equations. *Quarterly Journal of the Royal Meteorological Society*, **126**(563), 669 – 688.

Nastrom, G. D., & Gage, K. S. 1985. A climatology of atmospheric wavenumber spectra of wind and temperature observed by commercial aircraft. *Journal of the Atmospheric Sciences*, **42**, 950 – 960.

Nelder, J. A., & Mead, R. 1965. A Simplex Method for Function Minimization. *The Computer Journal*, **7**(4), 308 – 313.

Pawlowski, D. J., & Ridley, A. J. 2008. Modeling the thermospheric response to solar flares. *Journal of Geophysical Research*, **113**(A10).

Payne, T. J. 2008. A linear-stability analysis of the semi-implicit semi-Lagrangian discretization of the fully-compressible equations. *Quarterly Journal of the Royal Meteorological Society*, **134**(632), 779 – 786.

Press, W. H., Teukolsky, S. A., Vetterling, W. T., & Flannery, B. P. 1993. *Numerical Recipes in FORTRAN; The Art of Scientific Computing*. Second edn. Numerical Recipes. Cambridge University Press.

Purser, R. J., & Leslie, L. M. 1988. A Semi-Implicit, Semi-Lagrangian Finite-Difference Scheme Using High-Order Spatial Differencing on a Nonstaggered Grid. *American Meteorological Society Journals*, **116**(October), 2069 – 2080.

Ridley, A. J., Deng, Y., & Tóth, G. 2006. The global ionosphere-thermosphere model. *Journal of Atmospheric and Solar-Terrestrial Physics*, **68**(8), 839 – 864.

Roble, R. G. 1983. Dynamics of the Earth's Thermosphere. *Reviews of Geophysics and Space Physics*, **21**(2), 217 – 233.

Roble, R. G., Ridley, E. C., & Dickinson, R. E. 1987. On the global mean structure of the thermosphere. *Journal of Geophysical Reseach: Space Physics*, **92**(A8), 8745 – 8758.

Salby, M. L. 1996. *Fundamentals of Atmospheric Physics*. International Geophysics Series, vol. 61. London: Academic Press.

Sauer, H. H., & Wilkinson, D. C. 2008. Global mapping of ionospheric HF/VHF radio wave absorption due to solar energetic protons. *Space Weather*, **6**(12).

Shaw, T. A., & Shepherd, T. G. 2007. Angular Momentum Conservation and Gravity Wave Drag Parameterization: Implications for Climate Models. *Journal of the Atmospheric Sciences*, **64**(April), 190 – 203.

Shinagawa, H., Iyemori, T., Saito, S., & Maruyama, T. 2007. A numerical simulation of ionospheric and atmospheric variations associated with the Sumatra earthquake on December 26, 2004. *Earth, Planets and Space*, **59**(9), 1015 – 1026.

Sinnhuber, M., Nieder, H., & Wieters, N. 2012. Energetic Particle Precipitation and the Chemistry of the Mesosphere/Lower Thermosphere. *Surveys in Geophysics*, **33**(6), 1281 – 1334.

Skamarock, W. C., & Klemp, J. B. 2008. A time-split nonhydrostatic atmospheric model for weather research and forecasting applications. *Journal of Computational Physics*, **227**(7), 3465 – 3485.

Space Weather Prediction Center (SWPC). 2008. *Relativistic Electron Forecast Model (REFM) documentation.* Tech. rept. NOAA, Boulder, Colorado.

Sutton, E. K., Forbes, J. M., & Nerem, R. S. 2005. Global thermospheric neutral density and wind response to the severe 2003 geomagnetic storms from CHAMP accelerometer data. *Journal of Geophysical Research*, **110**(A9).

Taktakishvili, A., Kuznetsova, M., MacNeice, P., Hesse, M., Rastätter, L., Pulkkinen, A., Chulaki, A., & Odstrcil, D. 2009. Validation of the coronal mass ejection predictions at the Earth orbit estimated by ENLIL heliosphere cone model. *Space Weather*, **7**(3).

Thuburn, J. 2006. Vertical discretizations giving optimal representation of normal modes: Sensitivity to the form of the pressure-gradient term. *Quarterly Journal of the Royal Meteorological Society*, **132**, 2809 – 2825.

Thuburn, J., Wood, N., & Staniforth, A. 2002. Normal modes of deep atmospheres. I: Spherical geometry. *Quarterly Journal of the Royal Meteorological Society*, **128**(584), 1771 – 1792.

Trefethen, L. N. 1982. Group Velocity in Finite Difference Schemes. *Society for Industrial and Applied Mathematics Review*, **24**(2), 113 – 136.

Ullrich, P. A., Melvin, T., Jablonowski, C., & Staniforth, A. 2013. A proposed baroclinic wave test case for deep- and shallow-atmosphere dynamical cores. *Quarterly Journal of the Royal Meteorological Society*, **140**(682), 1590 – 1602.

United States Committee on Extension to the Standard Atmosphere (COESA). 1976. *U.S. Standard Atmosphere 1976.* U.S. Government Printing Office, Washington, D.C.

Vadas, S. L. 2007. Horizontal and vertical propagation and dissipation of gravity waves in the thermosphere from lower atmospheric and thermospheric sources. *Journal of Geophysical Research: Space Physics*, **112**(A6).

Vallis, G. K. 2006. *Atmospheric and Oceanic Fluid Dynamics.* Cambridge University Press.

Vichnevetsky, R. 1981. Energy and group velocity in semi discretizations of hyperbolic equations. *Mathematics and Computers in Simulation*, **23**(4), 333 – 343.

Vichnevetsky, R. 1987a. Wave Propagation Analysis of Difference Schemes for Hyperbolic Equations: A Review. *International Journal for Numerical Methods in Fluids*, **7**(5), 409 – 452.

Vichnevetsky, R. 1987b. Wave propagation and reflection in irregular grids for hyperbolic equations. *Applied Numerical Mathematics*, **3**(1-2), 133 – 166.

Walterscheid, R. L., Schubert, G., & Brinkman, D. G. 2003. Acoustic waves in the upper mesosphere and lower thermosphere generated by deep tropical convection. *Journal of Geophysical Reseach: Space Physics*, **108**(A11).

Wood, N., Staniforth, A., White, A., Thuburn, J., Allen, T., Davies, T., Diamantakis, M., Dubal, M., Gross, M., Melvin, T., Smith, C., & Zerroukat, M. 2014a (February). *ENDGame Formulation.* Technical background report Version 4.00. The Met Office, Exeter, UK.

Wood, N., Staniforth, A., White, A., Allen, T., Diamantakis, M., Gross, M., Melvin, T., Smith, C., Vosper, S., Zerroukat, M., & Thuburn, J. 2014b. An inherently mass-conserving semi-implicit semi-Lagrangian discretization of the deep-atmosphere global non-hydrostatic equations. *Quarterly Journal of the Royal Meteorological Society*, **140**(682), 1505 – 1520.

World Meteorological Organization. 2008 (April). *The Potential Role of WMO in Space Weather.* Tech. rept. World Meteorological Organization, Geneva, Switzerland.

Yeh, K. C., & Liu, C. H. 1974. Acoustic-gravity waves in the upper atmosphere. *Reviews of Geophysics*, **12**(2), 193 – 216.

Zettergren, M. D., & Snively, J. B. 2013. Ionospheric signatures of acoustic waves generated by transient tropospheric forcing. *Geophysical Research Letters*, **40**(20), 5345 – 5349.